

Graduate School for Cellular and Biomedical Sciences

University of Bern

Insight on neuroendocrine neoplasms from patient- derived cell culture systems

PhD Thesis submitted by

Simon April-Monn

for the degree of

PhD in Biomedical Sciences

Supervisor

Prof. Dr. Aurel Perren

Institute of Pathology (IFP)

Faculty of Medicine of the University of Bern

Co-advisor

Prof. Dr. Mark. A. Rubin

Department for BioMedical Research (DBMR)

Faculty of Medicine of the University of Bern



Accepted by the Faculty of Medicine, the Faculty of Science and the Vetsuisse Faculty of the University of Bern at the request of the Graduate School for Cellular and Biomedical Sciences

Bern,

Dean of the Faculty of Medicine

Bern,

Dean of the Faculty of Science

Bern,

Dean of the Vetsuisse Faculty Bern

Acknowledgement

I am incredibly grateful to my supervisors, Prof. Aurel Perren and PD Dr. Ilaria Marinoni, for the opportunity to contribute to their vision and their pursuit of improving the lives of PanNEN patients searching for alternative therapy options. I appreciate you helping me learn to prioritize my tasks without losing sight of the overall picture. Thank you for being a mentor and for all the great scientific conversations we have had about neuroendocrine neoplasms, a fascinating field, which is full of exciting questions and aspects and has captivated me. You showed me that being willing to leave some blanks is essential to success and that learning to do so is an ongoing process and requires lifelong learning.

I want to thank Dr. Philipp Kirchner for sharing his phenomenal computational skills allowing me to improve my coding and explore new bioinformatic paths. I enjoyed our critical and constructive discussions on new strategies, robust experimental designs, and meaningful readouts. Big thanks go to Renaud Maire for all his technical assistance in the lab, his supportive attitude, and his stoic mindset. I also want to thank all current and former lab members for keeping a vivid atmosphere, especially Dr. Magdalena Skowronska, Dr. Annunziata Di Domenico, Dr. Valentina Andreasi, Dr. Tabea Wiedmer, Umara Rafiqi, Dr. Martin Sadowski, Tsilla Sunier, Dr. Aziz Chouchane and Simona Avanthay.

Many thanks go to current and former members of the translational research unit, especially to Loredana Daminescu, Carmen Cardozo, Dr. Irene Centeno Ramos, and Dr. José Alberto Galván Hernández for their fantastic work and their invaluable expertise in every regard of tissue processing. I also am grateful to them for creating a friendly and positive work environment and helping wherever and whenever possible.

I want to thank my office mate, Dr. Elham Kashani, for her heartfelt nature and her kind and motivating words at any time. Many thanks to Dr. Joel Zindel and Dr. Philipp Zens for the brainstorming sessions and exchanges on technical and methodological advances. Also, I want to thank all the other research groups in experimental pathology, the clinicians, as well as all the people from the technical support team for creating a stimulating working atmosphere.

I am thankful for all the fruitful collaborations during my PhD. To Prof. Bertram Wiedenmann and Dr. Katharina Detjen, in particular, I am indebted for their unwavering confidence in me, their enthusiasm for my ideas, and willingness to share their knowledge and advice at every stage of the project and excel my research. I want to thank Dr. Marco Schiavo Lena for sharing his clinical knowledge and for being available anytime to discuss on NEN histopathology.

I'd like to thank the members of my PhD thesis committee. I want to thank my mentor Prof. Marianna Kruithof-de Julio, for her valuable input during the project evaluations keeping the administrative parts lean and efficient. I want to thank Prof. Mark Rubin for his time, constructive feedback, and personal and scientific advice. I want to thank Prof. Jérôme Cros for evaluating my thesis as an external co-referee.

On a personal note, I thank my friends and my family for their support throughout my study years and for keeping faith in me. Finally, I thank my beloved wife Sandra for her incredible support, her patience, and her utmost belief in me and in my abilities to succeed in whatever I want to do.

Abstract

Pancreatic neuroendocrine neoplasms (PanNENs) are rare cancers that originate in islet cells of the pancreas. PanNENs appear clinically and biologically extremely heterogeneous. While highly proliferative cases are invariably lethal, slower-proliferating neuroendocrine neoplasms (NENs)—representing predominant cases—have unpredictable clinical courses varying from indolent to malignant. Until now, surgery remains the only curative option with remission rates higher than 50%. In contrast to many other malignancies, there are no molecular characteristics and biomarkers supporting treatment decisions in advanced patients, and treatment selection remains a matter of empirical and clinician-based judgment. Better strategies are required to assign the appropriate treatment to the appropriate patient, prevent unnecessary treatment, and select a potentially effective therapy for each patient. Recent comprehensive next-generation sequencing (NGS) screens in patients helped to extend our biological understanding of the disease. Nonetheless, the lack of relevant complementary preclinical models and the rarity of PanNEN disease are two major obstacles to further translational progress. Developing more personalized *in vitro* models for studying functional dependencies in these tumors is, therefore, an urgent unmet need in the field.

The overall goal of this thesis was to study patient-specific cancer vulnerabilities in PanNENs that can guide more personalized pharmacological treatment approaches in PanNEN therapy. The underlying central hypothesis was that combining patient-derived tumoroid cultures and molecular tumor profiling provides a composite biomarker for standard-of-care treatments and novel preclinical pharmacotherapies for PanNEN disease.

In this thesis, we present an *in vitro* PanNEN screening platform that facilitates world-wide sample collection, efficient processing, characterization, and screening of tumor tissues from human patients. Using this setup, we achieved high success rates in cell isolation, three-dimensional (3D) culture, and *in vitro* drug screening—even within low abundant specimens. Patient-derived (PD) tumoroids retain key biological characteristics of the original tumors, including the expression of neuroendocrine markers and hormone secretion. Notably, PD tumoroids replicate the growth phenotypes of the original tumors. Extensive transcriptional characterization further demonstrated the high similarity between PD tumoroids and original tumors. Time-course drug screening of first-line and exploratory therapies and hierarchical cluster analysis dissected distinctive sensitivity profiles likely reflecting individual patient responses. Profiling individual high-grade gastroenteropancreatic neuroendocrine neoplasms (GEP-NENs) patients and aligning *in vitro* and molecular drug responses to the clinical

response reconfirmed that PD tumoroids mimic clinical response to cisplatin and temozolomide *in vitro*. Moreover, investigating molecular stress responses in PD tumoroids *in silico*, we discovered and functionally validated Lysine demethylase 5A (KDM5A) and interferon-beta (IFNB1) as two co-vulnerabilities that act synergistic in combination with cisplatin and may present novel therapeutic options.

In summary, patient-derived cell culture models offer the possibility to study individual tumor characteristics and serve as a valuable preclinical tool that allows the assessment of patient-specific treatment strategies. Our data demonstrate that PD tumoroids may be well suited for timely and meaningful *in vitro* pharmacotyping providing subsidiary therapy information. Based on these findings, we believe that our study has taken an important step toward justifying more personalized clinical protocols involving PD tumoroids in patients with neuroendocrine neoplasms. We anticipate that PD tumoroids and their broader application will aid in the identification of novel predictive biomarkers, thereby refining therapies and closing the gap between clinical and preclinical research in the neuroendocrine tumor field.

Table of content

Acknowledgement	I
Abstract	III
Table of content	V
1 Introduction	1
1.1 Pancreatic Neuroendocrine Neoplasm	1
1.1.1 General consideration and epidemiology	1
1.1.2 Classification and histopathology	1
1.1.3 Principal clinical manifestation	4
1.1.4 Clinical prognostic factors	5
1.1.5 Molecular genetics	5
1.1.5.1 Hereditary PanNETs	5
1.1.5.2 Sporadic PanNETs	6
1.1.5.3 NET G3	9
1.1.5.4 PanNECs	10
1.1.6 Therapy options	10
1.1.6.1 Management of local or locoregional disease	11
1.1.6.2 Management of advanced disease	11
1.1.6.3 A selection of frequently used therapeutical approaches	11
1.2 Epigenetics in PanNEN	15
1.2.1 Fundamentals in epigenetic regulation	15
1.2.2 Aberrant DNA methylation and epigenetic subtyping in PanNENs	17
1.2.3 Aberrant histone methylation and therapeutic options in PanNEN	19
1.2.3.1 Aberrant KDM5A signaling (H3K4 modulation)	20
1.2.3.2 Aberrant EZH2 signaling (H3K27 modulation)	21
1.2.4 Clinical implication of targeting epigenetics in cancer	23
1.3 Modeling pancreatic neuroendocrine neoplasm	25
1.3.1 Human preclinical models of neuroendocrine neoplasm	25

1.3.1.1	Human cell line models of PanNEN	25
1.3.1.2	Patient-derived models of PanNEN	26
1.3.2	Establishing three-dimensional <i>in vitro</i> cultures to model cancer	29
1.3.3	Testing drug sensitivity in three-dimensional <i>in vitro</i> cultures of cancer	31
1.3.4	Emerging opportunities from patient-derived three-dimensional <i>in vitro</i> cultures in preclinical research.....	32
1.3.4.1	Representation of genotypic and phenotypic patient characteristics <i>in vitro</i>	32
1.3.4.2	Mechanistic insight from tumor organoids	33
1.3.4.3	Drug testing and treatment selection in patient-derived tumoroid models ..	33
2	Rationale and objective of the project.....	35
3	Results	36
3.1	Project 1: Three-Dimensional Primary Cell Culture: A Novel Preclinical Model for Pancreatic Neuroendocrine Tumors	36
3.1.1	Specific introduction	36
3.1.2	Specific hypothesis and aims	36
3.1.3	Manuscript 1: “ <i>Three-Dimensional Primary Cell Culture: A Novel Preclinical Model for Pancreatic Neuroendocrine Tumors</i> ”	37
3.1.4	Extended discussion	60
3.2	Project 2: Tumoroids of advanced high-grade neuroendocrine neoplasms mimic patient chemotherapy responses and guide the design of personalized combination therapies	63
3.2.1	Specific introduction	63
3.2.2	Specific hypothesis and aims	63
3.2.3	Manuscript 2: “ <i>Tumoroids of advanced high-grade neuroendocrine neoplasms mimic patient chemotherapy responses and guide the design of personalized combination therapies</i> ”	64
3.2.4	Extended discussion	105
3.3	Project 3: EZH2 Inhibition as New Epigenetic Treatment Option for Pancreatic Neuroendocrine Neoplasms (PanNENs).....	108
3.3.1	Specific introduction	108

3.3.2	Specific hypothesis and aims	108
3.3.3	Manuscript 3: “ <i>EZH2 inhibition as new epigenetic treatment option for Pancreatic Neuroendocrine Neoplasms (PanNENs)</i> ”	109
3.3.4	Extended discussion	134
4	Overall Discussion and Outlook.....	136
5	References	142
6	Co-authorship publications	151
6.1	Manuscript 4: “ <i>Intraperitoneal microbial contamination drives post-surgical peritoneal adhesions by mesothelial EGFR-signaling</i> ”	151
6.2	Manuscript 5: “ <i>Combined Targeting of Pathogenetic Mechanisms in Pancreatic Neuroendocrine Tumors Elicits Synergistic Antitumor Effects</i> ”	165
6.3	Manuscript 6: “ <i>Validation of Immunohistochemistry for Canine Proteins Involved in Thyroid Iodine Uptake and Their Expression in Canine Follicular Cell Thyroid Carcinomas (FTCs) and FTC-Derived Organoids</i> ”	188
7	Curriculum vitae	VII
8	List of publications	VIII
9	Declaration of originality	IX

1 Introduction

1.1 Pancreatic Neuroendocrine Neoplasm

1.1.1 General consideration and epidemiology

Pancreatic neuroendocrine neoplasms (PanNEN) are a heterogeneous family of malignancies originating from neuroendocrine cells of the islets of Langerhans in the pancreas. The term “neuroendocrine” indicates that these cells exhibit mixed morphological and physiological attributes of both the neural and endocrine regulatory systems¹. A minimum of five individual neuroendocrine cell types have been described throughout the pancreas¹⁻³ and have been recognized in PanNENs thereby underlining the cellular heterogeneity and biological complexity found among these malignancies^{4,5}. Irrespective of their cellular origin, common to all PanNENs is their ability to synthesize and secrete amine and peptide secretory products⁶ which are stored in large dense-core vesicles⁷. Proteins, i.a. chromogranin A (CGA) and synaptophysin associated with these vesicles are utilized as specific neuroendocrine markers in diagnostic routine⁸. PanNENs are divided into pancreatic neuroendocrine tumors (PanNET) or neuroendocrine carcinomas (PanNEC). Incidence of PanNETs is estimated to be less than 1 per 100000 person per year (ppy) in the US and Europe⁹⁻¹², whereas PanNECs are even rarer with age-adjusted incidence rates of only ~0.07 per 100000 ppy in the US¹³. The five-year survival drastically differs between localized disease (79-94%), locally advanced disease (60-89%), and metastatic disease (27-58%)^{9,14}.

1.1.2 Classification and histopathology

Neuroendocrine neoplasms (NENs) are characteristically heterogeneous, whether from a genetic, biochemical, cellular, location, or symptomatic viewpoint⁴. General principles guiding the classification of both functioning and non-functioning neuroendocrine neoplasm irrespective of their location are based on morphological differentiation and proliferation rate, including well-differentiated low- (G1), intermediate- (G2), or high-grade (G3) neuroendocrine tumor (NET) or poorly differentiated neuroendocrine carcinoma (NEC)^{8,15}. Additionally, neoplasms with neuroendocrine and non-neuroendocrine tumor compartments consisting of at least 30% each are classified separately from their pure counterparts as (well- or poorly-differentiated) mixed neuroendocrine-non-neuroendocrine neoplasms (MiNEN)^{8,15}. NENs are graded according to their Ki-67 index and mitotic count in hot spots following the World Health Organization’s (WHO) guidelines^{8,15,16}.

Table 1 Classification and grading criteria for neuroendocrine neoplasms of the gastrointestinal tract and hepatopancreatobiliary organs. Adapted from ⁸

Terminology	Differentiation	Grade	Mitotic rate* (mitoses/2 mm ²)	Ki-67 index*
NET, G1	Well differentiated	Low	<2	<3%
NET, G2		Intermediate	2–20	3–20%
NET, G3		High	>20	>20%
NEC, small-cell type (SCNEC)	Poorly differentiated	High [†]	>20	>20%
NEC, large-cell type (LCNEC)			>20	>20%
MiNEN	Well or poorly differentiated [‡]	Variable [‡]	Variable [‡]	Variable [‡]

LCNEC, Large-cell neuroendocrine carcinoma; MiNEN, Mixed neuroendocrine–non-neuroendocrine neoplasm; NEC, Neuroendocrine carcinoma; NET, Neuroendocrine tumour; SCNEC, Small-cell neuroendocrine carcinoma.

*Mitotic rates are to be expressed as the number of mitoses/2 mm² as determined by counting in 50 fields of 0.2 mm² (i.e. in a total area of 10 mm²); the Ki-67 proliferation index value is determined by counting at least 500 cells in the regions of highest labelling (hot-spots), which are identified at scanning magnification; the final grade is based on whichever of the two proliferation indexes places the neoplasm in the higher-grade category.

[†]Poorly differentiated NECs are not formally graded, but are considered high-grade by definition.

[‡]In most MiNENs, both the neuroendocrine and non-neuroendocrine components are poorly differentiated, and the neuroendocrine component has proliferation indices in the same range as other NECs, but this conceptual category allows for the possibility that one or both components may be well differentiated; when feasible, each component should therefore be graded separately.

For staging, the Union for International Cancer Control/American Joint Committee on Cancer (UICC/AJCC) TNM staging system that was adopted from the European Neuroendocrine Tumor Society (ENETS) is in use ¹⁷. Neuroendocrine carcinomas are classified according to the TNM classification of adenocarcinomas of the same organ.

Table 2 TNM classification of tumors of the neuroendocrine pancreas (G1 and G2). Adapted from ¹⁷

T – Primary Tumour^{a)}

TX	Primary tumour cannot be assessed
T0	No evidence of primary tumour
T1	Tumour limited to pancreas ^{b)} 2 cm or less in greatest dimension
T2	Tumour limited to pancreas ^{b)} more than 2 cm but less than 4 cm in greatest dimension
T3	Tumour limited to pancreas ^{b)} more than 4 cm in greatest dimension or tumour invading duodenum or bile duct.
T4	Tumour perforates visceral peritoneum (serosa) or invades other organs or adjacent structures

N – Regional Lymph Nodes

NX	Regional lymph nodes cannot be assessed
N0	No regional lymph node metastasis
N1	Regional lymph node metastasis

M – Distant Metastasis

M0	No distant metastasis
M1	Distant metastasis
M1a	Hepatic metastasis(is) only
M1b	Extrahepatic metastasis(is) only
M1c	Hepatic and extrahepatic metastases

Stage

Stage I	T1	N0	M0
Stage II	T2 T3	N0	M0
Stage III	T4	N0	M0
	Any T	N1	M0
Stage IV	Any T	Any N	M1

a) For any T, add (m) for multiple tumours.

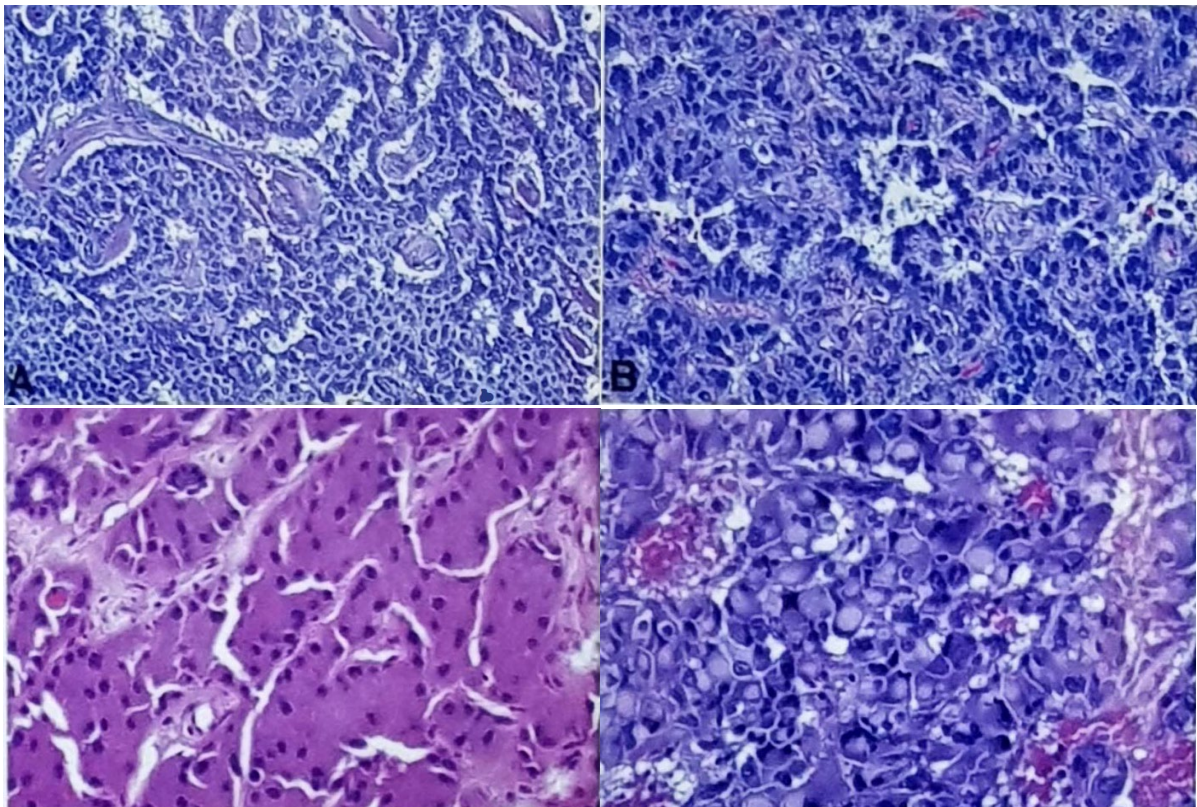
b) Invasion of adjacent peripancreatic adipose tissue is accepted but invasion of adjacent organs is excluded.

Rules for Classification: This classification system applies to well differentiated neuroendocrine tumours (carcinoid tumours and atypical carcinoid tumours) of the pancreas. High grade neuroendocrine carcinomas are excluded and should be classified according to criteria for classifying carcinomas of the pancreas.

Regional lymph nodes: The regional lymph nodes correspond to those listed under the appropriate sites for carcinoma.

Histomorphology in G1/G2 PanNETs shows an organoid architecture, but various other arrangements are also found, including nesting (solid), trabecular, patterns, tubuloacinar, and (pseudo)glandular patterns ^{8,15,16}. G3 PanNETs present overlapping morphological features with G1/G2 PanNETs but, as per definition, show higher mitotic activity ^{8,15}. G3 PanNET may also show marked nuclear pleomorphism, diffuse infiltrative patterns, and necrosis ^{8,15} which can make a distinction from NEC difficult even for experienced pathologists.

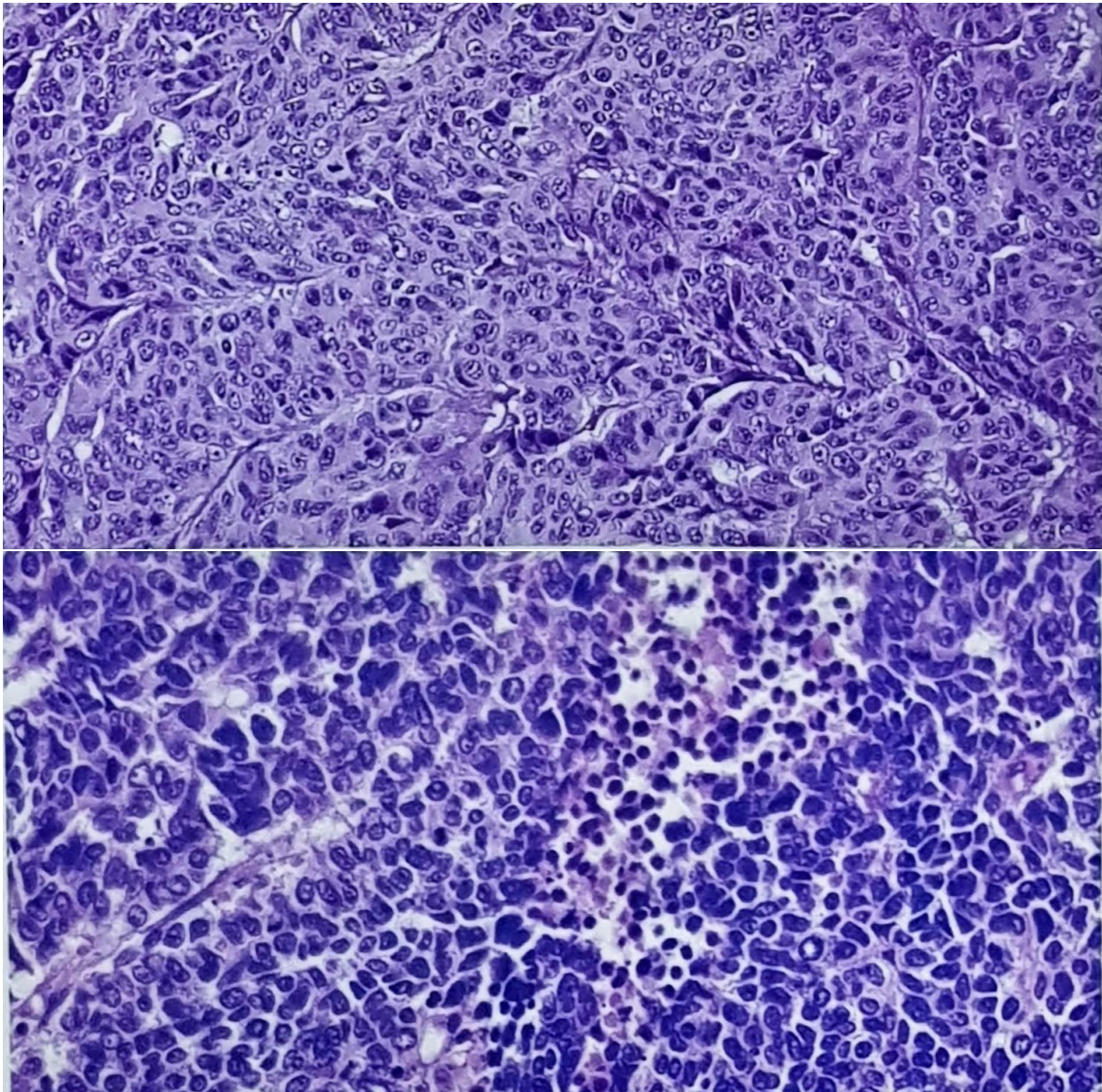
Figure 1 Example of non-functional pancreatic neuroendocrine tumor histomorphology. Reprinted from ¹⁵ © 2017, The Authors, with permission from Prof. V. Adsay and Dr. D. Klimstra.



(Top) Nesting/solid (left) and trabecular (right) architecture. **(Bottom)** Oncolytic non-functioning pancreatic neuroendocrine tumor with abundant granular eosinophilic cytoplasm (left). Pleomorphic non-functioning pancreatic neuroendocrine tumor with pleomorphic nuclei and rhabdoid-like cytoplasmic inclusions (right).

PanNECs are characterized by partial or complete loss of cytoarchitectural organization and the presence of necrosis. They can present as two morphological subtypes: The large-cell type (LC) presents with organoid, nesting, or solid sheet-like patterns with round or polygonal cells with a moderate amount of cytoplasm and large nuclei with prominent nucleoli and vesicular chromatin. The small-cell type (SC) shows diffuse infiltrative sheets of cells having minimal cytoplasm, a high nuclear to cytoplasmic ratio, and fusiform nuclei with inconspicuous nucleoli and finely granular chromatin ¹⁶.

Figure 2 Example of pancreatic neuroendocrine carcinoma histomorphology. Reprinted from ¹⁵ © 2017, The Authors, with permission from Prof. V. Adsay.



(Top) Pancreatic neuroendocrine carcinoma (poorly differentiated neuroendocrine neoplasm), large-cell type. Diffuse growth of relatively monotonous cells with a nested/organoid pattern compartmentalized by delicate vasculature, indicating neuroendocrine differentiation. Cytological atypia and prominent mitotic activity indicate this carcinoma's high-grade (poorly differentiated) nature. **(Bottom)** Pancreatic neuroendocrine carcinoma (poorly differentiated neuroendocrine neoplasm), small cell type. The cells have high-grade cytology, minimal cytoplasm, and a high nuclear-to-cytoplasmic ratio. Mitotic activity is brisk, and necrosis is readily evident.

1.1.3 Principal clinical manifestation

Tumors associated with clinical symptoms caused by abnormal secretion of hormones are considered functioning (F) (syndromic) NENs ^{8,15}

Functioning PanNENs represent ~15% of all PanNENs and are termed according to the predominant bioactive agent secreted causing clinical symptoms, e.g., insulinoma (insulin) related to hypoglycemia.

Non-functioning (NF) (non-syndromic) NENs are not associated with syndromes caused by hormonal hypersecretion but may still secrete peptide hormones and biogenic substances at lower levels^{8,15}. Due to the initial asymptomatic and nonspecific course, low-proliferating NF NENs can go undetected for years and are often diagnosed at advanced disease stages with regional or distant metastasis associated with poorer prognosis^{9,18}.

1.1.4 Clinical prognostic factors

Disease stage and tumor grade depict two important prognostic parameters and are essential in therapeutic decisions and the management of patients¹⁹⁻²¹. All PanNEN harbor a metastatic potential and are defined as potentially malignant²². PanNENs are highly prevalent at advanced disease stages, and a large proportion of patients (40-60%) present with metastasis^{9,14}. The most frequent metastatic sites for well-differentiated PanNETs include the liver (40-93%), lymph nodes, and bone (4-15%)²³⁻²⁶. Rarer sites include metastasis to the lung, brain, and peritoneum²⁷. The presence of extra-hepatic metastasis is associated with a poorer prognosis, whereas female sex, young age, absence of symptoms at diagnosis, and primary tumor resection are associated with a better prognosis^{9,28}.

1.1.5 Molecular genetics

1.1.5.1 Hereditary PanNETs

Hereditary PanNENs account for the minority (~10-20%) of all PanNENs²⁹. In a hereditary setting, PanNENs are multifocal, and the onset of the disease is earlier than in sporadic tumors¹⁹. Hereditary PanNENs are associated with cancer-predisposition syndromes such as multiple endocrine neoplasia type 1 (MEN1) or type 4 (MEN4) syndrome, von Hippel-Lindau (VHL) disease, tuberous sclerosis (TS), and neurofibromatosis type 1 (NF1). High *MEN1* mutational prevalence in pancreatic microadenomas (potential PanNET precursor lesions) in MEN1 syndrome patients^{30,31} further suggested a potent role of *MEN1* at early stages and tumor initiation^{29,32}.

Whole-genome mutational signature analysis revealed additional germline mutation in known neuroendocrine predisposition genes affecting *MEN1* (Menin 1), *VHL* (Von Hippel-Lindau Tumor Suppressor), and *CDKN1B* (Cyclin Dependent Kinase Inhibitor 1B) in 7% of patients

³³. Recently, several studies have revealed novel germline mutations affecting DNA damage repair machinery genes, but their clinical relevance is not yet clear. Germline inactivating gene mutation in *MUTYH* (MutY DNA glycosylase), a gene involved in DNA base excision repair, was coupled with a loss of heterozygosity ³³. Several germline mutations were found in *CHEK2* (Checkpoint Kinase 2), which is involved in homologous DNA damage repair ³³. In the same line, *BRCA2* (Breast cancer 2 DNA Repair Associated) mutation was found in one PanNET that harbored a highly prominent BRCA-deficiency mutational signature and a genomic instability pattern described in BRCA-deficient breast cancers ³³. Novel germline mutations were found in *PIF1* (PIF1 5'-To-3' DNA Helicase) ³⁴ and *ATM* (ATM Serine/Threonine Kinase) ³⁵, both affecting DNA damage repair, as well as *MAPKBPI* (Mitogen-Activated Protein Kinase Binding Protein 1) ³⁴ a member of the MAPK/ERK signaling pathway. Mutations in *ATM* have also previously been detected in a sporadic context ³⁶. Together these findings underlined that a larger than expected fraction of PanNETs may arise from germ line mutations.

1.1.5.2 Sporadic PanNETs

Most PanNETs occur sporadically, and several genes that cause hereditary NEN syndromes are also found in the sporadic setting ⁶. The mutational burden in PanNET is low (~0.82 mutations per megabase) ^{33,35}. Numerous recent larger scale and higher throughput genomic studies reconfirmed recurrent mutations in genes involved in several core areas that are targeted by a large and heterogenous number of alterations.

Chromatin remodeling (MEN1, SETD2, ARID2, SMARCA4, KMT2C/MLL3): Somatic mutation in *MEN1*, especially in non-functioning tumors, is one of the most frequently found alterations in PanNETs and has been described in many studies. A first whole-exome study in PanNETs identified mutations in *MEN1* in 44% of sporadic advanced patients (n=58) ³⁷ and described additional frequent mutations in chromatin remodeling genes *DAXX* (Death Domain Associated Protein) and *ATRX* (Alpha Thalassemia/Mental Retardation Syndrome X-Linked). Chromosomal instability was often found in PanNETs by comparative genomic hybridization ^{38,39}. A connection between loss of *DAXX* and *ATRX*, altered lengthening of telomeres (ALT), and chromosomal instability was elegantly described by Marinoni *et al.* ⁴⁰. *MEN1* encodes for menin, a scaffold protein that links chromatin regulatory complexes to specific transcription factors (i.a., *MYC* (MYC Proto-Oncogene, BHLH Transcription Factor), *CTNNB1* (Beta-Catenin)), converging into positive and negative regulation of gene expression ⁴¹. A prominent role of *MEN1* was associated with its role in coordinating chromatin-remodeling genes through epigenetic regulation: Menin recruits MLL (Mixed Lineage Leukaemia) 1 and 2/SET1-like

histone methyltransferase complexes, that specifically methylates histone 3 at lysine 4 (H3K4) enhancing transcriptional activity for various downstream genes ⁴²⁻⁴⁴. Recently, recurrent inactivating mutation and chromosomal rearrangement in other chromatin remodeling genes were described underscoring its important role in PanNET tumorigenesis. *SETD2* (SET Domain Containing 2, Histone Lysine Methyltransferase) and *ARID2* (AT-Rich Interaction Domain 2), involved in chromatin structure modification, were mutated in 18% and 13% of advanced well-differentiated PanNETs ⁴⁵. A whole-genome sequencing study in sporadic PanNETs (n=98) reconfirmed chromosomal rearrangements in these two genes and found additional gene alterations involved in chromatin remodeling, including *KMT2C/MLL3* (Lysine Methyltransferase 2C/Mixed Lineage Leukaemia 3) and *SMARCA4* (SWI/SNF Related, Matrix Associated, Actin Dependent Regulator Of Chromatin, Subfamily A, Member 4) ³³.

Altered lengthening of telomeres (DAXX and ATRX): Gene mutations in *DAXX* or *ATRX* were found in 18% and 25% of patients ³⁷. Protein loss and mutation in *DAXX* or *ATRX* are highly correlated with an ALT phenotype in PanNETs ^{40,46}. ALT is a telomerase-independent mechanism to maintain DNA telomere length allowing tumors to escape cellular senescence ^{47,48}. In the metastatic site, *ATRX/DAXX* mutation and ALT activation was associated with better prognosis ^{37,49}, whereas patients with loss of *DAXX* and *ATRX* expression and ALT in the primary tumor had poorer prognosis and showed chromosomal instability ^{40,49}. Loss of *DAXX/ATRX* was associated with larger tumors (>2cm), chromosomal instability, metastatic disease, and reduced relapse-free and tumor-specific survival ^{40,50} and absent in sporadic and familial incidental neuroendocrine microadenomas ⁵¹ altogether suggesting *DAXX/ATRX* alteration as a late event in PanNET progression. The role of aberrant *ATRX/DAXX* signaling exceeds telomere alteration and shows direct links to chromatin remodeling and DNA methylation, impacting tumorigenesis. *DAXX* and *ATRX* interact and form a histone chaperone complex responsible for the deposition of H3.3 (histone 3.3) in heterochromatic regions such as telomeric and pericentromeric regions ⁵²⁻⁵⁴ and retrotransposons ⁵⁵. *DAXX* interacts with *SUV39H1* (Suppressor Of Variegation 3-9 Homolog 1), an H3K9 methyltransferase 1, and *DNMT1* (DNA Methyltransferase 1), and epigenetically silences genes such as *RASSF1* (Ras Association Domain Family Member 1) ⁵⁶.

PI3K (Phosphatidylinositol 3-kinase)/MTOR (Mechanistic Target Of Rapamycin Kinase) signaling (TSC1, TSC2, VHL, PTEN, EWSR1 fusion products, DEPDC5): Aberrant activation of MTOR pathway including target genes *PTEN* (Phosphatase And Tensin Homolog), *TSC1* (Tuberous Sclerosis Complex Subunit 1), *TSC2* (Tuberous Sclerosis Complex Subunit 2) and

PIK3CA (Phosphatidylinositol-4,5-Bisphosphate 3-Kinase Catalytic Subunit Alpha), *DEPDC5* (DEP Domain Containing 5, GATOR1 Subcomplex Subunit) was found in 15% of PanNETs and was associated with poor prognosis^{33,37}. The MTOR pathway has a prominent role in cellular processes, including angiogenesis, cell cycle progression, DNA repair, apoptosis, gene expression, and epigenetic regulation⁵⁷⁻⁵⁹. Altered protein expression of TSC2 and PTEN was frequently found in non-functioning PanNETs where increased protein loss correlated with liver metastasis, shorter progression-free, shorter disease-free, and shorter overall survival⁶⁰. Additionally, previously unknown *EWSR1* (EWS RNA Binding Protein 1) fusion events (*EWSR1-BEND2*; *EWSR1-FLI1*) and amplification of *RET* (Ret Proto-Oncogene) receptor ligand *PSPN* (Persephin), both involved in the activation of MTOR signaling, were described³³. The innate dysregulation of PI3K/MTOR pathway may explain the improved overall survival found in a subset of advanced PanNETs undergoing everolimus treatment⁶¹. However, insufficient evidence supports the use of PI3K pathway mutations as a biomarker of treatment response⁶².

Other: Chromosomal rearrangements and somatic mutations were also found that inactivated genes implicated in cell cycle checkpoints such as *CDKN1C* (Cyclin Dependent Kinase Inhibitor 1C), *CDKN2A* (Cyclin Dependent Kinase Inhibitor 2A; P16), *CDKN1A* (Cyclin Dependent Kinase Inhibitor 1A), and *CDKN1B* (Cyclin Dependent Kinase Inhibitor 1B)^{33,50}. The role of isolated mutations alone provides a rationale for tumorigenesis in only half of the PanNETs, whereas for the rest, chromosomal or epigenetic mechanisms might play a fundamental role⁶³. Insulinomas have a discrete genetic basis regarding their somatic mutations^{33,37,64-67}. Recurrent *YY1* (YY1 Transcription Factor) mutation is considered a driver and was found in 15-32% of insulinomas⁶⁴⁻⁶⁷ but was absent in non-functional PanNETs³³. Copy number variation (CNV) patterns in insulinomas (chromosomes 7, 3p, 5q, and 13q) differ from CNV patterns in PanNETs and consist of early amplification events⁶⁶. The reason for this different behavior may be attributed to a different cell of origin and underlying susceptibilities. A direct origin of normal adult beta-cells or from a common progenitor is highly plausible⁶⁸.

Copy number aberration (CNA)/Chromosomal aberrations studies in PanNETs: Several studies have described an association between copy number aberration (CNA) profiles and molecular subtypes in PanNETs; Scarpa *et al.* described four CNV groups based on arm-length copy number patterns. A first group was characterized by recurrent pattern of whole chromosomal loss (RPCL) affecting multiple chromosomes (1,2,3,6,8,10,11,15,16,22)³³. This CNV group was enriched in G2, *DAXX/ATRX* mutated, ALT phenotype tumors and showed the

highest frequency of mutations in MTOR pathway genes ³³. A second CNV group showed limited copy number events mostly affecting losses in chromosome 11. Mutations were not limited to but frequent in MEN1, and the majority did not harbor an ALT phenotype ³³. A small third CNV group showed polyploidy with gains in all chromosomes and harbored the highest somatic mutation rate ³³. A fourth CNV group was characterized by aneuploidy and whole chromosomal gains complementary to losses of the RPCL group ³³. Other studies reported similar CNV profiles and recurrent chromosomal alteration in PanNETs: Hong *et al.* investigated the prognostic relevance of CNVs and succeeded in stratifying relapse risk in NF-PanNET based on found CNV patterns into moderate and high ⁶⁶. In clinically homogenous well-differentiated sporadic PanNETs, Lawrence *et al.* found two clinically relevant patterns of loss of heterozygosity (LOH), underlining the important role of chromosomal aberration. Recurrent LOH in several chromosomes had poor clinical outcomes, whereas LOH in only chromosome 11 showed better clinical outcomes ³⁵. A high number of chromosomal gains in small PanNETs (<3cm) were strongly associated with metastasis (73%), ALT positivity, DAXX/ATRX loss, and grade 2 tumors and showed a high rate of somatic mutation in driver and other genes ⁶⁹. A limited number of chromosomal events were associated with *DAXX/ATRX* wildtype and normal protein expression and less frequently associated with metastasis ⁶⁹. Altogether these findings underline the important role of chromosomal aberrations and hint toward a potential classification of PanNET depending on mutational profiles together with profiling chromosomal alterations and ALT status to stratify risk associated with PanNETs.

1.1.5.3 NET G3

NET G3s bear core driver mutations, as found in G1/G2 NETs with *MEN1*, *DAXX*, and *ATRX* mutations or protein loss as the three most prominent examples ⁷⁰. Especially in the case of pancreatic lesions, these mutations may assist the differential diagnosis of high-grade NETs and NECs in challenging histological cases ^{19,71,72}. Some PanNET G3 can, however, present expression characteristics that are not classically associated with neuroendocrine tumors, such as alteration in RB1 (Retinoblastoma Transcriptional Corepressor 1) (10%), P16 (CDKN2A) (20%), or TP53 (Tumor Protein P53) (30%) ⁷³ and since there is no dichotomic situation other approaches such as a four gene classifier for NEC (including TP53, APC (APC Regulator Of WNT Signaling Pathway), KRAS (KRAS Proto-Oncogene, GTPase), BRAF (B-Raf Proto-Oncogene, Serine/Threonine Kinase)) have been proposed to assist differential diagnosis ⁷⁰.

1.1.5.4 PanNECs

Molecular findings reinforced that poorly-differentiated NECs from a biological and genetic viewpoint represent a different disease than well-differentiated NET^{37,74}. *TP53* and *RB1* are two hallmark driver genes of PanNECs, affecting their ability to undergo cell-cycle arrest and enable DNA damage repair (DDR) if present^{70,75–79}. Mutation of *TP53* is found in 20 to 73% of cases^{74,80,81}, and accumulation of its gene product P53 in the nucleus in 65% to 100% of patients^{80,82–84}. *RB1* inactivating mutations and related loss of RB1 immunolabeling were reported in 74% (14/19) of poorly differentiated pancreatic NECs patients⁷⁴. In addition to mutation, TP53 and RB1 signaling can be dysregulated or suppressed by other means such as amplification of TP53 suppressor *MDM2* (MDM2 Proto-Oncogene)⁸⁵, mutation of TP53 paralogs *TP73* (Tumor Protein P73)^{70,86}, deletion or epigenetic silencing of *CDKN2A* which encodes for the RB1 signaling effector P16^{79,86}, and amplification of RB1 antagonist *CCNE1* (Cyclin E1)^{79,86}. Aberrant activation of MYC family proto-oncogenes (*MYC*, *MYCN*, *MYCL*), transcription factors that define cell lineage, are also found in GEP-NECs with predominant *MYC* amplification in up to 51% of cases^{70,76,78,79}. Dysregulation of receptor tyrosine kinase pathway, including activating mutation in *KRAS* and *BRAF* (predominantly V600E), and upregulation of PI3K/AKT (AKT Serine/Threonine Kinase 1)/MTOR pathway signaling, are also frequently found in GEP-NECs of different sites of origin^{78,87}. A recent WGS and WES (n=115) study distinguished two subgroups of pancreatic PD-NECs: A ductal-type (*KRAS*/*TP53*/*RB1*) and an acinar-type (*CTNNB1*/*CDKN2A*/*TP53*)⁸⁸. Various studies indicate that a significant fraction of PanNECs also displays frequent alteration in at least one epigenetic regulator with *ARID1A* (AT-rich interaction domain 1A), *KMT2* (histone lysine methyltransferase 2), and histone lysine demethylase (KMD) family genes as most prominent examples^{70,76,78,79,85,86,89,90}.

1.1.6 Therapy options

Management of PanNENs requires a multidisciplinary approach and adequate understanding of the aim of treatment (reduction of tumor burden vs. disease stabilization vs. symptom control) and sufficient information on important tumor characteristics, including proliferation status, expression of SSTR, tumor growth rate, and extent of the disease^{19,91}. Up-to-date, none of the available systemic therapy options can provide a cure to the patients¹⁹, and clearly defined measures predicting therapy response or therapeutic efficacy to a particular treatment are still elusive⁶.

1.1.6.1 Management of local or locoregional disease

For local or locoregional disease, surgery is considered the treatment of choice for NET G1 and NET G2 unless the operative risk is too high or the predictable postoperative functional consequences are too severe^{19,92}. In line, an extensive systematic review of pancreatic NETs described an improved long-term survival of resected non-metastatic patients⁹³. Although resection of the total tumor mass by surgery is currently the only curative approach still, 30% of patients will develop liver metastasis^{9,14,23–26}.

1.1.6.2 Management of advanced disease

Treatment sequencing and therapy options for advanced NENs are complex and consist of various approaches and therapeutical sequences, including somatostatin receptor agonist blockade, targeted radionuclides, immunotherapy (interferon), cytotoxic chemotherapy, rationally designed targeted drugs, external radiation, interventional radiological approaches, and surgery. The exact sequencing remains unclear and mostly depends on factors such as comorbidities of the individual patients and side-effects/toxicity profiles of the drugs¹⁹. The principal determinants that influence the therapeutic decision are tumor grade, tumor stage, hepatic tumor volume in case of liver metastasis, resectability of primary and metastatic tumor, presence of functional syndromes or syndromes associated with the tumor, prior treatments, and quality of life, taking into account that a patient can live for more than five years even with metastatic disease¹⁹. Systemic therapy aims to control clinical symptoms associated with the tumors and limit tumor growth leading to disease stabilization to a variable extent, depending on different prognostic factors, including grade and tumor extent¹⁹. Monitoring treatment response remains challenging since only a limited biomarker spectrum exists, and imaging approaches are not sensitive enough for exact discrimination⁴. In indolent lesions, RECIST criteria, commonly used in other (cancer) settings, are, for example, insensitive to assessing therapy response^{4,94}.

1.1.6.3 A selection of frequently used therapeutical approaches

Surgery: Up to 85% of patients with pancreatic NETs present hepatic metastasis¹⁸ but only in ~7–15% of patients can be completely resected⁹⁵. Surgery may play a role in metastatic disease in selected patients with predominant liver involvement⁹⁶. However, careful evaluation of tumor grading, distribution of lymph node metastasis, and primary site is needed¹⁹. Other forms

like palliative cytoreductive resection, e.g., debulking surgery in advanced NF GEP-NETs for alleviation of symptoms, can be considered, but the role seems not entirely clear ⁹⁶

Somatostatin analogs (SSA): Somatostatin analogs are synthetic, more stable, and more potent analogs of the neuropeptide somatostatin (SST) ⁹⁷. SST is considered a pan inhibitory agent for hormone release in the gastrointestinal tract ⁹⁸ and mediates its inhibitory effect through binding to at least five G-protein coupled somatostatin membrane receptors (SSTR 1-5) ⁹⁹. SST has been shown to exert cytostatic effects on tumor cells ¹⁰⁰. More than 80% of PanNETs express somatostatin receptors ^{101,102}, although the expression in SSTR subtypes varies ⁹⁷. The use of SSAs is standard first-line therapy in functioning NETs ⁹⁷ and has been demonstrated to stabilize tumor-associated symptoms (i.a., hormone hypersecretion, flushing, diarrhea) in ~25% of PanNET patients, especially in patients with lower proliferation (Ki-67 < 5%) and lower tumor volumes ^{97,103,104}. SSAs are exceptionally well tolerated and safe, showing only minor adverse side effects even after long-term usage ^{105,106}. However, effects on tumor growth are limited, with <5% of patients showing objective radiological tumor regression ^{103,104}.

Targeting the PI3K (Phosphatidylinositol 3-Kinase)/AKT/MTOR pathway: Everolimus inhibits the key regulatory protein mammalian target of rapamycin (MTOR) that has been related to various types of cancer ^{107,108}. MTOR, an intracellular serine/threonine protein kinase, recognizes and integrates various stress signals (e.g., nutrient and energy depletion, oxidative or hypoxic stress, and proliferative and survival signals) via the PI3K-AKT pathway and stimulates cell growth and angiogenesis ^{57-59,109}. Low expression of TSC2, a key inhibitor of the MTOR pathway, correlated with primary tumor progression and metastatic disease ⁶⁰. Additionally, aberrant AKT/MTOR pathway activation in advanced gastroenteropancreatic NETs ¹¹⁰ and recurrent mutation in several target genes ^{33,37} provide a rational for treatment; however, their implication as a therapeutical biomarker is not clear yet. The use of everolimus is recommended in progressive G1/G2 PanNETs ¹⁹. Several studies in advanced PanNET progressing during or after chemotherapy ¹¹¹ or in unresectable and metastatic PanNETs ^{61,112} demonstrated prolonged progression-free survival and high disease control rate yet with low overall response rates (<10%). Little data is available for NET G3 and NECs, but prospective phase II studies are running to evaluate its use as first- or second-line therapy in high-grade NENs ¹⁹.

Targeting Vascular Endothelial Growth Factor (VEGF) and VEGF Receptor: Sunitinib is a multi-targeted receptor tyrosine kinase (RTK) inhibitor targeting vascular endothelial growth factor receptors (VEGFR) 1 to 3 and platelet-derived growth factor receptors (PDGFR), KIT

(KIT Proto-Oncogene, Receptor Tyrosine Kinase), RET, and FLT3 (Fms Related Receptor Tyrosine Kinase 3)^{113,114}. Sunitinib impeded angiogenesis and destabilized existing vasculature and has been shown to reduce endothelial cell density and pericyte coverage of tumor vessels via blocking VEGFR 1 and 2 and PDGFR A and B in malignant pancreatic endocrine tumors of Rip1Tag2 mice¹¹⁵. However, preclinical evidence suggested the resurgence of angiogenesis and invasive tumor behavior (“rebound vascularization”) after an initial tumor stabilization and chemotherapy in advanced NENs¹¹⁶. VEGF has been implicated as key driver of angiogenesis in pancreatic neuroendocrine tumors^{116,117}. In malignant pancreatic endocrine tumors, a widespread expression of PDGFR A and B and VEGF receptors 1 to 3 was demonstrated^{118–120}. A phase III trial reconfirmed significantly improved progression-free survival in well-differentiated PanNETs¹²¹, as seen in previous studies^{122,123}. However, objective response rates were low (<10%), and serious adverse events were reported¹²¹.

Peptide receptor radiation therapy (PRRT): Peptide receptor radiation therapy (PRRT) uses radiolabeled somatostatin analogs targeting SSTR on cell surfaces. The emission of beta radiation from the coupled therapeutic radioisotope eradicates SSTR-expressing tumor cells and cells within closer proximity¹²⁴. PRRT is a therapeutic option in progressive SSTR-positive NETs with homogenous SSTR expression in all lesions assessed by SSTR imaging¹⁹. Several phase II trials and observational studies in non-functioning SSTR expressing GEP-NETs reported overall response rates ranging from 4% to 39%^{125–128}. Retrospective studies of PRRT in NEN G3 supported the therapeutic consideration with disease control rates of 30-80%, PFS of 9-23 months, and overall survival of 19-53 months. Significant better results were seen in the subset of patients with Ki-67 <55% compared to patients with higher Ki-67 scores^{129–132}.

Chemotherapy in advanced NENs: Systemic chemotherapy is recommended for patients with advanced PanNETs with an aggressive clinical course and in NEN G3 of any site¹⁹. However, therapy-induced alterations in neuroendocrine tumor biology have been reported upon systemic therapy, such as augmentation of grade after pause-rechallenge with DNA alkylating agents¹³³ or morphological and proliferative switches upon DNA intercalating agents¹³⁴ and clear recommendations for second-line therapy in NECs are missing¹³⁵.

DNA alkylating agents: Antitumoral efficacy of several DNA alkylating agents (streptozotocin, dacarbazine, temozolomide) has been well documented for PanNENs. Alkylating-agent-based treatments are the therapy of choice in metastatic PanNETs, especially in cases with elevated proliferation index ($\geq 10\%$) and/or high metastatic tumor volume, with symptoms and/or spontaneous or treatment-induced progression^{19,136}. High-grade NET patients with a Ki-67

<55% were more responsive to temozolomide treatment than platinum-based chemotherapy¹³⁷. Temozolomide, a pro-drug, is a cytotoxic agent inducing DNA alkylation at of O6 positions of guanine (O6-alkylguanine adducts), leading to base pair mismatch and futile cycles of DNA processing inducing single- and double-strand breaks that trigger cell death^{138,139}. Temozolomide can be used as monotherapy or in combination with capecitabine (CAP), showing comparable overall response rates of ~30%¹⁴⁰. The importance of O6-Methylguanine (O6-MG)-DNA-methyltransferase (*MGMT*) expression and responsiveness has been frequently reported in various tumors, especially in brain cancer¹⁴¹. The *MGMT* gene encodes for the DNA-repair protein O6-alkylguanine (O6-AG) DNA alkyl transferase (AGT; also commonly referred to as MGMT). This DNA repair protein acts independently to remove DNA alkyl adducts¹⁴¹. MGMT-promoter methylation represses *MGMT* expression in tumors and increases responsiveness to chemotherapy¹⁴¹; however, its predictive value in therapy response in PanNET remains controversial¹⁴²⁻¹⁴⁵.

DNA intercalating agents: Cisplatin is a cytotoxic agent that covalently binds to DNA and thereby forms DNA adducts that cause distortion of DNA and activate various signal-transduction pathways, including DNA-damage recognition and repair, cell-cycle arrest, and programmed cell death¹⁴⁶. Platinum-based therapy is recommended in metastatic disease in high-grade nonresectable or metastatic NECs¹⁹. However, although the initial overall response rate may be high (30-67%), the median overall survival is limited (11-19 months), and resistance is frequently observed^{147,148}. In high-grade NETs (with Ki-67 <55%), usage of platinum-based therapy is not recommended¹⁹ since reported overall response rates were much lower than in NECs¹³⁷.

1.2 Epigenetics in PanNEN

The frequency of somatic mutations in PanNENs is low, with only a few therapeutically targetable oncogenic mutations^{33,35,37}. A large fraction of recurrent (driver) gene mutation involves epigenetic regulators such as *MEN1*, and *DAXX/ATRX* highlighting the importance of aberrant epigenetic mechanisms in PanNEN disease. Converging lines of investigation have underscored a link between epigenetic dysregulation and PanNEN development^{68,149–151}. Part of the tumor development could be understood as a consequence of the combined action of multiple epigenetic events. A better understanding of contributing epigenetic factors and dysregulated epigenetic pathways may be translated into clinical practice and pave the way for developing novel therapeutic options.

1.2.1 Fundamentals in epigenetic regulation

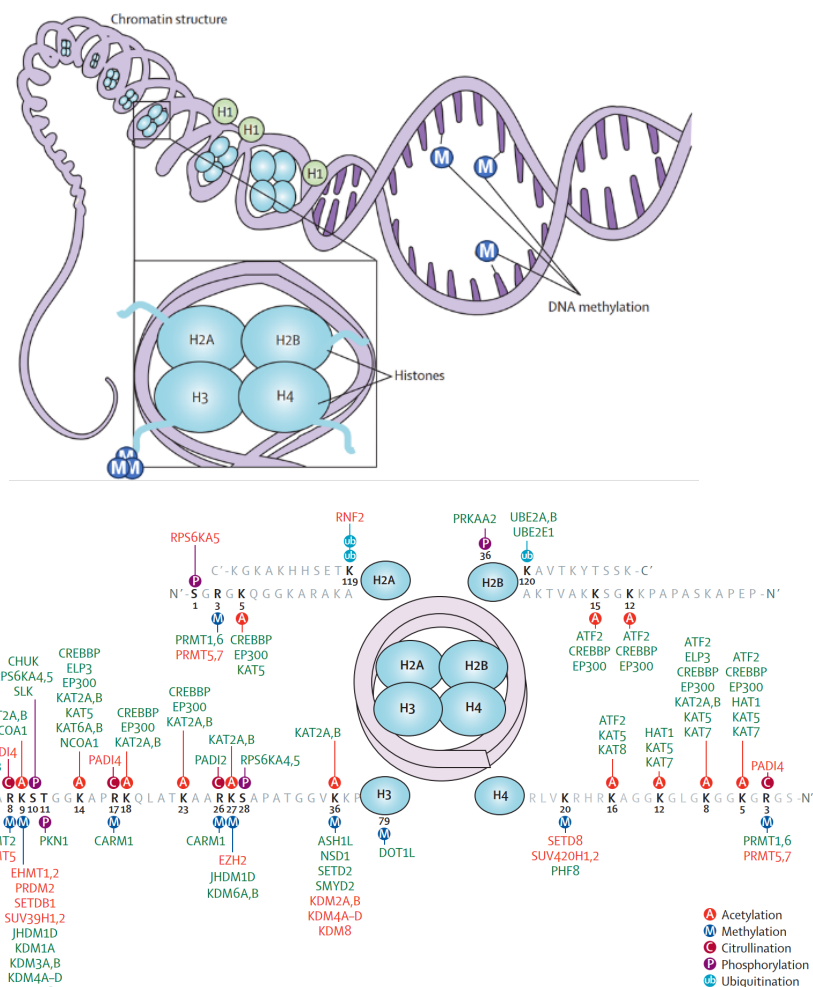
Epigenetics comprises DNA, histone proteins, and other chromatin assembly factors that are altogether structurally and functionally packed into chromatin¹⁵². Chromatin represents the essential medium through which gene activity and cellular phenotypes can be altered through accessibility and function. The nucleosomes, as the basic chromatin units, are built up by 146-bp segments of DNA wrapped around an octamer of histone proteins. The family of histone proteins consists of four canonical core histones (H2A, H2B, H3, H4), one linker histone (H1), and some additional variants with specific functions each. Each histone possesses a characteristic and flexible C- and N-terminus tail with specific amino acid residues that can be modified via covalent posttranslational modification (PTMs). Switches between active (euchromatin, permissive) and inactive (heterochromatin, repressive) states occur via epigenetic modulation, such as DNA methylation and chromatin remodeling¹⁵³.

DNA methylation of five-methylcytosine (5mC) is a corner stone of epigenetic regulation and genomic homeostasis and a highly stable mark that most often occurs in cytosines of CpG (Cytosine-phosphate-Guanine) dinucleotide sequences¹⁵⁴. Genomic loci with CpG-rich sites are called CpG islets and are frequently found in transcriptional start sites (TSS) of gene promoters¹⁵⁴. Hypermethylation of CpG islets is found in heterochromatin (inactive) regions, while hypomethylation commonly occurs in euchromatin (active) regions. Additionally, the position of the methylation impacts its regulatory function. Methylation at transcriptional start sites (TSS) blocks gene expression, whereas methylation in the gene body presumably stimulates the expression of genes¹⁵⁴. In DNA methylation, the protein family of DNA methyltransferases is involved in de novo DNA methylation and maintenance of pre-existing

marks by transferring a methyl group from S-adenosyl-L-methionine to cytosine ^{154,155}. DNA-demethylating enzymes of the ten-eleven translocation (TET) protein family reverse DNA methylation marks via oxidation steps ¹⁵⁴.

Chromatin remodeling includes incorporating specific histone variants, ATP-dependent chromatin-remodeling complexes (i.a. SWI/SNF (SWItch/Sucrose Non-Fermentable) complex), and post-translational modification of histone tails. Various posttranslational histone tail modifications cooperate to regulate chromatin states, including phosphorylation, ubiquitylation, sumoylation, APD ribosylation, acetylation, or methylation. Histone acetylation is crucial for active gene transcription and occurs at lysine residues of histone tails, and histone acetyltransferase (HATs) and histone deacetylase (HDAC) protein families tightly regulate this process ¹⁵⁶. Histone lysine methylation can exist in a mono-, di-, or tri-methylated state ¹⁵⁶. Histone lysine methyltransferase (KMTs) and histone lysine methylases (KDMs) orchestrate this complex regulatory system. KMTs are divided into several SET (Su (var)3-9, Enhancer of Zeste, Trithorax) domain KMTs, and one non-SET domain KMT, known as DOT1L ¹⁵⁶. SET-domain proteins transfer a methyl group from S-adenosyl-L-methionine (SAM) to the amino group of a lysine residue on the histone or other protein ¹⁵⁶. Most KMTs can methylate non-histone proteins, including P53, PCNA (Proliferating Cell Nuclear Antigen), STAT3 (Signal Transducer And Activator Of Transcription 3), RARA (Retinoic Acid Receptor Alpha), E2F1 (E2F Transcription Factor 1), FOXO3 (Forkhead Box O3), DNMT1, and KMT1C (Euchromatic Histone Lysine Methyltransferase 2) ¹⁵⁶. KDMs are comprised of two families of proteins: the 2-oxoglutarate-dependent Jumonji domain-containing KDM family (with three members) and the flavin-dependent KDM1 family (with 19 members) ¹⁵⁶. The effect of histone lysine methylation can either be epigenetically inactivating or activating, depending on the histone and the extent of methylation. Several additional protein families act as translators between histone modification and DNA methylation, including the Methyl-CpG-binding domain (MCB) family, the Kaiso protein family, and the SET-and Ring finger-associated (SRA) domain family. These proteins recruit and cooperate with the machinery for further genomic maintenance. Despite different substrates, the regulatory system of DNA methylation and histone modification is tightly codependent and directly influences each other ¹⁵⁷.

Figure 3 Epigenetic mechanisms regulating transcription and major post-translational modifications on histone tails. Reprinted from ¹⁵⁸ © 2013, Elsevier Ltd., with permission from Elsevier.



silencing. Most of these tumor suppressors can also be lost via mutation, corroborating a selective advantage in tumorigenesis. Hypermethylation of *RASSF1* was frequently found in PanNETs¹⁶⁷⁻¹⁷⁰, impairing its tumor suppressor function in cell cycle arrest and apoptosis via interaction with various proteins including RAS (Rat sarcoma virus) gene family, JNK (Mitogen-Activated Protein Kinase 8), APC, and CNKSR1 (Connector Enhancer Of Kinase Suppressor Of Ras 1). Hypermethylation of *CDKN2A*, which encodes for P16, a negative regulator of the cell cycle, was associated with early recurrence and reduced overall survival in PanNENs¹⁶⁷⁻¹⁷⁰. *TIMP3* (Tissue inhibitor of metalloproteinase-3) promoter was hypermethylated in a subgroup of PanNET patients (8/18) alongside with reduction in protein expression¹⁷¹. The higher frequency of *TIMP3* promoter hypermethylation in metastatic PanNET and its correlation with poorer prognosis indicates a role of *TIMP3* in disease aggressiveness and metastasis¹⁶⁵. *MGMT* promoter hypermethylation in brain cancer is a strong independent positive predictor of response to temozolomide, tumor regression, and prolonged overall survival^{141,172,173}. Several meta-analyses report a favorable prognosis in *MGMT* deficient PanNEN patients^{94,174}. However, the exact predictive value remains to be confirmed in ongoing prospective studies such as the *MGMT* NET trial (NCT03217097)¹⁷⁵.

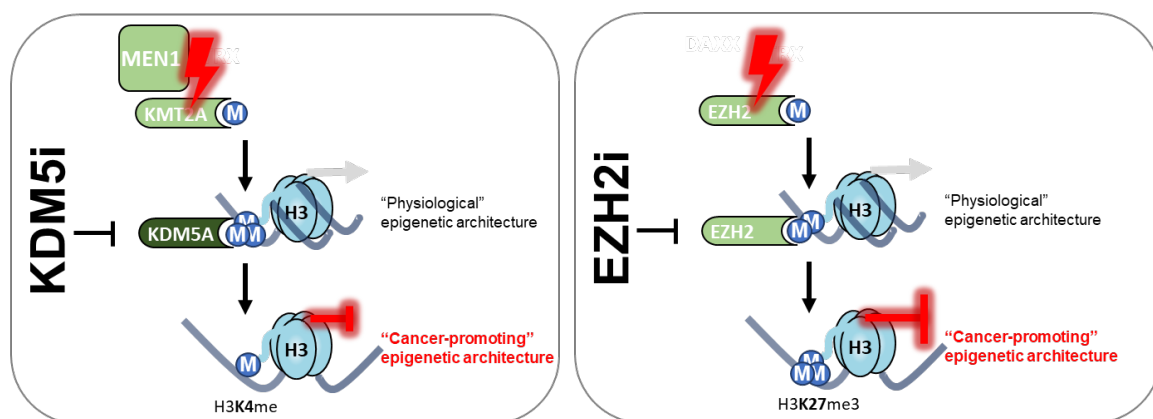
More recently, PanNEN subtyping based on genome-wide DNA methylation profiles took center stage. Increasing efforts started to address the prognostic value of epigenetic profiles and their association with clinical features or tumor progression. Integration of genome-wide DNA methylation and gene expression profiles in PanNETs distinguished *ATRX/DAXX/MEN1* mutant from wild-type tumors and normal pancreatic tissue^{150,176}. Patients with an *ATRX/DAXX/MEN1* signature showed poorer clinical outcomes, a repressive hypermethylation profile for 59 genes, including *PDX1* (Pancreatic And Duodenal Homeobox 1), a transcription factor necessary for pancreatic development and beta cell maturation, and activating hypomethylation in seven genes that involved in various cell functions¹⁵⁰. Hypermethylation of *PDX1* promoter at all four CpG islet promoters and decreased expression in *ATRX/DAXX/MEN1* mutant tumors suggested trans-differentiation of the tumor cells during development¹⁵⁰. Epigenetic differentiation profiles in PanNETs defined their cell of origin and were associated with distinct and specific genetic aberrations and variable tumor progression⁶⁸. In the same line, epigenetic profiling of super-enhancer signatures based on H3 lysine 27 acetylation in non-functioning PanNETs discovered two prognostic subgroups with different developmental features of alpha and beta cell identity¹⁴⁹. In the majority of cases, the expression of ARX (alpha-like) and PDX1 (beta-like) were mutually exclusive¹⁴⁹. PDX1 expression was mostly found in benign and low-stage tumors, whereas ARX expression was

found in both low- and advanced disease stages ¹⁴⁹. Only *DAXX/ATRX* status provided more information about the stage and risk of disease progression ¹⁴⁹. DNA methylation profiling in 57 PanNENs (43 PanNET, 14 PanNEC) differentiated neuroendocrine tumors from neuroendocrine carcinomas ¹⁵¹. DNA methylation profiles discriminated pancreatic from non-pancreatic NETs and revealed an additional subtype harboring a CpG island methylator phenotype (CIMP) related to gene alterations in DNA methylation and/or *MLH1* promoter hypermethylation ⁸⁸.

1.2.3 Aberrant histone methylation and therapeutic options in PanNEN

Emerging sequencing efforts in PanNENs revealed frequent mutations in genes encoding chromatin regulators that modify histones. Several KMT and KDMs have been implicated in PanNEN oncogenesis, including EZH2 (Enhancer of teste homolog 2) ^{177,178}, SETD2 ^{33,45,179} and KDM5A ^{42,70,180–182}.

Figure 4 Aberrant histone methylation and epigenetic drug targets in PanNENs. Illustrated by S.A.M.



(Left) Loss of function mutations or overexpression of epigenetic regulators of the H3K4-methylation axis leads to genomic compaction and a cancer-promoting, gene-repressive genomic state. Inhibition of KDM5A may revert aberrant epigenetic marks. **(Right)** Overexpression of EZH2 leads to hypermethylation in the H3K27-methylation axis and transcriptional silencing of associated gene loci. “Lightning bolts” (red) represents mutations.

Dynamic regulation of covalent histone modification at enhancers and promoters plays a vital role in the modulation of gene expression. Dysregulation in specific histone modifications could be an underlying reason for epigenetic reprogramming driving PanNET evolution. The prevalence of aberrant epigenetic modification in PanNENs as well as the inherent reversible nature of (DNA- and) histone methylation, puts epigenetics in the spotlight for therapeutical intervention.

1.2.3.1 Aberrant KDM5A signaling (H3K4 modulation)

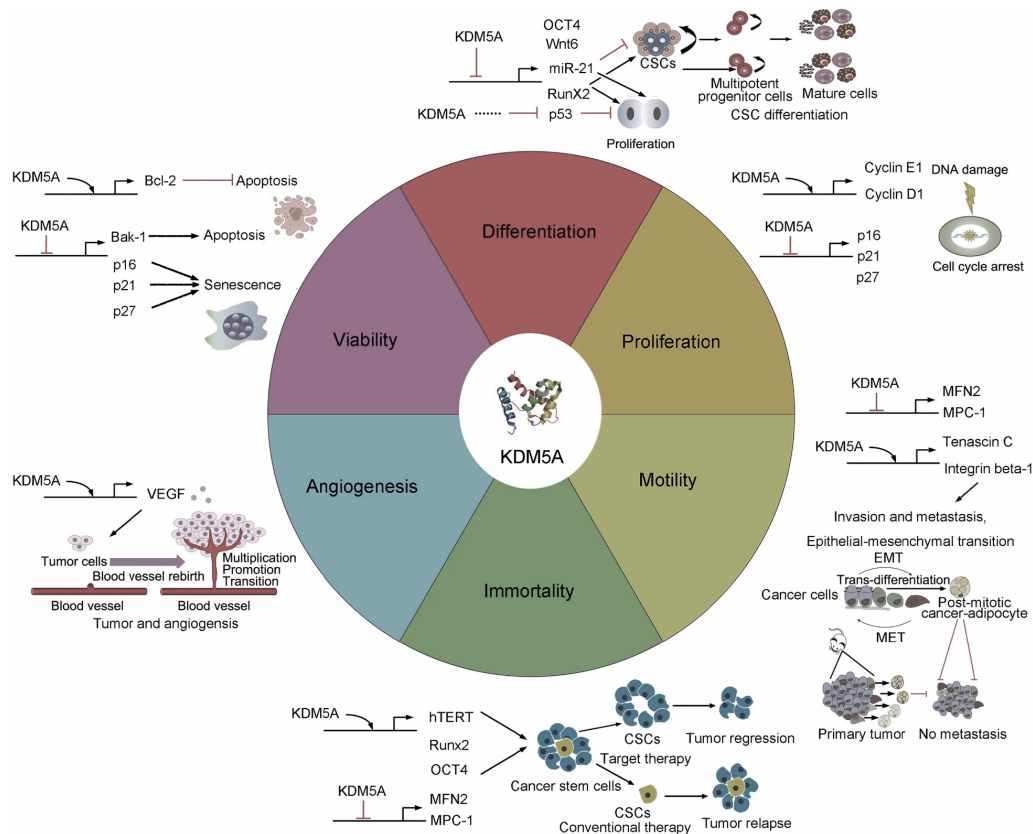
Lysine-specific demethylase 5A (KDM5A), also known as Jumonji/ARID domain-containing protein 1A (JARID1A) or retinoblastoma-binding protein 2 (RBP2), eliminates di- and trimethyl groups of histone 3 at lysine 4 (H3K4) ¹⁸³ and thereby repress the active chromatin mark H3K4me3/2/1. Additionally, KDM5A partners with binding proteins, including RB1 to affect transcription in a demethylase-independent manner ¹⁸⁴.

KDM5A as a transcriptional repressor has been increasingly linked to cancer via its role involved in cell cycle progression, cellular senescence, epithelial-mesenchymal transformation (EMT), migration, drug resistance of cancer cells repressing various targets including E-cadherin, MPC1 (Mitochondrial Pyruvate Carrier 1), TFPI2 (Tissue Factor Pathway Inhibitor 2), HMOX1 (Heme Oxygenase 1), and DAF (CD55 Molecule) ¹⁸⁵. A direct connection between KDM5A overexpression and tumorigenesis was first described in gastric cancer. Mechanistically its oncogenic regulatory role was linked to a decrease in cell cycle inhibitors P16, P21, and P27 and repression of cellular senescence ¹⁸⁶.

In non-small lung cancer, overexpression of KDM5A led to the inactivation of cell cycle inhibitor P27, whereas genes promoting cell cycle, including integrin B1, cyclin D1, and cyclin E1 were activated. Additionally, the oncogenic role of KDM5A was shown to depend on both demethylase-dependent activity and demethylase-independent functions interacting with binding proteins ¹⁸⁷. KDM5A overexpression correlated to cisplatin drug resistance in a non-small lung cancer cell line model ¹⁸⁸. KDM5A promoted the proliferation of drug-tolerant persister PC9 cells, which was reversed by KDM5A inhibition ¹⁸⁹. Remarkably similar, in a xenograft mouse model of prostate cancer emergence of more aggressive drug-tolerant cancer cells during long-term chronic etoposide exposure was mechanistically linked to overexpression of KDM5A ¹⁹⁰. In line, KDM5A overexpression resulted in temozolomide resistance, whereas knockdown of KDM5A restored drug sensitivity in glioblastoma cell line models ¹⁹¹. In a mouse model of small cell lung cancer, Kdm5a blocked differentiation and has led cancer cells to maintain neuroendocrine features facilitating tumorigenesis via inhibiting Notch signaling ¹⁹² as a corepressor of the Notch-Rbpjk (Recombination Signal Binding Protein For Immunoglobulin Kappa J Region) complex ¹⁹³. KDM5A expression was elevated in GEP-NETs (n=20/25), with the most evident elevation in metastatic sites ¹⁸². Gene amplification of KDM5A was highly prevalent in 52% (15/29) of GEP-NET G3 and in 47% (71/152) of GEP-NECs ⁷⁰. Hyperplastic pancreatic islet of *Men1(-/-)* mice displayed an aberrant global and promoter-specific decrease in H3K4me3 levels leading to downregulation of genes, including

insulin-like growth factor 2 mRNA binding protein (Igf2bp2)^{42,181}. Knock out of Kdm5a in *Men1* (-/-) mice reduced tumor burden¹⁸⁰ and partially restored epigenetically controlled gene expression of Igf2bp2 in hyperplastic pancreatic islets¹⁸¹. KDM5A demethylase activity has been shown to enhance the proliferation of the QGP1 cell line¹⁸².

Figure 5 The biological role and action mechanisms of KDM5A in cancer. Adapted from¹⁸³ © 2021, The Authors.



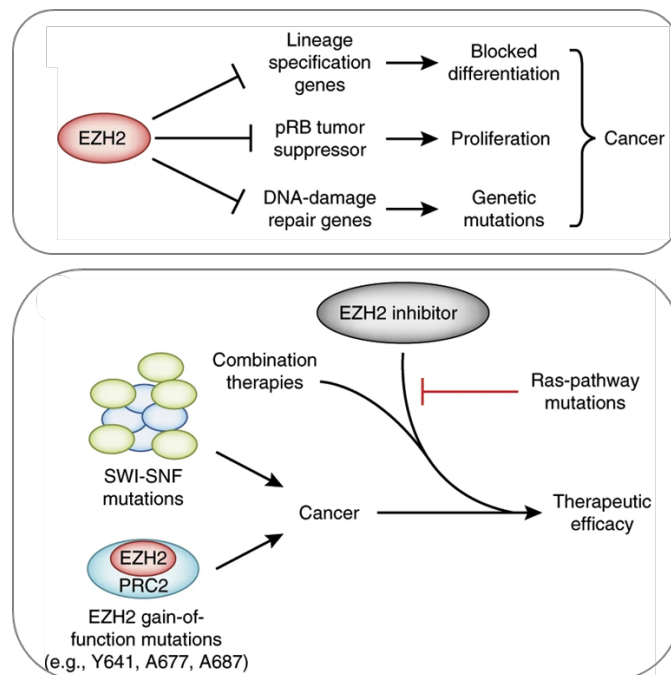
KDM5A mediates various physiological and pathological events, including cell motility, stemness, and epithelial-mesenchymal transition (EMT), in both homeostasis and disease, by activating or repressing transcription in demethylase-dependent or independent ways.

1.2.3.2 Aberrant EZH2 signaling (H3K27 modulation)

EZH2 is a methyltransferase that is overexpressed in many cancers. Very recently, EZH2 has been found overexpressed in a subset of PanNENs^{177,178}. As a catalytic subunit of the polycomb repressive complex 2 (PRC2) EZH2 mediates tri-methylation of histone H3 at Lys 27 (H3K27), facilitating chromatin compaction and epigenetic gene silencing¹⁹⁴. UTX (Ubiquitously transcribed tetratricopeptide repeat gene on the X chromosome, aka KDM6A), a histone demethylase, antagonizes EZH2 activity through the removal of methyl groups¹⁹⁵. EZH2 also methylates several non-histone proteins in the cytosol in a PRC2-dependent manner¹⁹⁴. Direct

methylation of the GATA4 (GATA Binding Protein 4) transcription factor, for instance, inhibits P300-mediated GATA4 acetylation, thereby promoting *GATA4* transcriptional repression and gene silencing¹⁹⁴. In addition, EZH2 also functions in a PRC2-independent manner as a co-activator for transcription factors. Specifically, phosphorylated EZH2 binds directly to and methylates STAT3, thereby boosting STAT3 activity and promoting tumorigenesis in brain cancer¹⁹⁴.

Figure 6 EZH2 as a therapeutic target in cancer. Adapted from¹⁹⁵ © 2016, Nature Publishing Group, a division of Macmillan Publishers Limited, with permission from Nature Publishing Group.



(Top) The roles of EZH2-mediated transcriptional silencing vary depending on the context. Hyperactive EZH2 can cause cancer by altering the expression of lineage specification genes, the pRB tumor suppressor, or DNA-damage repair genes. **(Bottom)** Cancers with *SWI/SNF* mutations or gain-of-function EZH2 mutations can be inhibited by EZH2 inhibition. Early preclinical evidence suggests that combination therapy with an EZH2 inhibitor may be beneficial in these cases. Furthermore, at least in the case of cancers caused by *SWI/SNF* mutations, mutations in Ras pathway genes can confer resistance to EZH2 inhibition.

Several lines of evidence indicate the role of EZH2 in the development and progression of cancer and draw a link of EZH2 to high proliferation rates, metastasis, and poor overall survival^{195–197}. Critical cancer-related transcription factors have been shown to activate *EZH2* transcription, including E2F transcription factor family¹⁹⁸, or in breast cancer models, transcription factors ELK1 (ETS Transcription Factor ELK1)¹⁹⁹ and HIF1A (Hypoxia Inducible Factor 1 Subunit Alpha)²⁰⁰. EZH2 overexpression and gain-of-function mutation in cancers confer a proliferative advantage with repression of tumor suppressor genes as well as repression of genes that drive cellular differentiation (i.a. *PI6*)^{195,196}. EZH2 is involved in the

cell cycle regulatory retinoblastoma-E2F pathway causing inhibition of the tumor suppressor pRB1 leading to increased cellular proliferation¹⁹⁸. Elevated EZH2 expression is primarily found in actively proliferating tissues¹⁹⁷. EZH2-mediated silencing of the DNA-damage repair pathway contributes to oncogenesis¹⁹⁵.

1.2.4 Clinical implication of targeting epigenetics in cancer

Chromatin has been identified early as a target for cancer therapeutics¹⁵². Unlike genetic mutation, epigenetic alterations can be reversed²⁰¹ and may therefore present an intriguing route to existing anticancer therapies. Despite increasing efforts in delineating the epigenetic code in neuroendocrine neoplasm, this has not translated directly into novel therapeutic options so far. The single completed phase II trial using histone deacetylase inhibitor in low-grade NENs (n=13) reported no responses but favorable disease stabilization with a median progression-free survival of 9.9 months²⁰². Similar anticipations as in other anticancer therapies also apply to epigenetic therapies: Epigenetic treatments are not a uniform treatment modality. Given the complexity of epigenetic regulation and underlying heterogeneity, it will be essential to adopt a precision medicine strategy for identifying robust predictive biomarkers for therapy selection. E.g., EZH2 inhibition demonstrated selected efficacy in patients with hematological malignancies or highly aggressive solid tumors with genetic alteration in the *SWI/SNF* chromatin remodeling complex (i.a. *SMARCA4*)²⁰³. Given a large amount of potential epigenetic targets, systematic approaches and preclinical models will be needed to identify and validate potential drug targets. A promising aspect lies in the potential of epigenetic drugs to modulate and enhance the sensitivity of tumors to other anticancer drugs, overcome therapy resistance, and counteract hallmarks of cancer. E.g., HDAC or DNMT inhibitors promote global chromatin relaxation that synergistically affects genotoxic agents and interferes with DNA-damage repair *in vitro*²⁰⁴. Moreover, HDAC inhibitor and PI3K/AKT/MTOR pathway inhibitors in early phase trials are combined with everolimus in patients with H3.3 or H3.1 K27M-mutant glioma (NCT03632317).

Limited tolerability of epigenetic therapies is a major challenge and will require lower dosing, identification of synergistic drug combinations, and targeted delivery in the future. The exact timing and treatment sequence is another important aspect of epigenetic cancer therapies. A delayed response was observed in some patients treated with EZH2 inhibitors²⁰³. The exact time it takes for epigenetic drugs to rewire transcriptional programs and translate into phenotypic changes in patients is not clear yet²⁰⁵. Overall, it will be crucial to deepen the understanding of epigenetic mechanisms not only in NENs but also in other solid cancers,

which might then guide the development of agents that can be used in precision medicine strategy.

1.3 Modeling pancreatic neuroendocrine neoplasm

1.3.1 Human preclinical models of neuroendocrine neoplasm

Preclinical cancer models allow studying complex tumor biology in a controlled setting and building a basis to explore and improve therapeutic strategies. A common problem in rare cancers such as PanNENs is the absence of a large arsenal of preclinical models. Human PanNEN cell line models have been difficult to establish due to the rarity and heterogeneity of the disease and the slow-proliferating nature of a large fraction of cases^{206–208}. Genetically modified mouse models (GEMMs) of PanNEN have been used to study the genotype-phenotype relationship *in vivo* and contributed to many preclinical studies^{116,209–211}. However, apart from the apparent difference between mice and men, several technical and biological limitations have been raised that make their usage impractical affecting potential advances in translational findings using GEMMs^{206–208}. For example, the latency of tumor development and growth can be extremely high for some of the GEMMs, especially in the MEN1-mutant background, where it can take well over a year until tumors develop in mice²¹². In one of the most commonly used PanNEN mouse models of malignant insulinomas (Rip1Tag2) a large-scale cross-species analysis revealed that important human genetic subtypes such as the MEN1-like cancers and diagnostic features are not represented²¹³. In recent years, there has been an increase in the use of primary cell cultures alongside a shift toward patient-centered disease modeling, which has put human models at the forefront.

1.3.1.1 Human cell line models of PanNEN

Although there are few human PanNEN cell lines, the low cost and ease of use of these models make them attractive for mechanistic studies and high-throughput preclinical drug screenings. BON1, QGP1, and NT3 represent well-established and most commonly used human PanNEN cell line models.

BON1 cell line was derived from a lymph node metastasis of a carcinoid pancreatic tumor of a 28-year-old man²¹⁴ and shows doubling times around 19 hours²¹⁵. BON1 cells express functional receptors for acetylcholine, serotonin (5-HT), isoproterenol, gastrin, and somatostatin²¹⁴ and secrete serotonin and IGF-1 as autocrine growth factors²¹⁴. Conditioned media from BON1 cell culture additionally contains large amounts of neurotensin, pancrestatin, and chromogranin A, all three mammalian types of transforming growth factor B (TGFB 1-3), as well as factors with a potent endothelial cell growth stimulatory activity^{216,217}.

QGP1, a carcinoembryonic antigen and somatostatin^{218,219} producing cell line, was derived from a well-circumscribed lesion of a primary pancreatic islet-cell “carcinoma” of a 61-year-old man²¹⁹ and shows doubling times around 43 hours²¹⁵.

Comprehensive genetic profiling revealed numerical and structural genomic alteration in both BON1 and QGP1 cell lines indicative of malignant high-grade and NEC-like features questioning their relevance as a model for lower-grade PanNETs^{215,220,221}. Likely, some of the mutations arise while the long-term culture of these models²¹⁵. BON1 harbor loss of function mutation in *TP53*, *TSC2*, and *NRAS*^{220,221}, homozygous loss of tumor suppressor *CDKN2 A and B*, and *CHEK2*²¹⁵ and constitutively active PI3K/AKT/MTOR signaling pathway²²¹. QGP1 showed high CNA and harbor amplification on *MDM2* and *HMG A2* (High Mobility Group AT-Hook 2) and mutation in *ATRX* and *TP53* and biallelic inactivation of *SETD2*, and a mutated gene copy in *MTOR*²¹⁵.

NT3 cell line was derived from a lymph node metastasis of a functional insulinoma obtained from a 33-year-old male patient²²². NT3 cells retain a slow-proliferating (15-25% Ki-67) and well-differentiated phenotype of the original tumor and express high levels of somatostatin receptor (SSTR 1 to 3 and 5)²²². NT3 cells harbor a homozygous missense mutation of *MEN1* and lack further genetic mutations. Interestingly, although slow-growing, subcutaneous xenotransplantation of NT3 cells showed a high take rate (94%) and tumor growth by four weeks²²².

Few other human PanNEN cell lines exist, e.g., human insulinoma cell lines (HNV PDX-PNET, CM)^{223,224} or lower-grade cell line model HuNET (VIPoma)²²⁵, APL1 (WD PanNET G1 liver metastasis)²²⁶. These models are less frequently used due to inherent difficulties in long-term maintenance *in vitro*, limited access, or missing proof of a stable phenotype. As for all immortalized cell lines, human PanNEN cell lines also possess an intrinsic limitation in how well these models represent the patient situation and disease heterogeneity. Mutational shifts and acquisition of novel mutation over long-term passaging²¹⁵, loss of neuroendocrine marker expression, and low efficiency in establishing novel cell lines from PanNENs pose an additional obstacle in the field.

1.3.1.2 Patient-derived models of PanNEN

In contrast to established cell line models and GEMMs, using primary cells derived from biopsies or surgical resections allows for the preservation and study of patient-specific genetic and phenotypic tumor properties. Due to the rarity of the disease, limited starting material, and

the intrinsic nature of neuroendocrine tumor cells, developing patient-derived models has been challenging. Nonetheless, a small number of models that can accurately reflect the individual human PanNEN disease have recently been described, indicating the field's growing interest in such models.

Patient-derived xenograft models: Patient-derived xenografts (PDX) preserve the original histologically and create a more realistic tumor environment. Although PDX commonly lack the immune cell environment, other stromal components are conserved and allow a highly relevant *in vivo* setting. There are few studies on PDX derived from PanNEN, and engraftment success has been reported to be extremely low: An attempt to establish patient-derived xenograft from 39 low- and intermediate-grade well-differentiation primary PanNETs yielded only one successful tumor xenotransplant, which was then used to test the antitumor activity of MTOR inhibitor sapanisertib in this everolimus-resistant tumor ²²⁶. In another study of 106 intestinal and pancreatic NETs, only one intestinal tumor with an atypical, NEC-like mutational profile (*CTNNB1* and *TP53* oncogenic mutation) could be repeatedly passaged and remained viable. Another three pancreatic and three intestinal specimens were successfully implanted and reached a size of 1500 mm³, but all failed to regrow after regrafting and showed no viable tumors but only fibrosis granulation tissue ²²⁷, underlining that xenotransplantation of PanNEN tumor cells remains a challenge.

Patient-derived culture models: Patient-derived cell culture models offer an alternative approach to PDX to study individual tumor characteristics and serve as a valuable preclinical tool that allows the assessment of patient-specific treatment strategies. Initial findings from patient-derived cell culture models were described in classical two-dimensional (2D) monolayer cultures. Culturing patient-derived cells in monolayers historically has been challenging due to their intrinsic capacity to form aggregates ²²⁸ and monolayer cell cultures were viable only for limited time periods (<72 hours). The use of bovine extracellular matrix facilitated cell adhesion and successful short-term culture to investigate the combinational efficacy of everolimus and two different somatostatin analogs and study its effects on AKT upregulation and SSTR2 trafficking ^{229,230}. In a similar setup, Falletta *et al.* successfully cultured 14 low- and intermediate-grade PanNETs and found an effect of IGF1 in the everolimus response ²³¹.

With advances in cell culture techniques, three-dimensional (3D) multicellular tumor spheres (e.g., tumoroids and tumor organoids) also found their way into PanNEN research. 3D *in vitro* models better recapitulate the complex cell-to-cell interaction and mimic a more realistic spatial

configuration to study tumor cells compared to monolayers, as will be discussed in more detail in **section 1.3.2**. Two human colorectal NEC organoids were characterized within the attempt to establish a colon cancer organoid biobank that represents diverse colorectal cancer (CRC) tumor subtypes ²³². Both NEC organoids reproduced the histopathological features of the clinical specimen and high expression of endocrine markers (CGA, SYN) similar to the original tumor tissue and harbored gene signatures distinct from other colorectal cancer models ²³². Genomic profiling revealed *TP53* mutations in both and additional mutations (*APC*, *BRAF*, *KRAS*) associated with colorectal adenocarcinoma in one of these NEC organoids ²³². Kawasaki *et al.* established 25 lines of NEN organoids from the pulmonary- and extrapulmonary origin, including one PanNET and two PanNEC organoid lines. Comprehensive molecular profiling reconfirmed their biological and pathohistological characteristics similar to parental tissue, including the absence of *TP53* and *RBI* mutations but the presence of *DAXX*, *DEPDC5*, and *TSC2* mutations found in the PanNET organoid ⁸⁶. Transcriptional profiling unveiled three molecular subtypes where PanNET organoids clustered closely with other GEP-NETs harboring high expression of known NET-specific markers such as ARX, SSTR 1 and 5, and GIPR (Gastric Inhibitory Polypeptide Receptor) ⁸⁶. In a limited set of three patient-derived GEP-NEC organoids established from 18G tumor biopsies, the *in vitro* drug sensitivity to cisplatin and everolimus aligned well with the patient clinical response ²³³. A perfusion bioreactor system providing a hydrogel 3D matrix for cellular organization allowed to incorporate both, tumor- and stromal cells from PanNETs patients in a controlled manner and to propagate patient-derived cells for up to 29 days *in vitro* ²³⁴. Even though few multicellular tumor sphere models for PanNENs have been established so far, the reports highlight that these models recapitulate patient-specific characteristics *in vitro* and underline their relevance in providing novel insights into NEN functional biology. So far, drug screening data derived from these models are scarce; however, the use of patient-derived 3D *in vitro* models for such purposes seems promising.

Tumors are complex systems depending on interaction with their native surrounding tumor microenvironment. The tumor microenvironment comprises stromal cells, extracellular matrix, infiltrating immune cells, vasculature, and other tissue-specific factors, altogether defining a highly dynamic network affecting the biology of the tumor. Organotypic slice cultures specifically address the aspect of TME, immune compartment, and maintenance of tumor-specific characteristics by culturing tumor tissue slices in a near *in vivo*-like controllable setting. Organotypic slice cultures of neuroendocrine liver metastasis from fresh patient specimens were viable for at least seven days and recapitulated common neuroendocrine clinical features

²³⁵. In addition to preserving the patient-specific histoarchitecture, these cultures were immunocompetent and actively secreted immune checkpoint receptors in an epithelium-dependent manner.²³⁵. Despite the scarcity of studies, these findings demonstrate the utility of organotypic slice cultures as patient-derived 3D culture models of tumor microenvironment components.

1.3.2 Establishing three-dimensional *in vitro* cultures to model cancer

The emergence of various 3D culture technologies in recent years has led to unprecedented possibilities to model human cancers *in vitro* ²³⁶. 3D culture model systems can vary in their complexity consisting of simple cellular aggregates of a single cell type up to highly complex engineered models consisting of various cell types, biomatrices, and additional extracellular components. The terminology used to describe such kind of culture systems is highly inconsistent throughout the literature ^{237–239}. However, the term “multicellular tumorspheres” appears to be a reasonable denominator for the majority of spheroidal 3D cancer cell culture models.

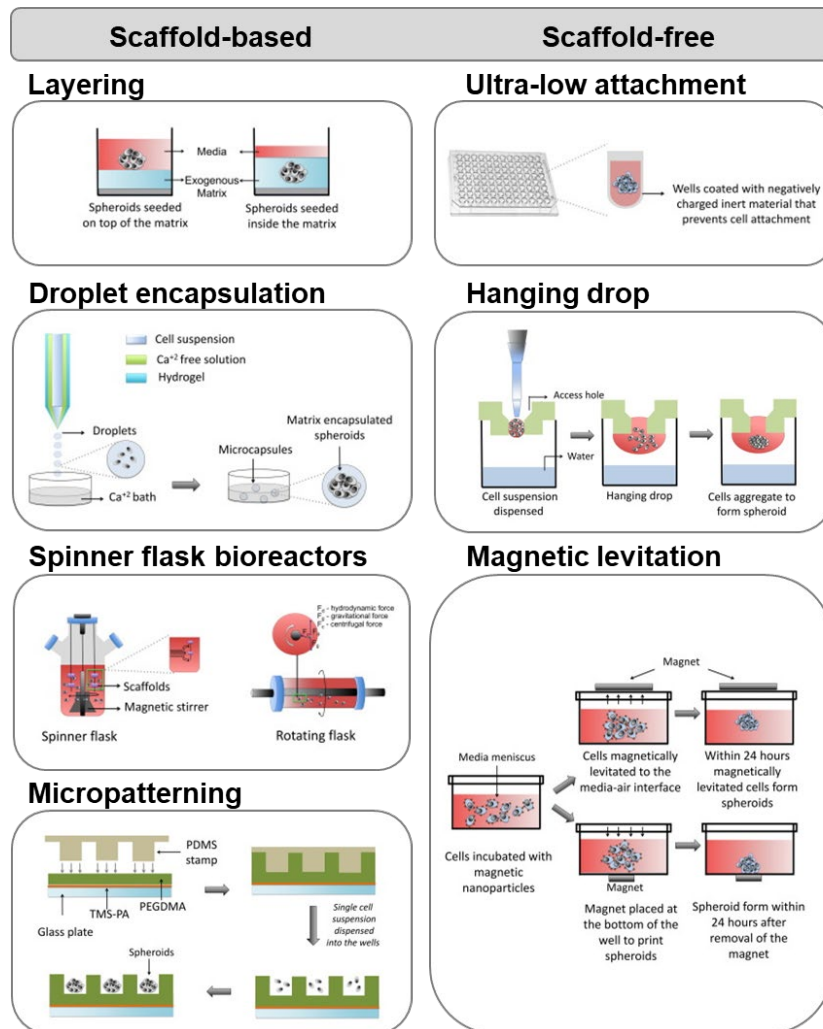
A popular type of multicellular tumor spheres is the so-called tumor organoids. The use of this terminology has become relatively loose ^{238,240}, and often it is not entirely clear what authors in their studies exactly mean when referring to tumor “organoids.” However, initially, the term organoid referred to hydrogel-embedded stem-cell derived multicellular spheres that, by specific growth factor supplements, differentiate and intrinsically organize into complex *in vivo* or organ-like healthy structures that reflect crucial tissue features in terms of overall architecture, the collection of differentiated cell types, and tissue-specific function ^{238,240–242}. In contrast, tumoroids more broadly describe cultures derived from tumors but not necessarily from clonal expansion of stem cells. Tumoroids use primary tumor cells as starting material to form cellular aggregates and three-dimensional structures *in vitro* with the goal of representing inter-patient heterogeneity and patient-specific features ^{238,243}.

Irrespective of the used terminology, the underlying core principle of all three-dimensional *in vitro* culture systems is to promote cellular interaction with its surroundings and to organize cells in a spatially relevant manner similar to the *in vivo* situation ²⁴⁴. The morphology of multicellular tumor spheroids varies from round, mass, and grape-like to stellate depending on the inherent nature of cultured cells and the culture conditions used ²⁴⁴. In classical two-dimensional monolayer cultures, cells lack such complex cellular interactions and undergo cytoskeletal rearrangement acquiring artificial cell polarity that can result in altered gene

expression and cell signaling²⁴⁴⁻²⁴⁷. Tumor cells cultured in 3D exceeding sizes of >300µm^{248,249} develop physicochemical gradients and zonal patterning of oxygen supply, nutrients, metabolites, growth factors, and various cellular processes. Peripheral cells are proliferating, mid-layer cells are quiescent, and in the innermost hypoxic core, cells undergo apoptosis or necrosis^{237,239}. Cells located in the outer rim thereby may reflect the *in vivo* situation of actively cycling tumor cells adjacent to capillaries while innermost cells become quiescent and eventually die via apoptosis or necrosis²³⁷, comparable to the *in vivo* situation in avascular tumor nodules, micrometastases or intracapillary microregions of solid tumors^{237,244,250-252}.

Methods for generating 3D cultures rely either on scaffold-based or scaffold-free techniques. Scaffolds are natural or (semi)synthetic polymeric hydrogels forming an extracellular environment to provide structural support signals to the cells. Matrigel is one of the most commonly used natural scaffolds and is comprised of secreted basement membrane extracts of Engelbreth-Holm-Swarm mouse sarcoma cells and includes collagen, entactin, laminin, and heparin sulfate proteoglycans²⁵³⁻²⁵⁵. Integrin-binding ligands on natural hydrogels facilitate signal transduction through cellular transmembrane proteins and enable a cellular response to changes in the microenvironment²⁴⁴. (Semi)synthetic hydrogels are increasingly used to provide well-defined polymers with additional features, e.g., stiffness or porosity of the matrix to mimic specific tumor microenvironmental aspects impacting gene expression and cell signaling^{256,257}. Tumor cells are enclosed into the matrix construct by various means, including layer systems²⁴⁴, droplet encapsulation²⁵⁸, spinner flask bioreactors²⁵⁹ or micropatterning²⁶⁰ leading to a three-dimensional organization. Scaffold-free techniques rely on gravitational forces to induce cellular self-aggregation either in ultra-low attachment polystyrene plates²⁶¹, in hanging drop systems^{244,262}, or by magnetic levitation²⁶³. Irrespective of the underlying technology, increasing efforts using 3D culture systems seek to determine whether these cultures can potentially improve drug development and clinical practice.

Figure 7 Techniques for generating multicellular tumor spheroids. Reprinted from ²⁴⁴ © 2016, Elsevier Ltd., with permission from Elsevier.



Schematic explains the various methods to generate multicellular tumor spheroids. Scaffold-based methods (left), scaffold-free methods (right).

1.3.3 Testing drug sensitivity in three-dimensional *in vitro* cultures of cancer

For many years, immortalized human 2D monolayer cultures were essential *in vitro* models for cancer studies ²³⁶. In preclinical drug discovery, 2D *in vitro* cancer models provide a valuable tool for large-scale high-throughput screenings due to their low cost and rapid turnaround time compared to *in vivo* animal models ²⁴⁴. Profiling a chemical library of over 200'000 small molecules against more than 100 lung cancer cell line models revealed over 100 chemical-genetic associations as novel targetable vulnerabilities ²⁶⁴. In a recent large-scale systematic drug combinational screen, Garnett *et al.* tested >2000 clinically relevant two-drug combinations in 125 cell line models of breast, colorectal and pancreatic cancer ²⁶⁵. Synergetic drug interactions were rare and highly context-dependent and primarily found in combinations of two targeted therapies. As a proof-of-concept, a promising combination of irinotecan (DNA

Topoisomerase I inhibitor) and CHEK1 inhibitor was additionally validated *in vivo*, underlining the importance of their findings²⁶⁵. However, differences in drug activity are often observed in 2D monolayer cultures compared to 3D cultures that commonly harbor decreased sensitivities as exemplified by the 2D/3D comparative study of breast cancer and HeLa cancer cells^{244,266}. These findings can be attributed to several factors differentiating 2D from 3D cultures, including differential drug distribution and permeability²⁶⁷, hypoxic areas²⁶⁸, cell-cell and cell-matrix adhesion, and altered gene expression^{239,261,269} described in the previous section. Many findings underscored that 3D cultures, by their spatial cellular architecture, more accurately mimic drug sensitivities found in solid tumors *in situ*^{237,270–273} and pointed out the rationale of using such formats in anticancer drug research^{237,239,250,251,274}.

1.3.4 Emerging opportunities from patient-derived three-dimensional *in vitro* cultures in preclinical research

A significant obstacle exists in the translation of preclinical findings into clinical practice. Relevant cancer models need to recapitulate the genetic- and phenotypic characteristics of the original tumor in order to provide reliable biomedical data^{251,275,276}. High failure rates (>92%) of lead compounds in clinical trials from phase I to launch²⁷⁷ can - to some extent - be attributed to preclinical trial stages. The difficulties in using appropriate models to predict drug efficacy in patients not only hinder drug development but also progress in identifying patient subgroups amenable to targeted therapies²⁷⁸. Although >1000 cancer cell line models exist, they represent only a fraction of the genotypic diversity found in most common human cancers²⁷⁹. Human cancer cell line models lose tissue-related functions and undergo genetic and transcriptional evolution, which may question their predictive power for drug responses²⁸⁰. Various studies comparing solid tumors and corresponding cell lines underscored differences in gene expression between the original tumor and the cell line model^{281–283}. Furthermore, rare cancers are poorly represented, and only a few or no cancer cell line models are established for uncommon cancers²⁸⁴.

1.3.4.1 Representation of genotypic and phenotypic patient characteristics *in vitro*

With technological advances, patient-derived cancer models established from fresh and cryopreserved specimens have found their way into research and have been adopted to study different cancer types. Various large-scale genomic and functional analyses of patient-derived multicellular tumor spheres underscored that these models faithfully recapitulate key features of original tumors both *in vitro* and *in vivo* after transplantation^{285–288}. Histo-morphology, as

well as mutational profiling in patient-derived tumor organoids, showed high similarity between the model and the original tumor^{288–291}. Transcriptional profiling in CRC organoids yielded expression heterogeneity and allowed stratification into known CRC subtypes indicating that relevant features are retained in the model²⁸⁸. Biopsy-derived CRC organoids and original tumors showed 90% concordance of somatic mutations and a high correlation between copy-number aberration profiles²⁹². The successful application of 3D culture techniques hence provides a unique opportunity to bridge the gap between *in vitro* cancer cell line cultures and *in vivo* models^{293,294}.

1.3.4.2 Mechanistic insight from tumor organoids

Nowadays, tumor organoids present one of the most popular 3D *in vitro* culture models used to study cancer. A landmark study presented optimized culture conditions that, for the first time, allowed long-term propagation and expansion of patient-derived tumor organoids representing colorectal cancer²⁹⁵. Matrigel, together with essential stem cell growth factors, TGF β - and MAPK inhibitor, served as a basis for successful culture²⁹⁵ and led to subsequent development of similar culture protocols in healthy tissues and malignant tissues of various cancers, including for example exocrine and endocrine pancreas^{86,285,289} or prostate²⁸⁶.

Their relative ease of manipulation and expansion *in vitro* allows the usage of state-of-the-art technologies. CRISPR/Cas9 technology was used to model colorectal cancer progression from healthy wildtype human colon organoids by stepwise modification of known driver genes, including *APC*, *TP53*, *KRAS*, and *SMAD4*²⁹⁶. Drug resistance to PARP inhibitors in mouse tumor organoids for BRCA1- and BRCA2-deficient cancers was linked to increased ABCB1 (ATP Binding Cassette Subfamily B Member 1, MDR1)-mediated drug efflux and rewiring of the DNA repair machinery as a result of loss of 53BP1 (Tumor Protein P53 Binding Protein 1) or MAD2L2 (Mitotic Arrest Deficient 2 Like 2, REV7)²⁹⁷. Overall, tumor organoids present a valuable and relevant platform for mechanistic or drug-genotype studies in 3D.

1.3.4.3 Drug testing and treatment selection in patient-derived tumoroid models

Depending on the amount of starting material, patient-derived multicellular spheroid models are compatible with higher throughput drug screens and are often used in combination with molecular profiling. Systematic evaluation and integration of functional and molecular data from individual patients could provide novel options for patient care in a personalized manner. In four late-stage cancer cases, complete genomic analysis together with high-throughput drug screens of targeted- and chemotherapeutic agents identified patient-specific novel treatment

options²⁹⁰. Interestingly in two cases, although harboring similar driver mutations in *PI3CA* and *PTEN*, the drug screen clearly distinguished these two patients from each other corroborating the importance of functional drug testing in addition to genetic profiling²⁹⁰. Testing a panel of organoids derived from chemo-naïve CRC patients confirmed known drug sensitivity-phenotype correlation such as the effectiveness of cetuximab in a subset of *KRAS* wildtype organoids but additionally identified differential activity in the absence of apparent genetic biomarkers, e.g., exquisite sensitivity of a subset of organoids to AKT 1 and 2 inhibitors²⁸⁸.

A fundamental question for translational applications of patient-derived 3D cancer models is whether the *in vitro* response in multicellular tumor spheroids predicts individual patient clinical response. These models can be established on a single-patient basis to compare *in vitro* sensitivity and clinical patient response and select individual patients for novel targeted therapies. Patient-derived tumor organoids from metastatic, heavily pretreated colorectal and gastroesophageal tumors showed high concordance in their response to anticancer agents compared to orthotopic mouse tumor xenografts as well as to patient clinical response²⁹¹. Similarly, patient-derived tumor organoids from primary pancreatic ductal adenocarcinomas retained the mutational spectrum and transcriptional subtypes of original tumors and exhibited a heterogeneous response to standard-of-care chemotherapies, which aligned well with patient outcomes²⁹⁸. Co-clinical and prospective clinical trials will be needed to validate the predictive power of patient-derived multicellular tumor spheres. Such efforts are running for several cancer entities (e.g., NCT 03170180, e.g., TUMOROID trial NL49002.031.14) and will help to determine the translational value of these patient-derived multicellular tumor spheroids.

2 Rationale and objective of the project

The overall goal of this thesis was to study patient-specific cancer vulnerabilities that can guide more personalized pharmacological treatment approaches in PanNEN therapy. The underlying central hypothesis was that combining patient-derived tumoroid cultures and molecular tumor profiling provides a composite biomarker for sensitivity to standard-of-care pharmacotherapies and novel preclinical compounds for PanNEN disease. The work is divided into three projects: Few *in vitro* studies in neuroendocrine patient-derived material exist. Missing preclinical human models of neuroendocrine neoplasm impede translational advances and exploration of novel therapeutic approaches. In **project 1**, “*Three-Dimensional Primary Cell Culture: A Novel Preclinical Model for Pancreatic Neuroendocrine Tumors*,” we aimed to develop a primary cell culture workflow that can be used to model pancreatic neuroendocrine tumors and to screen standard-of-care treatments *in vitro*.

A human organoid biobank of GEP-NEN has recently been presented and molecularly and functionally characterized⁸⁶. A bioreactor system incorporating stromal cells showed technical feasibility in culturing patient-derived PanNEN tissue²³⁴. However, the translational relevance of patient-derived neuroendocrine cell models has not been investigated side-by-side to patient clinical therapy response. Moreover, little information is available to understand the molecular drug response of neuroendocrine cancer cells upon chemotherapy. In **project 2**, “*Tumoroids of advanced high-grade neuroendocrine neoplasms mimic patient chemotherapy responses and guide the design of personalized combination therapies*,” we performed a proof-of-concept study in advanced high-grade GEP-NEN allowing us to directly compare *in vitro* and clinical therapy responses and investigate the molecular drug responses to find novel vulnerabilities for combinational therapy.

The role of epigenetics in the development and progression of PanNETs has become more evident. Although several driver genes relate to epigenetics, no epigenetic therapies for PanNETs are clinically approved. Dysregulation of epigenetic player EZH2 has been reported in various cancers; however, little is known about its role in PanNENs. In **project 3**, “*EZH2 Inhibition as New Epigenetic Treatment Option for Pancreatic Neuroendocrine Neoplasms*,” we aimed to study EZH2 and its association with clinical features, its role in PanNET tumorigenesis in mouse- and cell line models, and to clarify whether patient-derived 3D PanNEN cell culture is a suitable preclinical model for testing EZH2 as an epigenetic therapy option.

3 Results

3.1 Project 1: Three-Dimensional Primary Cell Culture: A Novel Preclinical Model for Pancreatic Neuroendocrine Tumors

3.1.1 Specific introduction

Cancer models of slow-proliferating pancreatic neuroendocrine tumors are scarce²⁰⁶⁻²⁰⁸. Missing appropriate cell line- and mouse models that accurately recapitulate the disease's underlying molecular spectra holds back translational discoveries and the advancement of therapeutical strategies for this rare cancer²⁹⁹. Several studies on other cancer types have shown that patient-derived cell cultures harbor the potential to bridge the gap between preclinical research and translational applications^{288,291,298,300}. So far, few *in vitro* studies with limited timespans and throughput have been conducted in patient-derived cell culture from human PanNETs^{229-231,301}. Reasons for this short-coming may have been cell intrinsic-, technical-, or logistic challenges of culturing rare, slow-proliferating pancreatic neuroendocrine tumors *in vitro*²⁰⁶⁻²⁰⁸. Three-dimensional *in vitro* culture systems represent a more physiological spatial configuration that better recapitulates complex cell-to-cell interactions and likely is more suitable for the culture of pancreatic neuroendocrine tumor cells²²⁸. Up to date, no 3D *in vitro* culture system of human neuroendocrine tumors exists, and it remains to be seen if such an approach allows establishing a potent preclinical model for drug testing

3.1.2 Specific hypothesis and aims

Hypothesis: Patient-derived 3D cultures recapitulate biological key features of original tumors *in vitro* and allow to test the drug sensitivity to (chemo)therapeutics *in vitro*

Aim 1) To establish and molecularly characterize a 3D human primary PanNET model

Aim 2) To tailor a PanNET screening workflow and test standard-of-care treatments *in vitro*

3.1.3 Manuscript 1: “*Three-Dimensional Primary Cell Culture: A Novel Preclinical Model for Pancreatic Neuroendocrine Tumors*”

Simon Leonhard April-Monn, Tabea Wiedmer, Magdalena Skowronska, Renaud Maire, Marco Schiavo Lena, Mafalda Trippel, Annunziata Di Domenico, Francesca Muffatti, Valentina Andreasi, Gabriele Capurso, Claudio Doglioni, Corina Kim-Fuchs, Beat Gloor, Maria Chiara Zatelli, Stefano Partelli, Massimo Falconi, Aurel Perren, Iliaria Marinoni

Neuroendocrinology [10.1159/000507669](https://doi.org/10.1159/000507669)

Reprinted from ³⁰² © 2020, S. Karger AG, with permission from S. Karger AG.

Author contribution (CRediT):

I was involved in **conceptualization** (ideas, formulation, and evolution of overarching research goals and aims), **methodology** (development and design of methodology, creation of models), **software** (programming and implementation of code and testing of existing computer code), **validation** (verification of the overall replication/reproducibility of experiments and results and other research outputs), **formal analysis** (application of statistical, mathematical, computational and other formal techniques to analyze and synthesize study data), **investigation** (conduction research and investigation processes, performing experiments and data collection), **data curation** (managing activities to annotate and maintain research data for initial and later use), **writing and preparation** of the original draft and **reviewing and editing** the final manuscript, **visualization**, and **project administration** (management and coordination of responsibility for the research activity planning and execution)

Three-Dimensional Primary Cell Culture: A Novel Preclinical Model for Pancreatic Neuroendocrine Tumors

Simon Leonhard April-Monn^{a,b} Tabea Wiedmer^{a,b} Magdalena Skowronska^a
Renaud Maire^a Marco Schiavo Lena^c Mafalda Trippel^a
Annunziata Di Domenico^{a,b} Francesca Muffatti^d Valentina Andreasi^d
Gabriele Capurso^d Claudio Doglioni^{c,e} Corina Kim-Fuchs^f Beat Gloor^f
Maria Chiara Zatelli^g Stefano Partelli^{d,e} Massimo Falconi^{d,e} Aurel Perren^a
Ilaria Marinoni^a

^aInstitute of Pathology, University of Bern, Bern, Switzerland; ^bGraduate School for Cellular and Biomedical Sciences, University of Bern, Bern, Switzerland; ^cUnit of Pathology, San Raffaele Scientific Institute, Milan, Italy; ^dPancreatic Surgery Unit, Pancreas Translational and Clinical Research Center, San Raffaele Scientific Institute, Milan, Italy; ^eUniversità Vita e Salute, Milan, Italy; ^fInselspital, University of Bern, Bern, Switzerland; ^gSection of Endocrinology and Internal Medicine, Department of Medical Sciences, University of Ferrara, Ferrara, Italy

Keywords

Pancreatic tumor · Neuroendocrine tumor · 3D culture · Preclinical model · Primary cells · Drug screening · Islet-like tumoroids · Spheroids · Organoids

Abstract

Molecular mechanisms underlying the development and progression of pancreatic neuroendocrine tumors (PanNETs) are still insufficiently understood. Efficacy of currently approved PanNET therapies is limited. While novel treatment options are being developed, patient stratification permitting more personalized treatment selection in PanNET is yet not feasible since no predictive markers are established. The lack of representative *in vitro* and *in vivo* models as well as the rarity and heterogeneity of PanNET are prevailing reasons for this. In this study, we describe an *in vitro* 3-di-

mensional (3-D) human primary PanNET culture system as a novel preclinical model for more personalized therapy selection. We present a screening platform allowing multicenter sample collection and drug screening in 3-D cultures of human primary PanNET cells. We demonstrate that primary cells isolated from PanNET patients and cultured *in vitro* form islet-like tumoroids. Islet-like tumoroids retain a neuroendocrine phenotype and are viable for at least 2 weeks in culture with a high success rate (86%). Viability can be monitored continuously allowing for a per-well normalization. In a proof-of-concept study, islet-like tumoroids were screened with three clinically approved therapies for PanNET: sunitinib, everolimus and temozolomide. Islet-like tumoroids

Simon Leonhard April-Monn and Tabea Wiedmer contributed equally to this work and shared first authorship. Aurel Perren and Ilaria Marinoni shared last authorship.

display varying in vitro response profiles to *distinct therapeutic regimens*. Treatment response of islet-like tumoroids differs also *between patient* samples. We believe that the presented human PanNET screening platform is suitable for personalized drug testing in a larger patient cohort, and a broader application will help in identifying novel markers predicting treatment response and in refining PanNET therapy.

© 2020 S. Karger AG, Basel

Introduction

In contrast to many other malignancies, there are no molecular characteristics and biomarkers supporting treatment decisions in pancreatic neuroendocrine tumors (PanNETs). While molecular mechanisms underlying PanNET development and disease progression are continuously further deciphered [1, 2] and numbers of clinically approved therapies are steadily rising, the treatment options for PanNET are still primarily chosen based on clinician judgment.

The lack of appropriate models and the rarity of PanNET disease are two major factors that hinder further advances in PanNET translational research. Testing more effective therapies as well as performing predictive studies are lagging behind. Currently, only a limited number of human PanNET cell lines are available – with BON1, QGP1 and CM being the most commonly studied [3–6]. It is pertinent to note that while these cell lines were used to experimentally dissect molecular mechanisms of NETs, they do not represent well-differentiated slow-proliferating PanNETs. All of these cell lines are highly proliferative and were found to differ fundamentally in their mutational genetic background compared to PanNETs. In fact, studies have shown a strong resemblance to poorly differentiated pancreatic neuroendocrine carcinomas rather than PanNETs [7–11]. Moreover, other authors have even questioned the tissue of origin of the aforementioned cell lines, raising a significant debate as to the translational relevance of work performed using these cell lines [11, 12]. Recently, Benten et al. [13] described NT-3 as a novel cell line that better reflects well-differentiated slow-proliferating PanNETs, which present the bulk of PanNETs. Nevertheless, the full molecular profile of NT-3 cells remains to be determined so that its similarity to the primary well-differentiated slow-proliferating subtype can be established. Moreover, neither available cell lines nor genetically engineered mouse models recapitulate the spectrum of different molecular subtypes found in human primary Pan-

NETs [2, 14]. A stronger focus on developing more personalized in vitro models for studying these tumors is therefore demanded urgently. Cultivation and expansion of patient-derived neuroendocrine cells has been challenging owing to their intrinsically poor capacity for in vitro proliferation. However, due to advances in cell culture techniques, cell models of well-differentiated slow-proliferating PanNET derived from primary tissue have recently been used to study drug response and dissecting its underlying molecular mechanisms. For example, studies on isolated human primary PanNET cells cultured in vitro indicated that such a model might be utilized to determine patient response to treatment [15–18]. However, the major limitations of all these studies are the short cultivation window of the cells, the non-physiological 2-dimensional (2-D) format with limited cell-cell interactions, as well as their small scale in terms of investigated treatments and patient numbers.

In recent years, there have been tremendous advances in the development of 3-dimensional (3-D) tissue culture techniques, including scaffold-free setups in ultra-low attachment plates or scaffold-based encapsulation cultures to allow cell growth in 3 dimensions [19–23]. Culture of cells in 3 dimensions mimics a more physiological architecture of a tumor tissue, including cell-cell contact and allowing the development of spatial differences in the culture system with respect to proliferation, cell death and hypoxia within spheroids [21, 24–26]. Additionally, cells kept in a 3-D format can be cultured and treated longer than in 2-D monolayers [21]. Cells cultured in 3 dimensions frequently display increased therapy resistance compared to cells cultured in 2 dimensions [27–29], where 3-D culture most likely better reflects the in vivo situation [30, 31]. For this reason, lately high-throughput screenings of pharmacological compounds were preferentially performed in 3-D-cultured cells [32–34].

With the presented study, we aimed for developing a platform to collect PanNET samples from multiple surgical centers, to isolate primary cells and to cultivate these cells in 3 dimensions retaining NET characteristics and finally to measure short- and long-term in vitro treatment response.

Lead Contact and Material Availability

Further information and request for resources and reagents should be directed to and will be fulfilled by the Lead Contact Dr. I. Marinoni (Ilaria.marinoni@pathology.unibe.ch).

Experimental Model and Subject Details

Primary Cell Culture

Isolated primary PanNET cells were maintained in AdvDMEM + GF medium (DMEM-F12, 5% FBS, Hepes 10 mM, 1% L-glutamine (200 mM), 1% penicillin (100 U/mL), 1% streptomycin (0.1 mg/mL), 1% amphotericin B (0.25 mg/mL) (Merck, Switzerland), 20 ng/mL EGF, 10 ng/mL bFGF (Thermo Fisher Scientific, USA), 100 ng/mL PlGF, 769 ng/mL IGF-1 (Selleckchem, USA)) and in 24-well Corning® Costar® ultra-low attachment (ULA) plates (Corning, USA) (500 μ L/well, $3\text{--}5 \times 10^5$ cells/well) in a humidified cell incubator (21% O₂, 5% CO₂, 37°C). For drug screen cells were resuspended in fresh AdvDMEM + GF medium supplemented with 123 μ g/mL growth-factor-reduced Matrigel® (Corning, USA) and plated in 96-well ULA plates (50 μ L/well, $3\text{--}4 \times 10^3$ cells/well).

To set up the PanNET screening platform including drug screening, we made use of primary material from a total of 16 PanNET patients depicted in online supplementary Table 1 (for all online suppl. material, see www.karger.com/doi/10.1159/000507669). Additionally, key resources used in this study are provided in Table 1.

Patient Studies

All patients agreed on the use of residual material and had signed an institutional informed consent. Patient characteristics are shown in online supplementary Table 1. The study was approved by the cantonal authorities (Kantonale Ethikkommission Bern, Ref.-Nr. KEK-BE 105/2015) and the Italian ethic commission (Comitato Etico, CE 252/2019).

Methods

Patient Samples and Cryopreservation

Fresh human PanNET tissue was obtained from patients diagnosed with PanNET undergoing surgery at the Inselspital Bern, Switzerland, or at the Pancreatic Surgery Unit, Pancreas Translational and Clinical Research Center, San Raffaele Scientific Institute, Milan, Italy. Tumor tissues of 16 PanNET patients were used for 19 isolations, 12 isolations for method establishment and 7 for a proof-of-concept drug screening. Patient characteristics are summarized in online supplementary Table 1.

Upon surgical resection a pathologist processed one mirror block of the tumor tissue to 8-mm³ blocks under sterile conditions avoiding necrotic regions. These blocks

were suspended in recovery cell culture freezing medium (Thermo Fisher Scientific, USA), cryopreserved using an isopropyl alcohol freezing container (Nalgene, USA) and stored in liquid nitrogen. The other mirror block was embedded in a microcassette, and fixation was performed with a PAXgene Tissue System according to the manufacturer's instructions. In short, tissue was incubated in a PAXgene Tissue FIX Container (Qiagen, Germany) at room temperature overnight. Fixated tissue was transferred into a PAXgene Tissue FIX Container (Qiagen, Germany) at 4°C until paraffin embedding (1–2 days) or kept at –20°C if embedding was not performed instantly.

Primary Cell Isolation and Culture

For primary cell isolation, tissue was thawed for 45–60 s in a 37°C water bath and cut into 1-mm³ pieces and washed with medium (advanced DMEM-F12, Hepes 10 mM, 1% L-glutamine, 1% penicillin-streptomycin-amphotericin B) and Dulbecco's phosphate-buffered saline (DPBS; Thermo Fisher Scientific, USA). After aspiration of the medium, the tissue was incubated in 5 mL digestion medium (10 mg/mL collagenase IV (Worthington, USA), 0.25% Trypsin-EDTA (Sigma-Aldrich, Switzerland), 10 mg/mL DNase (Roche, Switzerland) in advanced DMEM-F12, Hepes 10 mM, 1% L-glutamine, 1% penicillin-streptomycin-amphotericin B) in a gentleMACS™ dissociator (Miltenyi Biotec, Switzerland) for 1 h at 37°C (programme TDK_1). After digestion, trypsin was deactivated with AdvDMEM (advanced DMEM-F12, 5% FBS, Hepes 10 mM, 1% L-glutamine, 1% penicillin-streptomycin-amphotericin B), and cells were filtered through a 70- μ m smart strainer (Miltenyi Biotec, Switzerland) to remove debris of collagen. Red blood cells were lysed for 3 min with ACK lysis buffer (Thermo Fisher Scientific, USA) at room temperature. After 180 g centrifugation and aspiration of supernatant, the pellet was resuspended in AdvDMEM + GF medium (DMEM-F12, 5% FBS, Hepes 10 mM, 1% L-glutamine, 1% penicillin-streptomycin-amphotericin B, 20 ng/mL EGF, 10 ng/mL bFGF (Thermo Fisher Scientific, USA), 100 ng/mL PlGF, 769 ng/mL IGF-1 (Selleckchem, USA)). The cell suspension was plated in 24-well plates (cell + coated and tumor cells tested, Sarstedt, Germany) followed by a short spin for 30 s, at 200 g and incubation for 1 h (21% O₂, 5% CO₂, 37°C) to partially segregate fibroblasts by attachment. The supernatant was collected. For single cell dissociation the cell suspension was transferred into a 5-mL falcon tube and shortly spun down depending on cell/aggregate size. If large aggregates were present, cells were spun at 100–200 g; if smaller aggregates were present, cells were spun at 200–

Table 1. Key Resource Table

Reagent or resource	Source	Identifier
Antibodies		
Anti-human Ki-67 (1:200)	Dako	M7240
Anti-human synaptophysin (1:4,000)	Novocastra	27G12
Anti-human insulin (1:100)	Sigma	I-2018
Biological samples		
Human PanNET specimen	This study	n.a.
Primary human PanNET cell culture	This study	n.a.
Devices and consumables		
Gentle MACS™ dissociator	Miltenyi Biotec	n.a.
Cell + coated and tissue culture tested 24-well plates	Sarstedt	83.3922.300
24/96-well Corning® Costar® ultra-low attachment plates	Corning	CLS4515
PAXgene Tissue FIX Container	Qiagen	765312
PAXgene Tissue STABILIZER	Qiagen	765512
Infinite® 200 PRO plate reader	Tecan	n.a.
Automated immunostainer Bond RX	Leica Biosystems	n.a.
Automated Slide Scanner panoramic 250	3DHistech	n.a.
Chemicals and peptides		
Recovery freezing medium	Thermo Fisher Scientific	12648-010
Advanced DMEM-F12	Thermo Fisher Scientific	D6421
Collagenase IV	Worthington	LS004188 CLS-4
Trypsin-EDTA (0.25%)	Sigma Aldrich	T4049
DNase	Roche	10104159001
Ammonium-chloride-potassium lysis buffer	Thermo Fisher Scientific	A1049201
Epidermal growth factor	Thermo Fisher Scientific	PHG0311
Basal fibroblast growth factor	Thermo Fisher Scientific	PHG0026
Placenta growth factor	Selleckchem	264-PGB-010
Insulin-like growth factor 1	Selleckchem	100-11
Accutase	Thermo Fisher Scientific	A11105-01
Growth-factor-reduced matrigel	Corning	354230
Real-time Glo™ MT cell viability assay	Promega	G9712
Human plasma	Interregional Blood Transfusion SRC Epalinges	92040
Thrombin	Diagnostec	100-125
Sunitinib (S1042)	Selleckchem	S1042
Everolimus (S1120)	Selleckchem	S1120
Temozolomide (S1237)	Selleckchem	S1237

n.a., not available.

300 g. The cell pellet was washed with DPBS and incubated in Accutase (Thermo Fisher Scientific, USA) supplemented with DNase (10 mg/mL) (Thermo Fisher Scientific, USA). Cells were carefully dissociated by repeated (10–15×) passage through a 1-mL syringe and 26 G 0.45 × 13 mm Microlance™ (BD, Switzerland) until aggregates were not visible anymore. The cell number was estimated using a hemocytometer, and cells were seeded in AdvDMEM + GF medium in 24-well ULA plates (5 × 10⁵ cells/mL/well). After 2 days of recovery phase, cellular aggregates were collected in 15-mL falcon tubes and differ-

entially centrifuged at 120 g for 5 min to separate cells and aggregates from debris/apoptotic cells. Supernatant was aspirated to remove semi- and nonviable cells. Cells were counted and resuspended in fresh AdvDMEM + GF medium supplemented with 123 µg/mL growth-factor-reduced Matrigel and plated in 96-well ULA plates (50 µL/well, 3–4 × 10³ cells/well). The setup consisted of 6–9 DMSO-positive control wells, 6 no-cell-negative control wells and technical triplicates for each drug concentration.

Viability Measurement

RealTime-Glo™ MT Cell Viability (RTG) assay (Promega, Switzerland) was used to repeatedly monitor cell viability in 3-D human primary PanNET culture. The RTG assay was performed according to the manufacturer's instructions, and luminescence was measured in an Infinite® 200 PRO plate reader (Tecan, Switzerland). In brief, after 3 days of sphere formation, conditioned medium of each well was supplemented with additional 50 µL of fresh AdvDMEM + GF medium containing Matrigel and RTG assay reagents (2×) to a final volume of 100 µL. Growth factors and FBS were replenished from a concentrate (0.77 µL GFs (130×) + 5 µL FBS) every 3–4 days in each well using a multichannel pipette. A 6-h RTG baseline before adding drug compounds was recorded for every well at day 0 of the drug screen. For calculating the in vitro growth curve, relative luminescence unit (RLU) values were normalized to corresponding baselines. For calculating the in vitro drug response, RLU values were normalized first to corresponding baselines followed by normalization to the DMSO control wells of a particular day as described in more details in the paragraph “curve fitting and drug sensitivity data.”

Micro-Cell-Block from Islet-Like Tumoroids

Islet-like tumoroids corresponding to 3–5 × 10⁴ cells were collected in a 1.5-mL Eppendorf tube (either directly on the day of isolation [D0] or from 6–9 wells of a 96-well ULA plate at the end of a drug screen [D15]). Tumoroids were washed with DPBS and pelleted at 350–500 g. The supernatant was aspirated, and the cells were resuspended in human plasma derived from whole blood (Interregional Blood Transfusion SRC, Epalinges, Switzerland) and Thrombin (Diagnostec, Switzerland) (ratio 5:1) followed by 3-min incubation at room temperature. The clot was fixed with 4% PFA for 30–60 min protected from light. After a DPBS wash, the supernatant was aspirated and cells were incubated in a hematoxylin and DPBS solution (ratio 1:8) on a rocker shaker for 10–15 min at room temperature. The counterstained clot was transferred to a plastic microcassette for paraffin embedding. For immunohistochemistry the embedded material was cut into 2.5-µm-thick serial sections followed by deparaffinization, rehydration and antigen retrieval using an automated immunostainer (Bond RX, Leica Biosystems, Germany). Antigen retrieval was performed for Ki-67 (Dako M7240) with Tris for 30 min at 95°C, insulin (Sigma I-2018) and synaptophysin (Novocastra 27G12) with Tris for 30 min at 100°C. Antibodies were diluted as follows: Ki-67 1:200, insulin 1:4,000, syn-

aptophysin 1:100. Slides were counterstained with hematoxylin. Scans were acquired with an automated slide scanner Panoramic 250 (3DHistech, Hungary) at 20× magnification. Images were acquired using QuPath software [35].

Drug Preparation

Compounds (sunitinib (S1042), everolimus (S1120) and temozolomide (S1237)) were obtained from commercial vendors and stored as stock aliquots at –80°C. A 5-point, 625-fold concentration range was used for all compounds in order to have enough data points and a sufficient large drug concentration window to calculate reliable absolute IC₅₀ values [36]. The starting dosage for each compound was selected based on IC₅₀ screens in cancer cell lines publicly available online (see Cancerrxgene.org, PharmacDB, Cancer Drug Resistance DB), from literature search and/or from in vitro data from pilot human primary cell cultures and/or from PanNET cell lines (QGP1, NT3, BON1).

Curve Fitting and Drug Sensitivity Data

Drug-response curve data consisted of 6–9 DMSO-positive controls, 6 no-cell-negative controls, and 5 drug-response points for a 625-fold concentration range. For IC₅₀ calculation RLU values that were derived from an RTG assay from short-term treatment on day 3 and long-term treatment on day 7 of each well were weighted and normalized as the following: RLU values from each 6-h RTG baseline measurement (RLU_x d0) were scaled with the overall minimal value of day 0 for each plate (RLU_{min} d0) and transferred into a baseline weight (RLU_x weight) for each well to minimize well-to-well variability:

$$RLU_x \text{ weight} = \frac{RLU_x \text{ d0}}{RLU_{\min} \text{ d0}} \quad (1)$$

Each RLU value from day 3 was then accordingly weighted to its baseline weight:

$$RLU_x \text{ d3/7 weight} = \frac{RLU_x \text{ d3/7}}{RLU_x \text{ weight}} \quad (2)$$

The percentage response from weighted RLU was calculated by normalizing each value to no-cell-negative control (0%) and DMSO-positive control (100%) intervals. These data points were fitted in a 4-parametric linear-regression model [34, 37] with two constraints, top = 100% and bottom = 0%, to estimate corresponding IC₅₀. IC₅₀ value differences of >4-fold were clustered in strong-responder and weak-responder groups. In case of an IC₅₀

value >2.5-fold higher than the highest tested target-concentration samples were considered as non-responder (NR).

Quantification and Statistical Analysis

QuPath Image Analysis

Using QuPath software [35] digital-scanned hematoxylin-eosin and synaptophysin tissue sections were first preprocessed in the built-in visual stain editor using default settings for estimation of stain vectors to improve staining quality. Each tissue section was then superimposed with a 1,000- μm grid box. In each tissue section one representative tile out of the grid box was selected by a cytopathologist (M.T.) as a training set. Using a watershed segmentation method, positive and negative cells were automatically detected within each representative tile. Two pathologists (M.T., A.P.) then manually reconfirmed positive cell detection based on histomorphological features including cellular and nuclear shape, tumor cell nest formation, tumor columns, nuclear “salt and pepper” structure, nuclear and cytoplasmic staining intensity. A minimum of $\geq 1,000$ cells were selected for each training set and a total of 67 parameters (including perimeter, circularity, staining optical density, etc.) were included for training of the random-trees machine learning classifier. The auto-update tool within QuPath allowed real-time reconfirmation of training efficiency/accuracy. These cell detection parameters were applied on the whole tissue slides by creating a script which performed automated cell classification/annotation. Detection results were extracted from QuPath and imported and analyzed within R.

Graph Pad Prism (Version 8.2.1) and R statistical environment were used for data analysis and visualization in the R version 3.6.2 (2019-12-12) platform: x86_64-w64-mingw32/x64 (64-bit). Attached base packages: Grid; stats; graphics; grDevices; utils; datasets; methods; base. Other attached packages: 81) scales_1.1.0; (2) MASS_7.3-51.4; (3) reshape2_1.4.3; (4) ConsensusClusterPlus_1.50.0; (5) circlize_0.4.8; (6) ComplexHeatmap_2.2.0; (7) RColorBrewer_1.1-2; (8) Rmisc_1.5; (9) plyr_1.8.5; (10) lattice_0.20-38; (11) plotrix_3.7-7; (12) cowplot_1.0.0; (13) forcats_0.4.0; (14) stringr_1.4.0; (15) dplyr_0.8.3; (16) purrr_0.3.3; (17) tidyr_1.0.0; (18) tibble_2.1.3; (19) ggplot2_3.2.1; (20) tidyverse_1.3.0; (21) broom_0.5.3; (22) readr_1.3.1.

Hierarchical Clustering Analysis of Drug Response Profiles

Using the ConsensusClusterPlus pipeline [38], the number and membership of clusters was determined for drug response profiles based on patient-specific IC_{50} values of all three drug treatments. Distances were calculated using Pearson's correlation sorted by an agglomerative hierarchical clustering algorithm. The WardD2 algorithm was used for subsampling, and the final consensus matrix was determined by group average.

Gene Expression Analysis

Mean expression values of growth factor receptors were analyzed in publicly available data of 26 PanNET patients. RNAseq data were downloaded from the ICGC Data Portal (PAEN-AU project). QC, mapping/alignment and raw count quantification is described in Scarpa et al. [2]. From RSEM data output for our downstream analysis we chose the FPKM (fragments per kilobase of exon per million fragments mapped) normalization method to account for sequencing depth and gene length for all raw read counts. A list of all available growth factor receptor was acquired from the UniProt Knowledgebase [39]. Expression values of all targets were transformed into a 0-to-1 scale for each patient to allow inter-patient comparability. Mean values for each target receptor were then calculated in all of the 26 PanNET patients:

$$\text{Expression value} = \text{mean}(\text{scaled}_{0,1}[\text{FPKM normalized raw counts}]) \quad (3)$$

χ^2 Test and Monte-Carlo Simulation

A χ^2 test of independence was conducted among all variables of interest. In order to meet requirements for χ^2 test statistic and to account for relatively small expected cell frequencies our data set was resampled using a Monte Carlo simulation (replication = 1×10^5) allowing to calculate p value estimates.

Data and Code Availability

The original RNAseq data set from human primary PanNET is publicly available at the ICGC Data Portal (PAEN-AU project). The complete expression data of growth factor receptors are available in the supplementary data sheet. The code supporting the current study has not been deposited in a public repository because the analysis code was generated from generic R packages, but the code is available from the corresponding author on request.

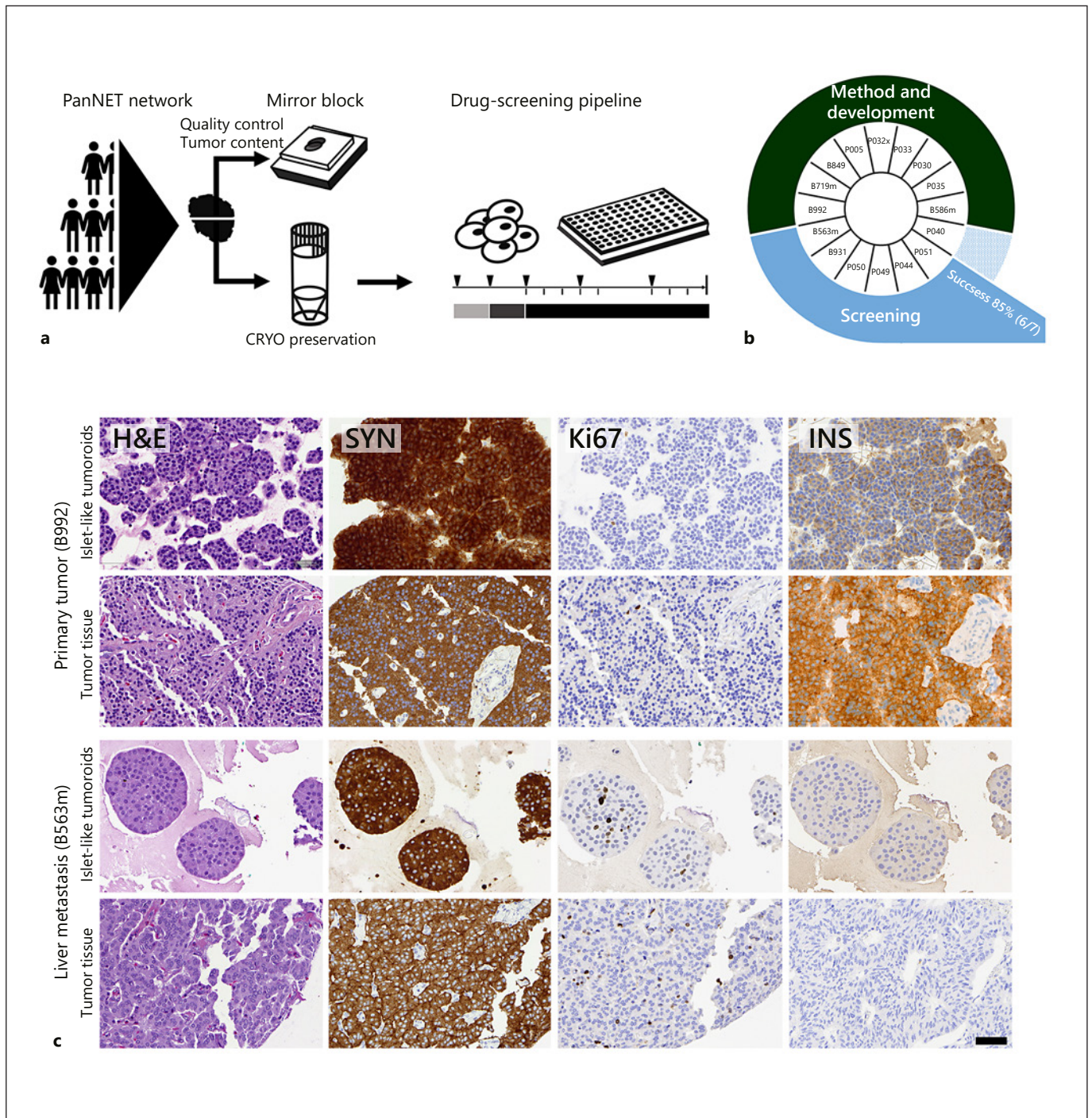


Fig. 1. Human primary PanNET cells form islet-like tumoroids and retain a neuroendocrine phenotype in vitro. **a** Schematic representation of human PanNET screening platform. **b** Venn diagram displaying usage of human PanNET patient material (outer circle) and individual patients (inner circle). The success rate for drug screening in PanNET patient material was 86% (6/7). Detailed log of cell isolation is provided in the online supplementary data file 1. **c** Representative hematoxylin-eosin (HE) and immunohistochemistry staining of islet-like tumoroids from B992 and

original primary tumor tissue B992 (top) and islet-like tumoroids from B563m and original metastatic tumor tissue from B563m (bottom). Cultured cells were formalin-fixed and embedded after 14 days in PanNET culture medium. Formalin-fixed primary PanNET tissue or cultured cells were stained for hematoxylin-eosin (HE), synaptophysin (SYN), insulin (INS) and Ki-67. Immunohistochemistry slides were counterstained with hematoxylin. Scale bar, 50 μ m.

Results

Cryopreservation Allows a Multicenter Approach

PanNET tumors are rare, therefore a collaborative network is crucial. Here we propose a novel platform for an effective multicenter approach which permits biobanking of cryopreserved PanNET tissues from multiple surgical centers by a single central institution which performs primary cell isolation and drug testing (Fig. 1a). After tumor resection, half of the specimen was formalin-free PAX-gene-fixed and paraffin embedded. These so-called mirror blocks served as controls for sample quality and were used to preassess patient-specific PanNET characteristics and tumor cell content in hematoxylin-eosin stainings and synaptophysin immunohistochemistry – a NET biomarker routinely used in clinics for diagnosis of PanNET. The other half was immediately cryopreserved in recovery freezing medium and later shipped and processed for primary cell isolation and in vitro drug screening.

Development of a 3-D Human Primary PanNET Cell Culture Model

Within this study, we performed 19 isolations from samples of 16 PanNET patients. Patient characteristics are summarized in online supplementary Table 1. In the first part of the study (12 patients), we set up the sampling, isolation and culture conditions. Two additional isolations were used for live-cell imaging to observe tumoroid formation. In the proof-of-concept part of the study (7 patients, including 3 patients who were also included in the method and development cohort), we tested the suitability of the setup for in vitro drug screening (Fig. 1b). During method development, we successfully isolated small aggregates and single cells from cryopreserved patient material in 73% (8/11) (online supplementary data file 1). Age, sex and other clinical parameters such as WHO grade, TNM staging and Ki-67 indices did not reveal a significant association with the isolation success and/or cellular yield (online suppl. Fig. 1A).

In 3 patient samples, isolation did not yield aggregates or single cells, which we attribute to the collection of largely acellular fibrotic or necrotic tissue as revealed from hematoxylin-eosin staining of corresponding mirror blocks (online suppl. Fig. 1B). Therefore, careful macroscopic selection of viable cellular tumor regions is crucial. Upon implementation of SOPs for sampling at the surgical centers, we observed strong quality improvements. In 2 patient samples (P005, P051) yielding successful cell isolation, we detected overgrowth of fibro-

blasts after 15 days (online suppl. Fig. 1C). This led us to implement a low FBS concentration in the culture medium and to include a partial fibroblast reduction step during cell isolation. Thus, the cell suspension was plated on coated plastic for 2 h followed by gently rinsing for the collection of low-adhesive nonstromal cells. Two tumor cell extracts (P032x, P033) were negative for synaptophysin immunohistochemistry (IHC) staining on conventional cytospin preparations and hence excluded for further culture. However, a post hoc analysis by a cytopathologist (M.T.) revealed that these cells were tumoral cells (online suppl. Fig. 1D). Consequently, to assess tumor cell content accurately, we implemented a formalin-fixating paraffin-embedding technique termed Micro-Cell-Block. Micro-Cell-Blocks retain cellular- and tumoroid morphology and require only a low cell number. Micro-Cell-Blocks on the day of isolation (D0) served as an internal quality control to assess successful fibroblast removal and to guide decision for continuation of the drug screening pipeline. Micro-Cell-Blocks at the end of the experiment (D15) allowed to quantify tumor cell content from synaptophysin immunohistochemistry and to reconfirm target cell identity on hematoxylin-eosin staining.

To account for more physiological cell culture conditions a PanNET-specific culture medium was developed combining literature and human transcriptomic data from 26 low-grade PanNETs [2]. We selected growth factors that were frequently reported in the PanNET literature [13, 15, 40] and for which – except of EGFR – all the target receptors (FGFR1, IGFR1/2, FLT1/VEGFR1, EGFR) were within the upper expression quintile (<28/151) of all currently available growth factor receptors and related proteins [40] in human PanNET patients (online suppl. Fig. 1A). Additionally, PanNET culture medium was supplemented with a low percentage of extracellular matrix. Several findings showed improved in vitro culture from Matrigel complementation due to scaffolding support [41–45]. Low concentration Matrigel supplementation stabilized PanNET culture, without leading to a transient artificially increased cellular growth as seen with higher supplementation (data not shown).

Human Primary PanNET Cells Form Islet-Like Tumoroids and Retain a Neuroendocrine Phenotype in vitro

After isolation and cell culture refinement we performed live-cell imaging in two human PanNET samples. We isolated single cells from cryopreserved primary PanNET tissue (B992) and PanNET liver metastasis (B563m).

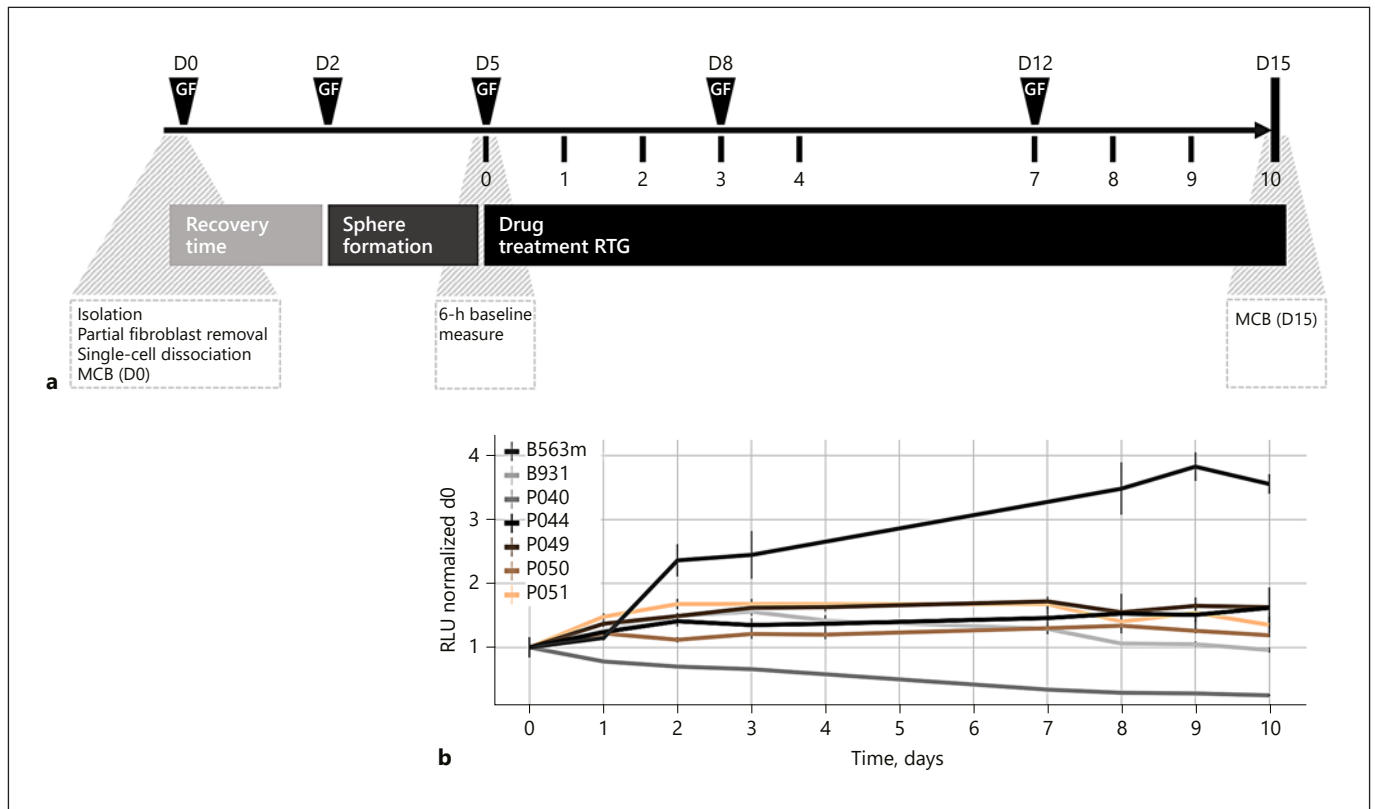


Fig. 2. 3-D human primary PanNET in vitro model for a personalized drug-screening platform. **a** Detailed schematic representation of in vitro 3-D drug-screening pipeline in human primary PanNET cells. GF, growth factor replenishment; thin ticks + digit, RTG viability assessment; MCB, Micro-Cell-Block. **b** In vitro growth curve of all screened primary PanNET samples using the metabolic surrogate assay RealTime-Glo (RTG) in 3-D human pri-

mary PanNET culture. Cells were cultured in AdvDMEM + GF and a low percentage of matrigel in 0.16% DMSO for 10 days. Normalization was calculated based on per-well 6-h RTG baseline measurement. Data represent means \pm SEM ($n = 7$, 3 technical replicates). RLU, relative luminescence unit.

Isolated cells from both patient specimens were viable. Live-cell imaging for 12 days revealed that isolated cells formed structures similar to extracted murine islets [46] which we hence termed islet-like tumoroids (online suppl. Fig. 2B). Islet-like tumoroids reached a more defined round structure after 72 h through aggregation and thereafter remained stable in volume (online suppl. Fig. 2C, suppl. video). Fourteen days after isolation, histomorphology of the islet-like tumoroids was examined and compared to corresponding mirror blocks. Islet-like tumoroids from primary and metastatic PanNET patient samples retained expression of synaptophysin, confirming that most of the cells consisted of tumor cells with preserved neuroendocrine phenotype (Fig. 1c). Furthermore, islet-like tumoroids from B992 expressed insulin as the original tumor tissue. The low percentage of Ki-67-positive tumor cells (2%) in vitro matched with the prolifera-

tion index described in the original tumor tissue (Ki-67 index <2%) (Fig. 1c, top, online suppl. Table 1). Similarly, the percentage of proliferating cells was retained in the metastatic PanNET sample (B563m), with a Ki-67 index of 12% in the original tumor tissues and 15% in cultured cells, respectively (Fig. 1c, bottom, online suppl. Table 1).

Setting Up an in vitro Drug Screening Pipeline for Islet-Like Tumoroids

After the successful pilot experiment, we sought to implement a pipeline for in vitro drug screening (Fig. 2a). Following a 2-day recovery phase after initial isolation, cells were replated from a 24-well format into a 96-well format. By this time, the majority of semi- and nonviable cells from isolation had segregated from viable cells. As seen in previous live-cell imaging analysis (online suppl. Fig. 2B, C), during 72-h incubation in the 96-well plate,

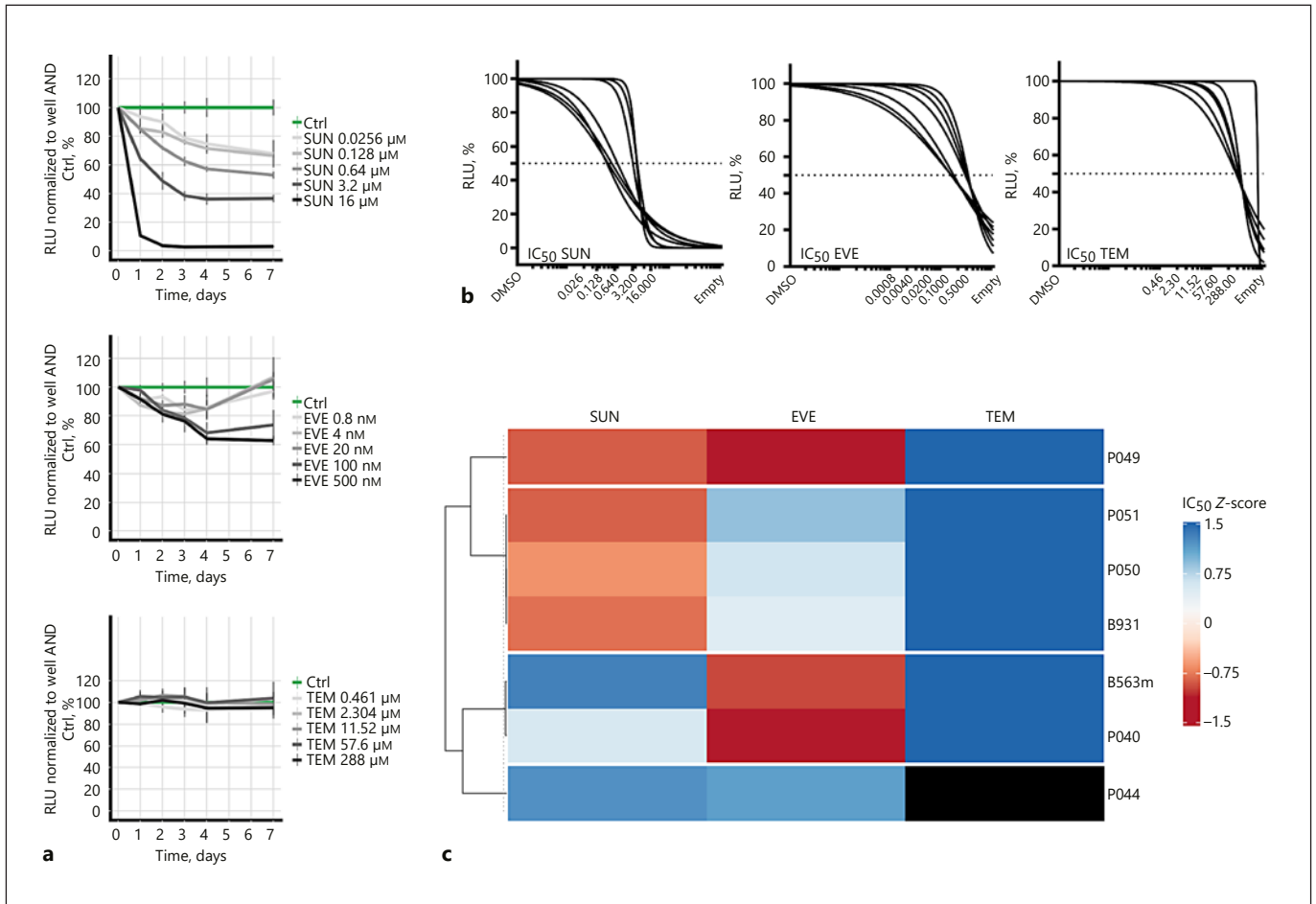


Fig. 3. Effect of standard of care pharmacological treatments on cell viability in 3-D human primary PanNET culture. **a** Representative in vitro viability curves using the metabolic surrogate assay RealTime-Glo (RTG) in 3-D human primary PanNET culture (P050) treated with 0.16% DMSO (control, Ctrl) or indicated treatment sunitinib (SUN), everolimus (EVE) and temozolomide (TEM) for 10 days. Normalization was calculated based on per-well 6-h RTG baseline measurement and corresponding DMSO control of the respective day. For all tested compounds a 5-point, 625-fold concentration range was used based on vast literature research and in-house in vitro preliminary studies. Data represent means \pm SEM ($n = 1$ per patient, 3 technical replicates). RLU, rela-

tive luminescence unit. **b** In vitro dose response curves of screened PanNET patient displaying IC₅₀ for SUN, EVE and TEM after short-term (72 h) treatment. Treatment responses (means \pm SEM) were fitted into a 4-parameter logistic regression model in GraphPad software to calculate absolute IC₅₀. Data represent fitted curve means ($n = 7$). Dotted line, absolute IC₅₀. **c** Heat map comparing absolute IC₅₀s for SUN, EVE and TEM in 3-D human primary PanNET culture after short-term (72 h) treatment. The heat map was derived using the WardD2 clustering method with displaying Pearson's clustering distance using ComplexHeatmap R-package [38]. The color code represents the scaled IC₅₀ (Z score) for each drug. Each row represents an individual patient.

cells formed islet-like tumoroids with only minor changes thereafter indicating a suitable time point for starting the drug treatment. Growth factors were replenished on days D2, D5, D8 and D12 after initial isolation. Due to low cell numbers available from PanNET specimens we selected RTG – a metabolic nonlytic assay – as a surrogate of cell viability. Pretreatment 6-h baseline measurements were recorded to normalize on an individual well basis and to correct for variability in cell number. Viability of

islet-like tumoroids in each well was repeatedly (8 \times) monitored over a time course of 10 days before storing the cell material for further downstream analysis.

PanNET Screening Pipeline in Control Conditions

As a proof-of-concept experiment, we tested the PanNET drug-screening pipeline with 7 patient samples. Tumor cells were successfully isolated in all 7 PanNET specimens. Quantification of tumor cells in mirror blocks of

original tumor tissue showed variable tumor content within tissues and among patients ($70 \pm 18\%$, $n = 7$) (online suppl. Fig. 3A, B). Yet, assessment of hematoxylin-eosin stainings and synaptophysin immunohistochemistry on Micro-Cell-Blocks on the day of isolation (D0) by a cytopathologist (M.T.) reconfirmed successful selection of tumor cells after isolation and fibroblast depletion in all samples used for drug screenings ($93 \pm 15\%$, $n = 7$) (online suppl. Fig. 3A, B). Moreover, successful culture of tumor cells was also reconfirmed in Micro-Cell-Blocks at the end of each experiment (D15) ($95 \pm 11\%$) (online suppl. Fig. 3A, B). In all patient samples, islet-like tumoroids were formed and remained viable in 85% (6/7) for 15 days in culture.

Following the metabolic activity of untreated islet-like tumoroids over the time course of 10 days, we observed an association between in vitro proliferation and Ki-67 index in original tumor tissue in the majority of samples: the metastatic patient sample (B563m) with a Ki-67 index of 15% in the original tumor tissue displayed the highest signal increase (3.8-fold), while in 4 patient samples with lower Ki-67 indices (P049, P050, P051, B931) the signal only increased between 1.1- and 1.7-fold (Fig. 2b). In patient sample P044 this association was weak exhibiting a 1.6-fold increase despite a Ki-67 index of 18% in the original tumor tissue. P040 was the only sample with a decreasing signal in the untreated condition; hence, long-term time points (>72 h) from this particular patient sample were not included in further analysis.

In vitro Drug Response in Islet-Like Tumoroids Shows Distinctive Sensitivity Profiles

To assess whether 3-D human primary PanNET culture could be exploited to predict patient drug response in vitro, we evaluated the effect of three clinically approved PanNET treatments on cell viability [47]. 3-D human primary PanNET cultures from 7 different patients were screened for response to sunitinib, everolimus and temozolomide. A 5-point, 625-fold drug concentration range ensured a sufficient exploratory drug screening window for accurate IC_{50} estimation based on mathematical modeling [36]. As starting points IC_{50} s from publicly available databases were interrogated for each drug, followed by pilot assessments of their antiproliferative effect in PanNET cell lines and murine primary cells (data not shown) as well as further literature research. Cells were treated for 10 days, and viability was repeatedly monitored at 8 time points during drug screening. Drug response profiles differed clearly among the three standard of care treatments. Dose-dependent effects of sunitinib and everolimus were observed in all tested patient sam-

ples (Fig. 3a, online suppl. Fig. 4A). Interestingly, comparing interpatient drug responses we detected varying treatment sensitivities among patients (online suppl. Fig. 4A). IC_{50} values determined after short-term (72 h) treatment displayed two clearly distinct groups within sunitinib treatment and within everolimus treatment harboring >4 -fold differences in respective IC_{50} (Fig. 3b). Also consensus clustering matrix and hierarchical cluster analysis ($k = 4$) displayed robust response groups for short-term (72 h) treatments (Fig. 3c): a strong-responder group with samples sensitive to both treatments (P049), a group responding either primarily to everolimus (P049, P040, B563m) or to sunitinib (P050, B931, P051) – which was considered as mixed-responder group – and a weak-responder group including one sample insensitive to all treatments (P044). Importantly, in an integrative hierarchical cluster analysis, short-term treatment IC_{50} s – for the majority of patients – clustered closely together with long-term treatment IC_{50} s emphasizing robustness of the readouts (online suppl. Fig. 4B). Interestingly, in 1 case (B931) differences between short-term and long-term treatment were detected (online suppl. Fig. 4B).

Discussion/Conclusion

Current murine and human cell line models do neither accurately represent human well-differentiated slow-proliferating PanNETs, nor distinct human molecular subtypes, nor interpatient variability. In this study, we present a human PanNET screening platform allowing multicenter sample collection of cryopreserved patient specimens with an 86% success rate in primary cell isolation and cell culture. Isolated cells of well-differentiated slow-proliferating PanNET can be cultured in 3 dimensions and screened in vitro assessing response profiles to standard of care treatments for PanNETs. Since the cell number was the major limiting factor, we established protocols that are optimized for minimal amounts of resection specimens.

We present cryopreservation as a solution to make multicenter studies possible, thereby overcoming the issue of the rarity of PanNET samples. While difficult to implement in different centers, this generation of “living cell repositories” is promoted as innovative biobanking setting [48] and increasingly used in translational cancer research [49]. To account for more physiological conditions, growth factor supplementation for our PanNET culture medium was based on a combination of literature research [13, 15, 40], transcriptomic analysis of growth factor receptors as well as pilot experiments testing different growth factor concen-

trations and combinations. Final PanNET culture medium composition was selected according to best retention of viability during a 15-day period to minimize selection. This approach is clearly different from classical organoid approaches, where the culture medium selects for stem cell-like cells, and where these cells are kept individually in a biomatrix in order to produce clonal organoids [50, 51]. The aim of our presented “tumoroid” model is to in vitro treat a similar tumor cell composition as present in the patient. Following this approach, we can obtain a remarkable success rate of 86%, but we acknowledge that classical organoid models have many other advantages such as the potential to intervene mechanistically [52–54]. With a retention of $\pm 70\%$ of isolated cells in experiments before drug screening we believe that selection bias is minimal and that we are capable of treating the majority of cells representing the original tumor [55]. Compared to the limited number of studies using primary PanNET tissues in 2-D culture [15–18], we observe a reproducibly extended life span of the isolated cells up to 15 days. Longer experiments would also be possible at least in a subgroup of tumors; however, typically we did observe major responses already during the first 3 days of treatment.

We show that primary cells isolated from PanNET express original tumor characteristics and retain their neuroendocrine phenotype after 15 days. Interestingly, isolated cells form islet-like tumoroids in vitro. Similarly, nonneoplastic endocrine pancreatic cells are physiologically structured as islets. Kojima et al. reviewed the history of abundant findings which revealed that single cell suspension of endocrine pancreatic tissue from several species form islet-like structures and reconstitute their original architecture in vitro [56]. Currently, we do not know whether this reflects an endocrine specific phenotype or an even broader epithelial phenotype.

With the conditions presented, isolation and culture were successful in 6 out of 7 patients (86%). Only 1 sample (P040) showed a loss of viability after 7 days and was excluded from further long-term treatment analysis. During 3-D culture, all G1 PanNET patient samples expectedly displayed only marginal growth, whereas the metastatic patient sample B563m (Ki-67 index of 15%) showed the highest growth in vitro (3.8-fold in 10 days). One G2 sample (P044, Ki-67 index of 18%) exhibited a somewhat lower growth of 1.6-fold in 10 days. It seems not surprising to infrequently observe a rather weak association of Ki-67 index and in vitro proliferation. Indeed, a clear linear correlation of Ki-67 index to tumor growth rate has not been demonstrated clinically, to our knowledge. Biologically, proliferation represents only one aspect out of

many: we neither have knowledge about a different fraction of cell death within our PanNET specimen nor do we know exact durations of cell cycles for the isolated cells from individual patient specimens.

In vitro treatment with clinically approved chemotherapeutics for advanced PanNET disease revealed overall distinctive response profiles and drug sensitivities based on IC_{50} s. Comparing short-term (72 h) versus long-term treatment (7 days and 15 days) showed identical results in the majority of samples, indicating that these different time windows are potentially of minor importance. However, in 1 tumor (B931) we observed differences between short-term and long-term treatment. While it might not be important to use long-term treatment for detecting primary response in sunitinib and everolimus treatment, prolonged treatment could be of potential importance for other chemotherapeutics. In our series, we do not see a clear response to temozolomide in all of the 7 PanNETs examined. A possible explanation for this is the mechanism of action of temozolomide, which is strongly linked to cellular proliferation. Cytotoxicity of temozolomide is mediated by O_6 -methylguanine adducts, which can mispair with thymine during DNA replication. The resulting futile cycles of DNA processing induce cytotoxic double-strand DNA breaks that trigger apoptosis [57, 58]. Due to the low proliferation rate of our samples a time window of 10 days may be still too short for a detection of measurable effects. In line with that, the metastatic patient sample (B563m) that proliferated in vitro shows at least a faint response to temozolomide in our screen – even if the IC_{50} estimation is still far from our tested drug concentration window (online suppl. Fig. 4A) and even if the sample has been scored as weak responder. We can exclude nonpotency of the chemotherapeutic compound itself since our implemented 625-fold concentration window (0.46–288.00 μM) covers a sufficiently large drug window tested in PanNET and glioblastoma cell lines (data not shown) to eliminate this as a potential bias.

In other tumor entities it has been shown that ex vivo drug response correlates with patients’ response in primary cell culture approaches similar to our setup (e.g. esophageal adenocarcinoma, breast cancer, and head and neck squamous cell carcinoma) [59–61] and in patient-derived xenograft models [62, 63]. Further studies are needed to evaluate whether the observed in vitro sensitivity will correlate with clinical response in PanNET patients as well. To answer this question, first a prolonged clinical follow-up is crucial. Secondly, a larger patient cohort will be needed to perform correlation analysis and to have enough statistical power. Full clinical follow-up data of all enrolled patients

are therefore collected. Chemotherapy-specific in vitro treatment duration and concentration range with the highest predictive value will be defined by comparison of clinical data with the in vitro drug response. Due to the non-lytic approach, the islet-like tumoroids are collected after the experiment and are available for next-generation-sequencing end point analysis, as is the original tumor material from patients. The presented PanNET screening platform might therefore serve as a basis for developing personalized treatment of PanNET patients, performing molecular fingerprinting on the original tissue to be able to potentially detect predictive markers.

We are well aware that the present protocol still bears limitations. It depends on surgical resection specimens of PanNET metastases and high-stage tumors; however, most of these patients are diagnosed via biopsies of liver metastases. With further experience the protocol has the potential of being adapted to biopsy specimens as well – yet – some biological role must be proven first to ethically justify additional biopsies. The composition of growth factors could be further refined, and the culture system does not factor in stromal and inflammatory features potentially contributing also to tumor response.

In conclusion, we present a 3-D human primary PanNET screening platform as a new preclinical model, which reflects the characteristics of an individual tumor and has the capability to detect differential treatment response. Therefore, this model has the potential to pave the way towards more personalized medicine for PanNET patients in the future, including better patient stratification and identification of novel and experimental treatments.

Acknowledgment

We thank the Tissue Bank Bern (Bern, Switzerland) and the Translational Research Unit (Institute of Pathology, Bern, Switzerland) for their technical, material and administrative support and

References

- 1 Di Domenico A, Wiedmer T, Marinoni I, Perren A. Genetic and epigenetic drivers of neuroendocrine tumours (NET). *Endocr Relat Cancer*. 2017 Sep;24(9):R315–34.
- 2 Scarpa A, Chang DK, Nones K, Corbo V, Patch AM, Bailey P, et al; Australian Pancreatic Cancer Genome Initiative. Whole-genome landscape of pancreatic neuroendocrine tumours. *Nature*. 2017 Mar;543(7643):65–71.
- 3 Baroni MG, Cavallo MG, Mark M, Monetini L, Stoehrer B, Pozzilli P. Beta-cell gene expression and functional characterisation of the human insulinoma cell line CM. *J Endocrinol*. 1999 Apr;161(1):59–68.
- 4 Evers BM, Ishizuka J, Townsend CM Jr, Thompson JC. The human carcinoid cell line, BON. A model system for the study of carcinoid tumors. *Ann NY Acad Sci*. 1994 Sep;733(1):393–406.
- 5 Iguchi H, Hayashi I, Kono A. A somatostatin-secreting cell line established from a human pancreatic islet cell carcinoma (somatostatinoma): release experiment and immunohistochemical study. *Cancer Res*. 1990 Jun;50(12):3691–3.
- 6 Kaku M, Nishiyama T, Yagawa K, Abe M. Establishment of a carcinoembryonic antigen-producing cell line from human pancreatic carcinoma. *Gan*. 1980 Oct;71(5):596–601.
- 7 Doihara H, Nozawa K, Kojima R, Kawabata-Shoda E, Yokoyama T, Ito H. QGP-1 cells release 5-HT via TRPA1 activation; a model of human enterochromaffin cells. *Mol Cell Biochem*. 2009 Nov;331(1-2):239–45.
- 8 Gragnoli C. The CM cell line derived from liver metastasis of malignant human insulinoma is not a valid beta cell model for in vitro studies. *J Cell Physiol*. 2008 Aug;216(2):569–70.

the Cytopathology (Institute of Pathology, Bern, Switzerland) for technical support performing formalin-fixation and paraffin embedding in tissue and cell culture material. We also thank Dr. Joel Zindel, Mr. Philipp Zens and Mr. Hassan Sadozai for their constructive feedback on the manuscript drafts.

Statement of Ethics

Subjects (or their parents or guardians) have given their written informed consent, and the study protocol was approved by the cantonal authorities (Kantonale Ethikkommission Bern, Ref.-Nr. KEK-BE 105/2015) and the Italian ethic commission (Comitato Etico, CE 252/2019).

Disclosure Statement

All the authors declare no competing financial interest. There is no conflict of interest that could be perceived as prejudicing the impartiality of the research reported.

Funding Sources

The study was supported by Wilhelm Sander to Ilaria Marinoni and a Swiss Cancer League Grant (KLS 3360-02-2014) to Aurel Perren. Valentina Andreasi's PhD scholarship and Francesca Muffatti's research fellowship were supported by Gioja Bianca Costanza legacy donation.

Author Contributions

A.P., I.M., T.W. and S.L.A.M. designed the study. T.W. and S.L.A.M. developed the tumoroid methodology. T.W., M.S. and S.L.A.M. performed experiments and data acquisition. S.L.A.M. analyzed and visualized data. M.T. analyzed, scored and quantified immunohistochemistry. M.F., C.D., M.S.L., F.M., S.P., C.K.F. and B.G. provided patient biopsies and patient clinical information. R.M., M.S.L., A.D., V.A., M.C.Z., C.K.F., B.G. and M.S. provided administrative, technical or material support. A.P., I.M., T.W. and S.L.A.M. wrote the paper.

- 9 Jonnakuty C, Gragnoli C. Karyotype of the human insulinoma CM cell line—beta cell model in vitro? *J Cell Physiol.* 2007 Dec; 213(3):661–2.
- 10 Lopez JR, Claessen SM, Macville MV, Albrechts JC, Skogseid B, Speel EJ. Spectral karyotypic and comparative genomic analysis of the endocrine pancreatic tumor cell line BON-1. *Neuroendocrinology.* 2010;91(2): 131–41.
- 11 Siddique ZL, Drozdov I, Floch J, Gustafsson BI, Stunes K, Pfragner R, et al. KRJ-I and BON cell lines: defining an appropriate enterochromaffin cell neuroendocrine tumor model. *Neuroendocrinology.* 2009;89(4):458–70.
- 12 Boora GK, Kanwar R, Kulkarni AA, Pleticha J, Ames M, Schroth G, et al. Exome-level comparison of primary well-differentiated neuroendocrine tumors and their cell lines. *Cancer Genet.* 2015 Jul-Aug;208(7-8):374–81.
- 13 Benten D, Behrang Y, Unrau L, Weissmann V, Wolters-Eisfeld G, Burdak-Rothkamm S, et al. Establishment of the First Well-differentiated Human Pancreatic Neuroendocrine Tumor Model. *Mol Cancer Res.* 2018 Mar; 16(3):496–507.
- 14 Sadanandam A, Wullschleger S, Lyssiottis CA, Grötzinger C, Barbi S, Bersani S, et al. A Cross-Species Analysis in Pancreatic Neuroendocrine Tumors Reveals Molecular Subtypes with Distinctive Clinical, Metastatic, Developmental, and Metabolic Characteristics. *Cancer Discov.* 2015 Dec;5(12):1296–313.
- 15 Falletta S, Partelli S, Rubini C, Nann D, Doria A, Marinoni I, et al. mTOR inhibitors response and mTOR pathway in pancreatic neuroendocrine tumors. *Endocr Relat Cancer.* 2016 Nov;23(11):883–91.
- 16 Mohamed A, Romano D, Saveanu A, Roche C, Albertelli M, Barbieri F, et al. Anti-proliferative and anti-secretory effects of everolimus on human pancreatic neuroendocrine tumors primary cultures: is there any benefit from combination with somatostatin analogs? *Oncotarget.* 2017 Jun;8(25): 41044–63.
- 17 Mohamed A, Blanchard MP, Albertelli M, Barbieri F, Brue T, Niccoli P, et al. Pasireotide and octreotide antiproliferative effects and sst2 trafficking in human pancreatic neuroendocrine tumor cultures. *Endocr Relat Cancer.* 2014 Oct;21(5):691–704.
- 18 Wiedmer T, Blank A, Pantasis S, Normand L, Bill R, Krebs P, et al. Autophagy Inhibition Improves Sunitinib Efficacy in Pancreatic Neuroendocrine Tumors via a Lysosome-dependent Mechanism. *Mol Cancer Ther.* 2017 Nov;16(11):2502–15.
- 19 Aboulkheyr Es H, Montazeri L, Aref AR, Vosough M, Baharvand H. Personalized Cancer Medicine: An Organoid Approach. *Trends Biotechnol.* 2018 Apr;36(4):358–71.
- 20 Broguiere N, Isenmann L, Hirt C, Ringel T, Placzek S, Cavalli E, et al. Growth of Epithelial Organoids in a Defined Hydrogel. *Adv Mater.* 2018 Oct;30(43):e1801621.
- 21 Nath S, Devi GR. Three-dimensional culture systems in cancer research: focus on tumor spheroid model. *Pharmacol Ther.* 2016 Jul; 163:94–108.
- 22 Tuveson D, Clevers H. Cancer modeling meets human organoid technology. *Science.* 2019 Jun;364(6444):952–5.
- 23 Xu H, Lyu X, Yi M, Zhao W, Song Y, Wu K. Organoid technology and applications in cancer research. *J Hematol Oncol.* 2018 Sep; 11(1):116.
- 24 Huang L, Holtzinger A, Jagan I, BeGora M, Lohse I, Ngai N, et al. Ductal pancreatic cancer modeling and drug screening using human pluripotent stem cell- and patient-derived tumor organoids. *Nat Med.* 2015 Nov; 21(11):1364–71.
- 25 Pampaloni F, Reynaud EG, Stelzer EH. The third dimension bridges the gap between cell culture and live tissue. *Nat Rev Mol Cell Biol.* 2007 Oct;8(10):839–45.
- 26 Bresciani G, Hofland LJ, Dogan F, Giamas G, Gagliano T, Zatelli MC. Evaluation of spheroid 3D culture methods to study a pancreatic neuroendocrine neoplasm cell line. *Front Endocrinol (Lausanne).* 2019 Oct;10:682.
- 27 Ekert JE, Johnson K, Strake B, Pardinas J, Jarrantow S, Perkinson R, et al. Three-dimensional lung tumor microenvironment modulates therapeutic compound responsiveness in vitro—implication for drug development. *PLoS One.* 2014 Mar;9(3):e92248.
- 28 Luca AC, Mersch S, Deenen R, Schmidt S, Messner I, Schäfer KL, et al. Impact of the 3D microenvironment on phenotype, gene expression, and EGFR inhibition of colorectal cancer cell lines. *PLoS One.* 2013;8(3):e59689.
- 29 Riedl A, Schleder M, Pudielko K, Stadler M, Walter S, Unterleuthner D, et al. Comparison of cancer cells in 2D vs 3D culture reveals differences in AKT-mTOR-S6K signaling and drug responses. *J Cell Sci.* 2017 Jan;130(1):203–18.
- 30 McMillin DW, Negri JM, Mitsiades CS. The role of tumour-stromal interactions in modifying drug response: challenges and opportunities. *Nat Rev Drug Discov.* 2013 Mar;12(3):217–28.
- 31 Weiswald LB, Bellet D, Dangles-Marie V. Spherical cancer models in tumor biology. *Neoplasia.* 2015 Jan;17(1):1–15.
- 32 Pauli C, Hopkins BD, Prandi D, Shaw R, Fedrizzotti T, Sboner A, et al. Personalized In Vitro and In Vivo Cancer Models to Guide Precision Medicine. *Cancer Discov.* 2017 May; 7(5):462–77.
- 33 Tiriach H, Belleau P, Engle DD, Plenker D, Deschênes A, Somerville TD, et al. Organoid Profiling Identifies Common Responders to Chemotherapy in Pancreatic Cancer. *Cancer Discov.* 2018 Sep;8(9):1112–29.
- 34 van de Wetering M, Francies HE, Francis JM, Bounova G, Iorio F, Pronk A, et al. Prospective derivation of a living organoid biobank of colorectal cancer patients. *Cell.* 2015 May; 161(4):933–45.
- 35 Bankhead P, Loughrey MB, Fernández JA, Dombrowski Y, McArt DG, Dunne PD, et al. QuPath: open source software for digital pathology image analysis. *Sci Rep.* 2017 Dec; 7(1):16878.
- 36 Sebaugh JL. Guidelines for accurate EC50/IC50 estimation. *Pharm Stat.* 2011 Mar-Apr; 10(2):128–34.
- 37 Garnett MJ, Edelman EJ, Heidorn SJ, Greenman CD, Dastur A, Lau KW, et al. Systematic identification of genomic markers of drug sensitivity in cancer cells. *Nature.* 2012 Mar; 483(7391):570–5.
- 38 Wilkerson MD, Hayes DN. ConsensusClusterPlus: a class discovery tool with confidence assessments and item tracking. *Bioinformatics.* 2010 Jun;26(12):1572–3.
- 39 UniProt Consortium. UniProt: a worldwide hub of protein knowledge. *Nucleic Acids Res.* 2019 Jan;47 D1:D506–15.
- 40 Hilfenhaus G, Göhrig A, Pape UF, Neumann T, Jann H, Zdunek D, et al. Placental growth factor supports neuroendocrine tumor growth and predicts disease prognosis in patients. *Endocr Relat Cancer.* 2013 May;20(3):305–19.
- 41 Hughes CS, Postovit LM, Lajoie GA. Matrigel: a complex protein mixture required for optimal growth of cell culture. *Proteomics.* 2010 May;10(9):1886–90.
- 42 Kleinman HK, Martin GR. Matrigel: basement membrane matrix with biological activity. *Semin Cancer Biol.* 2005 Oct;15(5):378–86.
- 43 Kutschka I, Chen IY, Kofidis T, Arai T, von Degenfeld G, Sheikh Ahmad Y., et al. Collagen matrices enhance survival of transplanted cardiomyoblasts and contribute to functional improvement of ischemic rat hearts. *Circulation.* 2006 Jul;114(1 suppl):I–167.
- 44 Poincloux R, Collin O, Lizárraga F, Romao M, Debray M, Piel M, et al. Contractility of the cell rear drives invasion of breast tumor cells in 3D Matrigel. *Proc Natl Acad Sci USA.* 2011 Feb;108(5):1943–8.
- 45 Zheng W, Zhang W, Jiang X. Biomimetic collagen nanofibrous materials for bone tissue engineering. *Adv Eng Mater.* 2010 Sep; 12(9):B451–66.
- 46 Montesano R, Mouron P, Amherdt M, Orci L. Collagen matrix promotes reorganization of pancreatic endocrine cell monolayers into islet-like organoids. *J Cell Biol.* 1983 Sep;97(3):935–9.
- 47 Kaderli RM, Spanjol M, Kollár A, Bütikofer L, Gloy V, Dumont RA, et al. Therapeutic Options for Neuroendocrine Tumors: A Systematic Review and Network Meta-analysis. *JAMA Oncol.* 2019 Apr;5(4):480–9.
- 48 Bolck HA, Pauli C, Göbel E, Mühlbauer K, Dettwiler S, Moch H, et al. Cancer sample biobanking at the next level: combining tissue with living cell repositories to promote precision medicine. *Front Cell Dev Biol.* 2019 Oct;7:246.
- 49 Alkema NG, Tomar T, Duiker EW, Jan Meersma G, Klip H, van der Zee AG, et al. Biobanking of patient and patient-derived xenograft ovarian tumour tissue: efficient preservation with low and high fetal calf serum based methods. *Sci Rep.* 2015 Oct;5(1):14495.

- 50 Sato T, Vries RG, Snippert HJ, van de Wetering M, Barker N, Stange DE, et al. Single Lgr5 stem cells build crypt-villus structures in vitro without a mesenchymal niche. *Nature*. 2009 May;459(7244):262–5.
- 51 Sato T, Stange DE, Ferrante M, Vries RG, Van Es JH, Van den Brink S, et al. Long-term expansion of epithelial organoids from human colon, adenoma, adenocarcinoma, and Barrett's epithelium. *Gastroenterology*. 2011 Nov;141(5):1762–72.
- 52 Fujii M, Shimokawa M, Date S, Takano A, Matano M, Nanki K, et al. A Colorectal Tumor Organoid Library Demonstrates Progressive Loss of Niche Factor Requirements during Tumorigenesis. *Cell Stem Cell*. 2016 Jun;18(6):827–38.
- 53 Matano M, Date S, Shimokawa M, Takano A, Fujii M, Ohta Y, et al. Modeling colorectal cancer using CRISPR-Cas9-mediated engineering of human intestinal organoids. *Nat Med*. 2015 Mar;21(3):256–62.
- 54 Drost J, van Boxtel R, Blokzijl F, Mizutani T, Sasaki N, Sasselli V, et al. Use of CRISPR-modified human stem cell organoids to study the origin of mutational signatures in cancer. *Science*. 2017 Oct;358(6360):234–8.
- 55 Weeber F, Ooft SN, Dijkstra KK, Voest EE. Tumor Organoids as a Pre-clinical Cancer Model for Drug Discovery. *Cell Chem Biol*. 2017 Sep;24(9):1092–100.
- 56 Kojima N. In vitro reconstitution of pancreatic islets. *Organogenesis*. 2014 Apr-Jun;10(2):225–30.
- 57 Koumariou A, Kaltsas G, Kulke MH, Oberg K, Strosberg JR, Spada F, et al. Temozolomide in Advanced Neuroendocrine Neoplasms: Pharmacological and Clinical Aspects. *Neuroendocrinology*. 2015;101(4):274–88.
- 58 Fu D, Calvo JA, Samson LD. Balancing repair and tolerance of DNA damage caused by alkylating agents. *Nat Rev Cancer*. 2012 Jan;12(2):104–20.
- 59 Lohse I, Al-Ali H, Volmar CH, D Alvarez Trotta A, Brothers SP, Capobianco AJ, et al. Ex vivo drug sensitivity testing as a means for drug repurposing in esophageal adenocarcinoma. *PLoS One*. 2018 Sep;13(9):e0203173.
- 60 Majumder B, Baraneedharan U, Thiagarajan S, Radhakrishnan P, Narasimhan H, Dhanda-pani M, et al. Predicting clinical response to anticancer drugs using an ex vivo platform that captures tumour heterogeneity. *Nat Commun*. 2015 Feb;6(1):6169.
- 61 Naipal KA, Verkaik NS, Ameziane N, van Deurzen CH, Ter Brugge P, Meijers M, et al. Functional ex vivo assay to select homologous recombination-deficient breast tumors for PARP inhibitor treatment. *Clin Cancer Res*. 2014 Sep;20(18):4816–26.
- 62 Garralda E, Paz K, López-Casas PP, Jones S, Katz A, Kann LM, et al. Integrated next generation sequencing and avatar mouse models for personalized cancer treatment. *Clin Cancer Res*. 2014 May;20(9):2476–84.
- 63 Weroha SJ, Becker MA, Enderica-Gonzalez S, Harrington SC, Oberg AL, Maurer MJ, et al. Tumor grafts as in vivo surrogates for women with ovarian cancer. *Clin Cancer Res*. 2014 Mar;20(5):1288–97.

Supplementary Material April-Monn et al. (2020), *Neuroendocrinology*

Supplementary Table 1. Table summarizing clinical information of the primary PanNET patient cohort.

Supplementary Fig. 1.

(A) Association table showing estimated p-values from χ^2 -test of independence using Monte Carlo simulation. Association was estimated from all variables of interest from all PanNET patients used in this study (n=16). Iso-Success = Isolation success; Age_gr = Age grouped; Grade_WHO= WHO tumor grading system; TNM_AJCC= American Joint Committee on Cancer TNM-staging system; T_stage= Tumor stage; N_stage= Lymph node stage; M_stage= Metastasis stage; Cell_yield= Cell yield at isolation

(B-D) Stainings of formalin fixed paraffin embedded (FFPE) original tumor tissue (hematoxylin-eosin (HE), left) and Micro-Cell-Blocks (HE or synaptophysin (SYN), right) of samples derived from necrotic or acellular fibrotic tissue (B), samples with fibroblast overgrowth (C), and samples with few target cells (D). All stainings were assessed by two pathologists (M.T., A.P.). Scale bar = 250 μ m and 50 μ m.

Supplementary Fig. 2.

(A) Mean expression values of growth factor receptors in 26 PanNET patients. RNAseq data from Scarpa *et al.* [2] was downloaded from the ICGC Data Portal (PAEN-AU project). FPKM normalization method was applied to raw gene counts. A list of all available growth factor receptors was acquired from the UniProt Knowledgebase [39]. Complete expression data of growth factor receptor is available in Supplementary Data Sheet 1. Data represent mean \pm SD (n=26).

(B) Representative light micrographs of PanNET islet-like tumoroids from primary tumor (B992, left) and liver metastasis (B563m, right). Isolated cells were cultured in 24-well ultra-low attachment plates (ULA) for 14 days. Scale bar = 200 μ m.

(C) Representative time points from 12 days live-cell imaging of primary human PanNET (B992). A clear formation of islet-like tumoroids can be observed after 72 hours. Snapshots were taken from Supplementary Video. Specific time points (hh:mm) are indicated in every image.

Supplementary Fig. 3

(A) IHC staining and quantification of NET specific biomarker synaptophysin (SYN) in formalin fixed paraffin embedded (FFPE) in original tumor tissues and respective Micro-Cell-Blocks (MCB) of all screened patients (n=7). Tumor content (%) in original tumor tissue (left) was assessed by a

cytopathologist (M.T.) followed by building a classifier in QuPath software [35] to automate quantification (right). MCBs were individually analyzed by a cytopathologist (M.T.) comparing hematoxylin-eosin (HE) and SYN staining to estimate tumor content (%). Data (left) represent mean+SD (n=1-2 tissue punches per patient). Scale bar = 100µm (left), 50µm (right). Tissue= Original tumor tissue.

(B) Bar graph quantifying percentage of synaptophysin positive (SYN+) cells in original tumor tissue and 3-D human primary PanNET culture at day of isolation (MCB D0) and at 15 days (MCB D15), respectively. Data represent mean ± SD (n=7 individual patients). Tissue= Original tumor tissue.

Supplementary Fig. 4

(A) Line graphs of all screened PanNET patients (n=7) displaying IC50 for sunitinib (SUN), everolimus (EVE), temozolomide (TEM) 7 days after treatment. Treatment responses were fitted into a 4-parameter logistic regression model in GraphPad software to calculate absolute IC50. Data represent mean ± SEM (n=1 per patient, 3 technical replicates). Dotted line = Absolute IC50.

(B) Heat map comparing absolute IC50 for SUN, EVE, and TEM in 3D human primary PanNET culture at short-term (3 days, _d3) and long-term (7 days, _d7) drug treatment. Heat map was derived using WardD2 clustering method with displaying Pearson's clustering distance using ComplexHeatmap R-package. Color code represents scaled IC50 (z-score) for each drug. Vertical dashed line displays k-value from consensus clustering analysis. Each row represents patient response at d3 or d7 of the treatment.

Supplementary Video

Upon single cell isolation of sample B992, cells were seeded in a 96-well ULA plate (5000 cells/well). After two days of recovery, the plate was transferred to the Cell-IQ® (CM Technologies Oy, Tampere, Finland), a fully integrated incubator (37°C, 21% O₂, 5% CO₂) including an image acquisition system. Phase contrast images (20x) were captured with an integrated CDD camera every two hours for a duration of 235 hours with pre-defined positions. Images were processed using the Cell-IQ Analyser™ Cell Activation (Yokogawa) software.

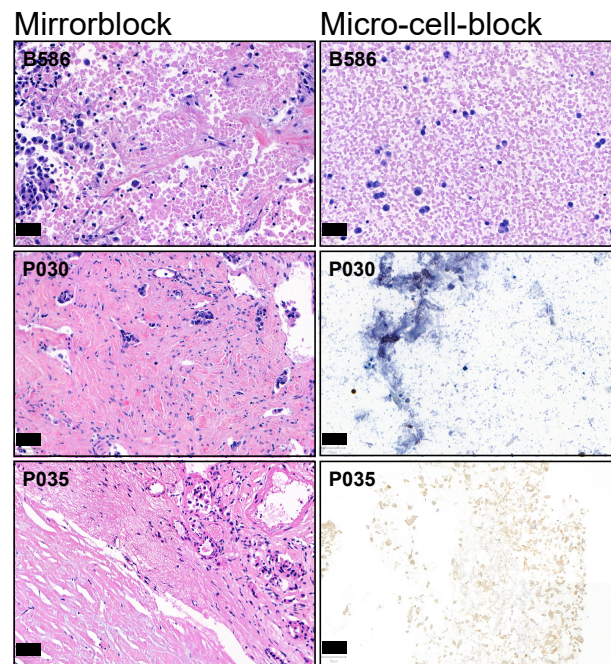
	Age	Grade [WHO]	Sex	Ki67 [%]	Size [cm]	T	N	M	TNM-staging [ENETS]	Site	Hormone secretion	Cohort
P005	65	G2	female	3	3	T3	N1	M0	3B	pancreas	Insulin	Method
B563m	65	G2	male	15	18.1	T4	NA	M1	4	liver	NF	Screen/Method
B586m	48	G2	female	5	2.5	NA	NA	M1	4	liver	NF	Method
B719	63	G2	female	5	5.5	T4	NA	M1	4	liver	NF	Method
B849	64	G1	female	1	2.4	T2	N0	M0	2A	pancreas	NF	Method
B931	46	G2	female	5	2.8	T1	N0	M0	1	pancreas	NF	Method
B992	81	G1	female	<2	2.3	T1	N0	M0	1	pancreas	NF	Method
P030	79	G2	male	7	4	T2	N1	M0	3A	pancreas	NF	Method
P032x	49	G3	male	25	3.2	T2	N1	M0	3A	pancreas	NF	Method
P033	67	G2	male	7	3	T2	N1	M0	3A	pancreas	NF	Method
P035	42	G2	male	4	2.2	T2	N0	M0	2A	pancreas	NF	Method
P040	55	G2	female	10	2.5	T2	N0	M0	2A	pancreas	NF	Screen
P044	19	G2	female	18	3,5	T3	N1	M0	3A	pancreas	NF	Screen
P049	66	G1	female	1	3.5	T2	N0	M0	2A	pancreas	NF	Screen
P050	58	G1	male	<1	2.5	T2	N1	M0	3A	pancreas	NF	Screen
P051	25	G1	female	<1	7.5	T3	N0	M0	2B	pancreas	NF	Screen/Method

Fig. S1

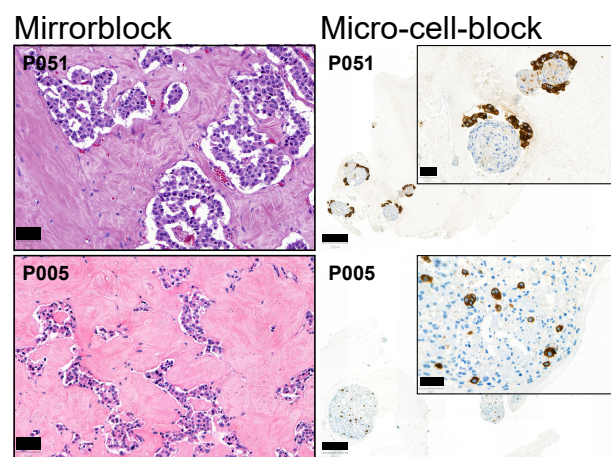
A

Iso_Success										
0.4	Age_gr									
0.1	0.8	Sex								
0.09	0.8	0.3	Grade_WHO							
0.4	1	0.4	0.5	TNM_AJCC						
0.6	0.8	0.2	0.9	2e-04	T_stage					
0.1	1	0.1	0.3	7e-04	0.6	N_stage				
1	0.8	1	1	0.3	0.6	0.6	M_stage			
0.007	0.05	0.6	0.3	0.2	0.07	0.1	1	Cell_Yield		
0.04	1	0.1	0.7	0.6	0.8	1	1	0.2	Tissue	

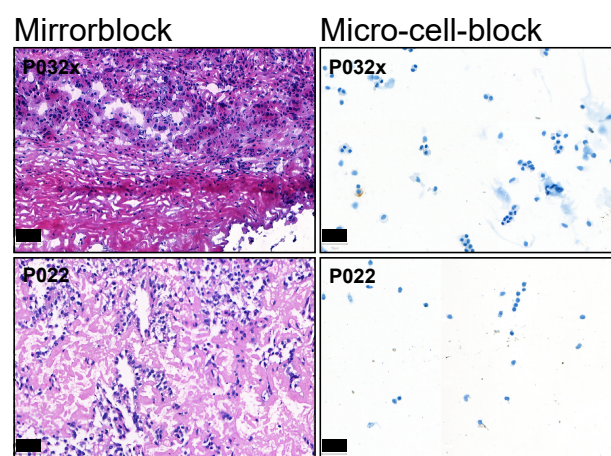
B

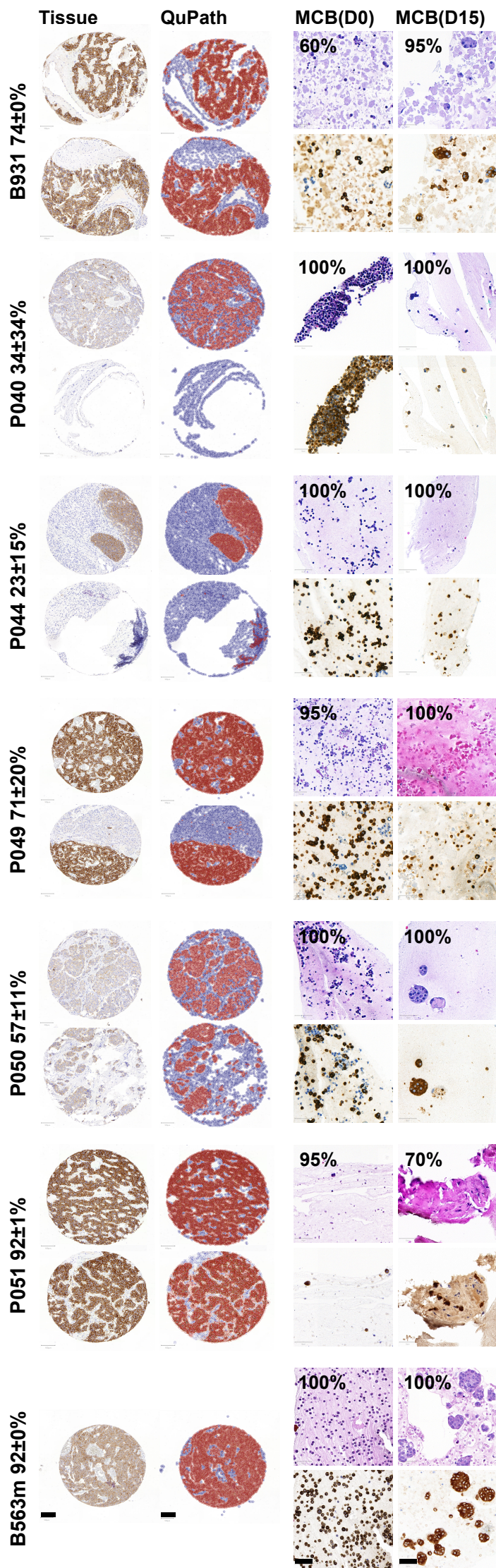
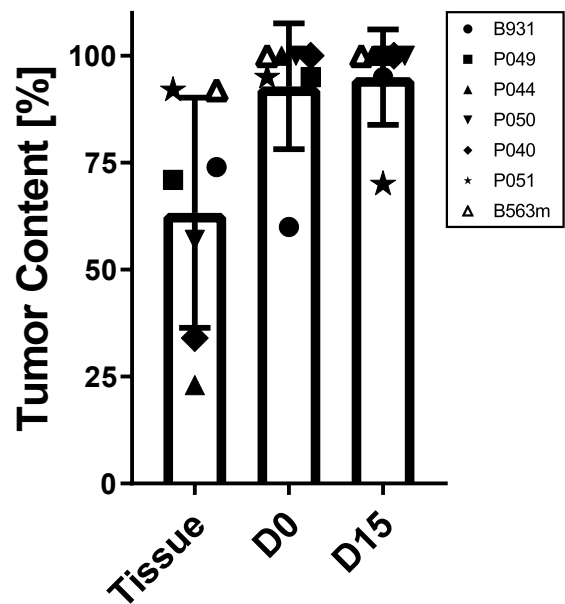


C

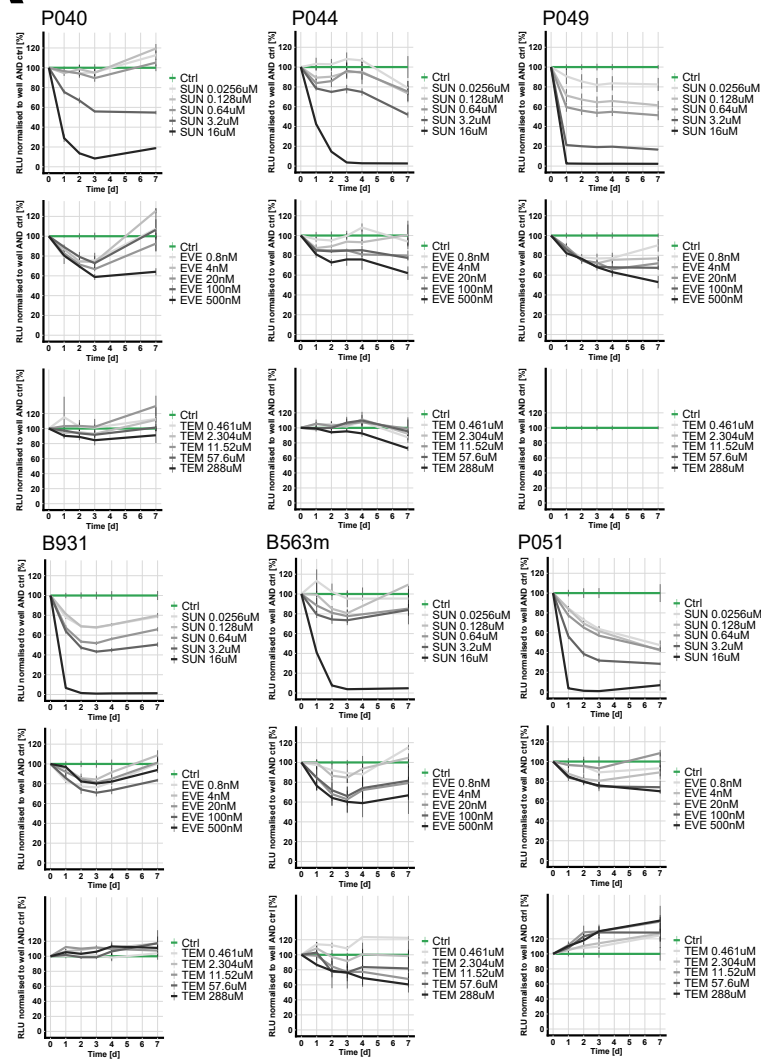


D

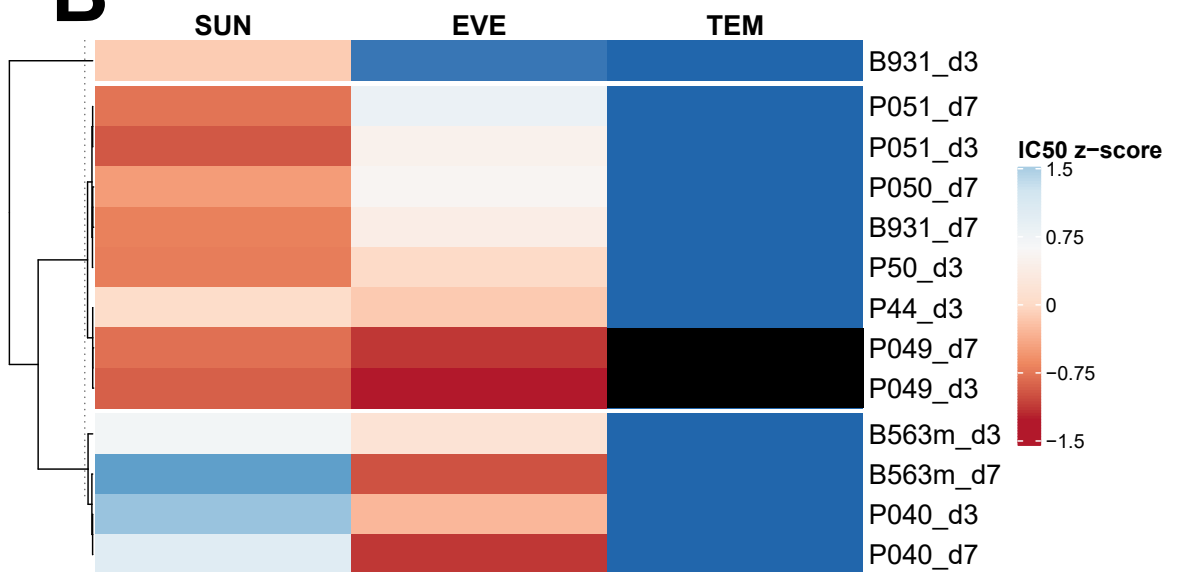


A**B**

A



B



3.1.4 Extended discussion

Tumoroids derived from patients are a valuable preclinical tool that can complement existing 2D cell lines and mouse models, particularly in the PanNEN field, where few representative options exist. As evidenced by our research, patient-derived tumoroids not only replicate the disease's biological hallmarks but may also mimic the drug sensitivity of individual patients *in vitro*.

The combination of a suspension technique with a low percentage of extracellular matrix demonstrated high culture success and facilitated relatively simple material handling for larger drug screens even in low abundant tissue specimens. This is in line with a subsequent report systematically benchmarking suspension techniques in colorectal, esophageal, and pancreatic cancer organoid lines from the Human Cancer Model Initiative³⁰³. This study showed improved efficiency and a wide range of applications including large-scale perturbation screens³⁰³. Similar approaches have successfully been utilized in other patient-derived cancer models^{287,298,304}. Cellular aggregation in suspension, rather than attachment to plastic surfaces, seems to be the preferred route for pancreatic endocrine cells allowing the formation of islet-like clusters *in vitro*²²⁸. Several earlier studies on human^{305,306} and canine³⁰⁷ pancreata reported that islet-cells intrinsically reconstitute their original architecture supporting biological functioning. Moreover, autocrine and paracrine signaling seems particularly important in neuroendocrine tumor cells³⁰⁸⁻³¹⁰. When compared to traditional monolayers, allowing cellular proximity in a three-dimensional architecture supported by a low extracellular matrix facilitates these functions. Overall, these findings support the use of our culture format in PanNETs, including slow-proliferative tumors.

Besides a suitable 3D culture technique to support cell maintenance, the composition of growth factor supplements is essential for longer-term culture success, as seen in the landmark study of colorectal cancer organoids²⁹⁵. The few reports of patient-derived PanNET cell cultures, limitations in organoid growth⁸⁶, and poor growth of G1/G2 NETs as patient-derived xenografts²²⁷ suggest that the quiescent status of G1- and G2 NETs is challenging for a stable propagation in current experimental models. It is unknown why some cancer cells undergo rapid cell death *in vitro*, but genetic instability or factors such as culture supplements may play a role^{278,311}. For the establishment of our PanNEN screening platforms, we prioritized a minimal medium containing growth factors that target highly expressed growth factor receptors identified in PanNETs and associated literature; EGF (Epidermal Growth Factor) and FGF (Fibroblast Growth Factor), which are required for the maintenance of NT3 cells, were

discovered to induce an epithelial-to-mesenchymal transition in these cell lines *in vitro*, resulting in spindle-shaped morphology and the loss of insulin expression ²²². These results demonstrate that neuroendocrine cells possess a high degree of *in vitro* plasticity in response to added growth factors. A growth stimulatory role of EGF and FGF2 was also reported in BON1 and QGP1 cells *in vitro* ³¹²⁻³¹⁴. IGF1 (Insulin Like Growth Factor 1) regulated *in vitro* proliferation and possessed a cytoprotective function in human PanNETs cells ²³¹. Similarly, enhanced and constitutive expression of IGF1 ligands and receptors led to autocrine and paracrine growth stimulation in GEP-NETs ^{308,309,315}. Elevated levels of PlGF (Placenta Growth Factor) found in the serum of PanNET patients positively correlated with higher tumor grades ³¹⁶. PlGF functioning as a pleiotropic cytokine supported neuroendocrine tumor growth *in vitro* and *in vivo* ³¹⁶. PlGF binds to FLT1 (VEGFR1) and to NRP1 (neuropilin-1), which both were highly expressed in our PanNET cohort, and can activate AKT ER-mediated canonical signaling pathway leading to enhanced tumor cell survival, proliferation, migration, and invasiveness ³¹⁶⁻³¹⁸.

The minimal medium established in this project is distinctive from the original human organoid medium ²⁹⁵, which was used for many other cancer model cultures. Interestingly, a recent study found that using the original human organoid medium did not allow for the culture of PanNEN samples ²³³, indicating that neuroendocrine tumor cells may require different growth factor supplements for *in vitro* maintenance. In the same line, most GEP-NEN tumor organoid lines, including three PanNEN organoid lines (PanNET G3 n=1; and PanNEC n=2), grew independent of WNT and RSPO (R-Spondin) ⁸⁶, which in contrast have proven to be an essential component for the culture of colorectal cancer organoids and organoid from other cancers. RSPO can interact with the Frizzled/LRP6 (LDL Receptor Related Protein 6) receptor complex in a manner that stimulates the WNT/ β -catenin signaling pathway ³¹⁹. In our transcriptomic data of human PanNETs, LRP5/6 (the receptors for WNT-3A) and Frizzled/LRP6 (receptor for RSPO) also exhibited considerably lower expression levels than EGFR (Epidermal Growth Factor Receptor), FGFR (Fibroblast Growth Factor Receptor), VEGFR1 and NRP1 receptors. Furthermore, A 83-01 (an inhibitor of transforming growth factor β kinase type 1 receptor) and Noggin (an antagonist of BMP (bone morphogenetic proteins)) as core components of the original organoid medium inhibit two growth factor receptors that we found highly expressed in PanNETs. In accordance with the high expression of TGFB-, BMP-, and PDGFR A and B observed in our data and previous research ³²⁰, adding these factors to the medium rather than pharmacologically inhibiting these signaling pathways may support the maintenance of PanNETs *in vitro*. Moreover, the addition of antioxidants N-

acetylcysteine amide and/or ROCK1 (Rho-Associated Protein Kinase 1) inhibitor Y-27632, which inhibits anoikis of embryonic stem cells³²¹, significantly helped in culturing colorectal organoids^{241,295} and might suppress apoptosis *in vitro*. Nicotinamide, also commonly used in the original organoid medium, maintained or enhanced the functions of pseudoislets obtained from pig neonatal or human fetal islets³²²⁻³²⁴ and therefore might be worth as a component of the culture medium²²⁸. HGF (Hepatocyte growth factor)/MET (Hepatocyte Growth Factor Receptor) axis which was essential in growth for low-grade PanNETs²²⁶ or TGFA (via EGFR)³¹²⁻³¹⁴ might also contribute to long-term maintenance. Other approaches, such as feeder layers or conditioned medium from tumor stromal cells mimicking niche factors secreted directly by the tumor microenvironment, may help to supplement niche factors for maintenance or propagation of PanNEN cultures^{314,320,325}.

Media dedicated screens will require more systematic approaches and setups, such as the Broad Institute's hybrid media screen, which allows for empirically sampling *ex vivo* media space and systematically testing growth factor parameters³²⁶. Careful validation and analysis of the cultures will be critical since specific enrichment and selection of cell clones may occur through media selection and impact functional readouts. In colorectal cancer organoids, specific genotypes of individual samples dictate the difference in *ex vivo* growth factor requirements^{241,295}, whereas in GEP-NEN genetic and non-genetic mechanisms seem of equal importance⁸⁶. In our short-term culture strategy, we retain 70% of the isolated cells prior to screening; thus, we believe the selection bias is minimal. However, only a systematic evaluation of clonality can provide a complete response to this question. Overall, the optimal growth conditions and culture medium for patient-derived PanNEN cells remain an unanswered but fundamental question to overcome technical obstacles for long-term culture and to carefully consider when conducting functional screens. Using the presented PanNET screening workflow, patient-derived tumor cells can be cultured, maintained, and screened for up to two weeks, allowing for more significant insights into the biology of NENs. In the next project, systematic functional drug screens will permit comparing the clinical response of patients with *in vitro* sensitivity in order to assess the model's translational relevance.

3.2 Project 2: Tumoroids of advanced high-grade neuroendocrine neoplasms mimic patient chemotherapy responses and guide the design of personalized combination therapies

3.2.1 Specific introduction

Neuroendocrine neoplasm displays heterogeneous clinical behavior that can vary from indolent to highly malignant. It is still not possible to predict therapy response based on specific molecular features of NENs. Ki-67 indices, tumor stage, and metastasis volume as most important prognostic markers that support therapy decisions, but therapy selection remains mostly based on empirical recommendations^{19,299}. To improve the treatment of patients with advanced or metastatic disease, additional strategies and tools are needed to allocate the correct treatment to the right patient, prevent unnecessary treatment by identifying non-responders or to select a potentially effective therapy for an individual patient. The absence of well-characterized *in vitro* and animal disease models representative of the human disease impedes the discovery of predictive therapeutic biomarkers and the exploration of novel therapeutic approaches. Patient-derived three-dimensional culture models more accurately mimic the disease and the actual patient situation, allowing us to retrieve and shift the focus towards more personalized information. These models demonstrated translational and predictive relevance for several cancers, including pancreatic ductal and colorectal cancer^{285,288,298}. Very recently, NEN organoid lines and organotypic slice cultures were established and recapitulated important neuroendocrine features of the disease^{86,232-234}. However, such patient-derived models remain scarce, and the translational relevance of using patient-derived culture systems has not been investigated for NEN.

3.2.2 Specific hypothesis and aims

Hypothesis: Combining *in vitro* drug screening with molecular tumor profiling will help to find biomarkers for existing standard-of-care pharmacotherapies and will allow testing of chemotherapeutics for GEP-NENs in a more relevant preclinical setting.

Aim 1) To apply 3D drug screening workflow to advanced high-grade GEP-NEN patient-derived tumoroids

Aim 2) To correlate *in vitro* sensitivity with patient clinical data

Aim 3) To assess molecular stress response to first-line therapies *in vitro* and to use them as a basis to find novel treatment co-vulnerabilities

3.2.3 Manuscript 2: “Tumoroids of advanced high-grade neuroendocrine neoplasms mimic patient chemotherapy responses and guide the design of personalized combination therapies”

Simon L. April-Monn, Katharina Detjen, Philipp Kirchner, Mafalda A. Trippel, Tobias Grob, Renaud S. Maire, Attila Kollàr, Katharina Kunze, David Horst, Martin C. Sadowski, Jörg Schrader, Ilaria Marinoni, Bertram Wiedenmann and Aurel Perren

Nature Communications, under review

A revised and expanded version of this manuscript is deposited on BioRxiv at

<https://www.biorxiv.org/content/10.1101/2022.12.10.519855v2.full.pdf+html>

Author contribution (CRediT):

I was involved in **conceptualization** (ideas, formulation, and evolution of overarching research goals and aims), **methodology** (development and design of methodology, creation of models), **software** (programming and implementation of code and testing of existing computer code), **validation** (verification of the overall replication/reproducibility of experiments and results and other research outputs), **formal analysis** (application of statistical, mathematical, computational and other formal techniques to analyze and synthesize study data), **investigation** (conduction research and investigation processes, performing experiments and data collection), **data curation** (managing activities to annotate and maintain research data for initial and later use), **writing and preparation** of the original draft and **reviewing and editing** the final manuscript, **visualization**, and **project administration** (management and coordination of responsibility for the research activity planning and execution)

1 **Title:** *“Tumoroids of advanced high-grade neuroendocrine neoplasms mimic*
2 *patient chemotherapy responses and guide the design of personalized*
3 *combination therapies”*

4

5 **Authors and affiliations:**

6 Simon L. April-Monn (1,2), Katharina Detjen (3), Philipp Kirchner (1), Mafalda A. Trippel (1), Tobias Grob (1),
7 Renaud S. Maire (1), Attila Kollàr (4), Katharina Kunze (5), David Horst (5), Martin C. Sadowski (1), Jörg Schrader
8 (6), Ilaria Marinoni (1), Bertram Wiedenmann (3)* and Aurel Perren (1,7)*

9

10 1 Institute of Pathology, University of Bern, 3008 Bern, Switzerland

11 2 Graduate School for Cellular and Biomedical Sciences, University of Bern, 3008 Bern, Switzerland

12 3 Charité - Universitätsmedizin Berlin, corporate member of Freie Universität Berlin and Humboldt-Universität zu Berlin,
13 Hepatology and Gastroenterology, Berlin, Germany

14 4 Department of Medical Oncology, Inselspital, Bern University Hospital, University of Bern, Freiburgstrasse, CH-3010 Bern,
15 Switzerland

16 5 Institute of Pathology, Charité Universitaetsmedizin Berlin, Rudolf-Virchow-Haus, Berlin, Germany

17 6 Department of Medicine, University Medical Center Hamburg-Eppendorf, 20251 Hamburg, Germany

18 7 Bern Center for Precision Medicine, University & University Hospital of Bern, 3008 Bern, Switzerland

19 **Running title (60):** *"PD tumoroids predict therapy response of GEP-NEN patients"*

20

21 **Keywords (5):** Gastroenteropancreatic neuroendocrine neoplasm; NEC; Precision medicine; Drug
22 screening; Organoid

23

24 **Additional information**

25 **Financial support,** including the source and number of grants, for each author

26 The study was supported by the Swiss Cancer Research Foundation to A.P. (KFS-4227-08-2017) and

27 Wilhelm Sander to I.M. and a generous donation by Dr. M. Gunzenhauser and B. Piepgras to B. W.

28 **Corresponding author:** Aurel Perren, aurel.perren@unibe.ch, phone: +41 31 632 32 22

29 **Conflict of interest disclosure statement:** The authors declare no potential conflicts of interest.

30 **Word count: Main (3734 words)** methods (2126 words)

31 **Total number of figures and tables:** Five main figures and one main table

32 **Statement of translational relevance (120–150 words):**

33 Precision medicine approaches are needed to improve clinical success in managing patients with
34 high-grade gastroenteropancreatic neuroendocrine neoplasms. Disease rarity and lack of suitable
35 models limit refinement of current and development of novel (co-)treatments based on mechanistic
36 insights. We sought to use patient-derived (PD) tumoroids as a model for the tumor *in situ* and to
37 gain personalized subsidiary therapy information for GEP-NEN patients. In a representative cohort of
38 these rare patients, we demonstrate utility within clinically relevant timespans allowing a direct
39 comparison of clinical follow-up with *ex vivo* drug sensitivities in PD tumoroids. Biological key
40 features and drug sensitivities were highly preserved in PD tumoroids, affirming their relevance in
41 response prediction and providing strong arguments for prospective validation. Our functional
42 findings from molecular stress responses in PD tumoroids and their synergistic vulnerabilities inform
43 the rational design of personalized combination therapy and may open new routes in clinical
44 situations where standard therapies are exhausted.

45 **ABSTRACT (250 words)**

46 **Purpose:** Advanced high-grade gastroenteropancreatic neuroendocrine neoplasm (GEP-NEN) are
47 highly aggressive and heterogeneous epithelial malignancies with poor clinical outcomes. No
48 therapeutic predictive biomarkers exist, and representative preclinical models to study their biology
49 are missing. Patient-derived (PD) tumoroids enable fast *ex vivo* pharmacotyping and provide
50 subsidiary biological information for more personalized therapy strategies in individual patients.

51 **Experimental Design:** PD tumoroids were established from biobanked surgical resections of
52 advanced high-grade GEP-NEN patients. Using targeted *in vitro* pharmacotyping and next-generation
53 sequencing of patient samples and matching PD tumoroids, we profiled individual patients and
54 compared treatment-induced molecular stress response and *in vitro* drug sensitivity to the observed
55 clinical response to chemotherapy.

56 **Results:** We demonstrate high success rates in culturing PD tumoroids of high-grade GEP-NENs
57 within clinically meaningful timespans. PD tumoroids recapitulate biological key features of high-
58 grade GEP-NEN and mimic clinical response to cisplatin and temozolomide *in vitro*. Moreover,
59 investigating treatment-induced molecular stress responses in PD tumoroids *in silico*, we discovered
60 and functionally validated Lysine demethylase 5A (KDM5A) and interferon-beta (IFNB1) as two
61 vulnerabilities that act synergistically in combination with cisplatin and may present novel
62 therapeutic options in high-grade GEP-NENs.

63 **Conclusion:** Patient-derived tumoroids from high-grade GEP-NENs represent a relevant model for
64 screening drug sensitivities of individual patients within clinically relevant timespans and provide
65 novel functional insights into drug-induced stress responses. Clinical patient response to standard-of-
66 care chemotherapeutics matches with drug sensitivities of PD tumoroids. Together, our findings
67 provide a functional precision oncology approach that may expand personalized therapeutic options
68 in a cancer with a high clinical need for more patient-centered therapies.

69 INTRODUCTION

70 High-grade gastroenteropancreatic neuroendocrine neoplasm (GEP-NEN) – comprising poorly
71 differentiated neuroendocrine carcinomas (GEP-NEC) and well-differentiated neuroendocrine tumors
72 (GEP-NET) – are highly aggressive and heterogeneous epithelial malignancies. With current therapies,
73 the median overall survival for metastatic GEP-NECs is less than one year(1–4). High-grade GEP-NET
74 patients can have slightly better outcomes but with high and unpredictable variations in survival (3).
75 Platinum-based chemotherapy is frequently used in GEP-NECs treatment. Therapeutic strategies are
76 adopted from small-cell lung cancers (SCLC) due to their apparent clinical- and histomorphological
77 similarities (5–7). Temozolomide-based chemotherapy is currently in clinical use for high-grade GEP-
78 NET (8) as response rates of platinum-based therapies seem lower (9). No predictive therapeutic
79 biomarkers for high-grade GEP-NENs are in clinical use, and precise therapeutic regimens are based
80 on small case series (5,6). This modus operandi has increasingly been scrutinized because uniform
81 therapy does not account for the heterogeneity found among patients (1,10,11). Due to the rarity
82 and heterogeneity of the disease, more extensive multi-arm clinical trials in GEP-NEN are challenging
83 to perform. Furthermore, current preclinical models are unable to improve the drug evaluation
84 process as patient-derived (PD) xenografts of GEP-NENs show very low success rates, and the few
85 available NEN cell lines fail to accurately recapitulate the biology of high-grade GEP-NENs (12,13).
86 Thus, the lack of suitable models limits the therapeutic development of novel treatments and co-
87 treatments based on mechanistic insights, which remains a pressing unmet need in the field.
88 We recently described a patient-derived 3-D tumoroid model that facilitates multi-center collections,
89 efficient processing, characterization, and screening of low abundant tumor tissues from human low-
90 grade NET with high success rates (14). Moreover, an organoid biobank of neuroendocrine
91 neoplasms including NECs has been described by Sato and colleagues (15). However, the potential
92 translational relevance of high-grade patient-derived 3-D GEP-NEN models has not been
93 investigated.

94 Here, using targeted *in vitro* pharmacotyping and next-generation sequencing in tumor tissues and
95 matching patient-derived (PD) tumoroids from a unique patient cohort of advanced high-grade GEP-
96 NENs, we profiled individual patients and aligned *in vitro* and molecular drug responses to the clinical
97 response. We demonstrate high success rates in culturing PD tumoroids of high-grade GEP-NENs
98 within clinically meaningful time frames. We show that PD tumoroids recapitulate biological key
99 features of high-grade GEP-NEN and mimic clinical response to cisplatin and temozolomide *in vitro*.
100 Moreover, investigating molecular stress responses in PD tumoroids *in silico*, we discovered and
101 functionally validated Lysine demethylase 5A (KDM5A) and interferon-beta (IFNB1) as two
102 vulnerabilities that act synergistic in combination with cisplatin and may present novel therapeutic

103 options in high-grade GEP-NENs. Together, our findings support the translational relevance of PD
104 GEP-NEN tumoroids in providing patient-centered subsidiary treatment information.

105 **MATERIALS & METHODS**

106 **Patient studies/cohort**

107 A cohort of eight high-grade GEP-NEN was assembled from two ENETS Centers of Excellence,
108 including six patient samples from the University Hospital Charité Berlin (Germany) and two patient
109 samples from the Institute of Pathology Bern (Switzerland). Inclusion criteria were histopathologic
110 diagnosis of G3 gastroenteropancreatic neuroendocrine neoplasm, availability of both tumor tissue-
111 and matching cryomaterial, and sufficient tumor purity (>70%). All cases were reviewed by a board-
112 certified pathologist (A.P.) and reclassified according to WHO 2019 criteria (ISBN 978-92-832-4499-8)
113 with additional immunostainings (Table 1 and Supplementary Table S1). TNM staging was based on
114 the 8th edition UICC/AJCC (ISBN: 978-1-119-26356-2). Treatment and outcome information were
115 obtained from interdisciplinary NEN tumor board records of both centers. The final case review was
116 based on all information of immunohistochemistry, clinical records, and mutational status from
117 targeted sequencing. The cohort included 3 female and 5 male patients with ages varying from 39 to
118 70 years (mean = 58.0; SD = 11.8). Comprehensive cohort features, patient demographics, and
119 patient characteristics are reported in Table 1 and Supplementary Tables 1 and 2. The study was
120 approved by the Cantonal Authorities (Kantonale Ethikkommission Bern, Ref.-Nr. KEK-BE 105/2015)
121 according to Swiss Federal Human Research Act and the ethics committee at Charité
122 Universitätsmedizin Berlin (Ref.-Nr. EA1/229/17).

123 All patients alive at the time of study initiation agreed on the use of residual material and had signed
124 an institutional informed consent. For archival samples from deceased patients, data were
125 anonymized prior to analyses, which restricted follow-up to existing clinical annotations

126

127 **Cancer mutation panel**

128 The TruSight Oncology 500 Kit (TSO500, Illumina) was used for DNA library preparation and
129 enrichment following the manufacturer's protocol. 80 ng of DNA were sheared on a Covaris E220
130 ultrasonicator. DNA fragments were end-repaired, and adapters containing unique molecular
131 identifiers (UMIs) were ligated to each fragment end. Fragments enriched by capture hybridization
132 were analyzed by high-throughput sequencing on a NovaSeq 6000 instrument (Illumina). TSO500
133 alignment and variant calling was performed using the TSO500 bioinformatics pipeline v2.1.0. UMI-
134 filtered total read counts were 103 M ±19 M, median exon coverage was 1131 ± 253, median DNA
135 insert size 136 ± 14, and % aligned reads 98.9 ± 1.0. Sources of population frequencies that were
136 used for auto-classification of benign variation include gnomAD (RRID:SCR_014964) and ExAC
137 (RRID:SCR_004068). Annotations of oncogenic effects of identified variants were retrieved from the

138 OncoKB precision oncology knowledge database (RRID:SCR_014782). OncoPrint function from
139 ComplexHeatmap v2.6.2 (PMID 27207943) (RRID:SCR_017270) was used for visualization.

140

141 **Primary and cell line culture:** For the study, we focused on naïve passage PD tumoroids to
142 minimize clonal drifts (16). All therapeutic studies were completed over a time course of twelve days.
143 All screening plates contained vehicle control wells (DMSO-treated, n = 10) and blank wells (medium-
144 only, n = 6). For each plate, the raw fluorescent intensity values were normalized to a relative scale
145 using the blank (B) value. Fluorescence is measured relative to the baseline of each well (BC)
146 (Relative scale = (Fluorescence of treated cells – B)/(BC – B)).

147 **Primary cell isolation and culture:** Cryopreserved tumor tissues were used for *in vitro* drug
148 screening. For primary cell isolation, micro-cell block manufacture, and quantification, we followed
149 the previously described workflow (14).

150 **NEN cell line culture:** The QGP1 cell line (RRID:CVCL_3143) was purchased from the Japanese Health
151 Sciences Foundation in 2011. QGP1 cells were kept in RPMI 1640 medium (10% FBS, 100 IU/mL
152 penicillin, 0.1 mg/mL streptomycin). The BON1 cell line (RRID:CVCL_3985) was provided by E.J.M.
153 Speel in 2011. BON1 cells were cultured in DMEM-F12 (10% FBS, 100 IU/mL penicillin, 0.1 mg/mL
154 streptomycin). The NT3 cell line was a kind gift from J. Schrader. NT3 cells were kept in RPMI 1640 +
155 growth factor medium (10% FBS, 100 IU/mL penicillin, 0.1 mg/mL streptomycin, 20 ng/mL EGF, 10
156 ng/mL bFGF) and cultured in collagen IV coated culture flasks. All cells were kept in a humidified
157 incubator at 5% CO₂ and 37 °C and cultured for no longer than two months. For all cell lines, short
158 tandem repeat (STR) analysis by PCR was performed (QGP1 in 2011/2016/2020; BON1 in
159 2014/2016/2020; NT3 in 2018/2020). QGP1 cells were authenticated by their specific cancer cell
160 profile. A BON1 and NT3 specific cancer cell profile does not exist yet, but contamination with other
161 common cell lines can be excluded due to non-match to any known cancer cell line profile.
162 Expression of the specific neuroendocrine markers chromogranin A and synaptophysin was routinely
163 tested by IHC.

164 **Compounds:** Temozolomide (#S1237, Selleckchem), cisplatin (#4333164, Teva Pharma), CPI-455
165 (#S6389, Selleckchem), IFNB1b (#I7662-14S, Biomol) were obtained from commercial vendors and
166 stored as stock aliquots as indicated by the manufacturers. Drug concentrations for
167 chemotherapeutics (cisplatin; temozolomide) were selected based on physiologically relevant
168 concentrations at the respective drug's C_{max}, defined as the maximum tolerated serum
169 concentration of the respective drug from published human studies (17).

170 Concentrations for combinational exploratory compounds (CPI-455, IFNB1b) were based on primary
171 literature and in-house *in vitro* testing a 625-fold concentration range and optimized to induce a
172 range of responses across classical NEN cell lines (BON1, QGP1). Compounds were screened at

173 equidistant 5-point, 625-fold concentration ranges using four technical replicates for the long-term
174 (168 hours) chemotherapeutics screens or in equidistant 3-point, 625-fold concentration ranges with
175 three technical replicates for short-term (24 hours) combinational screens (18).

176 ***In vitro* drug screening:** Typically, 3000 - 5000 cells were plated per well. Cell numbers were
177 quantified using RealTime-Glo™ MT Cell Viability (RTG) Assay (Promega, #G9712). Assay plates were
178 incubated at 37 °C in a humidified atmosphere at 5% CO₂ for 72 hours to allow sphere formation.

179 **Evaluating drug sensitivity to mono chemotherapeutics:** After a baseline measurement (day 0),
180 spheroids were tested with titrations of cisplatin, temozolomide, or DMSO (0.16%) as vehicle control.
181 Assay plates were incubated, and luminescence measurement of RTG was recorded at 96 hours and
182 168 hours using an Infinite 200 PRO plate reader (Tecan). The *in vitro* experiments and sensitivities to
183 treatments were scored by a blinded experimenter. **GR metrics:** Raw luminescence values were
184 normalized to each individual baseline control value at day 0 for the same well. *In vitro* responses
185 were converted into parametrized drug sensitivity metrics scoring the readouts on a per-division
186 basis using GR metrics v1.16.0 workflow described elsewhere (19).

187 **Evaluating drug sensitivity to combinational therapy:** After a baseline measurement (day 0),
188 spheroids were dosed with titrations of cisplatin, IFN β 1b, or CPI-455 alone or all possible
189 combinations using a full factorial drug design. Assay plates were incubated, and luminescence
190 measurements were recorded at 24 hours using an Infinite 200 PRO plate reader. **Classifying drug
191 interaction and drug potency in combinational therapy:** The analysis was based on the combination
192 index theorem, a mechanism-independent model for the assessment of drug interaction and drug
193 potency (18,20). Raw luminescence values in the presence of the drug were normalized to the
194 baseline control values and the DMSO-treated controls at 24 hours. Technical replicates were
195 averaged to yield a mean relative cell count per condition. From this, the observed inhibition (%) and
196 fractional inhibition effects (fa) were calculated for visualization and downstream analysis. Drug
197 interaction- and drug potency metrics were extracted based on the CompuSyn v1.0 workflow (21).
198 The degree of drug interaction was summarized by drug combination indices (CI), describing the
199 deviation of the observed drug combination activity from isoactive monotherapies in an isobologram
200 (18). Drug potency parameters (Dose Reduction Index (DRI); Effect at Dose X (DE)) were derived from
201 the median-effect equation (18).

202

203 **Nucleic acid extraction:** Genomic DNA was extracted from fresh frozen tumor tissue using
204 DNA Purification Micro Kit (Norgen Biotek, #50300). Total RNA was extracted from fresh frozen
205 tumor tissue or cultured cells using Single Cell RNA Purification Kit (Norgen Biotek, #51800). Nucleic
206 acid quantification was performed using Qubit DNA/RNA HS detection kit (Thermo Fisher Scientific, #

207 Q32852). Quality control metrics were analyzed using a Femto Pulse system with an Ultra Sensitivity
208 RNA kit (Agilent, #FP-1201-0275).

209

210 **Immunohistochemistry:** For immunohistochemistry, the paraffin-embedded material was cut
211 into 2.5- μ m-thick serial sections followed by deparaffinization, rehydration, and antigen retrieval
212 using an automated immunostainer (Bond RX, Leica Biosystems). Antigen retrieval was performed in
213 Tris-EDTA buffer for 30 min at 95°C for Ki-67 (1:200, Dako, M7240), ATRX (1:400, Sigma-Aldrich,
214 HPA001906), MCT4 (1:50, Santa Cruz, sc376140 D1), SOX9 (1:100, Cell Signalling, 82630T D8G8H),
215 ARX (1:1500, R&D Systems, AF7068), PDX1 (1:100, R&D Systems, MAB2419); in Tris-EDTA buffer for
216 30min at 100°C for synaptophysin (1:100, Novocastra, 27G12), CgA (1:400, CellMarque, 238M-94
217 LK2H10), SSTR2A (1:50, BioTrend, SS-8000-RM UMB-1); in proteinase K solution for Trypsin 1
218 (1:20000, Chemicon, MAB1482); in citric buffer for 30min at 100° for DAXX (1:40, Sigma-Aldrich,
219 HPA008736), RB1 (1:200, BP Pharmingen, 554136 G3-245); in citric buffer for 20 min at 95°C for TP53
220 (1:800, Dako, M7001 DO-7), BCL-10 (1:1000, Santa Cruz, sc-5273 331.3). The duration of primary
221 antibody incubation was 30 min at the specified dilutions. Visualization was performed using
222 OptiView DAB IHC Detection Kit (Roche, #760700), using DAB (3,3'-Diaminobenzidine) as a
223 chromogen. Slides were counterstained with hematoxylin. Scans were acquired with an automated
224 slide scanner Panoramic 250 (3DHistech), at 20x magnification. Images were acquired using QuPath
225 software (PMID: 29203879).

226

227 **Bulk RNA sequencing**

228 **Library preparation and sequencing:** Sequencing libraries were prepared from RNA using the
229 SMARTer Stranded Total RNA-Seq Kit v3 for picogram input material (Takara, #634488). Libraries
230 were sequenced as paired-end 101 bp (tumoroid samples) or paired-end 81 bp (original tumor
231 tissues) reads on a NovaSeq 6000 (Illumina) platform at ~30M reads/sample. Reads were
232 demultiplexed and converted to FASTQ format using bcl2fastq v2.20.0.422 (RRID:SCR_015058).
233 Cutadapt v2.5 (PMID 28715235) (RRID:SCR_011841) was used to trim Illumina adapter sequences
234 and mask 3' homopolymers longer than 10 bp. Reads containing more than 20 masked bases or
235 being shorter than 65 bp (tumoroid samples) or 50 bp (original tumor tissue) were removed.
236 Trimmed reads were mapped against a custom list of ribosomal RNAs and repetitive RNA elements
237 with bwa v0.7.17 (PMID 19451168) (RRID:SCR_010910), discarding mapping reads. At each step,
238 FastQC v0.11.7 (RRID:SCR_014583) was used to track read quality. Processed reads were mapped to
239 the human genome (GRCh37, GENCODE annotation v37) with STAR v2.7.3a (PMID 23104886)
240 (RRID:SCR_004463). Mapped reads were deduplicated based on the 8bp UMI located in the R2 using

241 UMI-tools v0.5 (PMID 28100584) (RRID:SCR_017048) with the default directional method.
242 Deduplicated reads were assigned to GENCODE v37 genes in subread v2.0.1 (PMID 24227677)
243 (RRID:SCR_009803). One drug-treated sample from the tumoroid culture of patient C5501m had to
244 be excluded due to low input and library quality. **Differential gene expression:** For the comparison of
245 original tumor tissue and tumoroids, the expression data was normalized using smooth quantile
246 normalization (qsmooth v1.8.0) (PMID 29036413). Differentially expressed genes were determined
247 using limma voom (PMID 25605792) (RRID:SCR_010943) in combination with the
248 duplicateCorrelation function to model repeated measurements of the same patient. For drug-
249 treated tumoroids, differential expression was determined with DESeq2 v1.32.0 (PMID 25516281)
250 (RRID:SCR_000154). Previous gene expression studies have demonstrated that a focus on sublethal
251 drug concentrations avoided artificially exaggerated non-specific cellular stress or death processes of
252 high drug dosages (22,23). Hence sublethal concentrations of cisplatin (0.53uM) and temozolomide
253 (11.52uM) were analyzed to determine the drug-related mode of action. Treatment-independent
254 expression variability was modeled using surrogate variable analysis (SVA) from sva v3.40.0 (24)
255 (PMID 17907809) (RRID:SCR_002155). All available surrogate variables were added to the DESeq2
256 model. Log2 expression fold changes of highly variable genes were shrunk using the apegIrn v1.14.0
257 algorithm (PMID 30395178). Differentially expressed genes from cisplatin treatment were analyzed
258 in metascape (PMID 30944313). **Hierarchical clustering and consensus clustering:** Consensus
259 clustering of original tumor tissues and tumoroids was performed with ConsensusClusterPlus v1.54.0
260 (PMID 20427518) (RRID:SCR_016954) on the Pearson correlation of the 2000 most variable genes
261 (innerLinkage: Ward.D2, finalLinkage: Average). **Functional enrichment analysis:** UpSetR v1.4.0
262 (PMID: 28645171) was used to visualize intersections between gene sets. For the comparison of
263 original tumor tissue and tumoroids, differentially expressed genes (adjusted p-value < 0.05) were
264 selected, and enrichment of Gene Ontology terms was tested in topGo v2.44.0 (PMID: 16606683)
265 (RRID:SCR_014798) (Kolmogorov-Smirnov, adjusted p-value < 0.01). The GO graph was modeled by
266 the weight01 algorithm, excluding terms with less than five members. Gene set enrichment analysis
267 (GSEA) (RRID:SCR_003199) was performed in clusterProfiler v.3.18.1 (PMID: 22455463)
268 (RRID:SCR_016884) based on the log2 expression fold changes. **Perturbational profiling in cMap:** The
269 top and bottom 150 genes from drug versus control-treated tumoroids (adjusted p-value < 0.05,
270 sorted by the Wald statistic) were compared against the compendium of perturbational reference
271 signatures from Connectivity Map (L1000, Touchstone v1.0) (25) (RRID:SCR_015674). Connectivity
272 map scores (τ) for all available knock-down (kd), overexpression (oe), and compound perturbagens
273 were extracted. To estimate the robustness of matching signatures, the input lists of differentially
274 expressed genes were rarified or permuted.

275 **Data availability** Sequence data that support the findings of this study have been deposited in
276 Gene Expression Omnibus (GEO) with the primary accession code [GSE213504](#). The code supporting
277 the current study was adapted from published R packages and other software. All code is available
278 from the corresponding author on request.

279 RESULTS

280 In-depth characterization of the high-grade GEP-NEN patient cohort

281 To investigate the potential of patient-derived tumoroids to model advanced malignant GEP-NENs
282 and better understand the disease biology, we conducted a retrospective cohort study of human
283 high-grade GEP-NEN patients that underwent surgery at the University Hospital of Bern (CH) and
284 Charité University Hospital Berlin (DE). Cases with available matched fresh-frozen and cryopreserved
285 G3 NEN tumor tissues were retrieved from a systematical retrospective review of hospital biobank
286 records. From 1987 to 2022 a total of eight patients were identified from all cryopreserved GEP-NEN
287 patient samples (n=311) (Fig. 1A), reflecting the rarity of this type of tissue resource, as most patients
288 are diagnosed at an advanced metastatic stage and hence receive diagnostic biopsies rather than
289 surgery. The cohort comprises high-grade metastatic neuroendocrine tumors (NET G3, n=4),
290 neuroendocrine carcinomas (NEC, n=3) of gastric- (Ga), pancreatic- (Pan), or unknown primary (CUP)
291 site, and one acinar cell carcinoma which in original records was diagnosed as NEN but reclassified
292 during the case review (Table 1). Patient demographics, clinicopathological classification, and
293 comprehensive clinical course records can be found in Table 1 and Supplementary Tables S1 and S2.
294 Molecular analysis using next-generation targeted mutational profiling of cancer-related genes in
295 fresh frozen material from patient tumors revealed a low tumor mutation burden (TMB) (3.1 mt/Mb;
296 IQR 5.6 mt/Mb; median; IQR) except for two patients showing elevated TMB (aP90m 11.8 mt/Mb;
297 C8802p 16.4 mt/Mb) (Supplementary Table S1). Microsatellite instability (MSI) was low ($2.4\% \pm 1.9\%$;
298 mean \pm SD), and no copy number alterations were detected (Supplementary Table S1). Most
299 frequent single nucleotide variants (SNV) were missense mutations. Among all SNVs we found
300 prototypic genetic drivers of GEP-NET (MEN1, ATRX, TSC2, ROS1, SLX4) and GEP-NECs (TP53, APC,
301 SOX9, NF1, PIK3CG) in our samples (Fig. 1B, Supplementary Table S3), supporting histopathological
302 diagnosis in 6 of 8 cases. For two samples non-classical mutational combinations were detected,
303 discordant with histomorphological diagnosis (Table 1 and Supplementary Fig. 1A).

304

305 Phenotypic characteristics of high-grade GEP-NEN patient-derived tumoroids 306 resemble original tumor tissue

307 PD tumoroids were successfully generated from all cryopreserved tissue-matched specimens. We
308 first assessed whether PD tumoroids preserve relevant histomorphological features of original high-
309 grade GEP-NENs in culture. Alike in the original tumor tissue, high tumor content, tumor cell
310 morphology, and expression of diagnostic neuroendocrine biomarker synaptophysin was confirmed
311 by two board-certified pathologists (A.P., M.T.) based on cytology of micro-cell-blocks from cultured
312 cells (Fig. 2A, Supplementary Fig. S2A, Supplementary Table S4), underlining that these patient-

313 derived tumoroids preserve a neuroendocrine phenotype of GEP-NEN tumor cells. Moreover, focal
314 depositions of extracellular matrix (C9502m, C8802p, C5501m) and focal calcification (C9502m) were
315 also detected (Supplementary Fig. S2B) Supplementary Table S4). However, as intended by a
316 depletion step in the 3-D culture workflow, non-neoplastic cells, including fibroblasts and
317 macrophages, were less abundant in PD tumoroids compared to original tumor tissue
318 (Supplementary Fig. S2B, Supplementary Table S4).

319 Next, we assessed to what extent transcriptional expression patterns of original tumors were
320 retained in PD tumoroids using next-generation RNA sequencing. The consensus among gene
321 expression of original tumor tissues and tissue-matched PD tumoroids was high, as seen by an
322 unsupervised cluster analysis of the top 2000 most variable genes (Fig. 2B). Moreover, principal
323 component (PC) analysis of original tumor tissue and PD tumoroids further emphasized that patient-
324 specific expression patterns were systematically retained in culture (Supplementary Fig. S2C). In
325 contrast, gene expression in spheroids grown from two conventional NEN cell lines (QGP1 and NT3)
326 clearly diverged from patient samples (Supplementary Fig. S2D). Interestingly, PC1 (21% of total
327 variance) separated PD tumoroids from original tumor tissues (Supplementary Fig. S2C). To address
328 this further, we investigated differentially expressed genes in original tumor tissues and matched PD
329 tumoroids using unsupervised functional enrichment analysis. The largest fraction of significant
330 biological process gene ontology (GO) terms were linked to the tumor microenvironment, in
331 particular the immune cell compartment (9/10 Top10 GO BP) ($p_{ks} < 0.005$) (Fig. 2C; Supplementary
332 Fig. S2E; Supplementary Table S5). In particular, when selecting pathways most enriched in original
333 tumor tissue ($NES > 1.7$, $p\text{-adj} < 0.005$), adaptive- and innate immunity-, interleukin- and cytokine-
334 related GO terms were highly overrepresented (59/91 pathways), supporting that the depleted
335 immune cell compartment accounts for a large part of this difference (Fig. 2D, Supplementary Table
336 S5).

337 Altogether, both transcriptomic profiles and histomorphology underlined the biological complexity
338 found in PD tumoroids. Moreover, our findings demonstrated that GEP-NEN PD tumoroids retain
339 important traits of original GEP-NENs and harbor a degree of histological-, cellular-, and molecular
340 diversity that is closer to original tumors than conventional NEN cell lines.

341

342 **High-grade GEP-NEN patient-derived tumoroids mimic clinical response to** 343 **platin and temozolomide treatment *in vitro***

344 To test whether drug sensitivities in PD tumoroids would mimic clinical patient responses, we
345 performed *in vitro* drug pharmacotyping in all samples. Based on established first-line therapy
346 recommendations for GEP-NECs and high-grade GEP-NETs (5), we screened all PD tumoroids for their
347 *in vitro* sensitivity to cisplatin or temozolomide chemotherapy (Fig. 3A, Supplementary Table S6). *In*

348 *in vitro* responses from naïve-passage PD tumoroids were converted into parametrized drug
349 sensitivities using GR metrics to account for differences in proliferation rates among samples (19).
350 For both treatments, PD tumoroid drug sensitivities varied between patients (Supplementary Fig.
351 S3A+B), leading to a spectrum of drug sensitivity (Fig. 3B+C). Crucially, the *in vitro* sensitivity
352 observed in PD tumoroids was consistent with the patient clinical therapy response (Supplementary
353 Table S2). In the direct comparison to the nearest clinical responses (\pm 2 months) post- and/or pre-
354 operative to the patient cryo-specimen collection, the sensitivity in PD tumoroids perfectly mimicked
355 clinical patient responses for both temozolomide (n=2) as well as cisplatin (n=1) therapy (Fig 3B+C).
356 The functional readout derived from the screen also complemented the few pathological and clinical
357 features (Ki-67 index, differentiation, TP53/RB1/KRAS mutational status, MGMT promoter
358 methylation status) that in individual cases are currently recommended for consolidation before
359 therapy selection (5) (Supplementary Fig. S3B). Notably, both patients with an accentuated and long-
360 lasting response to their systemic therapy (P6*/C8802p and P1*/aP321m) also exhibited high *in vitro*
361 drug sensitivity (Fig. 3B+C, Supplementary Table S2). Moreover, in agreement with their clinical
362 records, PD tumoroids from these patients were exclusively sensitive to either cisplatin- or
363 temozolomide-based treatment (Fig. 3B+C).

364 Overall, these findings suggested that patient-specific drug sensitivities and inter-patient
365 susceptibilities are retained in PD GEP-NEN tumoroids and that their culture provides sensitive and
366 direct functional information on *in vitro* drug responses.

367

368 **Transcriptional perturbational profiling in high-grade GEP-NEN PD tumoroids** 369 **defines adaptive stress response to chemotherapy**

370 Next, we asked whether molecular perturbation profiles from PD tumoroids might give mechanistic
371 insights into the adaptive stress responses and reveal novel treatment vulnerabilities. To address
372 this, we generated transcriptional perturbation profiles from matched PD tumoroids following DMSO
373 control, cisplatin, or temozolomide treatment. PCA of these profiles revealed that patient-specific
374 expression differences were stronger than cisplatin- or temozolomide-induced expressional effects
375 (Supplementary Fig. S4A). Grouping the cohort by their cisplatin- or temozolomide *in vitro*
376 sensitivities did not provide a clear separation of more- or less-sensitive PD tumoroids regarding
377 global expression changes (Supplementary Fig. S4B). Furthermore, gene expression magnitude was
378 not correlated with the *in vitro* sensitivity (Supplementary Fig. S4C). To address this, we determined
379 treatment-*independent* sources of variation using surrogate variable analysis (SVA) (24). As expected,
380 these surrogate variables were also correlated with known biological variables highlighting the
381 contribution of patient age, gender, tumor type, Ki-67 index, and sequencing depth (Supplementary
382 Fig. S4D+E). Importantly, we found that the *in vitro* sensitivity was associated with the surrogate

383 variables (Supplementary Fig. S4D). Thus, testing differential gene expression factoring in all
384 surrogate variables yielded a clear cisplatin-induced perturbation signature (327 DEGs, FDR = 0.1, p-
385 adj < 0.05) (Fig. 4A) with strong enrichment in significant p-values in the p-value distribution
386 (Supplementary Fig. S4F). Since the differential expression results for temozolomide were smaller (28
387 DEGs, FDR = 0.1, p-adj < 0.05, Supplementary Fig. S4F) we focused our further analysis on cisplatin.
388 Pathway (REACTOME; KEGG; WIKI) and GO gene set enrichment analysis on cisplatin-induced
389 perturbation signatures revealed well-known underlying themes such as response to chemical stress
390 or DNA damage (Fig. 4B), DNA repair, and apoptosis (Supplementary Fig. S4G) (26). Interestingly,
391 histone H3K4 methylation was also prominently involved (Fig. 4B). To dissect this further, we
392 compared the cisplatin-induced perturbational signature to the Connectivity Map (cMap) (25), a
393 large perturbation signature database (Fig. 4c). When focusing on pathways annotated in cMap as
394 "DNA directed compounds", Amonafide – a DNA intercalating agent – was among the top-ranked
395 compounds with a very high connectivity score ($\tau = 96.05$). In contrast, temozolomide – a DNA
396 alkylating agent - showed a nearly neutral connectivity score ($\tau = -6.38$), corroborating the specificity
397 of the cisplatin-induced perturbation signature (Supplementary Fig. S4H, Supplementary Table S7).

398

399 **IFNB1 and KDM5A genetic perturbation induces inverse expression signatures** 400 **to cisplatin chemotherapy of high-grade GEP-NEN PD tumoroids**

401 Due to cancer escape mechanisms and the inevitable emergence of resistance to monotherapies,
402 formulating effective combinational chemotherapies has become fundamental to modern cancer
403 therapy (27–31). Using the cisplatin-induced perturbation signature, we sought to identify possible
404 combinational treatment options. To prioritize and evaluate complementary combinations, we
405 examined perturbation candidates resulting in gene expression signatures inversely related to
406 cisplatin-treated PD tumoroids. We found that overexpression of Interferon Beta 1 (*IFNB1*) and
407 knock-down of Lysine Demethylase 5A (*KDM5A*) in cMap's core cell panel (3147 treatments) were
408 among the top-ranked hits and showed highly inverse connectivity map scores (*IFNB1*, rank 15, $\tau = -$
409 99.54; *KDM5A*, rank 52, $\tau = -97.68$) (Fig 4C; Supplementary Table S7). This pattern was highly robust
410 and specific; upon systematic degradation of input query signatures (top 150/125/100/75 up- and
411 downregulated DEGs (p-adj < 0.05), *IFNB1* and *KDM5A* remained among the top-ranked hits with
412 highly inverse connectivity map scores ($\tau < -91.00$) whereas random permutation and selection of
413 genes led to a complete loss of these ranks and insignificant connectivity scores (757/3195, $\tau = -$
414 49.47; 289/3195, $\tau = -71.76$) (Supplementary Fig. S4I+J; Supplementary Table S7).

415 Altogether, these findings indicated that molecular stress responses in PD tumoroids are specific and
416 can be exploited for *in silico* prediction of treatment vulnerabilities.

417 ***In silico* predicted combinational therapies induce effective and synergistic**
418 **treatment responses in patient-derived GEP-NEN tumoroids.**

419 To evaluate the functional activity of *in silico* predicted candidates in combinational drug therapy, we
420 applied human recombinant IFN β 1 or KDM5A-inhibitor together with cisplatin in high-grade PD
421 tumoroids and NEN cell line spheroids. Synergistic drug interaction and combined drug potency were
422 analyzed based on the combination index theorem (18,20). The degree of drug interaction was
423 summarized as a drug combination index (CI) and the drug potency was based on the inhibitory effect
424 and the dose reduction achieved in the combination treatment (Fig. 5A).

425 High-grade GEP-NEN tumoroids were susceptible to mono- and combinational treatment with
426 recombinant IFN β 1 or KDM5A inhibitor (Supplementary Fig. S5A+B). The overall inhibitory effect of
427 cisplatin monotherapy at a physiologically relevant concentration (C_{max} 14.4 μ M; inhibition $0.29 \pm$
428 0.24 , mean \pm SD) was then used to select a reference level to compare drug interaction and drug
429 potency among tumoroids. In line with our *in silico* findings, exposure to CPT+IFN β 1 combination
430 indicated synergistic drug interaction in five of the screened tumoroids (5/9) ($CI=0.43 \pm 0.32$, mean \pm
431 SD) (Supplementary Fig. S5C). Similarly, exposure to CPT+KDM5A combination yielded synergistic
432 drug interaction in three tumoroids (3/6) ($CI= 0.43 \pm 0.23$, mean \pm SD) (Supplementary Fig. S5D). In
433 PD tumoroids where synergy was detected, the combinational dosages necessary to reach
434 equipotent inhibitory effects were considerably lower than in their respective monotherapies
435 (Supplementary Fig. S5E+F). This resulted in highly favorable dose-reduction indices (DRI $\gg 1$) for
436 each individual drug (Fig. 5B+C), emphasizing the higher potency of combination therapy.
437 Together, our data indicate that NEN PD tumoroid screening and perturbational profiling can be
438 successfully applied for the timely assessment of standard-of-care therapies as well as experimental
439 drugs. Moreover, our analysis of therapy-induced adaptive stress responses revealed two clinically
440 attractive co-vulnerabilities, which proved direct functional significance in patient-derived and cell
441 line GEP-NEN tumoroids.

442 **DISCUSSION**

443 Therapeutic target discovery, validation, and translational applications face severe obstacles in rare
444 cancers such as high-grade GEP-NEN. The selection of therapies for high-grade GEP-NENs is largely
445 based on clinical experience in the absence of large clinical trials (1,11) and predictive biomarkers (5).
446 Our data demonstrate that high-grade GEP-NEN PD tumoroids are well suited for rapid *in vitro*
447 pharmacotyping and provide biological and potentially therapeutic information for this lethal
448 malignancy.

449 A major hurdle in the study of uncommon cancers – as a direct consequence of their rarity – is the
450 lack of existing preclinical disease models (12,13). For the first time, we concomitantly provide a
451 patient-derived model system of high-grade GEP-NEN together with the extensive characterization of
452 matched tissues and comprehensive clinical follow-up. Cytology confirmed high tumor content in PD-
453 tumoroid cultures intermixed with few non-neoplastic cells, including fibroblasts and macrophages.
454 Functionality was shown by the retention of neuroendocrine protein expression (Fig. S2). Moreover,
455 inter-patient molecular transcriptional patterns were maintained in tissue-matched PD tumoroids,
456 further underlining that key biological features are recapitulated in this model (Fig. 2). Interestingly,
457 we observed a clear difference between transcriptomes of classical NEN cell line and the patient
458 material, underscoring the importance of patient-derived models.

459 Flanking the existing clinical practice with additional evidence obtained from patient-specific models
460 may represent an alternative to address the unmet need for rational-based and possibly personalized
461 treatment decisions. Our findings show that PD tumoroids of high-grade GEP-NEN patients mimic
462 patient response to established first-line chemotherapies (Fig. 3, Supplementary Fig. S3). We report
463 that GEP-NEN PD tumoroids show a wide range of treatment responses among different patients. We
464 also observed a striking match with patient clinical response, including treatment-refractory pairs of
465 patient tumors and PD tumoroids. While we are aware of the limited cohort size in the present study,
466 our results align with other studies of similar sizes in various cancer entities; clinical applicability
467 using patient-derived *in vitro* models has been successfully demonstrated, e.g., in colorectal cancer
468 (32,33), pancreatic cancer (34), and lung cancer (35).

469 We demonstrate efficient and highly successful processing of low abundant GEP-NEN tissues using
470 minimized cell requirements, including critical quality control steps, and ensuring a turnaround time
471 of only two weeks (Fig. 2+3, Supplementary Fig. S2+3). Compared to previously reported procedures
472 of 2 to 6 months in other precision medicine studies (35,36), short turnaround applies better to the
473 clinical course of these patients. Indeed, especially in high-grade NEN with very short survival times,
474 such a fast turnaround is important to ensure timely therapy decisions. Other groups like Sato *et al.*
475 reported limited success rates in generating NEN organoid lines and the lengthy organoid expansion

476 process over several months up to years (15). While this approach is needed for allowing mechanistic
477 studies, it is less suitable in a clinically urgent scenario of rapidly progressive malignant GEP-NENs.
478 Although our workflow is based on short-term culture and individual tumor specimens, the analysis
479 can be expanded by additional screens if sufficient material is available. Moreover, tissue
480 requirements for a targeted *in vitro* screen are applicable for tumor biopsies, which will facilitate
481 translational applications. As our results are based on a small number of patients, only larger
482 prospective studies will be able to evaluate the predictive relevance in more detail. Prospective
483 studies may also include clinically applied combination therapy of etoposide and temozolomide,
484 which were not yet included in the presented proof-of-concept study. Such studies also seem
485 meaningful for evaluating more suitable second-line therapies in these highly aggressive tumor types
486 when first-line therapies have failed.

487 Molecular drivers that determine the divergent clinical course of G3 NET and NEC are poorly
488 understood, and individual treatment decisions remain challenging. Because advanced tumors are
489 often resistant to monotherapies, increasing efforts are undertaken by combining antineoplastic
490 agents to achieve better efficacy at reduced therapeutic dosages (27–31,35,37,38). Patient-to-
491 patient heterogeneity (37), intra-tumoral heterogeneity (39), and intracellular pathway dysregulation
492 (40) open up new avenues for the usage of combinational therapy to induce potent responses that
493 cannot be achieved with monotherapy alone (41). Our study revealed a strategy for selecting co-
494 treatments to cisplatin chemotherapy based on gene expression profiles. We demonstrate that the
495 cisplatin-induced molecular stress response in high-grade GEP-NEN PD tumoroids is specific and
496 mirrors perturbational effects (Fig. 4, Supplementary Fig. S4). The underlying assumption was that
497 highly inverse signatures to cisplatin-monotherapy might be ideal candidates for combinational
498 treatments. Targeting these candidates in combination with cisplatin may severely corrupt the
499 cellular signaling state, thus being fatal to the cancer cells. Using these perturbational profiles
500 allowed us to pinpoint Lysine Demethylase 5A (KDM5A) and interferon beta 1 (IFN1B) as two novel
501 candidates for combinational therapy (Fig. 4, Supplementary Fig. S4).

502 KDM5A is a histone demethylase that often functions to repress target genes at transcriptional start
503 sites (42). Only recently the role of KDM5A in neuroendocrine differentiation and tumorigenesis has
504 been described (43,44). Kaelin *et al.* demonstrated that Kdm5a promotes SCLC tumorigenesis *in vivo*
505 and tumor proliferation proposing KDM5A inhibition as a therapeutic strategy. Genomic analysis of
506 GEP-NENs has shown copy number gains of *KDM5A* in 45%-52% of the tumors (10). Importantly,
507 discoveries from these studies align very well with our presented data highlighting a prominent role
508 of KDM5A in neuroendocrine neoplasms. Upon combinational treatment with cisplatin, we see
509 strong synergism and clinically attractive efficacies in three tested GEP-NENs (Fig. 5, Supplementary
510 Fig. S5).

511 Interestingly, a functional relationship between KDM5A and cisplatin susceptibility has been
512 described in lung adenocarcinoma, pointing towards altered chromatin regulation as a potential
513 molecular mechanism for drug tolerance (45). Of note, the sample which displayed no effect from
514 the KDM5A+cisplatin combination harbored a mutational disfunction upstream of the H3K4
515 methylation axis. Mutations in lysine methyltransferase 2A (KMT2A) and menin (MEN1), both
516 important regulators for H3K4 methylation, may have corrupted the combinational effect.

517 Type I interferons (IFN- α and IFN- β) are pro-inflammatory cytokines that can rapidly cause myriad
518 downstream effects in tumor cells and promote antitumor immunity in immune cells (46,47). Type I
519 interferons activate transcription factors of the signal transducer and activator of transcription (STAT)
520 family, initiating the synthesis of proteins from interferon-stimulated genes (47). As FDA-approved
521 mono- or combinational therapy, Type I interferons were confirmed to result in tumor regression
522 and/or prolonged survival in a diversity of other highly proliferative hematological and disseminated
523 solid malignancies(46). Interestingly, IFN- α was clinically used in advanced low-grade GEP-NETs (48–
524 50) but was superseded by other regimens (e.g., somatostatin analogs) (51). Recently, two separate
525 studies proposed the clinical attractiveness of using IFN- β in treating GEP-NETs due to effective
526 inhibition of cell proliferation and stimulation of apoptosis at low dosages in cell lines *in vitro* (52,53).

527 In a clinically more relevant scenario of patient-derived high-grade GEP-NET tumoroids, we now
528 demonstrate that IFNB1 is associated with the GEP-NEN perturbational signature. Subsequently,
529 exposure to Cisplatin+IFNB1 revealed strong synergism and high therapeutic efficacy in a subset of
530 high-grade GEP-NEN tumoroids (Fig. 5, Supplementary Fig.S5). Taken together, the proposed
531 combinational approach may represent a clinically attractive option for high-grade GEP-NETs, where
532 very few treatment recommendations and options exist so far (3,5).

533 To what extent the KDM5A- or IFNB1 combinations are NEC- or NET G3-specific will require a larger
534 cohort and additional mechanistic delineation. At the same time, it will be interesting to evaluate
535 exact treatment schedules and/or therapeutic priming *in vitro*. A recent extensive and
536 comprehensive high throughput combinational drug screen in breast, colon, and pancreatic cancer
537 indicated that chemotherapeutics combined with apoptotic inducers or cell cycle inhibitors are highly
538 promising combinations for translational applications (27). Both KDM5A and IFNB1 fall into this
539 category, and our study further underlines the functional potency of such a combination. Thus,
540 KDM5A and IFNB1 may present clinically attractive Achilles Heels for high-grade GEP-NEN in
541 combinational therapy with cisplatin.

542 In summary, our data demonstrate that GEP-NEN PD tumoroids may be well suited for timely and
543 meaningful *in vitro* pharmacotyping providing subsidiary therapy information. Based on this, we
544 believe that our study has put forward a crucial step justifying more personalized clinical protocols
545 using PD tumoroids in patients with aggressive high-grade GEP-NEN later-line therapies.

546 **ACKNOWLEDGMENTS**

547 We thank the Tissue Bank Bern (Bern, Switzerland) and the Translational Research Unit (Institute of
548 Pathology, Bern, Switzerland) for their technical, material, and administrative support and the
549 Cytopathology (Institute of Pathology, Bern, Switzerland) for technical support performing formalin-
550 fixation and paraffin embedding in tissue and cell culture material.

551 **AUTHOR CONTRIBUTIONS (CRediT)**

552 **Conceptualization:** S.L.A.M., B.W., A.P.; **Methodology:** S.L.A.M., P.K.; **Software:** S.L.A.M., P.K.; **Validation:**
553 S.L.A.M., K.D., P.K.; **Formal Analysis:** S.L.A.M., P.K.; **Investigation:** S.L.A.M., K.D., P.K., M.A.T., T.G.; **Resources:**
554 A.K., K.K., D.H., J.S., M.C.S., I.M., B.W., A.P.; **Data Curation:** S.L.A.M., K.D., P.K., R.M.A.; **Writing—Original Draft**
555 **Preparation:** S.L.A.M., K.D., B.W., A.P.; **Writing—Review and Editing:** S.L.A.M., K.D., P.K., I.M., B.W., A.P.;
556 **Visualization:** S.L.A.M.; **Supervision:** B.W., A.P.; **Project Administration:** S.L.A.M., B.W., A.P.; **Funding**
557 **Acquisition:** I.M., B.W., A.P.

558 All authors have read and agreed to the published version of the manuscript.

559 REFERENCES

- 560 1. Dasari A, Mehta K, Byers LA, Sorbye H, Yao JC. Comparative study of lung and extrapulmonary poorly differentiated neuroendocrine
561 carcinomas: A SEER database analysis of 162,983 cases. *Cancer*. 2018;124:807–15.
- 562 2. Dasari A, Shen C, Halperin D, Zhao B, Zhou S, Xu Y, et al. Trends in the Incidence, Prevalence, and Survival Outcomes in Patients
563 With Neuroendocrine Tumors in the United States. *JAMA Oncol*. 2017;3:1335–42.
- 564 3. Heetfeld M, Chougnet CN, Olsen IH, Rinke A, Borbath I, Crespo G, et al. Characteristics and treatment of patients with G3
565 gastroenteropancreatic neuroendocrine neoplasms. *Endocr Relat Cancer*. 2015;22:657–64.
- 566 4. Sorbye H, Welin S, Langer SW, Vestermark LW, Holt N, Osterlund P, et al. Predictive and prognostic factors for treatment and
567 survival in 305 patients with advanced gastrointestinal neuroendocrine carcinoma (WHO G3): the NORDIC NEC study. *Ann Oncol*
568 *Off J Eur Soc Med Oncol*. 2013;24:152–60.
- 569 5. Pavel M, Öberg K, Falconi M, Krenning EP, Sundin A, Perren A, et al. Gastroenteropancreatic neuroendocrine neoplasms: ESMO
570 Clinical Practice Guidelines for diagnosis, treatment and follow-up. *Ann Oncol*. 2020;31:844–60.
- 571 6. Garcia-Carbonero R, Sorbye H, Baudin E, Raymond E, Wiedenmann B, Niederle B, et al. ENETS Consensus Guidelines for High-Grade
572 Gastroenteropancreatic Neuroendocrine Tumors and Neuroendocrine Carcinomas. *Neuroendocrinology*. 2016;103:186–94.
- 573 7. Strosberg JR, Coppola D, Klimstra DS, Phan AT, Kulke MH, Wiseman GA, et al. The NANETS Consensus Guidelines for the Diagnosis
574 and Management of Poorly Differentiated (High-Grade) Extrapulmonary Neuroendocrine Carcinomas. *Pancreas*. 2010;39:799–800.
- 575 8. Al-Toubah T, Pelle E, Valone T, Haider M, Strosberg JR. Efficacy and Toxicity Analysis of Capecitabine and Temozolomide in
576 Neuroendocrine Neoplasms. *J Natl Compr Canc Netw*. 2021;20:29–36.
- 577 9. Elvebakken H, Perren A, Scoazec J-Y, Tang LH, Federspiel B, Klimstra DS, et al. A Consensus-Developed Morphological Re-Evaluation
578 of 196 High-Grade Gastroenteropancreatic Neuroendocrine Neoplasms and Its Clinical Correlations. *Neuroendocrinology*.
579 2021;111:883–94.
- 580 10. Venizelos A, Elvebakken H, Perren A, Nikolaienko O, Deng W, Lothe IMB, et al. The molecular characteristics of high-grade
581 gastroenteropancreatic neuroendocrine neoplasms. *Endocr Relat Cancer*. 2022;29:1–14.
- 582 11. Brennan SM, Gregory DL, Stillie A, Herschtal A, Mac Manus M, Ball DL. Should extrapulmonary small cell cancer be managed like
583 small cell lung cancer? *Cancer*. 2010;116:888–95.
- 584 12. Rinke A, Auernhammer CJ, Bodei L, Kidd M, Krug S, Lawlor R, et al. Treatment of advanced gastroenteropancreatic neuroendocrine
585 neoplasia, are we on the way to personalised medicine? *Gut*. 2021;70:1768–81.
- 586 13. Detjen K, Hammerich L, Özdirik B, Demir M, Wiedenmann B, Tacke F, et al. Models of Gastroenteropancreatic Neuroendocrine
587 Neoplasms: Current Status and Future Directions. *Neuroendocrinology*. 2021;111:217–36.
- 588 14. April-Monn SL, Wiedmer T, Skowronska M, Maire R, Schiavo Lena M, Trippel M, et al. Three-Dimensional Primary Cell Culture: A
589 Novel Preclinical Model for Pancreatic Neuroendocrine Tumors. *Neuroendocrinology*. 2021;111:273–87.
- 590 15. Kawasaki K, Toshimitsu K, Matano M, Fujita M, Fujii M, Togasaki K, et al. An Organoid Biobank of Neuroendocrine Neoplasms
591 Enables Genotype-Phenotype Mapping. *Cell*. 2020;183:1420–1435.e21.
- 592 16. Ben-David U, Ha G, Tseng Y-Y, Greenwald NF, Oh C, Shih J, et al. Patient-derived xenografts undergo mouse-specific tumor
593 evolution. *Nat Genet*. 2017;49:1567–75.
- 594 17. Liston DR, Davis M. Clinically Relevant Concentrations of Anticancer Drugs: A Guide for Nonclinical Studies. *Clin Cancer Res*.
595 2017;23:3489–98.
- 596 18. Chou T-C. Theoretical Basis, Experimental Design, and Computerized Simulation of Synergism and Antagonism in Drug Combination
597 Studies. *Pharmacol Rev*. 2006;58:621–81.
- 598 19. Hafner M, Niepel M, Chung M, Sorger PK. Growth rate inhibition metrics correct for confounders in measuring sensitivity to cancer
599 drugs. *Nat Methods*. 2016;13:521–7.
- 600 20. Chou T-C, Talalay P. Quantitative analysis of dose-effect relationships: the combined effects of multiple drugs or enzyme inhibitors.
601 *Adv Enzyme Regul*. 1984;22:27–55.
- 602 21. Chou T-C. Drug Combination Studies and Their Synergy Quantification Using the Chou-Talalay Method. *Cancer Res*. 2010;70:440–6.
- 603 22. Woo JH, Shimoni Y, Yang WS, Subramaniam P, Iyer A, Nicoletti P, et al. Elucidating Compound Mechanism of Action by Network
604 Perturbation Analysis. *Cell*. 2015;162:441–51.
- 605 23. Bansal M, Yang J, Karan C, Menden MP, Costello JC, Tang H, et al. A community computational challenge to predict the activity of
606 pairs of compounds. *Nat Biotechnol*. 2014;32:1213–22.
- 607 24. Leek JT, Storey JD. Capturing Heterogeneity in Gene Expression Studies by Surrogate Variable Analysis. *PLOS Genet*. 2007;3:e161.
- 608 25. Lamb J, Crawford ED, Peck D, Modell JW, Blat IC, Wrobel MJ, et al. The Connectivity Map: Using Gene-Expression Signatures to
609 Connect Small Molecules, Genes, and Disease. *Science*. 2006;313:1929–35.
- 610 26. Kelland L. The resurgence of platinum-based cancer chemotherapy. *Nat Rev Cancer*. 2007;7:573–84.
- 611 27. Jaaks P, Coker EA, Vis DJ, Edwards O, Carpenter EF, Leto SM, et al. Effective drug combinations in breast, colon and pancreatic
612 cancer cells. *Nature*. 2022;1–8.
- 613 28. Sicklick JK, Kato S, Okamura R, Schwaederle M, Hahn ME, Williams CB, et al. Molecular profiling of cancer patients enables
614 personalized combination therapy: the I-PREDICT study. *Nat Med*. 2019;25:744–50.
- 615 29. Al-Lazikani B, Banerji U, Workman P. Combinatorial drug therapy for cancer in the post-genomic era. *Nat Biotechnol*. 2012;30:679–
616 92.
- 617 30. Ramaswamy S. Rational Design of Cancer-Drug Combinations. *N Engl J Med*. 2007;357:299–300.
- 618 31. Fitzgerald JB, Schoeberl B, Nielsen UB, Sorger PK. Systems biology and combination therapy in the quest for clinical efficacy. *Nat*
619 *Chem Biol*. 2006;2:458–66.
- 620 32. Ooft SN, Weeber F, Dijkstra KK, McLean CM, Kaing S, van Werkhoven E, et al. Patient-derived organoids can predict response to
621 chemotherapy in metastatic colorectal cancer patients. *Sci Transl Med*. 2019;11:eaay2574.
- 622 33. Vlachogiannis G, Hedayat S, Vatsiou A, Jamin Y, Fernández-Mateos J, Khan K, et al. Patient-derived organoids model treatment
623 response of metastatic gastrointestinal cancers. *Science*. 2018;359:920–6.
- 624 34. Tiriach H, Belleau P, Engle DD, Plenker D, Deschênes A, Somerville TDD, et al. Organoid Profiling Identifies Common Responders to
625 Chemotherapy in Pancreatic Cancer. *Cancer Discov*. 2018;8:1112–29.
- 626 35. Crystal AS, Shaw AT, Sequist LV, Friboulet L, Niederst MJ, Lockerman EL, et al. Patient-derived models of acquired resistance can
627 identify effective drug combinations for cancer. *Science*. 2014;346:1480–6.
- 628 36. Zehir A, Benayed R, Shah RH, Syed A, Middha S, Kim HR, et al. Mutational landscape of metastatic cancer revealed from prospective
629 clinical sequencing of 10,000 patients. *Nat Med*. 2017;23:703–13.

630 37. Palmer AC, Sorger PK. Combination Cancer Therapy Can Confer Benefit via Patient-to-Patient Variability without Drug Additivity or
631 Synergy. *Cell*. 2017;171:1678-1691.e13.

632 38. Gillies RJ, Verduzco D, Gatenby RA. Evolutionary dynamics of carcinogenesis and why targeted therapy does not work. *Nat Rev*
633 *Cancer*. 2012;12:487-93.

634 39. Gerlinger M, Rowan AJ, Horswell S, Larkin J, Endesfelder D, Gronroos E, et al. Intratumor Heterogeneity and Branched Evolution
635 Revealed by Multiregion Sequencing. *N Engl J Med*. 2012;366:883-92.

636 40. Hyman DM, Taylor BS, Baselga J. Implementing Genome-Driven Oncology. *Cell*. 2017;168:584-99.

637 41. Diaz JE, Ahsen ME, Schaffter T, Chen X, Realubit RB, Karan C, et al. The transcriptomic response of cells to a drug combination is
638 more than the sum of the responses to the monotherapies. *eLife*. 2020;9:e52707.

639 42. Pedersen MT, Helin K. Histone demethylases in development and disease. *Trends Cell Biol*. 2010;20:662-71.

640 43. Oser MG, Sabet AH, Gao W, Chakraborty AA, Schinzel AC, Jennings RB, et al. The KDM5A/RBP2 histone demethylase represses
641 NOTCH signaling to sustain neuroendocrine differentiation and promote small cell lung cancer tumorigenesis. *Genes Dev*.
642 2019;33:1718-38.

643 44. Lin W, Cao J, Liu J, Beshiri ML, Fujiwara Y, Francis J, et al. Loss of the retinoblastoma binding protein 2 (RBP2) histone demethylase
644 suppresses tumorigenesis in mice lacking Rb1 or Men1. *Proc Natl Acad Sci*. 2011;108:13379-86.

645 45. Sharma SV, Lee DY, Li B, Quinlan MP, Takahashi F, Maheswaran S, et al. A Chromatin-Mediated Reversible Drug-Tolerant State in
646 Cancer Cell Subpopulations. *Cell*. 2010;141:69-80.

647 46. Borden EC, Sen GC, Uze G, Silverman RH, Ransohoff RM, Foster GR, et al. Interferons at age 50: past, current and future impact on
648 biomedicine. *Nat Rev Drug Discov*. 2007;6:975-90.

649 47. Stark GR, Darnell JE. The JAK-STAT Pathway at Twenty. *Immunity*. 2012;36:503-14.

650 48. Eriksson B, Oberg K. An update of the medical treatment of malignant endocrine pancreatic tumors. *Acta Oncol*. 1993;32:203-8.

651 49. Oberg K, Eriksson B. The role of interferons in the management of carcinoid tumours. *Br J Haematol*. 1991;79:74-7.

652 50. Creutzfeldt W, Bartsch HH, Jacubaschke U, Stöckmann F. Treatment of gastrointestinal endocrine tumours with interferon-alpha
653 and octreotide. *Acta Oncol*. 1991;30:529-35.

654 51. Kvols LK, Moertel CG, O'Connell MJ, Schutt AJ, Rubin J, Hahn RG. Treatment of the malignant carcinoid syndrome. Evaluation of a
655 long-acting somatostatin analogue. *N Engl J Med*. 1986;315:663-6.

656 52. Vitale G, Herder WW de, Koetsveld PM van, Waaijers M, Schoordijk W, Croze E, et al. IFN- β Is a Highly Potent Inhibitor of
657 Gastroenteropancreatic Neuroendocrine Tumor Cell Growth In vitro. *Cancer Res*. 2006;66:554-62.

658 53. Zitzmann K, Brand S, Toni END, Baehs S, Göke B, Meinecke J, et al. SOCS1 Silencing Enhances Antitumor Activity of Type I IFNs by
659 Regulating Apoptosis in Neuroendocrine Tumor Cells. *Cancer Res*. 2007;67:5025-32.

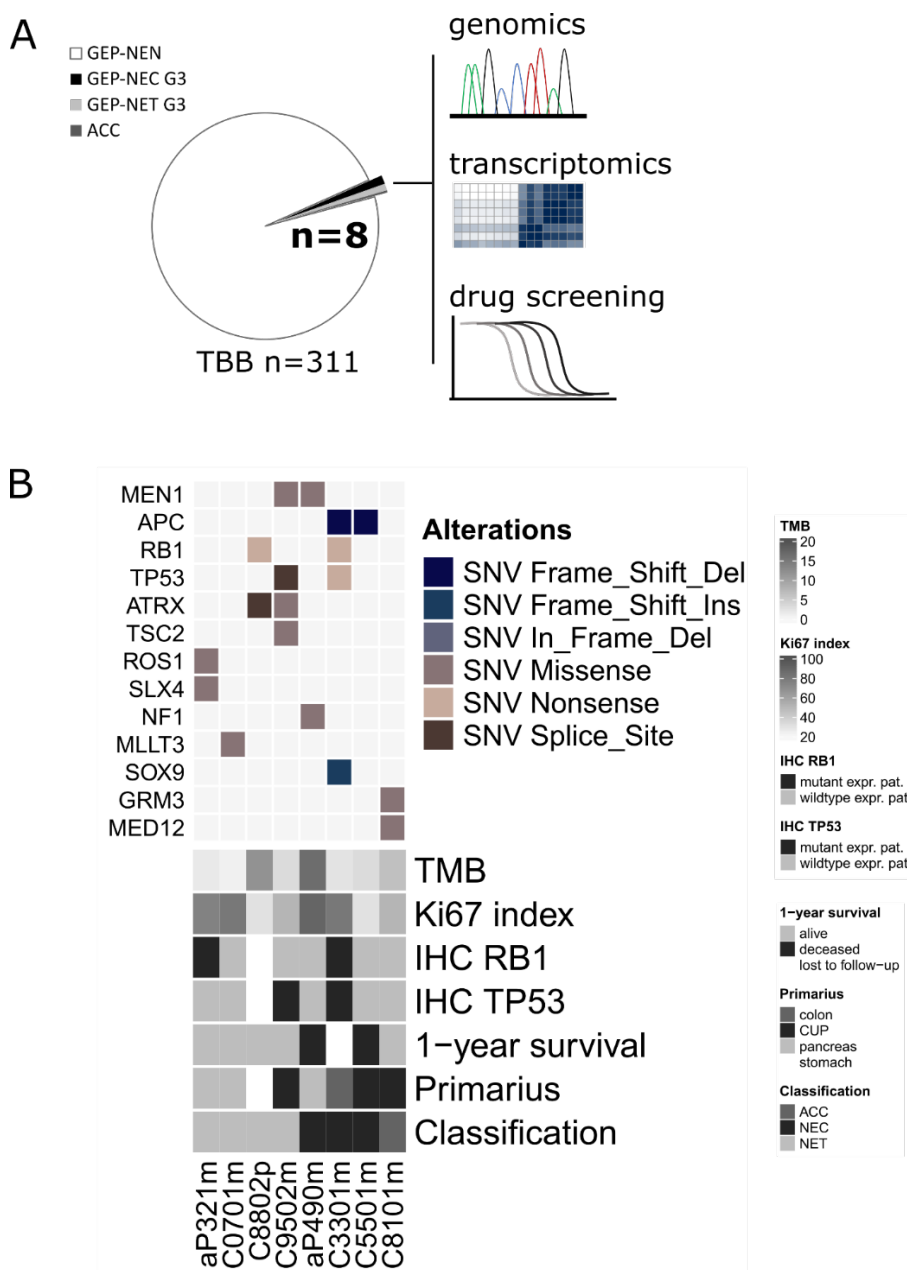
660 **TABLES**

Patient_ID	aP321m	C0701m	C8802p	C9502m	aP490m	C3301m	C5501m	C8101m
Sex	m	m	m	f	m	m	f	f
Age at surgery [y]	66	69	66	57	53	70	39	44
Tissue source	liver metastasis	liver metastasis	primarius	liver metastasis	liver metastasis	liver metastasis	metastasis ovary	liver metastasis
Primary tumor localisation	pancreas	pancreas	stomach	CUP	pancreas	colon	CUP	CUP
1-year survival	alive	alive	alive	alive	deceased	lost to follow-up	deceased	alive
Classification	NET	NET	NET	NET	NEC	NEC	NEC	ACC*
Morphology subtype	NA	NA	NA	NA	Large-cell	Small-cell	Large-cell	Large-cell
Histological differentiation	WD	WD	WD	WD	PD	PD	PD	NA
CgA	weak positive (+)	moderate positive (++)	NA	moderate positive (++)	strong positive (+++)	negative (-)	strong positive (+++)	weak positive (+)
Ki67	75	80	30	50	90	80	30	50
MCT4	nevative (0)	heterogenous (2)	NA	heterogenous (2)	heterogenous (2)	heterogenous (2)	positive (1)	heterogenous (2)
PDX1	positive	negative (-)	NA	negative (-)	negative (-)	negative (-)	negative (-)	negative (-)
RB1	mutant expr. pat.	wildtype expr. pat.	NA	wildtype expr. pat.	wildtype expr. pat.	mutant expr. pat.	wildtype expr. pat.	wildtype expr. pat.
SOX9	positiv	negative (-)	NA	negative (-)	strong positive (+++)	positive	negative (-)	positiv
SSTR2A	moderate positive (++)	negative (-)	NA	moderate positive (++)	negative (-)	negative (-)	weak positive (+)	negative (-)
SYN	strong positive (+++)	strong positive (+++)	positive (++)	strong positive (+++)	strong positive (+++)	strong positive (+++)	strong positive (+++)	negative (-)
TP53	wildtype expr. pat.	wildtype expr. pat.	NA	mutant expr. pat.	wildtype expr. pat.	mutant expr. pat.	wildtype expr. pat.	wildtype expr. pat.
DAXX	negative (-)	negative (-)	NA	NA	positive	NA	NA	NA
ATRX	positive	X	NA	NA	positive	NA	NA	NA
ARX	positive	negative (-)	NA	NA	negative (-)	NA	NA	NA
TRY1	negative (-)	negative (-)	negative (-)	negative (-)	negative (-)	negative (-)	negative (-)	positive
BCL10	negative (-)	negative (-)	negative (-)	negative (-)	negative (-)	negative (-)	negative (-)	positive

661

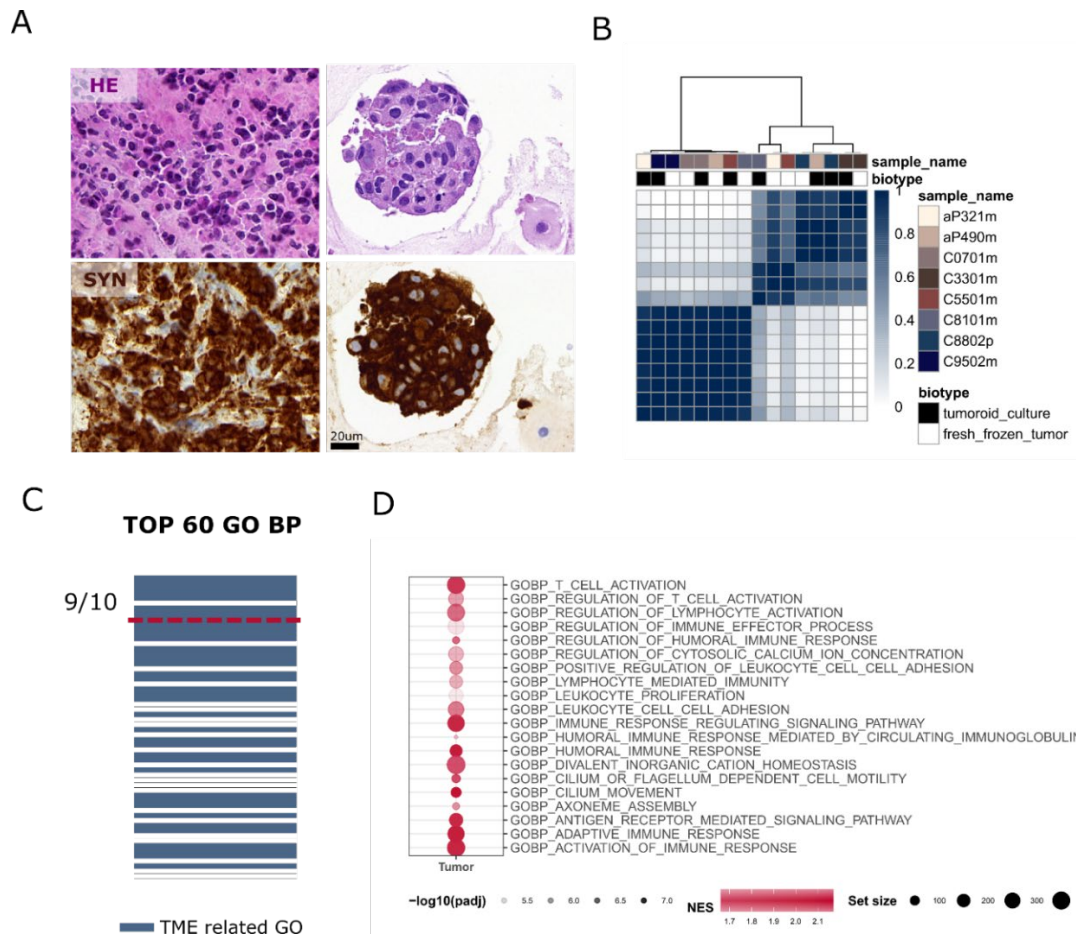
662 **Table 1: Patient demographics and clinicopathological classification**

663 *At initial diagnosis clinical differentiation between NET G3 and NEC was ambiguous. Due to an unexpected
664 clinical course deviation, a second opinion was obtained, which suggested a NET G3 differential diagnosis. The
665 evaluation of the collected cryospecimen after therapy showed signs of an acinar cell differentiation.



667
 668 **Figure 1 Study overview and clinical presentation of high grade GEP-NEN patient cohort**
 669 **A)** Schematic diagram of study outline, material processing, and analysis performed in the present
 670 study. TBB tumor biobank
 671 **B)** Oncoplot showing common genetic alterations of GEP-NENs found in the study cohort together
 672 with a selection of clinical parameters. The upper panel indicates specific types of single nucleotide
 673 variations (SNV) found in fresh frozen original tumor tissue from high-grade GEP-NEN patients. The
 674 lower panel displays the patient's clinical parameters, including tumor mutation burden (TMB;
 675 mutation/Mb) and 1-year survival, IHC-based proliferation status (Ki-67; percent positive cells per
 676 tissue), RB1 protein expression, TP53 protein expression, location of primarius, and the diagnostic
 677 classification.

678 NET neuroendocrine tumor, NEC neuroendocrine carcinoma, ACC acinar cell carcinoma CUP cancer
679 of unknown primary Mutant expr. pat. Mutant expression pattern (TP53 loss of protein (0% positive
680 tumor cells) or overexpression ($\geq 90\%$ positive tumor cell; RB1 complete loss of protein), wildtype
681 expr. pat. wildtype expression pattern.



682

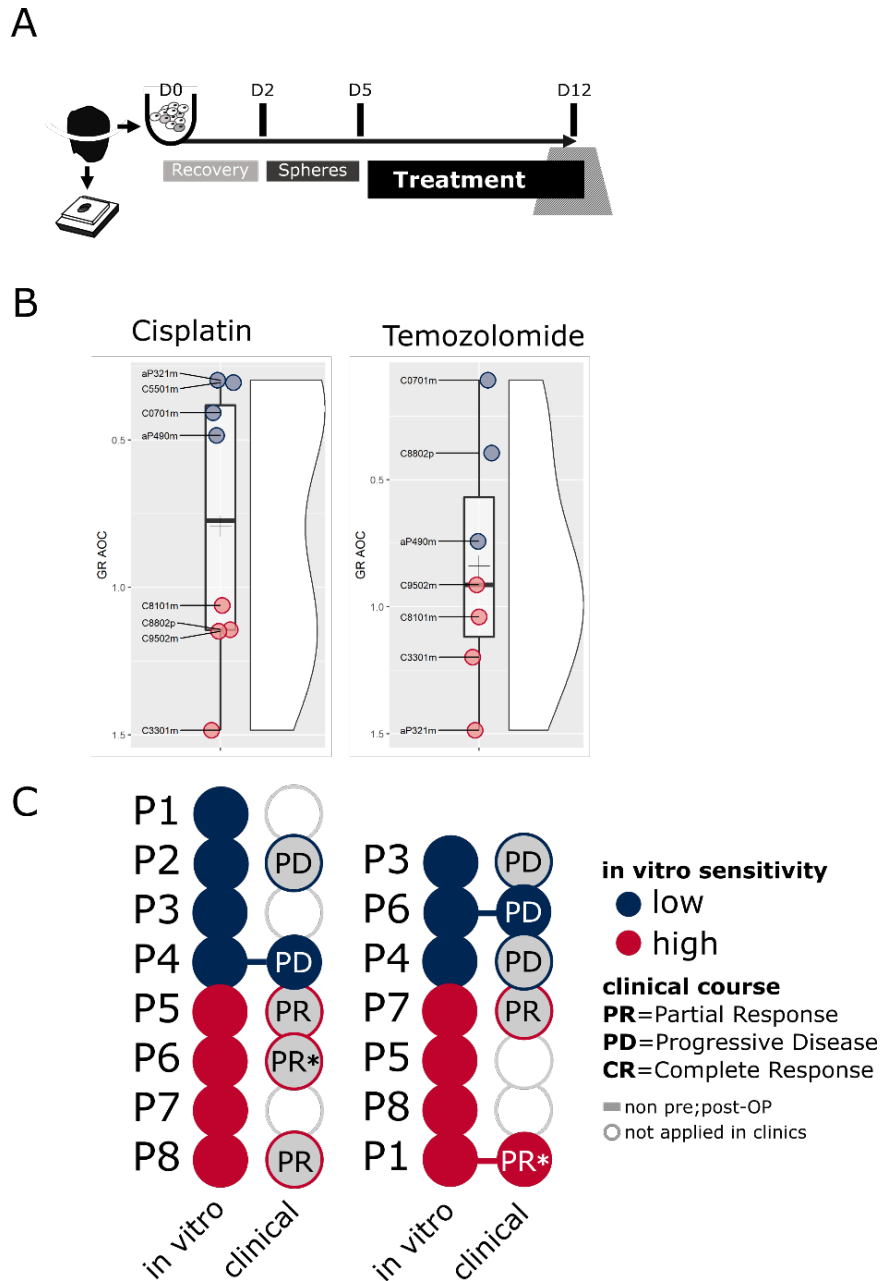
683 **Figure 2 Patient-derived tumoroids recapitulate key biological features of original tumors.**

684 **A)** Representative Hematoxylin and eosin (HE) staining and neuroendocrine diagnostic marker
 685 synaptophysin (SYN) immunolabeling in original tumor tissue and tissue-matched patient-derived
 686 (PD) tumoroids. Scale bar, 20um.

687 **B)** Consensus clustering of original tumor tissue and PD tumoroids according to the 2000 most
 688 variable genes by variance based on RNA sequencing. Cluster stability was reached for $k = 2$.
 689 Consensus cluster correlation is represented by the blue scale. Each column represents one sample.
 690 Biotypes and patient identifier are colored by class. The heatmap inner linkage was determined by
 691 Ward.D2 and the dendrogram (outer linkage) by an average of correlation scores.

692 **C)** Gene ontology (GO) enrichment comparing original tumor tissues and PD tumoroids. Displayed are
 693 the 60 most significantly enriched GO terms of biological processes (p -ks < 0.005 , Kolmogorov-
 694 Smirnov test). Tumor-micro-environment (TME) related GO terms are indicated in blue. In the top
 695 ranks (red line), nine GO terms are directly linked to the immune cell compartment.

696 **D)** Gene set enrichment analysis comparing original tumor tissues with PD tumoroids. Displayed are
 697 the top-ranked and most significantly enriched gene sets (GO biological processes) found in original
 698 tumor tissue. Dots represent GO term enrichment: Red color indicates normalized positive
 699 enrichment score (NES) > 1.7 ; Transparency indicates Benjamini-Hochberg adjusted p-values (p -adj);
 700 Size indicates the number of genes within the specific gene set.



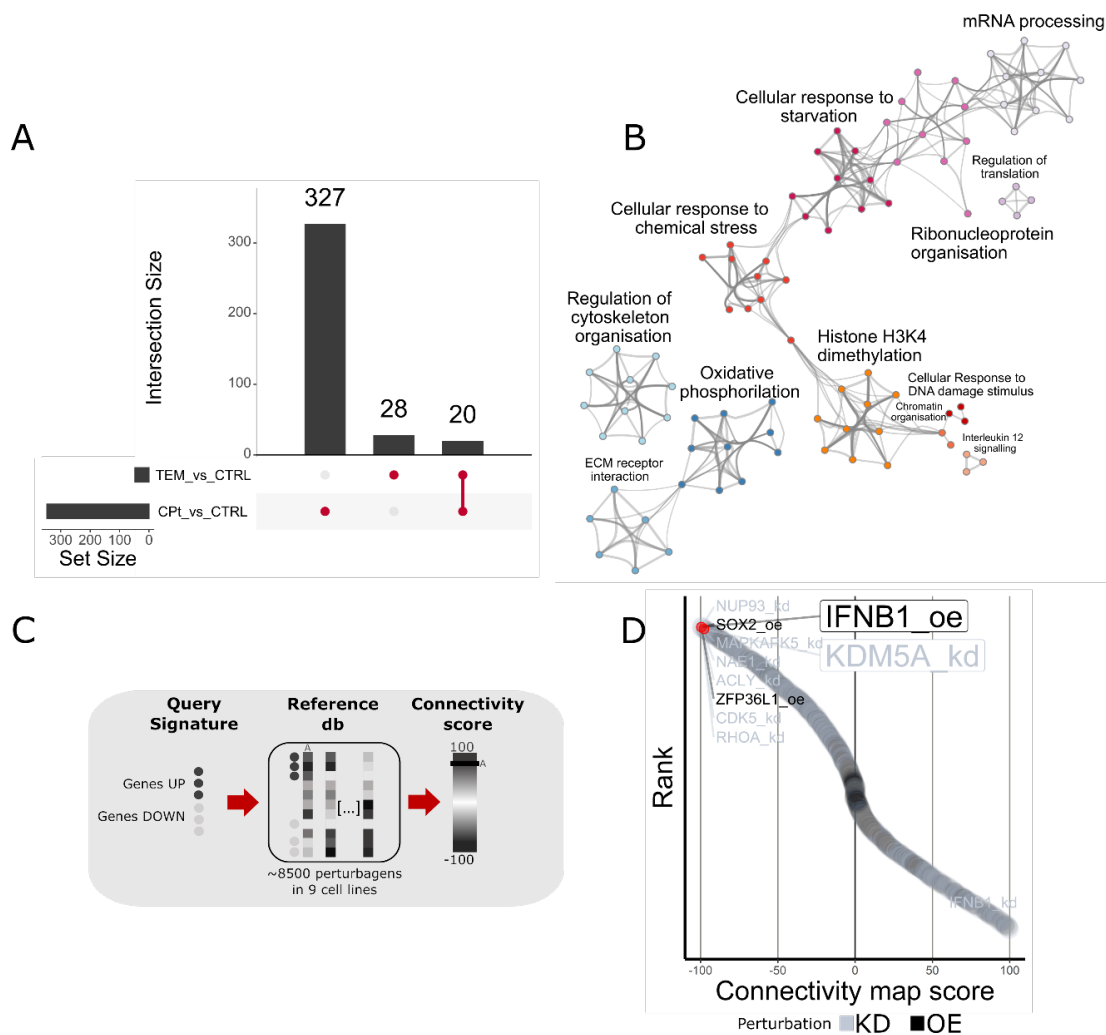
701

702 **Figure 3 Patient-derived GEP-NEN tumoroids mimic clinical patient response**

703 **A)** Schematic diagram of in vitro drug screening workflow in patient-derived GEP-NEN tumoroids.

704 **B)** Effect of cisplatin and temozolomide treatment on viability in PD tumoroids. PD tumoroids were
 705 treated with DMSO (Ctrl), cisplatin, or temozolomide for 168 hours. In vitro sensitivities were
 706 converted into parametrized drug sensitivity metrics using GR metrics (GR AOC).

707 **C)** Comparison between in vitro sensitivity of PD tumoroids and clinical patient response. Circles
 708 connected with lines represent patients with clinical therapy results adjacent to pre-/post-operative
 709 specimen collection.



710

711 **Figure 4 Molecular stress response in patient-derived tumoroids reveals IFNB1 and KDM5A as**
 712 **targets for combination therapy with cisplatin.**

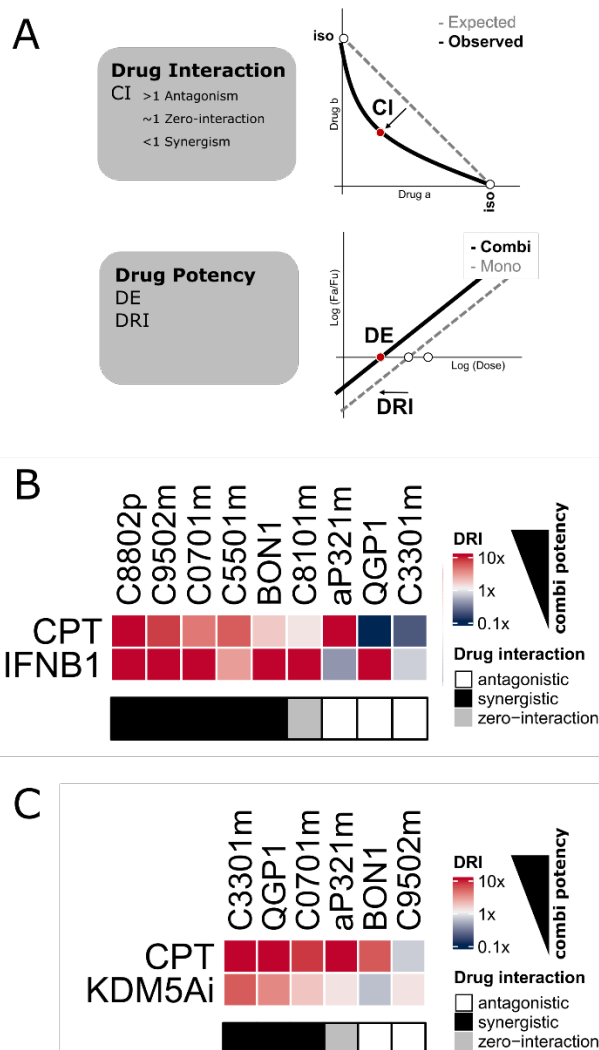
713 **A)** UpSet plot of differentially expressed genes in patient-derived (PD) tumoroids treated with
 714 cisplatin (CPT) or temozolomide (TEM). Highlighted are the number of genes specific for either CPT or
 715 TEM stress response or genes shared between both.

716 **B)** Network representation of pathway and GO biological processes from cisplatin-induced stress
 717 response genes (n=327). Each node represents an enriched term and is colored by its cluster.

718 **C)** Schematic diagram of connectivity map (cMap) workflow to detect connectivity between stress
 719 response signatures from PD tumoroids (top 150 up- or down-regulated genes) and perturbational
 720 signatures in the data base.

721 **D)** Waterfall plot of cMap targets inducing inverse response signatures (connectivity map score $\tau < 0$) to
 722 cisplatin-induced stress response in PD tumoroids. The list of top hits (red rectangle) is
 723 magnified (right). τ stands as a standardized measure ranging from -100 to +100; A τ of -90 indicates
 724 that only 10% of reference perturbations showed stronger connectivity to the query (25).

725 Overexpression (oe) of IFNB1 and knockdown (kd) of KDM5A induce highly inverse signatures to the
 726 cisplatin-induced stress response.



727

728 **Figure 5** Combinational treatment of cisplatin and KDM5A or IFNB1 induces synergistic and potent
 729 treatment response in vitro.

730 **A)** Schematic representation of parameters to assess combinational therapy. Drug interaction was
 731 assessed by determining the combinational index (CI) as the deviation of the observed drug
 732 combination activity from isoactive monotherapies (iso) at a defined effect level. **Drug potency**
 733 parameters were derived from the median-effect equation by calculating the dosage required to
 734 reach a specific effect level (DE) and by calculating the dose reduction index (DRI), describing the
 735 fold-change of required dosage in combination therapy compared with required dosage in respective
 736 monotherapy.

737 **B+C)** Heatmap displaying drug potency parameters for combinational therapy in patient-derived (PD)
 738 tumoroids. The color scale indicates the drug reduction index (DRI) relative to the combination
 739 treatment. Red (high DRI) or blue (low DRI) indicate higher or lower drug doses required for an
 740 equipotent inhibitory effect in monotherapy. Drug interaction was classified into synergistic (black),
 741 antagonistic (white), or zero-interaction (grey) based on CI.

742 **Supplementary Material**

743 **Supplementary Table 1:** Demographics, clinical description, and MSI

744 **Supplementary Table 2:** Clinical course records

745 **Supplementary Table 3:** Mutational profiling

746 **Supplementary Table 4:** Cytology of patient-derived tumoroids

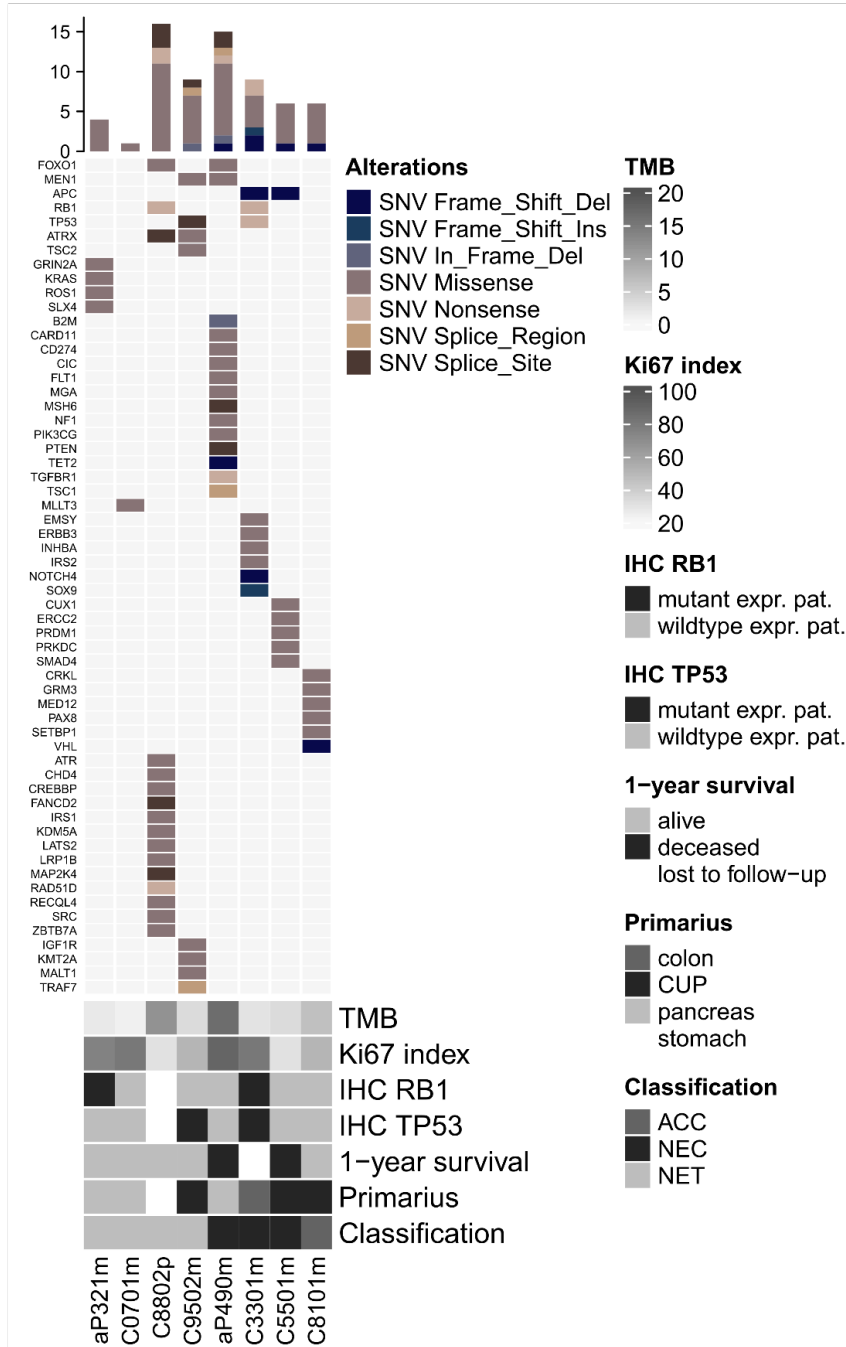
747 **Supplementary Table 5:** Gene Ontology and GSEA of PD tumoroids vs original tumor tissue

748 **Supplementary Table 6:** GRmetrics

749 **Supplementary Table 7:** cMAP signatures

750 **Supplementary Figures S1 to S5**

A



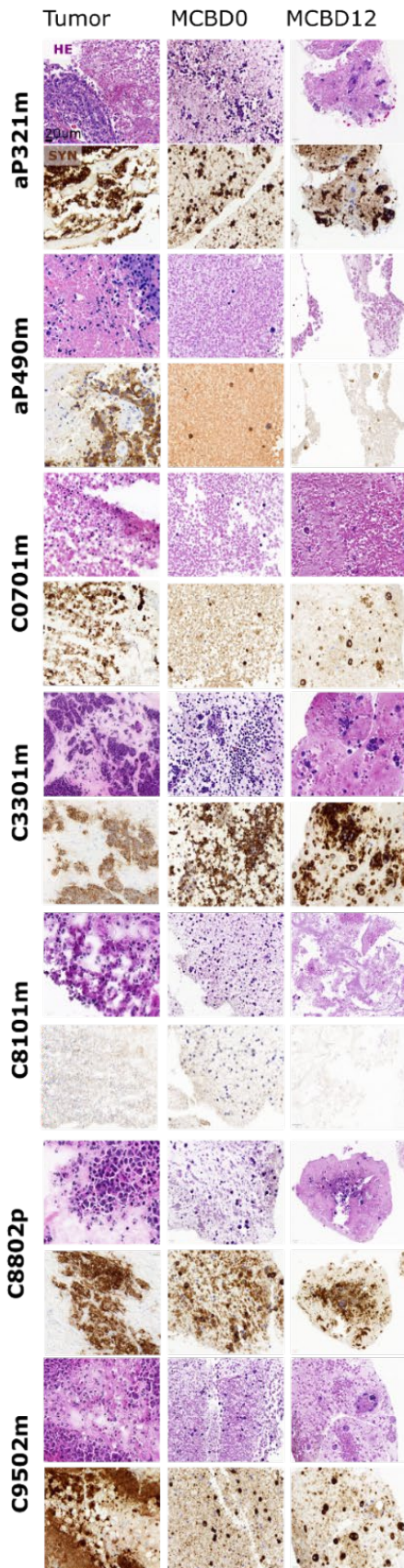
751

752 **Supplementary Figure S1 Detailed histomorphological-, mutational-, and clinical description of high**
 753 **grade GEP-NEN patient cohort.**

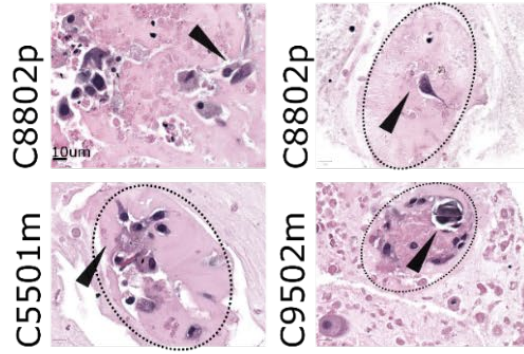
754 **A)** Oncoplot showing all detected genes harboring alterations and a selection of clinical parameters
 755 from GEP-NEN patients. The top panel indicates mutation counts per patient. The middle panel
 756 indicates types of single nucleotide variations (SNV) found in fresh frozen original tumor tissue from
 757 high-grade GEP-NEN patients. The lower panel indicates clinical parameters, including tumor
 758 mutation burden (TMB; mutation/Mb) and 1-year survival, IHC-based proliferation status (Ki-67;
 759 percent positive cells per tissue), RB1 protein expression, TP53 protein expression, location of
 760 primarius, and the diagnostic classification.

761 NET neuroendocrine tumor, NEC neuroendocrine carcinoma, ACC acinar cell carcinoma, CUP cancer
762 of unknown primary, MSI microsatellite instable, Mutant expr. pat. Mutant expression pattern (TP53
763 loss of protein (0% positive tumor cells) or overexpression ($\geq 90\%$ positive tumor cell; RB1 complete
764 loss of protein), wildtype expr. pat. wildtype expression pattern.

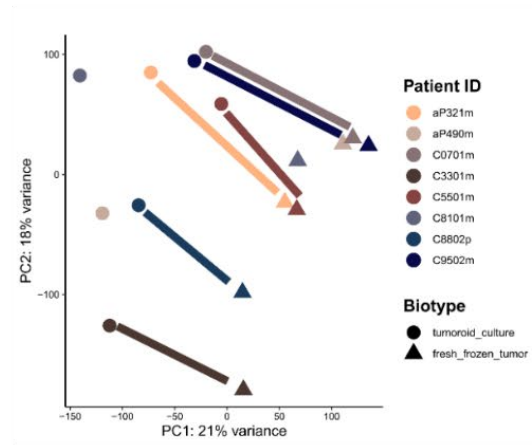
A



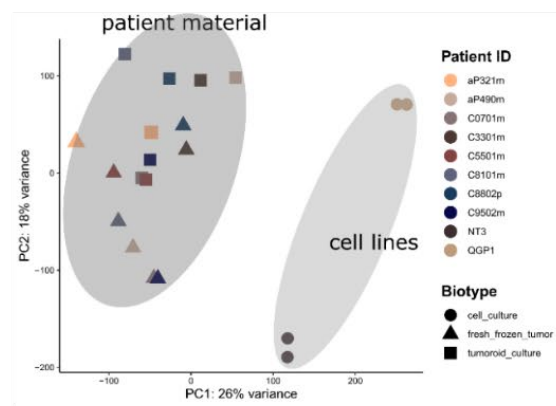
B



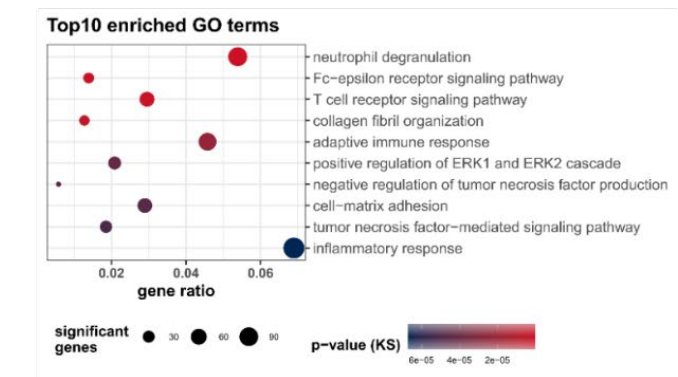
C



D



E



765

766

Supplementary Figure S2 Histomorphological and molecular characterization of patient-derived

767

GEP-NEN tumoroids

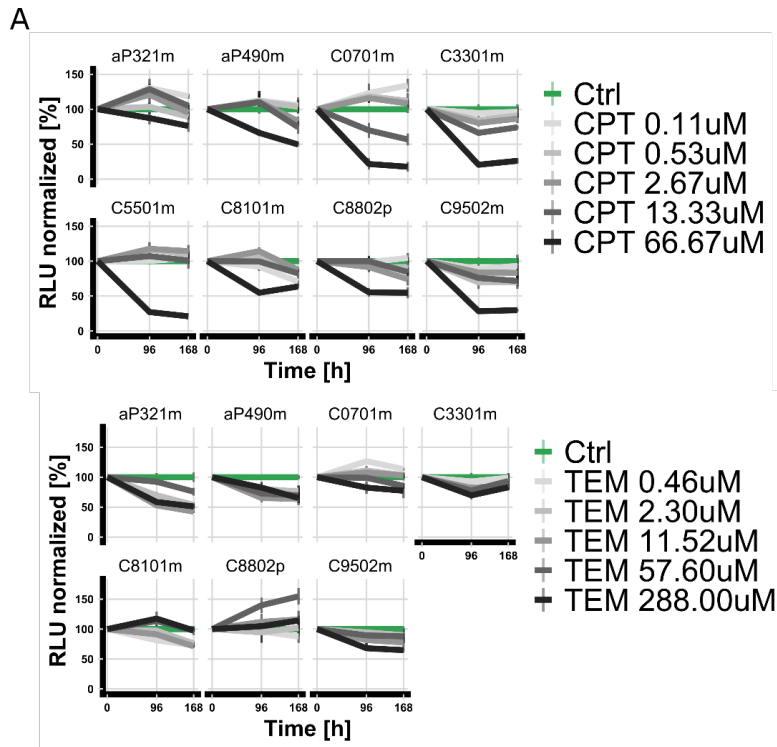
768 **A)** Representative Hematoxylin and eosin (HE) staining and synaptophysin (SYN) immunolabeling in
769 original tumor tissue and patient-derived (PD) tumoroids. Cells were formalin-fixed and embedded
770 into micro-cell-blocks directly after isolation (MCB D0) and after 12 days in culture (MCB D12). PD
771 tumoroids and corresponding mirror blocks from fresh frozen original tumors were stained for HE or
772 SYN. IHC slides were counterstained with hematoxylin. All stainings were assessed by two board-
773 certified pathologists. Scale bar = 20 μ m.

774 **B)** Representative HE stainings in MCB of PD tumoroids after 12 days in culture. Black arrows and
775 dotted lines highlight solitary fibroblast, focal deposition of extracellular matrix, or focal
776 calcifications. Scale bar, 10 μ m.

777 **C)** Principle component analysis (PCA) of gene expression in original tumor tissue and tissue-matched
778 PD tumoroids. Patient-specific expression patterns are systematically retained in culture (solid lines).

779 **D)** PCA of gene expression in original tumor tissue, tissue-matched PD tumoroids, and NEN cell line
780 spheroids (NT3, QGP1). Gene expression in NEN cell line spheroids diverges from patient material
781 and builds a separate cluster (light-grey circle).

782 **E)** Top 10 significantly enriched gene ontology (GO) terms of biological processes (p -ks < 0.005). 8 out
783 of 10 GO terms are related to the immune cell compartment. P-values were determined by the
784 Kolmogorov-Smirnov test.



B

Patient ID	Therapy	Clinical course	PDT sensitivity	Differentiation	Ki67 [%]	RB1 status	TP53 status	KRAS status
C5501m	Cisplatin	non-responder	low	PD	<55	wildtype	wildtype	wildtype
aP490m	Cisplatin	non-responder	low	PD	>55	wildtype	wildtype	wildtype
C8802p	Cisplatin	responder	high	WD	<55	mutant	wildtype	wildtype
C3301m	Cisplatin	responder	high	PD	>55	mutant	mutant	wildtype
C8101m	Cisplatin	responder	high	NA	<55	wildtype	wildtype	wildtype
C0701m	Cisplatin	NA	low	WD	>55	wildtype	wildtype	wildtype
aP321m	Cisplatin	NA	low	WD	>55	mutant	wildtype	mutant
C9502m	Cisplatin	NA	high	WD	<55	wildtype	mutant	wildtype

Patient ID	Therapy	Clinical course	PDT sensitivity	MGMT status
C8802p	Temozolomide	non-responder	low	unmethylated
C0701m	Temozolomide	non-responder	low	unmethylated
aP490m	Temozolomide	non-responder	low	unmethylated
C9502m	Temozolomide	responder	high	unmethylated
C3301m	Temozolomide	responder	high	unmethylated
aP321m	Temozolomide	NA	high	unmethylated
C8101m	Temozolomide	NA	high	unmethylated
C5501m	Temozolomide	NA	NA	unmethylated

785

786 **Supplementary Figure S3 In vitro pharmacotyping in patient-derived GEP-NEN tumoroids.**

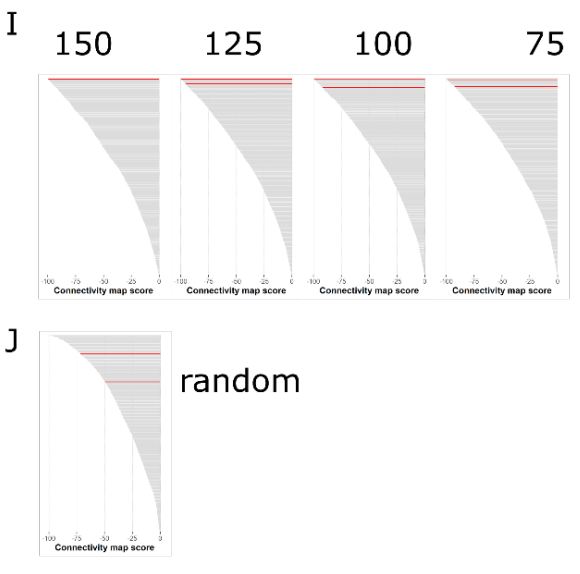
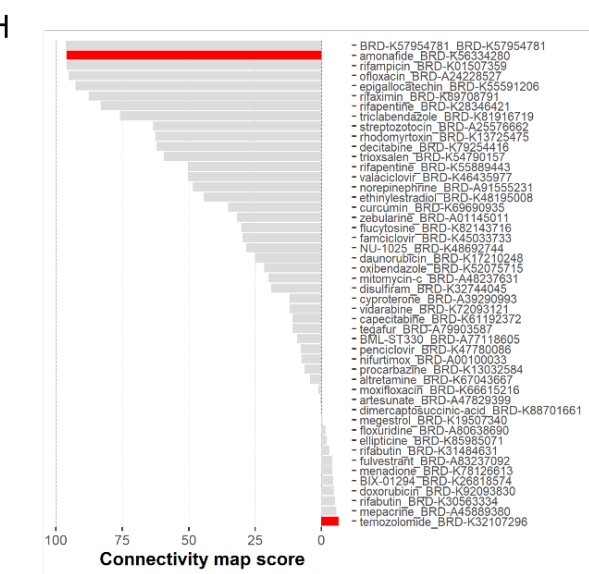
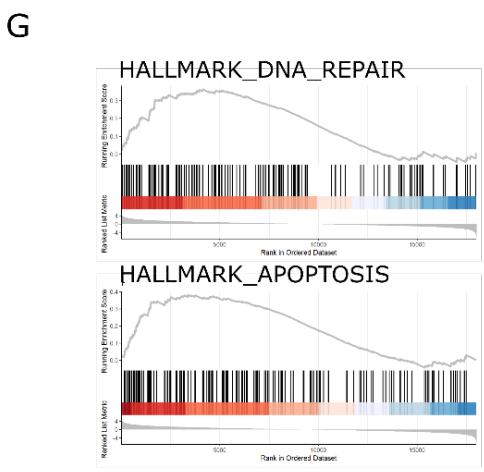
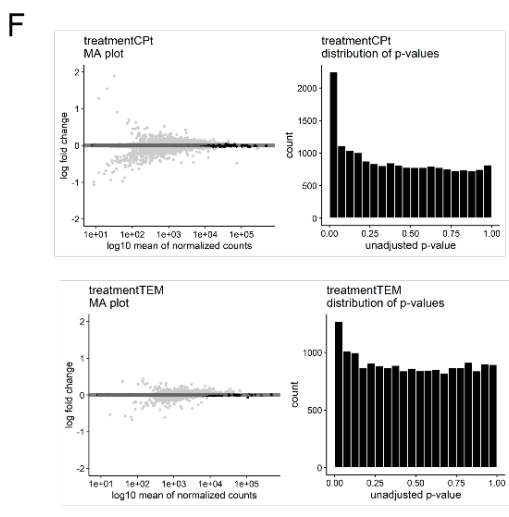
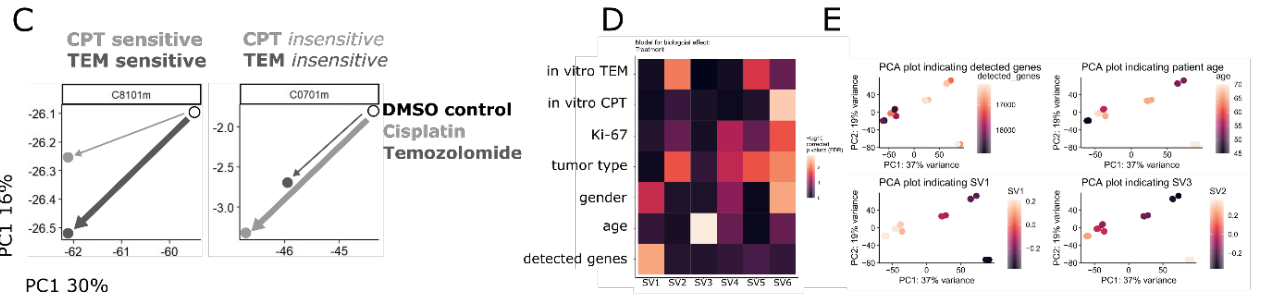
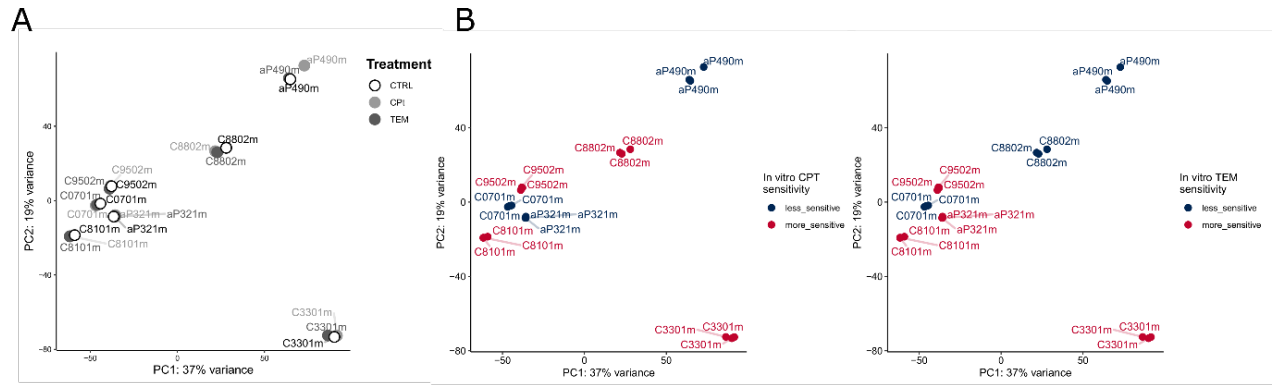
787 **A)** In vitro viability curves from patient-derived (PD) tumoroids treated for 96 and 168 hours.

788 Cisplatin (CPT) or temozolomide (TEM) data points are normalized to corresponding DMSO control

789 (Ctrl) for each specific patient. Data represent mean \pm SEM (n=1, three technical replicates).

790 **B)** Overview of clinical course, in vitro sensitivity in PD tumoroids, and pathological clinical features

791 associated with clinical responsiveness.



792
793

Supplementary Figure S4 Characterization of molecular stress response in PD tumoroids.

794 **A+B)** Principal component analysis (PCA) of gene expression in patient-derived (PD) tumoroids either
795 treated with DMSO as a control (Ctrl) or treated with cisplatin (CPT) or temozolomide (TEM) at
796 sublethal dosages. Parametrized in vitro sensitivity is indicated by color.

797 **C)** Representative PCA indicating the magnitude of gene expression change (top 2000 genes) in CPT
798 or TEM treated PD tumoroids either more sensitive (C8101m) or less sensitive (C0701m) for both of
799 the treatments.

800 **D)** Heatmap indicating association of known covariates with estimated surrogate variables (SV).
801 Association was tested using linear models for continuous covariates and Kruskal-Wallis tests for
802 categorical covariates. P-values were corrected for multiple testing using the false discovery rate
803 (FDR) cutoff < 0.01 .

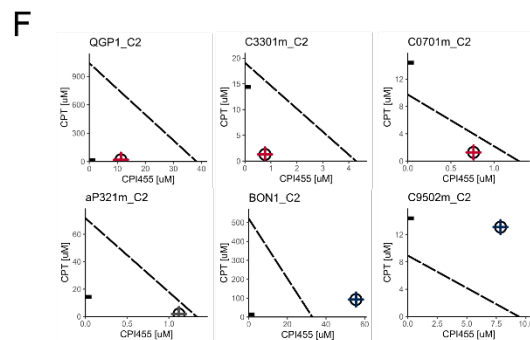
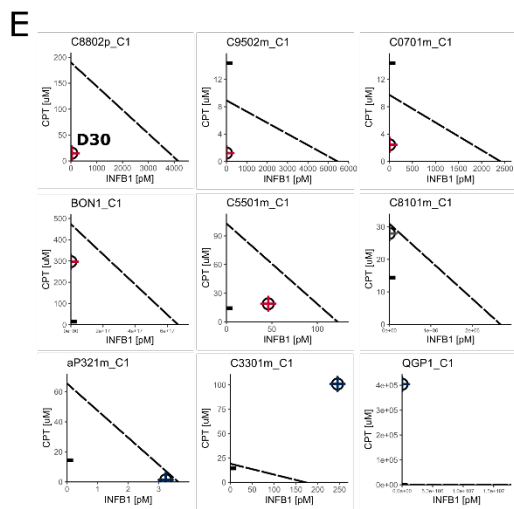
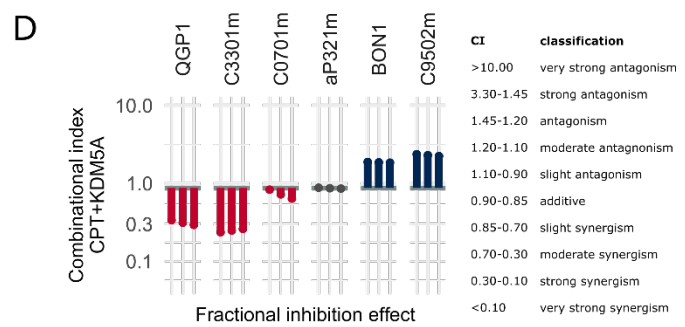
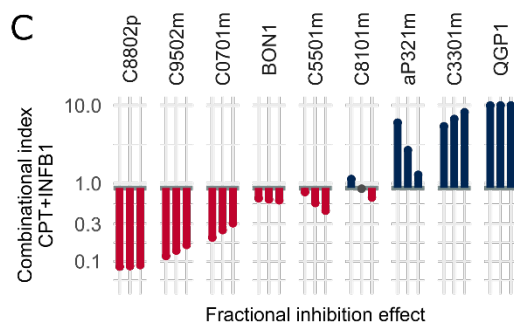
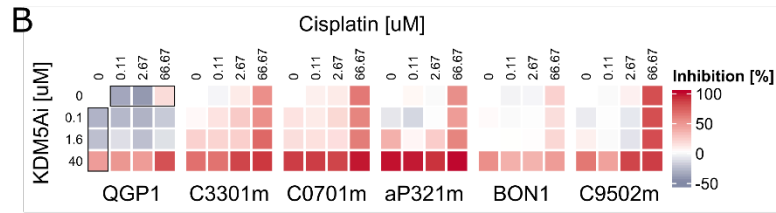
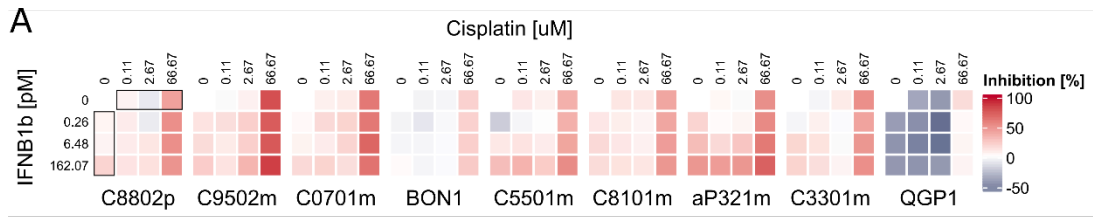
804 **E)** Representative PCA highlighting overlap of selected SVs with known covariates, including the
805 number of detected genes and patient age.

806 **F)** Mean-average (MA) plot of gene expression changes induced by treatment. Differential gene
807 expression was compared between DMSO control PD tumoroids and PD tumoroids treated with
808 sublethal dosages of CPT or TEM. Significantly differentially expressed genes ($p\text{-adj} < 0.05$) with an
809 FDR < 0.1 are highlighted in light grey (left). Histogram of p-values for genes with mean normalized
810 count larger than 1 (right) indicates enrichment in significant p-values.

811 **G)** Gene set enrichment plot showing enrichment of DNA repair and apoptosis in cisplatin-induced
812 stress responses of PD tumoroids. Upper panel displays the running sum of gene sets and the leading
813 edge. Lower panel represents \log_2 fold-change ranked detected genes in RNAseq.

814 **H)** Waterfall plot of DNA-directed compounds in cMAP and their similarity (connectivity map score $>$
815 0) to the cisplatin-induced stress response. Amonafide (DNA intercalating agent) shows high
816 similarity to cisplatin-induced stress response, whereas temozolomide (DNA alkylating agent) shows
817 low similarity.

818 **I+J)** Waterfall plot assessing the robustness of detecting KDM5A and IFNB1 in cMAP top inverse
819 ranks. KDM5A and IFNB1 are highlighted in red. cMAP output remains stable upon systematic
820 degradation of the number of input query genes (top). Random permutation leads to loss of top
821 ranks and insignificant connectivity map scores.



822

823 **Supplementary Figure S5 Assessment of combinational drug treatment in patient-derived**
 824 **tumoroids.**

825 **A+B)** Drug response heatmap of mono- and combinational treatment of cisplatin and recombinant
 826 IFNB1 or KDM5A inhibitor (CPI-455) in a full matrix design. The short-term treatment response was
 827 assessed after 24 hours, and inhibition was normalized to DMSO control for each sample.

828 **C+D)** Bar graph indicating drug interaction between cisplatin and IFNB1 or KDM5A in PD tumoroids.
 829 Three representative fractional inhibition effect levels (0.25, 0.30, 0.35) were chosen based on the
 830 overall inhibitory effect of cisplatin monotherapy at physiologically relevant concentrations (14.4uM

831 C_{max}; inhibition 0.29). Shown are combination index (CI) in red (synergistic), blue (antagonistic), or
832 grey (zero-interaction).

833 **E+F**) Isobologram showing drug interaction between cisplatin and IFN β 1 or KDM5A in PD tumoroids
834 at a 30% inhibition effect level. The dashed line indicates the zero-interaction isobole of isoactive
835 monotherapies. Isoactive drug combination are indicated by crossed circles in red (synergistic), blue
836 (antagonistic), or grey (zero-interaction). The physiological dosage of cisplatin (c_{Max}) is indicated by
837 the black line on the y-axis.

3.2.4 Extended discussion

Mouse- and cell line models of GEP-NEN do not adequately represent the molecular diversity of human patients. This proof-of-concept study demonstrated the feasibility and translational relevance of patient-derived GEP-NEN tumoroids, paving the way for more personalized medicine approaches. The two-week short-term culture workflow achieves high success rates and quick turnaround times. In this instance, the *in vitro* drug sensitivity corresponded well to the patient's clinical response. In a smaller scale study of three gastrointestinal NEC organoids established from 18G core biopsies, the *in vitro* and clinical patient responses were corresponding; however, the culture success rate in establishing organoids was only 10% (3/31)²³³. Therefore findings from our presented workflow support the idea of rapid ex-vivo drug testing without prior establishment and expansion of long-term patient models³²⁶.

Our research revealed a high level of molecular heterogeneity in the patient samples, making clinical classification more difficult. Some patients' genetic- and histomorphological characteristics were inconsistent, as illustrated by a patient with a clear NEC histomorphology but *MEN1* and *PTEN* mutations that are more compatible with NETs. Since most of these patients received several lines of therapies before the culture specimen collection, heavy pretreatment may be linked to these heterogeneous genetic profiles. Transcriptional profiling yielded no apparent separation between GEP-NEC and GEP-NET G3 samples in our cohort. However, a recent study reported a distinction between GEP-NECs and GEP-NET based on transcriptional profiling⁸⁸. This discrepancy might stem from several aspects: Their larger cohort size (NEC n=17, NET G3 n=3) allows a higher-powered and more fine-grained clustering. Interestingly, in their analysis, the two largest clusters separate a branch of NEC patients from another branch consisting of a mixture of NEC and NET G3 samples, indicating that the separation might not be so clear. Moreover, for their comparison, all NET G3 patients had much lower Ki-67 < 50%, whereas the NEC patients showed proliferation indices clearly above 60%, which may also impact the molecular profiles of these samples and harbor clearer separation. Additionally, a large part of their NEC samples were treatment-naïve prior the culture specimen collection. Incorporating our data into this GEP-NEN transcriptomic dataset could shed light on whether our samples cluster differently within a larger cohort.

In light of complex molecular heterogeneity and the lack of therapeutic biomarkers, functional information provides an additional layer that may support clinical decisions and prioritization of drug candidates in addition to conventional clinical molecular assessments. Genetic-, transcriptional-, or histomorphological therapy biomarkers are not established for GEP-NENs

¹⁹. Although, for example, response to everolimus was associated with MTOR pathway protein expression, gene mutations of pathway members or aberrant expression were found in a smaller proportion of patients than expected from clinical trials ^{35,327}. Regardless of molecular classification, we discovered detectable differences in tumoroids' *in vitro* drug responses, which likely reflect actual interpatient drug sensitivity. Furthermore, alterations in gene expression in patient-derived tumoroids after drug treatment aided in the discovery of therapeutic co-vulnerabilities, emphasizing the importance of multimodal analysis, including genomics, transcriptomics, and functional assays, in order to advance therapeutic approaches. We hope to present additional arguments supporting a more extensive cohort pilot study using additional biopsies in our culture workflow.

It would be interesting to clarify the role of KDM5A and IFNB1 in GEP-NENs from a mechanistic standpoint. This will require existing, stable, and more manageable preclinical models. High-grade NET/NEC organoid libraries from fore-, mid-, and hindgut exist ^{86,233}, and it would be worth screening these additional models for combinational efficiency and correlating the output with their molecular background.

Interestingly, in a previous study, loss of *Kdm5a* (*Rbp2*) inhibited proliferation in islet-cell tumors, decreased tumor burden, and enhanced survival in *Men1*-deficient mice ¹⁸⁰. Using additional mouse models of high-grade tumors (e.g., Rip1Tag2) or xenograft models (e.g., zebrafish) would help demonstrate the safety and efficacy of combinational pharmacological inhibition *in vivo*. Another appealing aspect would be determining whether the combination of KDM5A and IFNB1 is more effective in treating NET G3 or NECs. Intriguingly, QGP1 and BON1 exhibited inverse synergy to both combinational treatments, suggesting that distinct molecular backgrounds may indeed influence combinational sensitivities. In human GEP-NENs, elevated levels of KDM5A were detected in RNA and protein levels ¹⁸². Interestingly, the subcellular localization of KDM5A was different between NETs (cytoplasm) and NECs (nuclear), suggesting different biological roles in these two cancer entities ¹⁸². Since there are few effective treatments for high-grade GEP-NETs, the combination with clinically approved interferons ¹⁹ may be a promising combinational strategy to improve treatment efficacy.

A potent role of interferons in the induction of apoptosis has been shown in cell line models of GEP-NENs *in vitro* ^{328,329}. Based on our research, we determined that combining chemotherapy and interferon beta would reduce individual drug doses while maintaining the same effects. Reduced dosages may result in improved patient drug tolerance. Our *in vitro* workflow permits

us to evaluate these combinations or other promising targets in greater detail and may serve as a solid foundation for future translational research.

3.3 Project 3: EZH2 Inhibition as New Epigenetic Treatment Option for Pancreatic Neuroendocrine Neoplasms (PanNENs)

3.3.1 Specific introduction

Despite therapeutic advances, surgery remains the only curative therapy in PanNENs^{19,136,330}. Some tumors are non-resectable, and a large proportion of patients receiving surgery will eventually show recurrence³³¹. PanNENs harbor only a few oncogenic mutations that are therapeutically targetable^{33,37}. Common PanNEN driver genes *ATRX*, *DAXX* and *MEN1* and other frequently mutated genes such as *SETD2* and *MLL3*³³ and *ARID1A*^{70,332,333} are all involved in chromatin structure remodeling and underline the importance of epigenetic modulation in PanNEN development. Epigenetic aberrations are targetable and reversible²⁰¹ and enhance the effectiveness of anticancer treatments in several cancer types²⁰⁵. Targeting epigenetic aberrations may present novel therapeutic targets in PanNENs, and patient-derived PanNEN cell culture allows for testing and prioritizing promising epigenetic drugs for future clinical studies. EZH2, a histone methyltransferase functions as the catalytic subunit of the PRC2 and is involved in the transcriptional silencing of target genes¹⁹⁶. EZH2 inhibitors have been successfully applied in clinical phase I/II studies in *EZH2*-mutated lymphoma patients^{203,334}. The only previous study of EZH2 in GEP-NENs correlated its protein expression with tumor cell proliferation and P53 expression³³⁵. So far, the role of EZH2 in PanNEN has not been investigated further.

3.3.2 Specific hypothesis and aims

Hypothesis: Targeting commonly found aberrant epigenetic modifications is an effective treatment for a subset of advanced PanNENs

Aim1) To investigate EZH2 expression in a collection of PanNEN patient samples

Aim2) To determine whether inhibition of methyltransferase EZH2 is eligible as a treatment option for PanNENs

3.3.3 Manuscript 3: “*EZH2 inhibition as new epigenetic treatment option for Pancreatic Neuroendocrine Neoplasms (PanNENs)*”

Simon Leonhard April-Monn, Valentina Andreasi, Marco Schiavo Lena, Martin Carl Sadowski, Corina Kim-Fuchs, Michelle Claudine Buri, Ketkar Avanee, Renaud Maire, Annunziata Di Domenico, Jörg Schrader, Francesca Muffatti, Claudio Doglioni, Stefano Partelli, Massimo Falconi, Aurel Perren and Ilaria Marinoni

Cancers [10.3390/cancers13195014](https://doi.org/10.3390/cancers13195014)

Reprinted from ¹⁷⁷ © 2021, The Authors.

Author contribution (CRediT):

I was involved in **conceptualization** (ideas, formulation, and evolution of overarching research goals and aims), **methodology** (development and design of methodology, creation of models), **software** (programming and implementation of code and testing of existing computer code), **validation** (verification of the overall replication/reproducibility of experiments and results and other research outputs), **formal analysis** (application of statistical, mathematical, computational and other formal techniques to analyze and synthesize study data), **investigation** (conduction research and investigation processes, performing experiments and data collection), **data curation** (managing activities to annotate and maintain research data for initial and later use), **writing and preparation** of the original draft and **reviewing and editing** the final manuscript, and **visualization**.

Article

EZH2 Inhibition as New Epigenetic Treatment Option for Pancreatic Neuroendocrine Neoplasms (PanNENs)

Simon Leonhard April-Monn ^{1,2,†}, Valentina Andreasi ^{1,3,4,‡}, Marco Schiavo Lena ⁵, Martin Carl Sadowski ¹, Corina Kim-Fuchs ⁶, Michelle Claudine Buri ¹, Avanee Ketkar ¹, Renaud Maire ¹, Annunziata Di Domenico ¹, Jörg Schrader ⁷, Francesca Muffatti ³, Claudio Doglioni ^{4,5}, Stefano Partelli ^{3,4}, Massimo Falconi ^{3,4}, Aurel Perren ^{1,8,*} and Iliaria Marinoni ^{1,*}

- ¹ Institute of Pathology, University of Bern, 3008 Bern, Switzerland; simon.april@pathology.unibe.ch (S.L.A.-M.); andreasi.valentina@hsr.it (V.A.); martin.sadowski@pathology.unibe.ch (M.C.S.); michelle.buri94@gmail.com (M.C.B.); avanee3894@gmail.com (A.K.); renaud.maire@pathology.unibe.ch (R.M.); annunziata.didomenico@gmail.com (A.D.D.)
- ² Graduate School for Cellular and Biomedical Sciences, University of Bern, 3012 Bern, Switzerland
- ³ Pancreatic Surgery Unit, Pancreas Translational and Clinical Research Center, San Raffaele Scientific Institute, 20132 Milan, Italy; muffatti.francesca@hsr.it (F.M.); partelli.stefano@hsr.it (S.P.); falconi.massimo@hsr.it (M.F.)
- ⁴ Faculty of Medicine and Surgery, Vita-Salute San Raffaele University, 20132 Milan, Italy; doglioni.claudio@hsr.it
- ⁵ Unit of Pathology, San Raffaele Scientific Institute, 20132 Milan, Italy; schiavolena.marco@hsr.it
- ⁶ Department of Visceral Surgery and Medicine, University Hospital Bern, University of Bern, 3008 Bern, Switzerland; corina.kim-fuchs@insel.ch
- ⁷ Department of Medicine, University Medical Center Hamburg-Eppendorf, 20251 Hamburg, Germany; jschrade@uke.de
- ⁸ Bern Center for Precision Medicine, University & University Hospital of Bern, 3008 Bern, Switzerland
- * Correspondence: aurel.perren@pathology.unibe.ch (A.P.); ilia.marinoni@pathology.unibe.ch (I.M.)
- † Sharing last authorship.
- ‡ Sharing first authorship.



Citation: April-Monn, S.L.; Andreasi, V.; Schiavo Lena, M.; Sadowski, M.C.; Kim-Fuchs, C.; Buri, M.C.; Ketkar, A.; Maire, R.; Di Domenico, A.; Schrader, J.; et al. EZH2 Inhibition as New Epigenetic Treatment Option for Pancreatic Neuroendocrine Neoplasms (PanNENs). *Cancers* **2021**, *13*, 5014. <https://doi.org/10.3390/cancers13195014>

Academic Editor: Natalia S. Pellegata

Received: 14 September 2021

Accepted: 1 October 2021

Published: 7 October 2021

Publisher's Note: MDPI stays neutral with regard to jurisdictional claims in published maps and institutional affiliations.



Copyright: © 2021 by the authors. Licensee MDPI, Basel, Switzerland. This article is an open access article distributed under the terms and conditions of the Creative Commons Attribution (CC BY) license (<https://creativecommons.org/licenses/by/4.0/>).

Simple Summary: Pancreatic neuroendocrine neoplasms (PanNENs) represent 3% of pancreatic neoplasms. Available therapies can induce stable disease only for a minority of patients. Overall survival ranges from 10 years for well-differentiated neuroendocrine tumors to as little as 10 months for more aggressive carcinomas (NECs). It has been shown that epigenetic aberrations are relevant for the development and progression of PanNENs. We found that increased expression of the methyl transferase EZH2 correlated with higher tumor grade and advanced disease status. Inhibition of EZH2 in vitro reduced cell viability and proliferation of PanNEN cell lines as well as of patient-derived islet-like tumoroids. Similarly, inhibition of EZH2 in a PanNEN transgenic mouse model reduced tumor burden. Our data indicate that EZH2 inhibition should be further investigated/considered as an epigenetic treatment for patients with high-grade PanNENs.

Abstract: Pancreatic neuroendocrine neoplasms are epigenetically driven tumors, but therapies against underlying epigenetic drivers are currently not available in the clinical practice. We aimed to investigate EZH2 (Enhancer of Zest homolog) expression in PanNEN and the impact of EZH2 inhibition in three different PanNEN preclinical models. EZH2 expression in PanNEN patient samples ($n = 172$) was assessed by immunohistochemistry and correlated with clinico-pathological data. Viability of PanNEN cell lines treated with EZH2 inhibitor (GSK126) was determined in vitro. Lentiviral transduction of shRNA targeting EZH2 was performed in QGP1 cells, and cell proliferation was measured. Rip1TAG2 mice underwent GSK126 treatment for three weeks starting from week 10 of age. Primary cells isolated from PanNEN patients ($n = 6$) were cultivated in 3D as islet-like tumoroids and monitored for 10 consecutive days upon GSK126 treatment. Viability was measured continuously for the whole duration of the treatment. We found that high EZH2 expression correlated with higher tumor grade ($p < 0.001$), presence of distant metastases ($p < 0.001$), and shorter disease-free survival ($p < 0.001$) in PanNEN patients. Inhibition of EZH2 in vitro in PanNEN cell lines and in patient-derived islet-like tumoroids reduced cell viability and impaired cell proliferation, while

inhibition of EZH2 in vivo in Rip1TAG2 mice reduced tumor burden. Our results show that EZH2 is highly expressed in high-grade PanNENs, and during disease progression it may contribute to aberrations in the epigenetic cellular landscape. Targeting EZH2 may represent a valuable epigenetic treatment option for patients with PanNEN.

Keywords: pancreatic neuroendocrine neoplasms; EZH2 (Enhancer of Zest homolog); tumor treatment; epigenetic treatment; histone modification

1. Introduction

Pancreatic neuroendocrine neoplasms (PanNENs) represent 3% of pancreatic tumors. PanNENs are a heterogeneous group of neoplasms with varying clinical behaviour, ranging from indolent, low-grade pancreatic neuroendocrine tumors (PanNETs) to malignant, highly aggressive neuroendocrine carcinomas (NECs). The WHO 2019 classification separates PanNETs from PanNECs based on cellular differentiation, genetic patterns, and histo-morphological features. The grading system, based on the percentage of Ki67-positive, proliferating tumor cells, further separates PanNETs into G1, G2, and G3 [1]. While G1 PanNETs may have an overall survival (OS) of more than 10 years, OS for G2 PanNET is roughly 6 years [2]. On the other hand, high-grade PanNENs show worse survival outcomes, with patients diagnosed with NECs surviving less than 10 months [3].

Well-differentiated G1 and G2 PanNETs present mutations in *MEN1*, *DAXX*, and *ATRX* in almost 40% of patients, while 15% carry mutations in genes encoding members of the mTOR pathway [4,5]. PanNECs are frequently mutated in *KRAS*, *SMAD4*, and *TP53*, and they additionally often display a loss of Rb1 [6]. Clinical management of PanNETs and PanNECs is challenging. Medical treatment schedules for advanced and progressing PanNETs commonly include somatostatin analogues (SSAs) as first-line therapy and either Everolimus, Sunitinib, Temozolomide, Streptozocin, or peptide receptor radionuclide therapy (PRRT) as second-line treatments. (Pan)NEC patients typically receive platinum-based chemotherapy as first-line therapy [7]. Unfortunately, none of these therapies is able to induce stable disease in a predictable way. Therefore, better and more personalized treatments are urgently needed.

Recently, the importance of epigenetics for the development and progression of PanNETs has become evident [8]. *DAXX*, *ATRX*, and *MEN1* are all involved in chromatin structure remodelling and maintenance [9]. Additionally, loss of H3K36me3 and ARID1A (AT-Rich Interaction Domain 1A), a member of the SWI/SNF family, has been described in T3/T4 and metastatic PanNETs [10]. Chromatin structure organization is dictated by specific histone modification patterns, which in turn are tightly regulated by specific enzymes. Histone modifications are fundamental in maintaining cell identity and in regulating processes such as cellular differentiation. Alteration of histone modification patterns and their regulating enzymes have been widely described in different cancer types. Hence, targeting such modifications has become an attractive treatment option.

EZH2 (Enhancer of Zest homolog) is a histone-lysine N-methyltransferase enzyme and a member of the polycomb-group proteins. As catalytic subunit of the polycomb repressive complex (PRC2), it is responsible for the trimethylation (me3) of lysine 27 (K27) on histone 3 (H3) to promote gene silencing [11,12]. Notably, EZH2 is found highly expressed in stem cells and downregulated in adult tissues (reviewed in [11]). EZH2 and the PRC2 complex regulate the expression of several genes involved in cell differentiation. There are many downstream pathways possibly contributing to cell transformation dependent on EZH2 alteration. Indeed, EZH2 downstream targets include *CDKN2A*, E-cadherin, *FOXC1*, as well as DNA repair pathways [11]. Overexpression of EZH2 has been described in several cancer types and has been associated with poor prognosis and aggressive disease [13]. Given the evidence for EZH2 as a cancer driver, the development of EZH2-specific inhibitors has been an active area of investigation. Several EZH2 inhibitors have shown promising results

in vitro, and several clinical trials have been successfully conducted [14–16]. Here, we show that high EZH2 expression is associated with advanced status and high aggressiveness of disease in PanNENs. Inhibition of EZH2 in PanNEN cell lines and patient-derived islet-like tumoroids impaired cell proliferation in vitro. Similarly, treatment of Rip1TAG2 mice, a transgenic PanNEC mouse model, with EZH2 inhibitor reduced tumor burden.

Altogether, our findings suggest that EZH2 inhibition may represent a potentially promising treatment option, especially for high-grade PanNENs.

2. Materials and Methods

2.1. Patient Collective

Patient characteristics are shown in Table 1.

Table 1. Clinico-pathological features of patients submitted to surgery for pancreatic neuroendocrine neoplasms (PanNENs).

Variable	n = 172 (%)
Gender	
Male	92 (53)
Female	80 (47)
Age, years	59 (49; 69) *
Tumor function	
Non-functioning	140 (81)
Insulinoma	29 (17)
Gastrinoma	2 (1)
Glucagonoma	1 (1)
Tumor size, cm	3 (2.4; 4.1) *
T stage **	
T1–T2	103 (60)
T3–T4	68 (40)
N stage **	
N0	77 (46)
N1	67 (40)
Nx	24 (14)
M stage **	
M0	128 (75)
M1	43 (25)
Tumor grade	
NET G1	79 (46)
NET G2	78 (45)
NET/NEC G3°	15 (9)
Ki67, %	3 (1.5; 8) *
DAXX/ATRX **	
Negative	59 (36)
Positive	107 (64)

* Expressed as median (interquartile range). ** T stage missing (n = 1), N stage missing (n = 4), M stage missing (n = 1), DAXX/ATRX status missing (n = 6). n = 5 NET G3, n = 10 NEC G3.

The study was approved by the Swiss cantonal authorities (Kantonale Ethikkommission Bern, Ref.-Nr. KEK-BE 105/2015) and the Italian ethics commission (Comitato Etico, CE 252/2019). All patient materials were used according to the human research act and had signed an institutional form of broad consent. Immunohistochemistry was performed on PanNET next-generation Tissue Micro Arrays (ngTMAs), including for 129 patients that underwent surgery at the Inselspital, Bern, Switzerland, between 1990 and 2020 (reported in part in [17]) and 43 additional patients who underwent surgery at S. Raffaele Hospital,

Milan, Italy, between 2017 and 2020. All cases were reclassified according to WHO 2017 criteria [18]. TNM staging was based on the eighth edition of the UICC/AJCC [19].

In brief, 2.5 μm sections from ngTMAs or whole blocks were used for immunohistochemistry of EZH2 (1:50, Cell Signaling, 5246) and H3K27me3 (Dilution, Cell Signaling, C36B11). The immunostainings for all antigens were performed with an automated staining system (Leica Bond RX; Leica Biosystems, Nunningen, Switzerland). Antigen retrieval was performed by heating Tris30 buffer at 95 °C for 30 min. The primary antibodies were incubated for 30 min at the specified dilutions. Visualization was performed using a Bond Polymer Refine Detection kit, using DAB as chromogen (3,3'-Diaminobenzidine). EZH2 scoring was performed using QuPath software (open source software for digital pathology image analysis) by automatically counting the number of tumor cells expressing EZH2 [20]. The mean nuclear optical density was used to define positive and negative tumor cells. H3K27me3 staining was scored as negative, heterogeneous, and positive. For both EZH2 and H3K27me3 scorings, only nuclear staining was considered positive. DAXX and ATRX immunohistochemistry were performed as previously described [17].

2.2. Cell Culture

The BON1 cell line was provided by E.J. Speel, Maastricht, Netherlands, in 2011. The QGP1 cell line was purchased from the Japanese Health Sciences Foundation, Osaka, Japan, in 2011. The NT3 cell line was a kind gift from J. Schrader and cultured as described [21]. Short tandem repeat (STR) analysis by PCR was performed for all cell lines (QGP1 in 2011, 2016, and 2020; BON1 in 2014, 2016, and 2020; NT3 in 2018 and 2020). QGP1 cells were authenticated. A BON1 and NT3 profile does not exist yet, but the profile of these cells did not match any known profile of cancer cell lines, thus excluding contamination from other lines. In addition, expression of the specific neuroendocrine markers chromogranin A and synaptophysin was routinely tested by IHC. For NT3, the cell culture flasks were coated with collagen IV for better attachment of the cells. BON1 cells were cultured in DMEM/F12 medium (Sigma), whereas QGP1 and NT3 cells were cultured in RPMI 1640 medium (Sigma). For all cell lines, the medium was supplemented with 10% FBS, 100 IU/mL penicillin, and 0.1 mg/mL streptomycin, and cells were kept in a humidified incubator at 5% CO₂ and 37 °C. Additionally, growth factors EGF (Gibco PHG0314) and FGF2 (Gibco PHG0024) were added to NT3 growth medium. After thawing, cells were cultured for approximately two months.

2.3. In Vitro Drug Treatment

2.3.1. MTT Assay

For treatment with GSK126 (Selleckchem), cells were plated in 96 wells and treated with 0.62 μM , 2.5 μM , 6.255 μM , and 12.5 μM , 25 μM , 25 μM , and 100 μM of GSK126 diluted in DMSO. Control cells were treated with 0.5% DMSO. The cells were incubated with 100 μL 10% MTT solution at 37 °C in 5% CO₂ for 40 min. After MTT removal, 200 μL of DMSO and 25 μL of Sorensen solution were added to lyse the cells. The intensity of the color was measured as absorbance at 570 nm on a Microplate Reader (SpectraMax, Molecular Devices, San Jose, CA, USA).

2.3.2. IncuCyte Real-Time Cell Confluence

Real-time cell proliferation as a function of cell confluence was measured by live microscopy with an IncuCyte S3 system (Essen BioScience, Newark, NJ, USA). BON1 and QGP1 cells were seeded in their respective cell culture medium at 5000 cells/well in 96-well Essen ImageLock™ plates (Essen BioScience, Newark, NJ, USA). After 48 h of culture, cells were treated in technical replicates ($n = 3$) with vehicle control (DMSO) or indicated concentrations of GSK126; plates were transferred to the IncuCyte S3 system, and images were acquired every 2 h for 4 days with a 10 \times objective. Measurements were normalized to the mean confluence (~25%) of all wells at $t = 0$. Representative images for $t = 48$ h are shown in Figure S2A (see also the Supplementary Materials).

2.4. Western Blotting

Non-histone proteins were extracted using RIPA buffer, and protein concentrations were measured using the Bradford assay. Histones were extracted using an acid extraction protocol. After washing with PBS, cells were scraped off in 30 μ L 0.4 M HCl and incubated on ice for 30 min with intermittent vortexing. The lysates were centrifuged at 10,000 rpm for 10 min at 4 °C. Supernatant was collected. To this, 360 μ L of ice-cold acetone was added and the tubes were kept at –20 °C overnight. The day after, lysates were centrifuged at 10,000 rpm for 10 min at 4 °C. The acetone containing supernatant was discarded and the histone-enriched pellet was resuspended in 30 μ L 4 M urea + Pi buffer. Protein concentration was measured using the Bradford assay. Histones were loaded onto precast gradient gels (4–15%) from Biorad (#4568085). Non-histone proteins were loaded onto gels (12%) made as per the manufacturer's instructions by mixing stacker and resolver solutions from Biorad (#1610180). After running, gels were activated in a Biorad Chemidoc MP system. Transfer was done on to PVDF membranes using a Trans Blot Turbo system from Biorad at 1.3A, 25 V, for 7 min. Post-transfer, total proteins were imaged with a Biorad Chemidoc MP system. After 1 h blocking, incubation with primary antibodies was performed overnight at 4 °C, followed by washing steps and incubation with secondary antibodies (DyLight 650 conjugate goat anti-rabbit and DyLight 550 conjugate goat anti-mouse (ImmunoReagents) and peroxidase-conjugated AffiniPure donkey anti-rabbit and donkey anti-mouse (Jackson ImmunoResearch)) for 1 h at room temperature. Chemiluminescent or fluorescent signals were detected using a ChemiDoc MP System (Biorad). Total protein expression for quantification of specific protein expression was measured by use of the stain-free gel technology and imaged with the Chemidoc MP System [22]. The primary antibodies EZH2 (1:1000, Cell Signaling, 5246), H3K27me3 (1:2000, Cell Signaling 9733), H3 total (1:5000 Abcam ab12079), and GAPDH (1:5000, Millipore MAB 374) were diluted in 5% BSA-TBST. Band intensity was measured using ImageJ and the area size calculation tool of the plotted lane (square pixel).

2.5. EZH2 Silencing

Short hairpin RNA (shRNA) against EZH2 (TRCN0000040074, TRCN0000040075), as well as a nontargeting shRNA control (SHC002), were delivered with a lentivirus expressing vector pLKO.1 (all from Sigma, MISSION shRNA). Lentivirus production and transduction were performed as described previously [23]. Cells were selected with 1.5 μ g/mL puromycin for 3–4 days. Knockdown efficiency was validated by immunoblotting of respective proteins.

2.6. In Vivo Experiments

Rip1TAG2 (C57BL/6) mice were kindly provided by G. Christofori (Basel, Switzerland). All experimental protocols were reviewed and approved by the Cantonal Veterinary Office of Bern (Bern, Switzerland). Mice were fed with food enriched in glucose starting from 10 weeks of age. Vehicle control (20% Captisol in sterile H₂O) and GSK126 (100 mg/kg, ST061, Selleckchem) was administrated daily by i.p. injection for three weeks. GSK126 stock was dissolved in 20% modified cyclodextrin (Captisol[®], LGND, USA) and sterile H₂O. In brief, Captisol was acidified to pH 4 using 1N acetic acid before adding GSK126 stock solution. The drug solution was stirred for two hours at 4 °C using sterile magnets. The solution was then sonicated for 1 min at 40% amplitude at 37 °C in an ultrasonic water bath, ensuring temperature did not exceed 40 °C. The final drug solution was adjusted to pH 4.5 using 1N acetic acid. After i.p. application (200 μ L per 20 g body weight), animal health status was monitored daily. At 13 weeks of age, animals were sacrificed and dissected. Tumor numbers (>1 mm) were counted by visual inspection. The tissues were then fixed in formalin overnight and embedded in paraffin. FFPE tissue was used for tumor burden quantification/assessment using QuPath software [20]. Digital-scanned consecutive IHC tissue sections were first pre-processed in the built-in visual stain editor using default settings for estimation of stain vectors. Total tumor area and all areas containing endocrine

(islet) cells were manually annotated and verified by a board-certified pathologist (SL. M.) on the first H&E tissue slide. These annotations were transferred onto (all) consecutive tissue slides for consistency. A watershed cell segmentation followed by positive cell detection was performed using customized/optimized parameters and individual thresholds for each specific IHC staining. Detection results were extracted from QuPath and imported into R environment for data analysis.

2.7. Primary Cells Treatment

For primary cell isolation, viability measurement, micro-cell block manufacture, and quantification, we followed the described protocol [24]. Fresh human PanNET tissue was obtained from patients diagnosed with PanNETs undergoing surgery at the Inselspital Bern, Switzerland, or at the Pancreatic Surgery Unit, Pancreas Translational and Clinical Research Center, San Raffaele Scientific Institute, Milan, Italy, as previously described [24]. Cryopreserved tumor tissues of six PanNET patients were used for in vitro drug screening. Patient characteristics are summarized in Table 2.

Table 2. Patient characteristics of treated islet-like tumoroids.

Patient	Gender	Age	Grade	Ki67	Stage	DAXX/ATRX	EZH2	Tumor Site	In Vitro Sensitivity
mP029	Female	55	NET G2	4%	II	Lost	6.3%	Primary	+
mP040	Female	55	NET G2	10%	II	Preserved	3%	Primary	+++
mP044	Female	18	NET G2	18%	III	Lost	1.3%	Primary	+
mP055	Female	69	NET G2	8%	III	Lost	0.3%	Primary	+
aP321	Male	66	NEC G3	50%	IV	Lost	23%	Liver metastasis	++
aP476	Male	65	NET G2	15%	IV	n.a.	0%	Liver metastasis	+++

NET, neuroendocrine tumor; NEC, neuroendocrine carcinoma; n.a., not available; + lower sensitivity; ++ intermediate sensitivity; +++ higher sensitivity.

2.7.1. Primary Cell Culture

Isolated primary PanNET cells were maintained in AdvDMEM + GF medium (DMEM-F12, 5% FBS, Hepes 10 mM, 1% L-glutamine (200 mM), 1% penicillin (100 IU/mL), 1% streptomycin (0.1 mg/mL), 1% amphotericin B (0.25 mg/mL) (Merck, Switzerland), 20 ng/mL EGF, 10 ng/mL bFGF (Thermo Fisher Scientific, USA), 100 ng/mL PIGF, 769 ng/mL IGF-1 (Selleckchem, USA)) and in 24-well Corning® Costar® ultra-low attachment (ULA) plates (Corning, USA) (500 µL/well, 3–5 × 10⁵ cells/well) in a humidified cell incubator (21% O₂, 5% CO₂, 37 °C). For drug screening, cells were resuspended in fresh AdvDMEM + GF medium supplemented with 123 µg/mL growth-factor-reduced Matrigel® (Corning, USA) and plated in 96-well ULA plates (50 µL/well, 3–4 × 10³ cells/well).

2.7.2. Primary Cell Isolation and Culture

Cells were isolated and cultured as previously reported [24]. In brief, washed pieces of 1 mm³ were dissociated in digestion medium (10 mg/mL collagenase IV (Worthington, USA), 0.25% Trypsin-EDTA (Sigma-Aldrich, Switzerland), and 0.2 mg/mL DNase (Roche, Switzerland) in advanced DMEM-F12, Hepes 10 mM, 1% L-glutamine, 1% penicillin-streptomycin-amphotericin B) using a gentle MACSTM dissociator (Miltenyi Biotec, Switzerland). Cells were filtered through a 70 µm strainer to remove collagen debris, and red blood cells were lysed with ACK lysis buffer (Thermo Fisher, Scientific, USA). After mechanical fibroblast removal and single-cell dissociation, cells were resuspended and maintained in AdvDMEM + GF medium. After 2 days of recovery phase, cells were counted and resuspended in fresh AdvDMEM + GF medium supplemented with growth-factor-reduced Matrigel and plated in 96-well ULA plates (3–4 × 10³ cells/well).

2.7.3. Viability Measurement in Islet-Like Tumoroids

The RealTime-Glo™ MT Cell Viability (RTG) assay (Promega, Switzerland) was used to continually monitor cell viability of 3D human primary PanNET cultures. The RTG

assay was performed according to the manufacturer's instructions, and luminescence was measured in an Infinite[®] 200 PRO plate reader (Tecan, Switzerland).

2.7.4. Micro-Cell-Blocks (MCBs) from Islet-Like Tumoroids

Islet-like tumoroids corresponding to $3\text{--}5 \times 10^4$ cells were collected (either directly on the day of isolation (D0) or from the 96-well ULA plate at the end of drug screening (D12)). Cells were captured in plasma-thrombin clots and fixed, counterstained with Hematoxylin, and embedded in paraffin. The, 2.5- μm -thick serial sections were stained as described above. Scans were acquired with a Panoramic 250 (3DHitech, Hungary) automated slide scanner at $20\times$ magnification. Images were acquired using QuPath software [20].

2.7.5. Curve Fitting and Drug Sensitivity Data

Drug-response curve data consisted of six to nine DMSO-positive controls, six no-cell-negative controls, and five drug-response points. A 5-point, 625-fold concentration range was used to calculate reliable absolute IC₅₀ values [25]. For IC₅₀ calculation, RLU values from a 7 day treatment were weighted and normalized using 6 h RTG-baseline measurements for each well, as described earlier [24]. Data points were fitted in a four-parameter linear (4PL) regression model with two constraints, Top = 100% and Bottom = 0%, to estimate the corresponding IC₅₀ [26,27]. Visualization was performed in R environment.

2.8. Correlation and Survival Analysis

Statistical analyses were performed with GraphPad Software. Unpaired or paired t-tests were used to compare groups. When the normality assumption was not met, the Mann–Whitney test or Kruskal–Wallis test were used to compare continuous variables between groups. Contingency tables were analyzed using Fisher's exact test. Cut-offs to define low, intermediate, and high EZH2 expression were defined using the median and the third quartile of EZH2 distribution as a continuous variable. Survival probability was estimated according to the Kaplan–Meier method. The log-rank test was used to compare disease-free survival between EZH2 categories. Sample size (n) refers to biological replicates unless otherwise stated. *, $p < 0.05$; **, $p < 0.01$; ***, $p < 0.001$; ****, $p < 0.0001$.

3. Results

3.1. EZH2 Expression in PanNEN Correlates with Advanced Disease Status and Features of Aggressiveness

To evaluate the expression of EZH2 in PanNEN tissues we performed immunohistochemistry (IHC) on a tumor microtissue collective of 172 patients who underwent surgery for PanNENs (Table 1).

As shown in Figure 1A, EZH2 expression in PanNENs was highly heterogeneous. The percentage of EZH2-positive tumor cells was scored for each patient. Based on EZH2 positivity, the samples were then divided in three categories, using the median (1.5%) and the third quartile (3%) of EZH2 distribution as cut-offs: $<1.5\%$ of positive tumor cells (EZH2^{low}); $1.5\% \leq x \leq 3\%$ of positive tumor cells (EZH2^{intermediate}); and $>3\%$ of positive tumor cells (EZH2^{high}). In 79% of PanNENs ($n = 136/172$), the percentage of tumor cells positive for EZH2 was $\leq 3\%$. Only 21% of tumors ($n = 36/172$) showed a percentage of EZH2-positive tumor cells $>3\%$. No significant differences in terms of EZH2 expression were observed according to the time of surgery ($p = 0.590$). In agreement with EZH2 function in regulating genes involved in cell cycle, EZH2 expression correlated with the Ki67 proliferative index ($p < 0.001$). Median Ki67 progressively increased across EZH2 categories, ranging from 1.5% (IQR 1; 4%) in samples with EZH2^{low} to 3.5% (IQR 1.5; 7%) in samples with EZH2^{intermediate} and up to 15% (IQR 5; 40%) in samples with EZH2^{high} (Figure S1A). When functioning tumors ($n = 32/172$) were excluded, the correlation between EZH2 expression and Ki67 proliferative index remained statistically significant (EZH2^{low}: median Ki67 2% (IQR 1; 4%), EZH2^{intermediate}: median Ki67 5% (IQR 2; 9.5%), EZH2^{high}: median Ki67 15% (IQR 7.5; 45%), $p < 0.001$). In line with this—as reported in other

tumor types—increased EZH2 expression was significantly associated with a higher tumor grade ($p < 0.001$). G1 PanNETs were the most represented group within the EZH2^{low} category ($n = 55/80, 69\%$), whereas G2 PanNETs were prevalent when EZH2 expression was intermediate ($n = 32/56, 57\%$) or high ($n = 21/36, 58\%$), as depicted in Figure 1B. A significant association between EZH2 expression and tumor grade was confirmed after exclusion of patients with functioning neoplasms ($p < 0.001$). Overall, 14 out of 15 G3 PanNENs showed positivity for EZH2 in >3% of tumor cells (Figure 1B). Indeed, we observed that PanNECs had >60% EZH2-positive cells in the majority of cases. Additionally, using publicly available RNA-sequencing data, we confirmed in silico that *EZH2* gene expression is higher in G2 and G3 tumors compared to G1 [5] (Figure 1C).

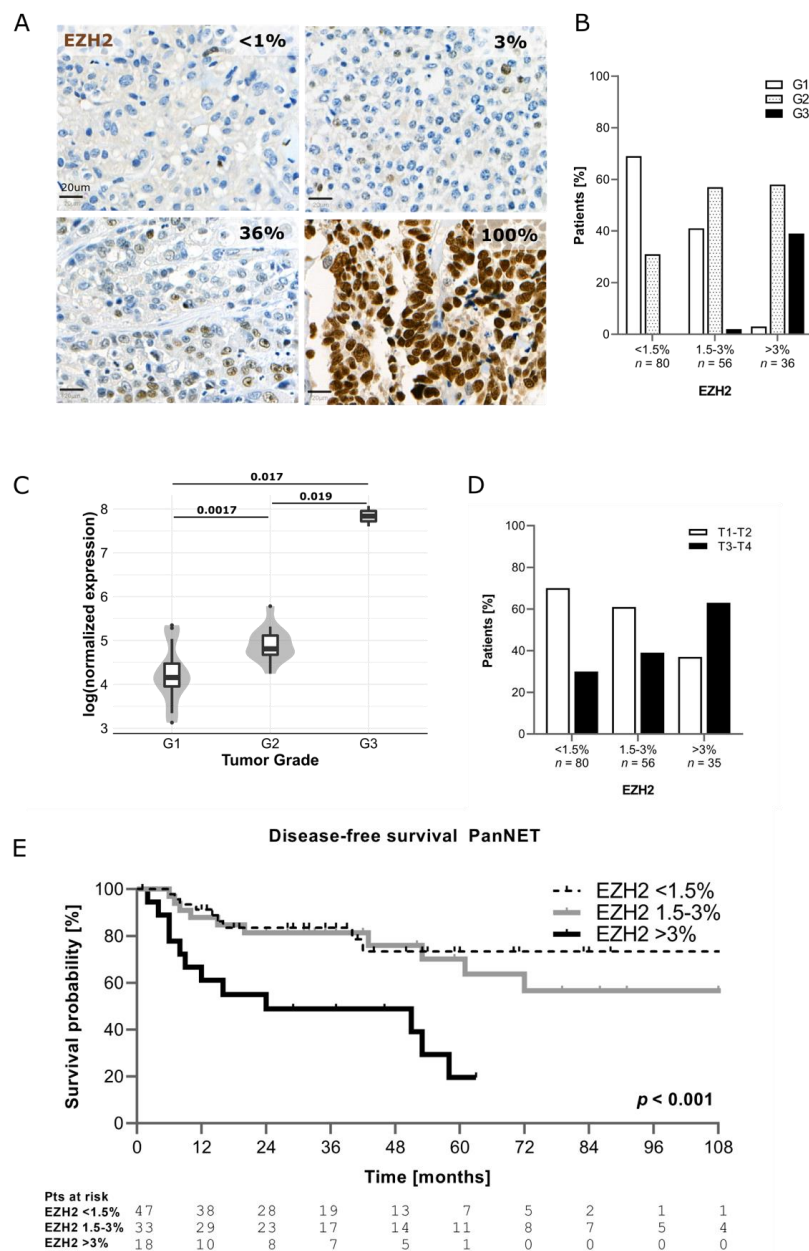


Figure 1. (A) Example of EZH2 expression in human tissue. (B) Correlation between EZH2 expression and tumor grade. (C) Correlation between EZH2 mRNA level and grade (data from Scarpa et al. 2017). (D) Correlation between EZH2 and T stage (T stage missing ($n = 1$)). (E) Comparison of disease-free survival between patients with low, intermediate, and high EZH2 expression (only PanNETs were included).

Significantly higher protein expression of EZH2 was also observed for patients with T3–T4 tumor stage compared to those with T1–T2 ($p = 0.004$) as well as in presence of nodal ($p = 0.008$) and distant metastases ($p < 0.001$) (Table 3 and Figure 1D).

Table 3. Correlation between EZH2 expression and clinico-pathological features.

Variables	EZH2 <1.5% <i>n</i> = 80	EZH2 1.5–3% <i>n</i> = 56	EZH2 >3% <i>n</i> = 36	<i>p</i>
T Stage				0.004
T1–T2	56 (70)	34 (61)	13 (37)	
T3–T4	24 (30)	22 (39)	22 (63)	
N stage				0.008
N0	39 (50)	28 (51)	10 (29)	
N1	24 (30)	21 (38)	22 (65)	
Nx	16 (20)	6 (11)	2 (6)	
M stage				<0.001
M0	70 (88)	41 (73)	17 (49)	
M1	10 (12)	15 (27)	18 (51)	
DAXX/ATRX				0.014
Preserved	57 (74)	34 (63)	16 (46)	
Lost	20 (26)	20 (37)	19 (54)	

T stage missing ($n = 1$), N stage missing ($n = 4$), M stage missing ($n = 1$), DAXX/ATRX status missing ($n = 6$).

Patients with EZH2^{high} showed distant metastases in 51% ($n = 18/35$) of cases compared to 12% ($n = 10/80$) of patients with EZH2^{low}. Interestingly, higher EZH2 positivity was found in samples negative for DAXX/ATRX ($p = 0.014$) (Table 3).

Follow-up data were available for 105 patients ($n = 98$ PanNETs, $n = 7$ PanNECs) and the median follow-up was 37 months (IQR 18–60 months). The recurrence rate in the whole study cohort was 30% ($n = 32/105$). Patients with EZH2^{high} showed also a shorter disease-free survival compared to those with EZH2^{low} and EZH2^{intermediate} ($p < 0.001$) (Figure 1E). Patients with EZH2^{low} and EZH2^{intermediate} showed better DFS compared to those with EZH2^{high} ($p = 0.016$), and also after excluding patients with functioning neoplasms ($n = 32$). This statistically significant difference in survival was also observed when patients with NECs were included in the analysis, as shown in (Figure S1B). No significant differences in H3K27me3 levels were observed between the different categories (Figure S1C).

3.2. Inhibition of EZH2 in PanNEN Reduced Cell Viability and H3k27me3 Levels

Given the expression of EZH2 in PanNEN and especially its higher expression in PanNEC patient samples, we investigated if pharmacological inhibition of EZH2 would impair cell growth and induce cell death in vitro. To this purpose, we first measured EZH2 protein expression in three PanNEN cell lines, BON1, QGP1 (both with mutations indicative of PanNECs), and NT3 (from a high-grade G2 PanNET), by Western blotting (Figure 2A). As expected from their origins, BON1 and QGP1 expressed high levels of EZH2, while it was expressed at lower levels in NT3 cells. Next, we pharmacologically targeted EZH2 with the competitive inhibitor GSK126. Monitoring of proliferation as a function of cell confluence in real-time revealed that GSK126 inhibited growth of QGP1 and BON1 cells in a dose-dependent manner (Figure 2B), with cell clusters being visibly smaller and containing fewer cells after 48 h of treatment (Figure S2A). After longer treatment periods and at higher GSK126 doses (25 μ M and 50 μ M), cells showed morphological signs of apoptotic cell death (loss of cell–cell contacts, membrane blebbing, cell shrinkage; data not shown and Figure S2A,B). Since loss of epigenetic activity might require longer treatment periods to establish a cellular phenotype, we measured cell viability using MTT assays after 3 and 6 days. As shown in Figure 2C, all three cell lines showed a decrease in cell viability in a dose- and time-dependent manner. All three cell lines displayed similar sensitivities to different drug concentrations with similar IC50 values: 18.0 μ M (BON1),

23.1 μM (QGP1), and 15.4 μM (NT3) for 3 days and 8.0 μM (BON1), 15.8 μM (QGP1), and 5.8 μM (NT3) for 6 days of treatment, respectively.

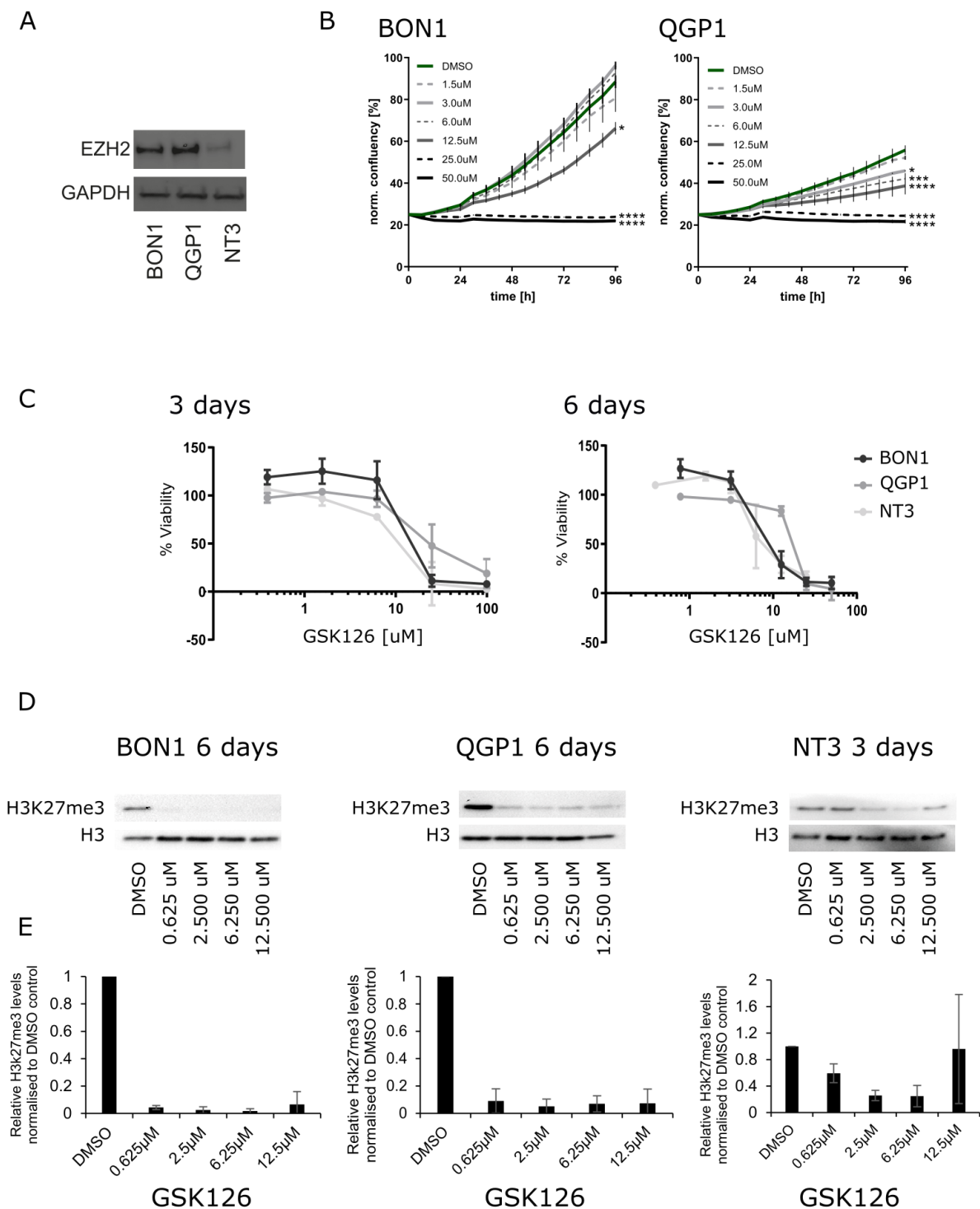


Figure 2. (A) Western blotting of EZH2 expression in PanNET cell lines: BON1, QGP1, and NT3. (B) IncuCyte S3 proliferation analysis of BON1 and QGP1 cells treated for 96 h with vehicle control (DMSO) and the indicated concentrations of GSK126. This is a representative result of two independent experiments. (C) MTT assays after EZH2 treatment with 0.62 μM , 2.5 μM , 6.255 μM , 12.5 μM , 25 μM , and 100 μM of GSK126 after 3 and 6 days. (D) Representative Western blotting of H3k27me3 after 6 days of treatment with 0.62 μM , 2.5 μM , 6.255 μM , and 12.5 μM GSK126 in BON1 and QGP1 and 3 days for NT3. (E) Quantification of H3K27me3 levels normalized to H3 total based on three replicates.

Thus, our data demonstrate that EZH2 inhibition with GSK126 is cytotoxic in PanNEN cells *in vitro*. In order to confirm that GSK126-mediated cytotoxicity was associated with loss of EZH2 methyltransferase activity, we quantified the tri-methylation levels of EZH2's histone downstream target, H3K27 (H3K27me3), after GSK126 treatment by Western blotting. We confirmed that H3K27me3 levels of QGP1 and BON1 cells were significantly and equally decreased by all tested concentrations of GSK126 in BON1 and QGP1 after 6 days of GSK126 treatment (Figure 2D,E). Due to a low number of NT3 cells and insufficient protein quantity after six days of GSK126 treatment, H3K27me3 levels in NT3 were assessed after three-day treatment only. However, this showed a significant reduction of H3K27me3 levels in a dose-dependent manner (Figure 2D,E). Together, these data demonstrate that EZH2 inhibition by GSK126 reduced its methyltransferase activity and affected cell viability in PanNEN cells *in vitro*.

3.3. Silencing of EZH2 in High-Grade PanNEN Cell Lines Impaired Cell Growth

To rule out any off-target effects from pharmacological GSK126 treatment, we silenced EZH2 by lentiviral transduction in the high-grade PanNEN cell line QGP1. Cells were transduced using lentivirus vectors of two different shRNA (40074 and 40075) and one scrambled shRNA control. ShRNA 40074 was less efficient than the shRNA 40075 and induced an EZH2 knockdown of 43% at day one and 29% at day seven of selection, respectively, while shRNA 40075 induced a knockdown of 70% at day one, which was reduced to 54% at day seven (Figure 3A). The downregulation was confirmed by IHC on cell blocks as well (data not shown). To investigate the role of EZH2 depletion on cell growth, we produced a growth curve using the MTT assay for 4 days after selection. Cells transduced with Sh-40075 showed an almost complete stop of proliferation, while cells transduced with Sh-40074 grew at a reduced rate when compared to scrambled controls (Figure 3B). Notably, the inhibition of proliferation was proportional to the efficiency of the knockdown. Altogether, these results strongly support a critical role for EZH2 in promoting cell survival and proliferation in high-grade PanNEN cell lines.

3.4. Anti-EZH2 Treatment of Rip1TAG2 Mice Reduced H3K27me3 Levels and Tumor Burden

Following up on this, we assessed the therapeutic effect of EZH2 inhibition *in vivo* in the Rip1TAG2 mouse model [28]. In this model, the simian virus 40 (SV40) large T-antigen (Tag) oncogene is expressed under the control of the rat insulin gene promoter (Rip), leading to multifocal development of insulin-producing β -cell carcinomas (insulinoma) in the islets of Langerhans in the pancreas [28]. Effects of EZH2 inhibition *in vivo* were assessed by comparing GSK126-treated mice ($n = 6$, 3F/3M) with littermate control mice ($n = 6$, 3F/3M) over the time course of three weeks starting from 10 weeks of age (Figure 3C). Consecutive formalin-fixed paraffin-embedded (FFPE) sections from resected pancreas were analyzed by a pathologist (SL. M.), and islets were annotated as normal islets (Ns), proliferative islets (PIs), hyperplastic islets (HPs), and tumors (Ts) (adapted from [29]) (Figure S3A). IHCs were quantified digitally using QuPath software. In this model, we observed an increase in EZH2 expression along different stages of tumorigenesis (Figure 3D). Inhibition of EZH2 decreased trimethylation of H3K27 in proliferative and hyperplastic islets as well as tumors, confirming the on-target effect of GSK126 (Figure S3B,C). We detected an unexpected but slight decrease in EZH2 expression in hyperplastic islets and tumors in treated mice, but the expression levels remained high in abnormal islets of both treated and untreated mice (Figure 3D and Figure S3B,C). We observed a significant reduction in tumor burden in GSK126-treated mice ($p = 0.00039$) (Figure 3E) and a tendency towards a reduction of the number of tumors (Figure S3D). No differences in the Ki67 percentage of positive cells and cleaved caspase 3 were detected (Figure S3E).

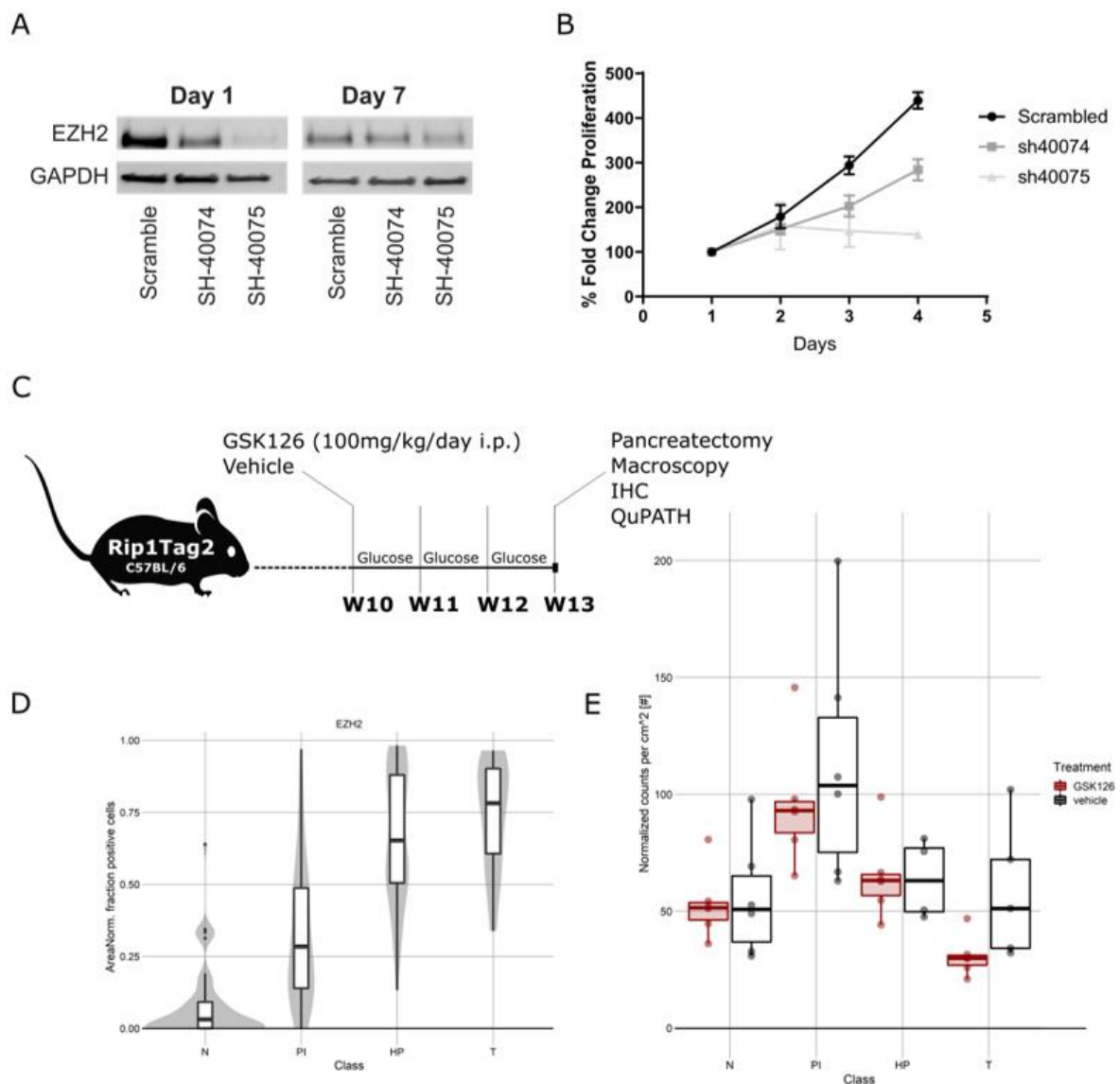


Figure 3. (A) Representative Western blot of EZH2 knockdown in QGP1 cells with SH40074, SH40075, and scrambled controls at 1 and 7 days after transduction. (B) Growth curve after transduction with SH40074, SH40075, and scrambled controls in QGP1. (C) Schematic representation of treatment of Rip1TAG2 mice. (D) EZH2 expression in Rip1TAG2 mice at different tumor stages: normal islet (N), proliferative islets (PI), hyperplastic islet (HP), and tumor (T). (E) Tumor burden in mice treated with EZH2 inhibitor and vehicle daily for 3 weeks from 10 weeks of age. Mice treated with EZH2 inhibitor presented a reduced tumor burden.

3.5. Treatment of Patient-Derived PanNET Tumoroids with EZH2 Inhibitors Reduced Cell Viability

Although EZH2 is highly expressed in PanNECs, we found that a subset of G2 PanNETs also express EZH2, albeit at a lower level. To assess if EZH2 inhibition may be a therapeutic option for PanNET patients, we treated patient-derived islet-like tumoroids isolated from six PanNET patients (two liver metastases and four primary tumors) with EZH2 inhibitor (GSK126) using our previously reported screening pipeline [24]. Patient characteristics are summarized in Table 2. Islet-like tumoroids were treated with GSK126 in a five-point, 625-fold concentration treatment scheme (0.06 μ M, 1.60 μ M, 0.32 μ M, 8.00 μ M, and 40 μ M). Tumoroids from different patients showed distinctive drug sensitivities (Figure 4A and Table 2).

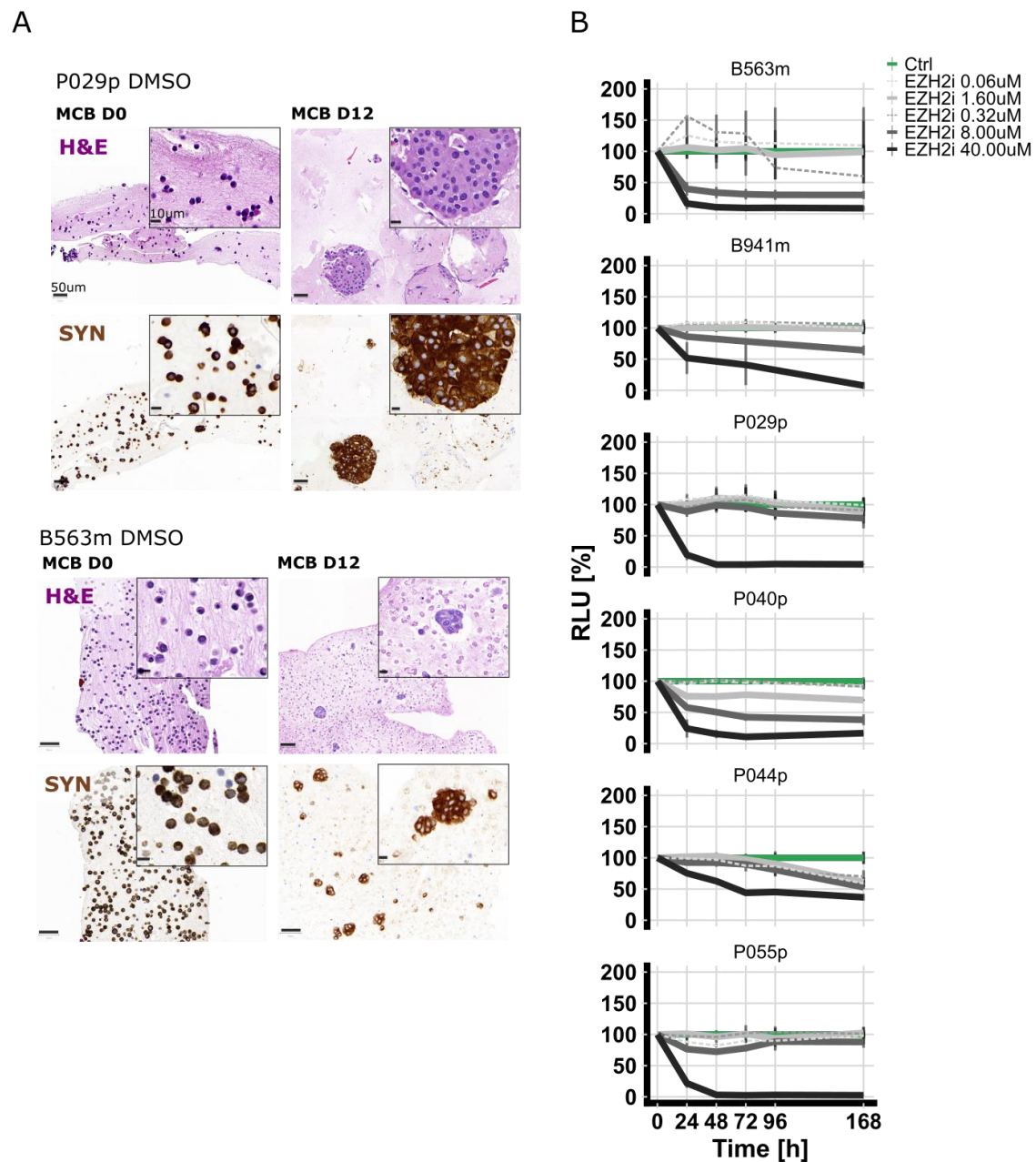


Figure 4. (A) In vitro viability curves using the metabolic surrogate assay RealTime-Glo (RTG) in 3D human primary PanNET culture treated with DMSO (control (Ctrl)) and GSK126 for 7 days. Data were first normalized per-well using a RTG baseline measurement for each individual well and then normalized to the average of the corresponding DMSO control of the respective day. Data represent means \pm SEM ($n = 1$ per patient, three technical replicates). RLU, relative luminescence unit. (B) Micro-cell-block of two representative samples. IHC of synaptophysin and H&E staining of samples from the day of isolation and DMSO-treated samples 12 days post-isolation.

Micro-cell-blocks of two representative islet-like tumoroids *before* and *after* treatment are shown in Figure 4B. To correlate the response measured in vitro with EZH2 expression of the corresponding tissue of origin, we performed IHC. EZH2 staining was scored as described above. EZH2 expression was low (<1.5% of positive tumor cells), intermediate ($1.5\% \leq x \leq 3\%$ positive tumor cells), and high (>3% of positive tumor cells) in the two remaining cases (Figure S4). No clear correlation was observed between EZH2 expression in the tumor tissue and drug sensitivity; however, the sample number was relatively small.

4. Discussion

In this work we demonstrated that a subset of PanNENs expressed EZH2 and that its expression highly correlated with higher tumor grade and disease stage. We showed that inhibition of EZH2 *in vitro* and *in vivo* in PanNEC and PanNET models reduced growth, cell survival, and tumor burden. Altogether, our results suggest that EZH2 inhibition may be a novel epigenetic treatment option for PanNEN patients.

PanNET development seems to be mainly driven by epigenetic changes; several lines of evidence demonstrated a possible progressive accumulation of epigenetic aberrations along PanNET expansion [8–10]. Epigenetic changes involve histone and DNA modifications, which can result in profound phenotypic changes. These epigenetic events are inherently reversible; hence, targeting such modifications in cancer has become a promising option. A plethora of drugs targeting specific enzymes responsible for histone modifications, such as methylation, acetylation, or phosphorylation, are either already in the clinics or in clinical trials, and many others are in preclinical development [30–32]. Targeting EZH2 is among one of the most promising epigenetic therapies in cancer treatment but has not yet been evaluated in PanNEN [14–16].

We found that EZH2 is particularly highly expressed in PanNECs and G3 PanNETs, with lower expression being present in G2 and G1 PanNETs. Based on these observations, we explored the option of treating both PanNECs and PanNETs with EZH2 inhibitor GSK126, using different *in vitro* and *in vivo* models.

EZH2 is expressed in many cancer types in correlation with advanced disease stage and high proliferation index [33]. Indeed, EZH2 expression is regulated by the pRB-E2F pathway, and it has been shown to be critical for cell replication. Hence, EZH2 is universally recognized as a marker of proliferation and a *bona fide* oncogene [34]. This is in agreement with our observation that EZH2 expression is highly correlated with Ki67 positivity in PanNENs. In a small study including 30 patients, increased EZH2 expression was described in human PanNETs with synchronous metastases compared to those with metachronous ones. However, no correlation with tumor grade was reported [35].

The EZH2 locus was found amplified in a subset of insulinomas, and overexpression of EZH2 was reported to induce replication of human beta cells as well as other normal islet cells [36]. In mouse models, EZH2 epigenetically represses CDKN2A/p16INK4A in pancreatic beta cells, and it is required for beta cell proliferation in juvenile mice [37].

Our results suggest a crucial role for EZH2 in mediating PanNEN cell proliferation. Silencing of EZH2 in PanNET cells by EZH2 inhibitor or siEZH2 showed a strong reduction in cell proliferation. This cytostatic effect most likely occurred via cell-cycle arrest, since it has been shown previously that gene silencing of EZH2 in cancer cell lines stopped proliferation and increased the number of cells in G1 and G2 [34]. EZH2 inhibition in PanNEN cell lines and in Rip1TAG2 mice resulted in reduction of global H3K27me3 levels, likely releasing the H3K27me3 gene repression at certain loci. Since GSK126 is highly selective, EZH2 methyltransferase-inhibition (see Selleckchem REF#S7061) off-target effects via other human methyltransferases are unlikely. However, due to EZH2's diverse molecular functions—from our data—we cannot delineate the exact mode of action. In PanNEN cell lines we noticed a reduction of H3K27me3 levels already at GSK126 dosages that showed no obvious impact on cell viability or proliferation, suggesting that other EZH2 effector functions might be relevant as well. Indeed, besides H3K27me3, the PRC2 complex methylates non-histone protein substrates as well. In addition, EZH2 via a PRC2-independent function methylates or directly interacts with other proteins, activating downstream pathways [33]. Via these three different mechanisms, EZH2 works as a hub for several pathways that are crucial for cancer development, such as cell-cycle progression, autophagy, apoptosis, DNA repair cell development, and lineage differentiation [33]. The lack of correlation between H3K27me3 and EZH2 expression in human tissue suggests that EZH2 may indeed function independently from PRC2 in PanNENs.

EZH2 expression in PanNENs increased with tumor grade and the majority of PanNECs showed positivity in more than 60% of tumor cells. Given the high percentage of

EZH2-positive cells in PanNECs, EZH2 inhibition may represent a promising therapeutic strategy for these tumors for which no targeted treatment is currently available.

In support of this, we found that EZH2 inhibition in Rip1TAG2 mice reduced tumor burden. Rip1TAG2 mice present with tumors that share similarities with human PanNECs in terms of morphology and aggressiveness [28]. Due to the transgenic large T-antigen, both P53 and RB are inactivated, similarly to PanNECs, which often present with *TP53* mutation and RB loss [28]. While we could see a reduction in tumor burden, we did not find clear changes in Ki67 and caspase-3, leaving open some questions on how EZH2 inhibition impairs tumor progression. While we observed reduction in tumor burden, we also observed a trend towards a reduction in the number of tumors. EZH2 expression in RipTag2 tumors increased with tumor size and animal age, suggesting that EZH2 inhibition may affect growth of late-stage tumors with higher EZH2 expression rather than of early-stage and small tumors. Similarly, EZH2 inhibition has been shown to reduce tumor burden and tumor growth in several preclinical models, such as lung cancer and lymphoma mouse models [38,39]. Interestingly, we found that low-grade PanNETs also express EZH2, albeit at lower levels. We recently established a protocol for cultivating patient-derived PanNET cells from fresh- and cryopreserved tumor tissue, which allows drug screening *ex vivo* [24]. Using this model, we tested the EZH2 inhibitor GSK126 on PanNET patient samples. Interestingly, we observed differences in GSK126 sensitivity among patients, suggesting a specific patient effect, despite lower EZH2 levels in lower grade PanNETs. These results suggest that EZH2 inhibition can also be relevant for the treatment of a subset of low-grade PanNETs, possibly in combination with other therapies.

Increasing evidence has recently demonstrated that EZH2 inhibition in combination with other treatments potentiates the antitumor effect of standard therapies. For example, EZH2 inhibition enhanced the effect of Temozolomide (TMZ) in TMZ-resistant glioblastoma cell lines [40].

Overall, our results indicate that EZH2 inhibition shows anti-tumoral effects in *in vitro*, *in vivo*, and *ex vivo* PanNEN models. EZH2 inhibition may represent a novel epigenetic treatment option for high-grade PanNEN.

5. Conclusions

In conclusion, we demonstrated that high EZH2 expression in PanNENs correlated with high grade, tumor stage, presence of metastases, and shorter disease-free survival and that EZH2 inhibition impaired cell viability and tumor burden. Notably, EZH2 expression was extremely high in highly proliferating PanNECs. Our data indicate that EZH2 inhibition may represent a novel, promising treatment option, especially for high-grade PanNENs.

Supplementary Materials: The following are available online at <https://www.mdpi.com/article/10.3390/cancers13195014/s1>. Supplementary methods: Quantitative single cell imaging of cell death. Figure S1. (A) Correlation between Ki67 (%) and EZH2 (Ki67 as continuous variable available in n = 159/172 patients). (B) Comparison of disease-free survival between patients with low, intermediate, and high EZH2 expression, including PanNECs. Patients with high EZH2 expression have significantly shorter survival $p = 0.001$. (C) Correlation between H3K27me3 level and EZH2 expression in PanNEN human tissues (H3K27me3 expression available in n = 130/172 patients). No significant correlation was detected. Figure S2. (A) Representative images of the InCyte S3 imaging of BON1 and QGP1 cells after treatment with vehicle control (DMSO) and GSK126 for 48 h. (B) Graphical representation of quantitative single-cell imaging of cell death of BON1 and QGP1 cells after propidium iodide (dead cells) and Hoechst 33342 staining (total cell count). Cells were treated in technical replicates (n = 3 wells, >1000 cells/well) with vehicle control (DMSO) or indicated concentrations of GSK126 and incubated for 48 h. After co-staining, replicate samples were automatically imaged with an InCell 2000 Analyzer and analyzed with CellProfiler software, and the percentage of dead cells was calculated relative to the total cell count. A ferroptosis activator ((1S,3R)-RSL3 0.5 μ M and 15 μ M) and protonophore for uncoupling of the electron transport chain (carbonyl cyanide 4-(trifluoromethoxy) phenylhydrazone, FCCP 20 μ M) were used as positive controls to induced cell

death. Figure S3. (A) Example of tumor classification in the Rip1TAG2 model and Ki67 staining. (B) EZH2 and H3K27me3 expression in control and GSK126-treated animals. While EZH2 expression did not change between treated and control mice, the H3K27me3 level significantly decreased after GSK126 treatment. (C) Quantification based on QuPath scoring of EZH2, H3K27me3, H3K36me3, and Ki67 across the different tumor stages in Rip1TAG2 GSK126-treated and control mice. (D) Tumor number in GSK126-treated and control mice. (E) Representative IHC for caspase-3 and Ki67 in treated and control mice. Figure S4. EZH2 immunohistochemistry on the original tumor tissue from which PanNETs tumoroids were isolated.

Author Contributions: Conceptualization, I.M., S.L.A.-M. and A.P.; Methodology, S.L.A.-M., V.A., A.K., M.C.B., M.S.L., M.C.S., R.M., A.D.D., F.M., J.S., C.K.-F., C.D., S.P. and M.F.; Software, S.L.A.-M. and M.C.S.; Validation, S.L.A.-M., V.A., A.K., M.C.B., M.S.L., M.C.S. and R.M.; Formal Analysis, S.L.A.-M., V.A., A.K., M.C.B., M.S.L., M.C.S., and R.M.; Investigation, S.L.A.-M., V.A., A.K., M.C.B., M.S.L., M.C.S. and R.M.; Resources, I.M. and A.P.; Data Curation, S.L.A.-M. and R.M.; Writing—Original Draft Preparation, I.M., S.L.A.-M., and A.P.; Writing—Review and Editing, S.L.A.-M., V.A., A.K., M.C.B., M.S.L., M.C.S., R.M., A.D.D., F.M., C.D., S.P., J.S., C.K.-F., M.F., I.M. and A.P. Visualization, S.L.A.-M., I.M. and V.A.; Supervision, I.M., and A.P.; Project Administration, I.M. and A.P.; Funding Acquisition, I.M. and A.P. All authors have read and agreed to the published version of the manuscript.

Funding: This research was supported by a Swill Cancer League grant to Aurel Perren, KLS-4227-08-2017, and SNF Marie Heim-Vögtlin PMPDP3_164484 and Tumour Forschung Bern grants to Ilaria Marinoni. Valentina Andreasi's PhD scholarship and Francesca Muffatti's research fellowship were supported by Gioja Bianca Costanza legacy donations.

Institutional Review Board Statement: The study was conducted according to the guidelines of the Declaration of Helsinki and approved by the cantonal authorities (Kantonale Ethikkommission Bern, Ref.-Nr. KEK-BE 105/2015) and the Italian ethics commission (Comitato Etico, CE 252/2019). All experimental protocols involving animals were reviewed and approved by the Cantonal Veterinary Office of Bern (Bern, Switzerland).

Informed Consent Statement: All the subjects involved in the study (or their parents or guardians) have given their written informed consent.

Data Availability Statement: The data presented in this study are available in the article.

Acknowledgments: We thank the Tissue Bank Bern (Bern, Switzerland) and the Translational Research Unit (Institute of Pathology, Bern, Switzerland) for their technical, material, and administrative support and the Cytopathology Unit (Institute of Pathology, Bern, Switzerland) for technical support performing formalin fixation and paraffin embedding in tissue and cell culture material. We thank Philippe Krebs for the support with the in vivo experiments. We thank the Microscope Imaging Center (MIC) of the University of Bern for technical support.

Conflicts of Interest: All the authors declare no conflict of interest.

References

- World Classification of Tumours Editorial Board. *WHO Classification of Tumours. Digestive System Tumours*, 5th ed.; IARC Press: Lyon, France, 2019.
- Dasari, A.; Shen, C.; Halperin, D.; Zhao, B.; Zhou, S.; Xu, Y.; Shih, T.; Yao, J.C. Trends in the Incidence, Prevalence, and Survival Outcomes in Patients With Neuroendocrine Tumors in the United States. *JAMA Oncol.* **2017**, *3*, 1335–1342. [[CrossRef](#)]
- Elvebakken, H.; Perren, A.; Scaozec, J.-Y.; Tang, L.H.; Federspiel, B.; Klimstra, D.S.; Vestermark, L.W.; Ali, A.S.; Zlobec, I.; Myklebust, T.Å.; et al. A Consensus-Developed Morphological Re-Evaluation of 196 High-Grade Gastroenteropancreatic Neuroendocrine Neoplasms and Its Clinical Correlations. *Neuroendocrinology* **2021**, *111*, 883–894. [[CrossRef](#)]
- Jiao, Y.; Shi, C.; Edil, B.H.; de Wilde, R.F.; Klimstra, D.S.; Maitra, A.; Schlick, R.D.; Tang, L.H.; Wolfgang, C.L.; Choti, M.A.; et al. DAXX/ATRX, MEN1, and mTOR pathway genes are frequently altered in pancreatic neuroendocrine tumors. *Science* **2011**, *331*, 1199–1203. [[CrossRef](#)] [[PubMed](#)]
- Scarpa, A.; Chang, D.K.; Nones, K.; Corbo, V.; Patch, A.-M.; Bailey, P.; Lawlor, R.T.; Johns, A.L.; Miller, D.K.; Mafficini, A.; et al. Whole-genome landscape of pancreatic neuroendocrine tumours. *Nature* **2017**, *543*, 65–71. [[CrossRef](#)] [[PubMed](#)]
- Konukiewitz, B.; Jesinghaus, M.; Steiger, K.; Schlitter, A.M.; Kasajima, A.; Sipos, B.; Zamboni, G.; Weichert, W.; Pfarr, N.; Klöppel, G. Pancreatic neuroendocrine carcinomas reveal a closer relationship to ductal adenocarcinomas than to neuroendocrine tumors G3. *Hum. Pathol.* **2018**, *77*, 70–79. [[CrossRef](#)] [[PubMed](#)]

7. Rinke, A.; Auernhammer, C.J.; Bodei, L.; Kidd, M.; Krug, S.; Lawlor, R.; Marinoni, I.; Perren, A.; Scarpa, A.; Sorbye, H.; et al. Treatment of advanced gastroenteropancreatic neuroendocrine neoplasia, are we on the way to personalised medicine? *Gut* **2021**, *70*, 1768–1781. [[CrossRef](#)] [[PubMed](#)]
8. Di Domenico, A.; Pipinikas, C.P.; Maire, R.S.; Bräutigam, K.; Simillion, C.; Dettmer, M.S.; Vassella, E.; Thirlwell, C.; Perren, A.; Marinoni, I. Epigenetic landscape of pancreatic neuroendocrine tumours reveals distinct cells of origin and means of tumour progression. *Commun. Biol.* **2020**, *3*, 740. [[CrossRef](#)]
9. Di Domenico, A.; Wiedmer, T.; Marinoni, I.; Perren, A. Genetic and epigenetic drivers of neuroendocrine tumours (NET). *Endocr. Relat. Cancer* **2017**, *24*, R315–R334. [[CrossRef](#)]
10. Roy, S.; LaFramboise, W.A.; Liu, T.-C.; Cao, D.; Luvison, A.; Miller, C.; Lyons, M.A.; O’Sullivan, R.J.; Zureikat, A.H.; Hogg, M.E.; et al. Loss of Chromatin-Remodeling Proteins and/or CDKN2A Associates With Metastasis of Pancreatic Neuroendocrine Tumors and Reduced Patient Survival Times. *Gastroenterology* **2018**, *154*, 2060–2063.e8. [[CrossRef](#)] [[PubMed](#)]
11. Kim, K.H.; Roberts, C.W.M. Targeting EZH2 in cancer. *Nat. Med.* **2016**, *22*, 128–134. [[CrossRef](#)]
12. Margueron, R.; Reinberg, D. The Polycomb complex PRC2 and its mark in life. *Nature* **2011**, *469*, 343–349. [[CrossRef](#)]
13. Varambally, S.; Dhanasekaran, S.M.; Zhou, M.; Barrette, T.R.; Kumar-Sinha, C.; Sanda, M.G.; Ghosh, D.; Pienta, K.J.; Sewalt, R.G.A.B.; Otte, A.P.; et al. The polycomb group protein EZH2 is involved in progression of prostate cancer. *Nature* **2002**, *419*, 624–629. [[CrossRef](#)]
14. Yap, T.A.; Winter, J.N.; Giulino-Roth, L.; Longley, J.; Lopez, J.; Michot, J.-M.; Leonard, J.P.; Ribrag, V.; McCabe, M.T.; Creasy, C.L.; et al. Phase I Study of the Novel Enhancer of Zeste Homolog 2 (EZH2) Inhibitor GSK2816126 in Patients with Advanced Hematologic and Solid Tumors. *Clin. Cancer Res. Off. J. Am. Assoc. Cancer Res.* **2019**, *25*, 7331–7339. [[CrossRef](#)] [[PubMed](#)]
15. Gounder, M.; Schöffski, P.; Jones, R.L.; Agulnik, M.; Cote, G.M.; Villalobos, V.M.; Attia, S.; Chugh, R.; Chen, T.W.-W.; Jahan, T.; et al. Tazemetostat in advanced epithelioid sarcoma with loss of INI1/SMARCB1: An international, open-label, phase 2 basket study. *Lancet. Oncol.* **2020**, *21*, 1423–1432. [[CrossRef](#)]
16. Morschhauser, F.; Tilly, H.; Chaidos, A.; McKay, P.; Phillips, T.; Assouline, S.; Batlevi, C.L.; Campbell, P.; Ribrag, V.; Damaj, G.L.; et al. Tazemetostat for patients with relapsed or refractory follicular lymphoma: An open-label, single-arm, multicentre, phase 2 trial. *Lancet. Oncol.* **2020**, *21*, 1433–1442. [[CrossRef](#)]
17. Marinoni, I.; Kurrer, A.S.; Vassella, E.; Dettmer, M.; Rudolph, T.; Banz, V.; Hunger, F.; Pasquinelli, S.; Speel, E.J.; Perren, A. Loss of DAXX and ATRX are associated with chromosome instability and reduced survival of patients with pancreatic neuroendocrine tumors. *Gastroenterology* **2014**, *146*, 453–460.e5. [[CrossRef](#)]
18. Lloyd, R.V.; Osamura, R.Y.; Kloppner, G.; Rosai, J. (Eds.) *WHO Classification of Tumours of Endocrine Organs*, 4th ed.; IARC: Lyon, France, 2017.
19. Brierly, J.D.; Gospodarowicz, M.K.; Witteking, C. (Eds.) *TNM Classification of Malignant Tumours*, 8th ed.; John Wiley & Sons: Oxford, UK; Hoboken, NJ, USA, 2017.
20. Bankhead, P.; Loughrey, M.B.; Fernández, J.A.; Dombrowski, Y.; McArt, D.G.; Dunne, P.D.; McQuaid, S.; Gray, R.T.; Murray, L.J.; Coleman, H.G.; et al. QuPath: Open source software for digital pathology image analysis. *Sci. Rep.* **2017**, *7*, 16878. [[CrossRef](#)]
21. Benten, D.; Behrang, Y.; Unrau, L.; Weissmann, V.; Wolters-Eisfeld, G.; Burdak-Rothkamm, S.; Stahl, F.R.; Anlauf, M.; Grabowski, P.; Möbs, M.; et al. Establishment of the first well-differentiated human pancreatic neuroendocrine tumor model. *Mol. Cancer Res.* **2018**, *16*, 496–507. [[CrossRef](#)]
22. Taylor, S.C.; Berkelman, T.; Yadav, G.; Hammond, M. A defined methodology for reliable quantification of Western blot data. *Mol. Biotechnol.* **2013**, *55*, 217–226. [[CrossRef](#)] [[PubMed](#)]
23. Tschan, M.P.; Fischer, K.M.; Fung, V.S.; Pirnia, F.; Borner, M.M.; Fey, M.F.; Tobler, A.; Torbett, B.E. Alternative splicing of the human cyclin D-binding Myb-like protein (hDMP1) yields a truncated protein isoform that alters macrophage differentiation patterns. *J. Biol. Chem.* **2003**, *278*, 42750–42760. [[CrossRef](#)]
24. April-Monn, S.L.; Wiedmer, T.; Magdalena, S.; Maire, R.S.; Schiavo Lena, M.; Trippel, M.; Di Domenico, A.; Muffatti, F.; Andreasi, V.; Capurso, G.; et al. 3D Primary Cell Culture: A Novel Preclinical Model For Pancreatic Neuroendocrine Tumors (PanNETs). *Neuroendocrinology* **2021**, *111*, 273–287. [[CrossRef](#)] [[PubMed](#)]
25. Sebaugh, J.L. Guidelines for accurate EC50/IC50 estimation. *Pharm. Stat.* **2011**, *10*, 128–134. [[CrossRef](#)]
26. van de Wetering, M.; Francies, H.E.; Francis, J.M.; Bounova, G.; Iorio, F.; Pronk, A.; van Houdt, W.; van Gorp, J.; Taylor-Weiner, A.; Kester, L.; et al. Prospective derivation of a living organoid biobank of colorectal cancer patients. *Cell* **2015**, *161*, 933–945. [[CrossRef](#)] [[PubMed](#)]
27. Garnett, M.J.; Edelman, E.J.; Heidorn, S.J.; Greenman, C.D.; Dastur, A.; Lau, K.W.; Greninger, P.; Thompson, I.R.; Luo, X.; Soares, J.; et al. Systematic identification of genomic markers of drug sensitivity in cancer cells. *Nature* **2012**, *483*, 570–575. [[CrossRef](#)]
28. Hanahan, D. Heritable formation of pancreatic beta-cell tumours in transgenic mice expressing recombinant insulin/simian virus 40 oncogenes. *Nature* **1985**, *315*, 115–122. [[CrossRef](#)]
29. Hanahan, D.; Folkman, J. Patterns and emerging mechanisms of the angiogenic switch during tumorigenesis. *Cell* **1996**, *86*, 353–364. [[CrossRef](#)]
30. Jiang, Z.; Li, W.; Hu, X.; Zhang, Q.; Sun, T.; Cui, S.; Wang, S.; Ouyang, Q.; Yin, Y.; Geng, C.; et al. Tucidostat plus exemestane for postmenopausal patients with advanced, hormone receptor-positive breast cancer (ACE): A randomised, double-blind, placebo-controlled, phase 3 trial. *Lancet Oncol.* **2019**, *20*, 806–815. [[CrossRef](#)]

31. Biran, N.; Siegel, D.S.; Vesole, D.H. The forgotten class of drugs for multiple myeloma: HDAC inhibitors. *Lancet. Haematol.* **2018**, *5*, e604–e605. [[CrossRef](#)]
32. Stein, E.M.; Fathi, A.T.; DiNardo, C.D.; Pollyea, D.A.; Roboz, G.J.; Collins, R.; Sekeres, M.A.; Stone, R.M.; Attar, E.C.; Frattini, M.G.; et al. Enasidenib in patients with mutant IDH2 myelodysplastic syndromes: A phase 1 subgroup analysis of the multicentre, AG221-C-001 trial. *Lancet Haematol.* **2020**, *7*, e309–e319. [[CrossRef](#)]
33. Duan, R.; Du, W.; Guo, W. EZH2: A novel target for cancer treatment. *J. Hematol. Oncol.* **2020**, *13*, 104. [[CrossRef](#)] [[PubMed](#)]
34. Bracken, A.P.; Pasini, D.; Capra, M.; Prosperini, E.; Colli, E.; Helin, K. EZH2 is downstream of the pRB-E2F pathway, essential for proliferation and amplified in cancer. *EMBO J.* **2003**, *22*, 5323–5335. [[CrossRef](#)]
35. Marconcini, R.; Faviana, P.; Campani, D.; Galli, L.; Antonuzzo, A.; Falcone, A.; Ricci, S. Enhancer of zeste homolog 2 (EZH2) expression in G1–G2 Pancreatic Neuroendocrine Tumor (pNET). *Ann. Oncol.* **2016**, *27*, iv21. [[CrossRef](#)]
36. Wang, H.; Bender, A.; Wang, P.; Karakose, E.; Inabnet, W.B.; Libutti, S.K.; Arnold, A.; Lambertini, L.; Stang, M.; Chen, H.; et al. Insights into beta cell regeneration for diabetes via integration of molecular landscapes in human insulinomas. *Nat. Commun.* **2017**, *8*, 767. [[CrossRef](#)] [[PubMed](#)]
37. Chen, H.; Gu, X.; Su, I.; Bottino, R.; Contreras, J.L.; Tarakhovsky, A.; Kim, S.K. Polycomb protein Ezh2 regulates pancreatic beta-cell Ink4a/Arf expression and regeneration in diabetes mellitus. *Genes Dev.* **2009**, *23*, 975–985. [[CrossRef](#)] [[PubMed](#)]
38. Zhang, H.; Qi, J.; Reyes, J.M.; Li, L.; Rao, P.K.; Li, F.; Lin, C.Y.; Perry, J.A.; Lawlor, M.A.; Federation, A.; et al. Oncogenic Deregulation of EZH2 as an Opportunity for Targeted Therapy in Lung Cancer. *Cancer Discov.* **2016**, *6*, 1006–1021. [[CrossRef](#)] [[PubMed](#)]
39. McCabe, M.T.; Ott, H.M.; Ganji, G.; Korenchuk, S.; Thompson, C.; Van Aller, G.S.; Liu, Y.; Graves, A.P.; Della Pietra, A., 3rd; Diaz, E.; et al. EZH2 inhibition as a therapeutic strategy for lymphoma with EZH2-activating mutations. *Nature* **2012**, *492*, 108–112. [[CrossRef](#)] [[PubMed](#)]
40. Fan, T.-Y.; Wang, H.; Xiang, P.; Liu, Y.-W.; Li, H.-Z.; Lei, B.-X.; Yu, M.; Qi, S.-T. Inhibition of EZH2 reverses chemotherapeutic drug TMZ chemosensitivity in glioblastoma. *Int. J. Clin. Exp. Pathol.* **2014**, *7*, 6662–6670. [[PubMed](#)]

Supplementary Materials

Supplementary Methods: Quantitative single cell imaging of cell death

The percentage of dead cells relative to total cell count was measured by quantitative single cell imaging of propidium- (dead cells) and Hoechst 33342-stained cells (alive and dead cells=total cells) as described previously with minor modifications [1]. BON1 and QGP1 cells were seeded at 20,000 cells/well in Ibidi optical 96-well plates (#89626, Ibidi) and incubated for 24 hours. Cells were treated in technical replicates (n=3) with vehicle control (DMSO) or indicated concentrations of GSK126. After 48 hours, cells were stained with Hoechst 33342 (5 µg/ml) and propidium iodide (50 µg/ml) at 37°C for 30 minutes, and >1000 cells/well (4-9 images) were imaged at 4x magnification using an automated fluorescence microscope (InCell 2000 Analyzer, GE Healthcare Life Sciences). Cell Profiler software (Broad Institute) was used for image segmentation and automated detection of stained nuclei [2]. The percentage of dead cells relative to vehicle control was calculated based on the ratio of PI-positive nuclei and total nuclei number.

References

1. Tousignant, K.D.; Rockstroh, A.; Poad, B.L.J.; Talebi, A.; Young, R.S.E.; Taherian Fard, A.; Gupta, R.; Zang, T.; Wang, C.; Lehman, M.L.; et al. Therapy-induced lipid uptake and remodeling underpin ferroptosis hypersensitivity in prostate cancer. *Cancer Metab.* **2020**, *8*, 11.
2. Carpenter, A.E.; Jones, T.R.; Lamprecht, M.R.; Clarke, C.; Kang, I.H.; Friman, O.; Guertin, D.A.; Chang, J.H.; Lindquist, R.A.; Moffat, J.; et al. CellProfiler: image analysis software for identifying and quantifying cell phenotypes. *Genome Biol.* **2006**, *7*, R100.

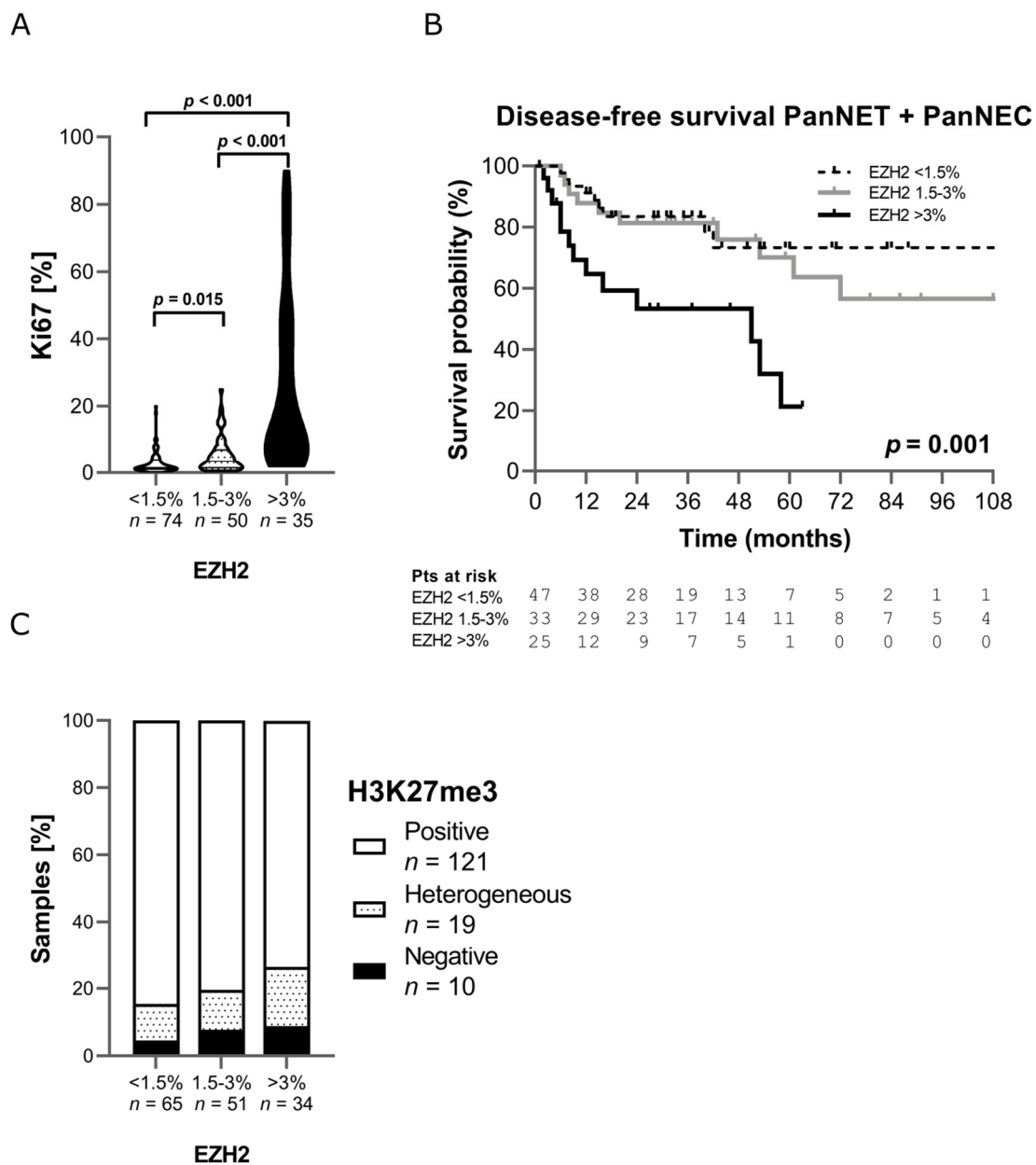
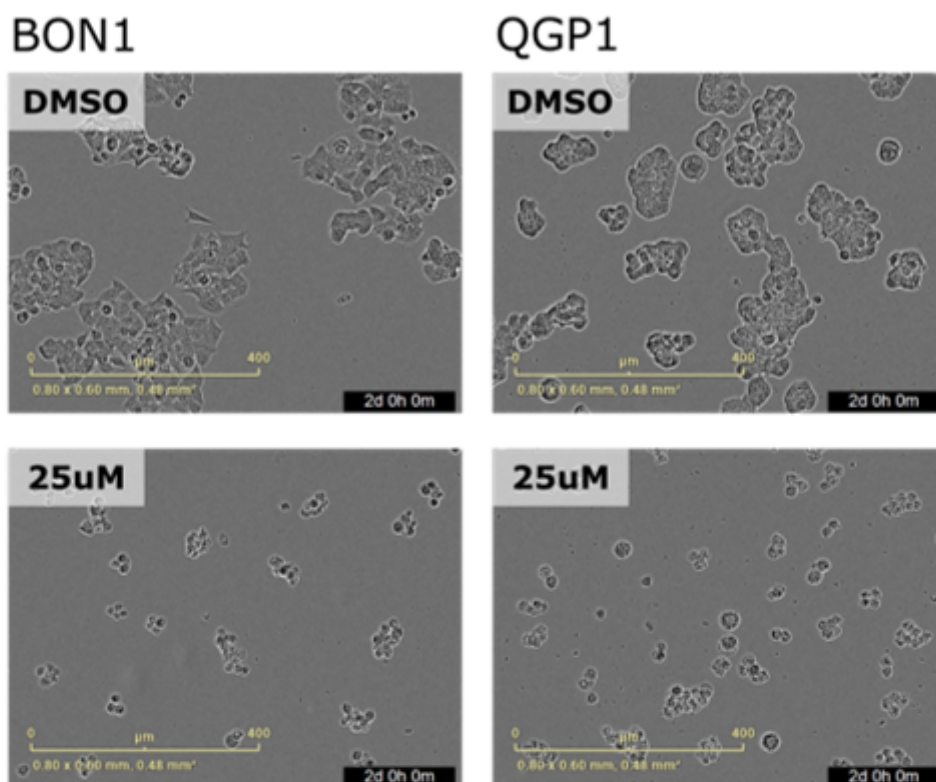


Figure S1. A) Correlation between Ki67 (%) and EZH2 (Ki67 as continuous variable available in n=159/172 patients). B) Comparison of disease-free survival between patients with low, intermediate, and high EZH2 expression including PanNECs. Patients with high EZH2 expression have significant shorter survival p=0.001. C) Correlation between H3K27me3 level and EZH2 expression in PanNEN human tissues (H3K27me3 expression available n=130/172 patients). No significant correlation was detected.

A



B

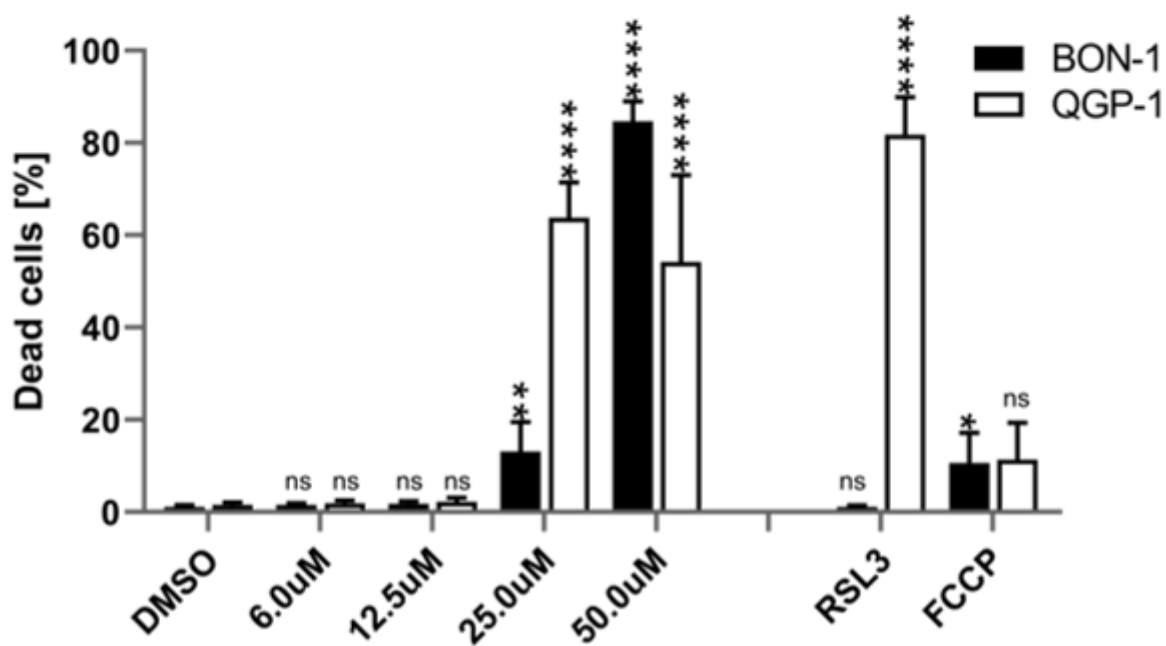


Figure S2. A) Representative images of the InCuCyte S3 imaging of BON1 and QGP1 cells after treatment with vehicle control (DMSO) and GSK126 for 48 hours. B) Graphical representation of quantitative single cell imaging of cell death of BON1 and QGP1 cells after propidium iodide (dead cells) and Hoechst 33342 staining (total cell count). Cells were treated in technical replicates (n=3 wells, >1000 cells/well) with vehicle control (DMSO) or indicated concentrations of GSK126 and incubated for 48 hours. After co-staining, replicate samples were automatically imaged with an InCell 2000 Analyzer,

analyzed by CellProfiler software, and the percentage of dead cells was calculated relative to the total cell count. A ferroptosis activator [(1S,3R)-RSL3 0.5 μ M and 15 μ M] and protonophore for uncoupling of the electron transport chain (Carbonyl cyanide 4-(trifluoromethoxy) phenylhydrazone, FCCP 20 μ M) were used as positive controls to induced cell death.

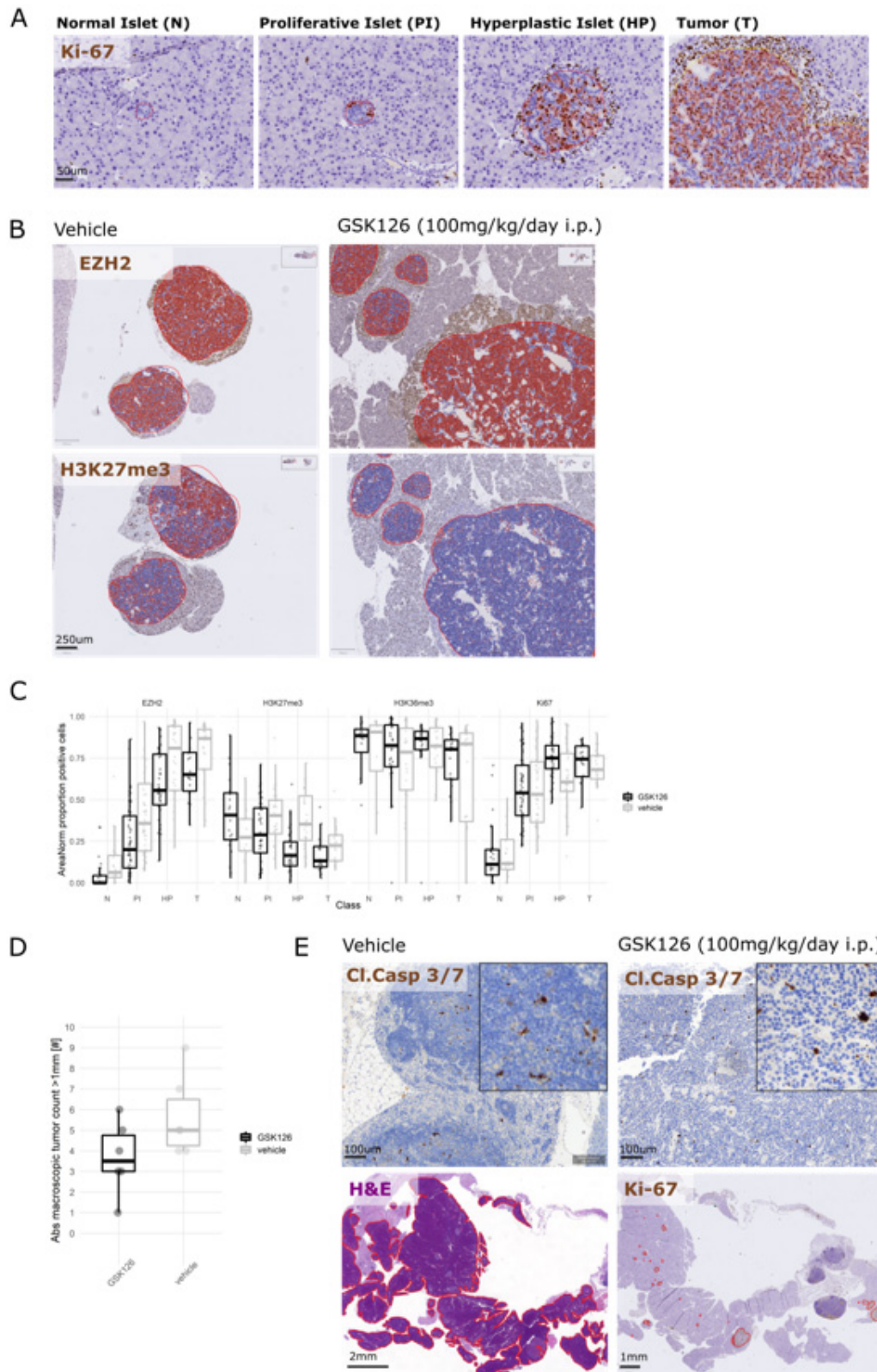


Figure S3. A) Example of tumor classification in the Rip1TAG2 model and Ki67 staining. B) EZH2 and H3K27me3 expression in control and GSK126 treated animals. While EZH2 expression does not change between treated and control mice, H3K27me3 level significantly decreased after GSK126 treatment. C) Quantification based on QuPath scoring of EZH2,

H3K27me3, H3K36me3 and Ki67 across the different tumor stages in Rip1tag2 mice GSK126 treated and control mice. D) Tumor number in GSK126 treated and control mice. E) Representative IHC for Caspase-3 and Ki67 in treated and control mice.

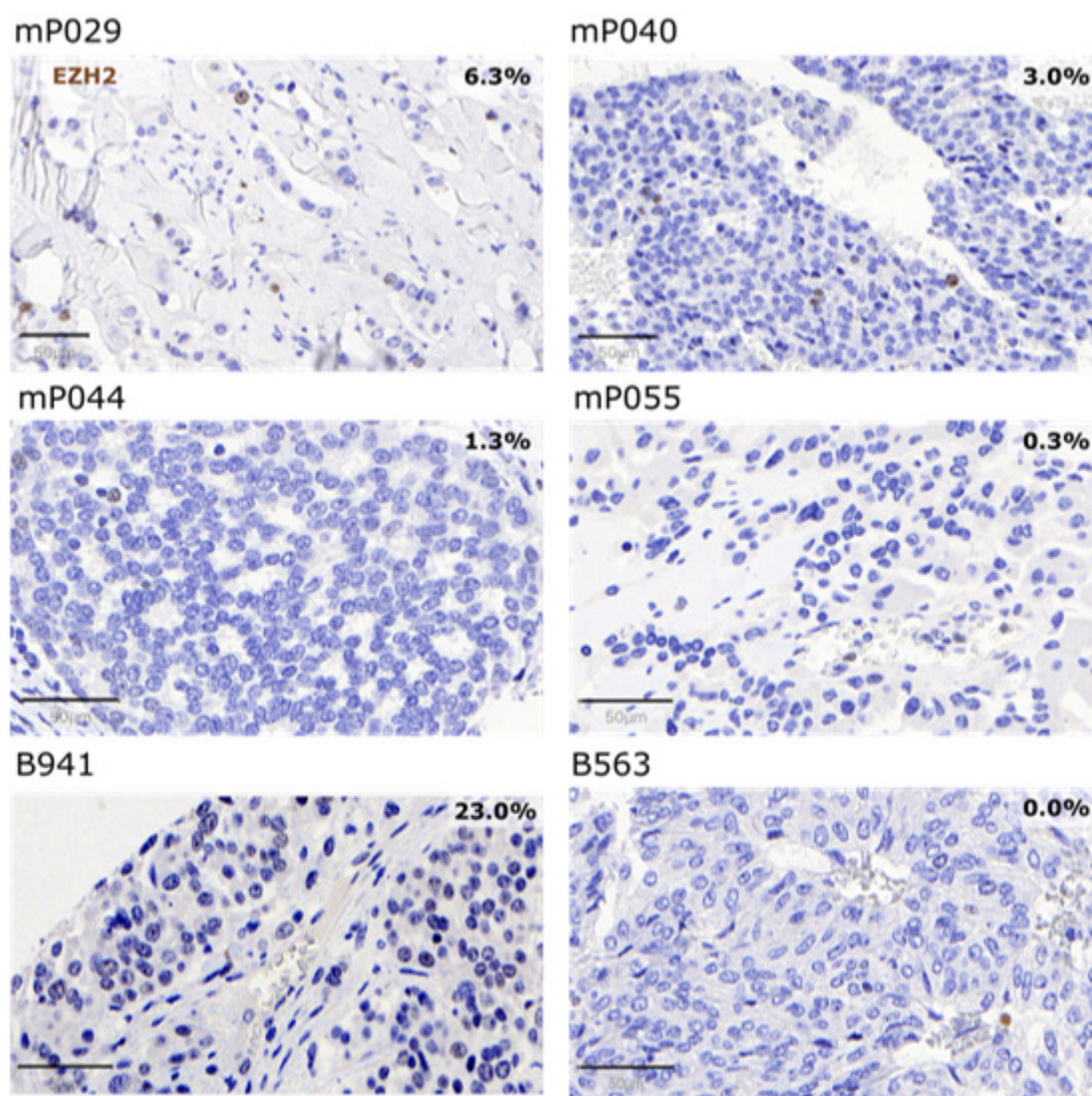


Figure S4. EZH2 immunohistochemistry on the original tumor tissue from which PanNETs tumoroids were isolated.

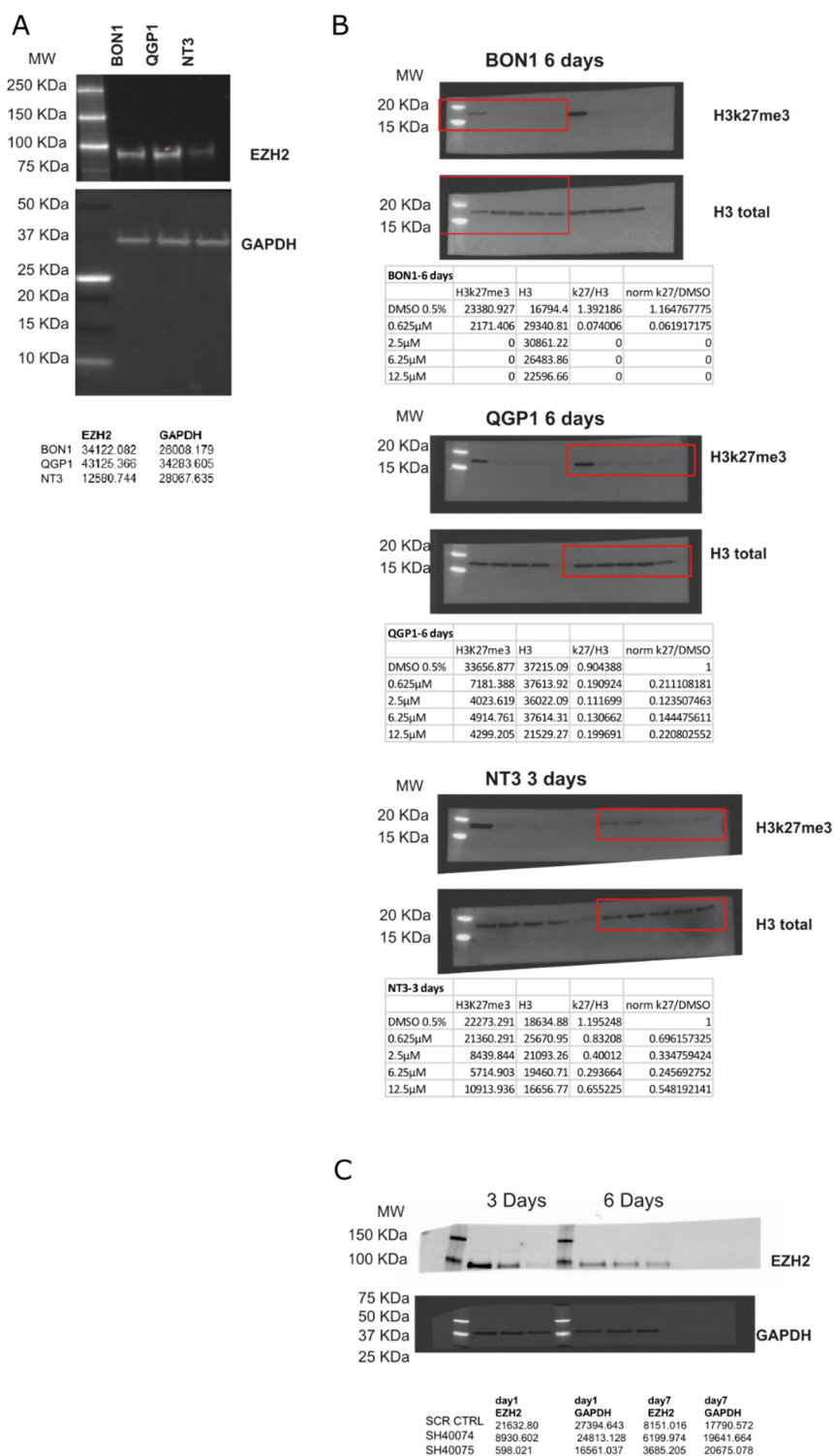


Figure S5. Original western blotting membranes with the ladder Precision Plus Protein Kaleidoscope (Biorad) A) EZH2 expression level in BON1, QGP1 and NT3 cell lines (Fig 2 B). B) H3K27me3 level after 6 days of GSK126 treatment in BON1 and QGP1 and 3 days in NT3 with the correspondent band intensity measurement (fig 2D). The membrane was cut at 25 KDa. Band intensity was measured using ImageJ and area size calculation tool of plotted lane (square pixel). C) EZH2 protein level after Sh-RNA lentivirus transduction in QGP1 and correspondent GAPDH (Fig. 3A).

3.3.4 Extended discussion

Epigenetic mechanisms are important in PanNEN progression^{68,149,151,336} and are commonly deregulated in this disease^{33,35}. Due to their reversible nature, epigenetic alterations may present alternative therapeutic targets in addition to standard therapeutical approaches.

In this study, we investigated the role of EZH2 in PanNENs and found a correlation between elevated EZH2 protein expression and tumor grade, Ki-67 indexes, and advanced disease status in a large patient cohort. We primarily observed increased EZH2 expression in high-grade PanNETs and PanNECs, highly proliferative cell lines QGP1 and BON1, and malignant insulinoma of the Rip1Tag2 mouse model. While some studies reported a diffuse protein expression in low- and intermediate-grade intestinal neuroendocrine tumors of 33 patients³³⁵ or in primary- and metastatic small intestinal neuroendocrine tumors (SI-NETs) from 38 patients³³⁷, other studies reported low to no expression in low- and intermediate-grade GEP-NETs¹⁷⁸. However, all of these studies reported an association between EZH2 expression and cellular proliferation. The positive association between high P53 protein expression and EZH2 immunoreactivity suggested a direct link to tumor cell proliferation in intestinal NETs³³⁵. Similarly, EZH2 expression was suggested as a biomarker for differentiating between GEP-NET G3 and GEP-NECs¹⁷⁸. In a cohort of 219 tissues from GEP-NEN and pulmonary NEN EZH2 expression was predominantly found in NENs with proliferation rates >20% and correlated with poor overall survival and NEC histology¹⁷⁸. High EZH2 expression was also detected in small-cell lung carcinomas and large-cell neuroendocrine carcinomas (23/23) but rarely in lung carcinoids suggesting its biological role in high-grade neuroendocrine carcinomas³³⁸. This is in line with the commonly found role of EZH2 in actively proliferating cells^{195–197} and suggests that EZH2 overexpression depicts a later(r) event in PanNEN progression.

We found that inhibiting the methyltransferase activity of EZH2 in PanNEN resulted in impaired cell growth *in vitro* and a decrease in tumor burden *in vivo*, as it was also observed in EZH2-deficient SI-NETs *in vitro* and a xenograft model³³⁷. However, despite that EZH2 inhibition decreased the tumor burden *in vivo*, we did not observe a difference in tumor proliferation or an increase in apoptosis. This is in line with other findings from a study using EZH2 inhibition (DZNep) in a BON1 cell line³³⁹. EZH2 inhibition suppressed global H3K27me3 (histone 3 lysine 27 tri-methylation) and reduced cell proliferation but did not induce apoptosis³³⁹. We did not see a correlation between H3K27me3 and EZH2 expression in our large PanNEN patient collective. Similarly, no correlation was found between H3K27me3 levels and EZH2 expression in a GEP-NEN patient cohort¹⁷⁸. In an SCLC cell line model EZH2

stabilized damage-specific DNA binding protein 2 (DDB2) and promoted nucleotide excision repair³⁴⁰. In line, EZH2 depletion but not EZH2 catalytic inhibition sensitized SCLC cells to cisplatin³⁴⁰. Altogether, these findings indicate that methyltransferase-independent functioning of EZH2 may also play a relevant role in PanNEN tumorigenesis.

Understanding the extent to which the cancer-promoting effects of EZH2 depend upon its enzymatic activity as compared to its nonenzymatic structural contributions to PRC2 integrity will be important for future drug development¹⁹⁶. A clinical trial (NCT02082977) using GSK126 in patients with lymphoma, multiple myeloma, and solid tumors failed due to insufficient evidence of clinical activity and did not justify further clinical investigation^{341,342}. EZH2 inhibition alone may not be sufficiently effective in anticancer therapy; hence improved efficacy by combinational therapy might be an alternative route for the use in PanNENs. The activity of EZH2 has been shown to be inhibited by AKT-mediated phosphorylation¹⁹⁶ and may therefore be carefully considered since AKT/PI3K/MTOR in PanNETs is commonly upregulated. A combination with MTOR inhibitors such as metformin, which also decreases AKT activation³⁴³, may show beneficial combinational effects with inhibition of EZH2. EZH2 inhibition demonstrated selected efficacy in patients with hematological malignancies or highly aggressive solid tumors with genetic alteration in the SWI/SNF chromatin remodeling complex²⁰³. *ARID1A*, the DNA-binding component of SWI/SNF complex, is frequently mutated in PanNENs^{33,344}, and EZH2 inhibition in these cancers may lead to synthetic lethality¹⁹⁶. Testing these and variable other epigenetic treatments on patients will not be possible. Therefore, primary PanNEN tumoroid cultures offer a unique method for identifying vulnerabilities and laying the groundwork for future mechanistic studies.

4 Overall Discussion and Outlook

The rarity and heterogeneity of PanNENs complicate translational advances and impedes therapeutic advancements. There are currently no predictive therapeutic biomarkers, and therapy selection is highly empirical¹⁹. Moreover, representative preclinical models to test existing and explore novel therapeutic approaches are missing²⁹⁹

In this project, we established and validated a primary cell culture workflow that facilitates preclinical studies in PanNENs using tumor specimens from patients. The suspension-based culture setup coupled with a low extracellular matrix is crucial to a successful culture. The three-dimensional configuration imitates a more physiologically relevant architecture by more accurately simulating cell-cell and cell-matrix interactions, incorporating tumor-like characteristics such as gradients (e.g., oxygen tension, nutrients, metabolites), and allowing zonal patterning (e.g., proliferation, necrotic core). This approach improved the few previous primary PanNEN cell cultures^{229-231,301} in a number of ways, including higher culture success rates, minimal required cell amounts, and reproducibly extended culture times of up to two weeks. Moreover, the suspension-based culture facilitates the natural aggregation of neuroendocrine tumor cells, an intrinsic property previously described in endocrine cells²²⁸, and may provide a more natural culture environment for these cells.

With increasing formats of three-dimensional models from various tissues, it becomes crucial to clearly define and describe the actual culture system. Since the terminology to refer to 3D culture systems is not used uniformly, it is even more important to state components relevant for the tumor biology. The culture media composition affects culture success and functional aspects. For example, different growth factor media selectively impacted the outgrowth of pancreatic ductal adenocarcinoma (PDAC) PD organoids and the selection of oncogenic mutations in these organoids³⁴⁵. Intriguingly, using a minimal medium that targets growth factor receptors essential for PanNEN function resulted in a greater culture success in our workflow than did the use of more generic growth factor cocktails supplemented in the majority of other cancer organoid models^{232,285,295}. Indeed, an unsuccessful culture of human PanNEN samples in the generic organoid medium²³³ underlines the importance of critical evaluation of the exact culture conditions. Further optimization of the minimal (Pan)NEN culture medium could be pursued, although systematic testing in low-abundant material poses limitations in experimental conditions to be tested.

Utilizing quality control steps and standardization with respect to technical- and analytic parameters is also essential for enhancing the reproducibility of tumoroid models derived from patients³⁴⁶. Streamlining the sampling of PanNEN specimens and optimizing cell requirements for *in vitro* screens helped overcome previous shortcomings. We implemented standardized cryopreservation protocols that simplified sample collection and facilitated experimental planning and international cooperation among different institutions. Furthermore, the non-lytic screening setup allowed us to retrieve maximal biological information, including downstream NGS analysis from rare and low-abundant tumor specimens. Micro-cell blocks before and after culture allowed for a comprehensive analysis of the cellular composition, implementation of growth rate (GR) metrics facilitated comparison among differentially proliferating tumors, and drug titrations centered on maximal plasma concentration (C_{max}) in patients provided physiologically more relevant insights derived from our system. Several studies used additional measurements to quantify technical noise between plates and to systematically assess the screening and assay quality^{298,345,347}. Documentation of these aspects that is rigorous and transparent allows for a more meaningful comparison of outcomes, which improves scientific advances in the field.

Patient-derived tumoroids recapitulated histomorphological and transcriptional key features of original tumor tissue. In our studies, we discovered that *in vitro* drug sensitivities varied between patients and pharmacotherapies, which was also confirmed in the proof-of-concept study in advanced high-grade GEP-NENs, indicating that patient-specific characteristics were retained in culture to a large extent. As a result, using patient-derived material from NEN patients enables the study of pharmacological perturbations to be more personalized and patient-centered.

Our short-term setup permits up to two weeks of culture time. However, due to the low-proliferative nature of PanNEN subtypes, cell expansion and *ex vivo* propagation of patient-derived cells is highly limited, as already reported in other studies⁸⁶. Therefore, advanced cell manipulation (such as CRISPR-Cas9) is currently not technically feasible in this setup. Only a handful of stable and expandable organoid lines, mostly from higher-grade tumors, have been successfully established for GEP-NENs^{86,232,233} but may be more suitable for such mechanistic-driven studies. In addition, at the Neuroendocrine Tumor Research Foundation (NETRF) and European Neuroendocrine Tumor Society (ENETS) conferences in 2021 and 2022, a number of research groups proposed strategies to artificially circumvent the slow-proliferative state of low- and intermediate-grade NEN cells *in vitro*, which could aid in overcoming this limitation.

It is still not entirely clear how long genetic and phenotypic heterogeneity is retained in non-clonal patient-derived cultures over longer times. However, for long-term culture models, careful consideration of a potential selection bias and/or introduction of genetic drifts³⁴⁸ must be made carefully. Studies in patient-derived colorectal cancer organoids indicate that genetic and cellular heterogeneity are chronologically modified²³². The genetic heterogeneity in CRC organoids was retained at the initial culture phase²³². However, mutational profiling in microsatellite stable and microsatellite instable organoids over longer terms indicated acquired *de novo* non-synonymous mutations, especially in microsatellite instable CRC organoids²³². Furthermore, fluorescent-labeled cell tracing revealed clonal dominance in CRC organoids after 30-40 days in culture²³². Two additional studies on human intestinal organoids reported an effect of medium composition on clonal evolution, indicating that media-dependent enrichment of cells with specific oncogenic mutations can occur *in vitro*^{296,349}. Therefore, mutational or functional analysis in longer-term cultures needs to be carefully interpreted, keeping in mind potential compositional drifts.

Another challenge is the exact definition of responder/non-responder *in vitro*. Larger patient cohorts will be required to validate whether the selected thresholds are robust enough. In addition to the rare patient cases where clinical response data is available, using known resistant- and sensitive cell lines for a particular treatment could help establish a more robust cutoff that segregates responders from non-responders *in vitro*. Additional readouts for drug response (e.g., apoptosis or cell death assays) could also help define *in vitro* sensitivity. However, it is currently unclear whether these assays correlate with patient clinical response, as has been shown in several studies using the current gold standard of metabolic surrogate assays^{287,291,298,300}. Alternative extracellular matrix components such as thermoreversible hydrogels (e.g., CyGel) may facilitate imaging tumoroids to derive additional readouts on cell viability upon drug treatment^{350,351}. Improvements to control uniform tumoroid size could be achieved using microcavity technologies (e.g., Corning Elplasia Plates) and enhancing comparability between different tumor specimens.

With the current system, the precise composition of tumor and stromal cells cannot be fully controlled. Nonetheless, factors secreted by the stromal compartment may contribute to the success of our short-term model compared to previous methods. Low throughput organotypic slice cultures, which incorporate the actual tumor microenvironment, have been successfully established for GEP-NENs^{234,235} and are better suited for studying complex interactions between stromal and tumoral compartments in greater detail.

The presented approach aims at a rapid *ex vivo* and simple drug screen of drug panels in the context of companion diagnostics that allow timely monitoring and potentially early interventions upon drug treatment. In an ideal scenario, PD tumoroids derived from a single patient could be used to assess *in vitro* sensitivity and draw conclusions about the patient's clinical response. Several studies using patient-derived tumor organoids for personalized medicine approaches have shown great promise^{291,300}, but additional research is required. Increasing efforts in molecular subtyping of PanNENs deciphered the clinical relevance of molecular profiles^{33,68,149,151,336}. NEN primary cell cultures, however, add a functional and mechanistic layer that may complement all of these efforts. Patient-derived tumor organoids and cell lines from a single PDAC patient were analyzed to comprehend adaptive processes in tumor evolution and treatment-induced selection pressure³⁵². Neither transcriptional PDAC subtyping nor genomics enables the implementation of molecularly informed therapies³⁵². Nevertheless, functional screening revealed relevant chemotherapy-induced treatment vulnerabilities, highlighting the significance of functional layers in precision medicine³⁵². Because tumor cell plasticity is frequently mediated by epigenetic mechanisms, combining DNA methylation and transcriptomic profiling with functional drug screens in PanNENs may be superior to any single modality alone. Thousands of potential anticancer therapies exist but have not been evaluated across most tumor entities³⁵³. Systematic testing in relevant patient-derived preclinical models allows assessing *in vitro* sensitivity for many compounds³⁴⁷ and may serve as a complementary approach to create a foundation for translational applications³²⁶. In this regard PanNEN tumoroids may allow evaluation of second-line therapies in a scenario of therapy resistance or tumor progression.

Our findings revealed another novel approach to studying functional NEN biology: transcriptome-based treatment discovery. Molecular perturbational profiling in GEP-NEN tumoroids at sublethal drug doses revealed two clinically relevant targets for cisplatin combination therapy, which were then validated in a subset of patient samples. Such insights into the molecular stress response in patient-derived GEP-NEN samples have not previously been reported in the field, and they may lay the groundwork for extensive mechanistic studies in organoid-, cell line-, or animal models. A recent large-scale screen of 2025 drug combinations in a panel of 125 cell lines, including breast, colorectal, and pancreatic cancer, highlighted the efficiency of combinational therapies in weak-to-moderate single agents²⁶⁵. Synergistic interactions were rare but significantly enriched in combinations of chemotherapeutics and apoptotic signaling, and cell-cycle targeting inhibitors²⁶⁵. Although at a much smaller scope, similar drug screens might also be established in patient-derived GEP-

NEN models using platforms such as Nexus at the Swiss Federal Institute of Technology in Zurich. Our findings show that variable intertumoral heterogeneity is reflected in differential drug sensitivity. Given the high tumor heterogeneity observed in PanNENs, further intra-tumor heterogeneity and tumor evolution research appear promising. In other cancer entities, patient-derived tumor organoid lines were a valuable tool for studying these aspects in a more controlled setting. A study in patient-derived tumor organoids reported that *in vitro* drug response differed between tumor lesions in a single colorectal cancer patient³⁰⁰. Similarly, patient-derived organoids from metastatic CRC were able to capture spatiotemporal intratumor mutational heterogeneity when established from multiple biopsies²⁹¹. A recent study in clonal organoids from human colorectal cancer showed that CRC organoids stably retain intra-tumor mutational-, methylation-, and transcriptional diversification, which was exploited to study tumoral evolution and biological response to therapeutics³⁵⁴. CRC organoid clones from the same patients revealed diversification of drug response (Roerink *et al.* 2018). Interestingly, differences in response to cancer drugs in closely related individual tumor cells were partially linked to driver mutations in cancer genes (e.g., *TP53*)³⁵⁴. Although cell expansion in general, and clonal expansion in particular, is currently severely restricted in patient-derived PanNENs tumoroids, studying different lesions *in vitro* may be possible and shed light on this aspect. The emergence of single-cell technologies may also allow for assessing PD tumoroids' clonal composition over multiple culture time points, providing novel insights into the complex cellular setup of PanNENs tumoroids and their biological functioning. Overall, using patient-derived multicellular tumor spheroids may allow researchers to study tumor heterogeneity in PanNEN patients and better understand how individual tumors respond to therapy. This could open up new avenues for determining the next therapeutic steps in situations where standard clinical options have been exhausted.

The correlation observed between PD tumoroid, and patient clinical response must be confirmed in larger GEP-NEN patient cohorts and clinical trials. A positive association in larger patient cohorts would support the use of PD tumoroids to complement existing strategies and enhance personalized medicine approaches to aid in treatment selection if observed in larger patient cohorts. It would also make a case for additional tissue sampling, which must be carefully weighed against the risks of complications and the patient's quality of life. Currently, our culture workflow relies on cryopreserved tumor resections. However, for translational application, this will need to be adapted to tumor biopsies. It will be essential to optimize and streamline the logistic collection, subsequent isolation, and culture conditions for fresh biopsies to minimize material loss. As highlighted in a recent prospective interventional organoid trial,

a sufficient cell yield and high culture success rates are among the most influential factors facilitating application in prospective clinical trials³⁰⁰. Furthermore, biopsies should ideally reflect the patient's situation directly prior to the upcoming therapeutic intervention, which is technically feasible given our workflow's short turnaround times. As previously discussed, rigorous quality controls for PD tumoroid cultures (e.g., internal controls, data quality, specimen quality) must be ensured for future clinical trials³⁴⁷. A critical parameter to be accounted for PD tumoroid-guided clinical trials will be the rational design of the drug screen³⁴⁷. Because intra-tumoral drug concentrations are not frequently assessed or reported for many drugs, testing the maximal plasma concentration (C_{max}) may provide a conservative but relevant estimate of drug sensitivity. Organoids of highly proliferative cells reach a critical size, limiting proliferative capacity and necessitating passaging, media renewal, and additional manipulation after 10-12 days^{303,355}. The 7-day exposure time implemented in our workflow may allow a sufficiently large window to observe *in vitro* sensitivities without requiring additional manipulation. Moreover, it allows realistically estimated growth rates, which can then be corrected using growth rate inhibition metrics^{356,357}, making the comparison between different PD tumoroids more accurate. Altogether, our presented setup aligns well with these critical parameters from pioneering organoid-guided clinical trials and may allow efficient translation into prospective trials. Such studies may resolve some of the current questions since patient-derived tumoroids may allow channeling molecular results into appropriate personalized therapy testing.

5 References

1. Schimmack, S., Svejda, B., Lawrence, B., Kidd, M. & Modlin, I. M. The diversity and commonalities of gastroenteropancreatic neuroendocrine tumors. *Langenbecks Arch. Surg.* **396**, 273–298 (2011).
2. Roth, K. A., Hertz, J. M. & Gordon, J. I. Mapping enteroendocrine cell populations in transgenic mice reveals an unexpected degree of complexity in cellular differentiation within the gastrointestinal tract. *J. Cell Biol.* **110**, 1791–1801 (1990).
3. Sjölund, K. Endocrine Cells in Human Intestine: An Immunocytochemical Study. 11 (1983).
4. Kidd, M., Modlin, I. M., Bodei, L. & Drozdov, I. Decoding the Molecular and Mutational Ambiguities of Gastroenteropancreatic Neuroendocrine Neoplasm Pathobiology. *Cell. Mol. Gastroenterol. Hepatol.* **1**, 131–153 (2015).
5. Klöppel, G. Classification and pathology of gastroenteropancreatic neuroendocrine neoplasms. *Endocr. Relat. Cancer* **18**, S1–S16 (2011).
6. Modlin, I. M. *et al.* Gastroenteropancreatic neuroendocrine tumours. 12 (2008).
7. Wiedenmann, B., John, M., Ahnert-Hilger, G. & Riecken, E.-O. Molecular and cell biological aspects of neuroendocrine tumors of the gastroenteropancreatic system. *J. Mol. Med.* **76**, 637–647 (1998).
8. Nagtegaal, I. D. *et al.* The 2019 WHO classification of tumours of the digestive system. *Histopathology* **76**, 182–188 (2020).
9. Dasari, A. *et al.* Trends in the Incidence, Prevalence, and Survival Outcomes in Patients With Neuroendocrine Tumors in the United States. *JAMA Oncol.* **3**, 1335–1342 (2017).
10. Fraenkel, M. *et al.* Incidence of gastroenteropancreatic neuroendocrine tumours: a systematic review of the literature. *Endocr. Relat. Cancer* **21**, R153–163 (2014).
11. Huguet, L., Grossman, A. B. & O’Toole, D. Changes in the Epidemiology of Neuroendocrine Tumours. *Neuroendocrinology* **104**, 105–111 (2017).
12. Leoncini, E. *et al.* Increased incidence trend of low-grade and high-grade neuroendocrine neoplasms. *Endocrine* **58**, 368–379 (2017).
13. Dasari, A., Mehta, K., Byers, L. A., Sorbye, H. & Yao, J. C. Comparative study of lung and extrapulmonary poorly differentiated neuroendocrine carcinomas: A SEER database analysis of 162,983 cases. *Cancer* **124**, 807–815 (2018).
14. Nuñez-Valdovinos, B. *et al.* Neuroendocrine Tumor Heterogeneity Adds Uncertainty to the World Health Organization 2010 Classification: Real-World Data from the Spanish Tumor Registry (R-GETNE). *The Oncologist* **23**, 422–432 (2018).
15. Lloyd, R., Osamura, R., Klöppel, G. & Rosai, J. *WHO Classification of Tumours of Endocrine Organs*. vol. 10 (World Health Organisation, 2017).
16. World Classification of Tumours Editorial Board. *WHO Classification of Tumours. Digestive System Tumours*. (IARC Press, 2019).
17. Brierley, J. D., Gospodarowicz, M. K. & Wittekind, C. *TNM Classification of Malignant Tumours, 8th Edition*. (Wiley & Sons, 2016).
18. Modlin, I. M., Lye, K. D. & Kidd, M. A 5-decade analysis of 13,715 carcinoid tumors. *Cancer* **97**, 934–959 (2003).
19. Pavel, M. *et al.* Gastroenteropancreatic neuroendocrine neoplasms: ESMO Clinical Practice Guidelines for diagnosis, treatment and follow-up. *Ann. Oncol.* **31**, 844–860 (2020).
20. Perren, A. *et al.* ENETS Consensus Guidelines for the Standards of Care in Neuroendocrine Tumors: Pathology - Diagnosis and Prognostic Stratification. *Neuroendocrinology* **105**, 196–200 (2017).
21. Rindi, G. *et al.* TNM staging of midgut and hindgut (neuro) endocrine tumors: a consensus proposal including a grading system. *Virchows Arch.* **451**, 757–762 (2007).
22. Bosman, Carneiro, Hruban & Theise. *WHO Classification of Tumours of the Digestive System*. (2010).
23. Kos-Kudła, B. *et al.* ENETS Consensus Guidelines for the Management of Bone and Lung Metastases from Neuroendocrine Tumors. *Neuroendocrinology* **91**, 341–350 (2010).
24. Madeira, I. *et al.* Prognostic factors in patients with endocrine tumours of the duodenopancreatic area. *Gut* **43**, 422–427 (1998).
25. Mazzaferro, V., Pulvirenti, A. & Coppa, J. Neuroendocrine tumors metastatic to the liver: how to select patients for liver transplantation? *J. Hepatol.* **47**, 460–466 (2007).
26. Nigri, G. *et al.* Treatment options for PNET liver metastases: a systematic review. *World J. Surg. Oncol.* **16**, 142 (2018).
27. Pavel, M. *et al.* ENETS Consensus Guidelines Update for the Management of Distant Metastatic Disease of Intestinal, Pancreatic, Bronchial Neuroendocrine Neoplasms (NEN) and NEN of Unknown Primary Site. *Neuroendocrinology* **103**, 172–185 (2016).
28. Hallet, J. *et al.* Exploring the rising incidence of neuroendocrine tumors: a population-based analysis of epidemiology, metastatic presentation, and outcomes. *Cancer* **121**, 589–597 (2015).
29. Esposito, I., Segler, A., Steiger, K. & Klöppel, G. Pathology, genetics and precursors of human and experimental pancreatic neoplasms: An update. *Pancreatol.* **15**, 598–610 (2015).
30. Hackeng, W. M. *et al.* Aberrant Menin expression is an early event in pancreatic neuroendocrine tumorigenesis. *Hum. Pathol.* **56**, 93–100 (2016).
31. Perren, A. *et al.* Multiple endocrine neoplasia type 1 (MEN1): loss of one MEN1 allele in tumors and monohormonal endocrine cell clusters but not in islet hyperplasia of the pancreas. *J. Clin. Endocrinol. Metab.* **92**, 1118–1128 (2007).
32. Klöppel, G., Anlauf, M., Perren, A. & Sipos, B. Hyperplasia to Neoplasia Sequence of Duodenal and Pancreatic Neuroendocrine Diseases and Pseudohyperplasia of the PP-cells in the Pancreas. *Endocr. Pathol.* **25**, 181–185 (2014).
33. Scarpa, A. *et al.* Whole-genome landscape of pancreatic neuroendocrine tumours. *Nature* **543**, 65–71 (2017).
34. Vandamme, T. *et al.* Hotspot DAXX, PTCH2 and CYFIP2 mutations in pancreatic neuroendocrine neoplasms. *Endocr. Relat. Cancer* **26**, 1–12 (2019).
35. Lawrence, B. *et al.* Recurrent loss of heterozygosity correlates with clinical outcome in pancreatic neuroendocrine cancer. *Npj Genomic Med.* **3**, 18 (2018).
36. Corbo, V. *et al.* Pancreatic endocrine tumours: mutational and immunohistochemical survey of protein kinases reveals alterations in targetable kinases in cancer cell lines and rare primaries. *Ann. Oncol.* **23**, 127–134 (2012).
37. Jiao, Y. *et al.* DAXX/ATRAX, MEN1, and mTOR Pathway Genes Are Frequently Altered in Pancreatic Neuroendocrine Tumors. *Science* **331**, 1199–1203 (2011).
38. Kim, D. H. *et al.* Allelic alterations in well-differentiated neuroendocrine tumors (carcinoid tumors) identified by genome-wide single nucleotide polymorphism analysis and comparison with pancreatic endocrine tumors. *Genes. Chromosomes Cancer* **47**, 84–92 (2008).
39. Zikusoka, M. N., Kidd, M., Eick, G., Latich, I. & Modlin, I. M. The molecular genetics of gastroenteropancreatic neuroendocrine tumors. *Cancer* **104**, 2292–2309 (2005).
40. Marinoni, I. *et al.* Loss of DAXX and ATRX Are Associated With Chromosome Instability and Reduced Survival of Patients With Pancreatic Neuroendocrine Tumors. *Gastroenterology* **146**, 453–460.e5 (2014).
41. Dreijerink, K. M. A., Timmers, H. T. M. & Brown, M. Twenty years of menin: emerging opportunities for restoration of transcriptional regulation in MEN1. *Endocr. Relat. Cancer* **24**, T135–T145 (2017).
42. Agarwal, S. K. & Jothi, R. Genome-Wide Characterization of Menin-Dependent H3K4me3 Reveals a Specific Role for Menin in the Regulation of Genes Implicated in MEN1-Like Tumors. *PLOS ONE* **7**, e37952 (2012).

43. Hughes, C. M. *et al.* Menin Associates with a Trithorax Family Histone Methyltransferase Complex and with the Hoxc8 Locus. *Mol. Cell* **13**, 587–597 (2004).
44. Yokoyama, A. *et al.* Leukemia Proto-Oncoprotein MLL Forms a SET1-Like Histone Methyltransferase Complex with Menin To Regulate Hox Gene Expression. *Mol. Cell. Biol.* **24**, 5639–5649 (2004).
45. Raj, N. P. *et al.* Next-generation sequencing (NGS) in advanced well differentiated pancreatic neuroendocrine tumors (WD pNETs): A study using MSK-IMPACT. *J. Clin. Oncol.* **34**, 246–246 (2016).
46. Heaphy, C. M. *et al.* Altered Telomeres in Tumors with ATRX and DAXX Mutations. *Science* **333**, 425–425 (2011).
47. Lovejoy, C. A. *et al.* Loss of ATRX, Genome Instability, and an Altered DNA Damage Response Are Hallmarks of the Alternative Lengthening of Telomeres Pathway. *PLOS Genet.* **8**, e1002772 (2012).
48. Luchini, C. *et al.* Alternative Lengthening of Telomeres (ALT) in Pancreatic Neuroendocrine Tumors: Ready for Prime-Time in Clinical Practice? *Curr. Oncol. Rep.* **23**, 106 (2021).
49. Singhi, A. D. *et al.* Alternative Lengthening of Telomeres and Loss of DAXX/ATRX Expression Predicts Metastatic Disease and Poor Survival in Patients with Pancreatic Neuroendocrine Tumors. *Clin. Cancer Res.* **23**, 600–609 (2017).
50. Roy, S. *et al.* Loss of Chromatin-Remodeling Proteins and/or CDKN2A Associates With Metastasis of Pancreatic Neuroendocrine Tumors and Reduced Patient Survival Times. *Gastroenterology* **154**, 2060–2063.e8 (2018).
51. de Wilde, R. F., Edil, B. H., Hruban, R. H. & Maitra, A. Well-differentiated pancreatic neuroendocrine tumors: from genetics to therapy. *Nat. Rev. Gastroenterol. Hepatol.* **9**, 199–208 (2012).
52. Drané, P., Ouarrhni, K., Depaux, A., Shuaib, M. & Hamiche, A. The death-associated protein DAXX is a novel histone chaperone involved in the replication-independent deposition of H3.3. *Genes Dev.* **24**, 1253–1265 (2010).
53. Goldberg, A. D. *et al.* Distinct Factors Control Histone Variant H3.3 Localization at Specific Genomic Regions. *Cell* **140**, 678–691 (2010).
54. Lewis, P. W., Elsaesser, S. J., Noh, K.-M., Stadler, S. C. & Allis, C. D. Daxx is an H3.3-specific histone chaperone and cooperates with ATRX in replication-independent chromatin assembly at telomeres. *Proc. Natl. Acad. Sci.* **107**, 14075–14080 (2010).
55. He, Q. *et al.* The Daxx/Atxr Complex Protects Tandem Repetitive Elements during DNA Hypomethylation by Promoting H3K9 Trimethylation. *Cell Stem Cell* **17**, 273–286 (2015).
56. Zhang, H. *et al.* Methylation of RASSF1A gene promoter is regulated by p53 and DAXX. *FASEB J.* **27**, 232–242 (2013).
57. Albanel, J., Dalmases, A., Rovira, A. & Rojo, F. mTOR signaling in human cancer. *Clin. Transl. Oncol.* **9**, 484–493 (2007).
58. Easton, J. B. & Houghton, P. J. mTOR and cancer therapy. *Oncogene* **25**, 6436–6446 (2006).
59. Mamane, Y., Petroulakis, E., LeBacquer, O. & Sonenberg, N. mTOR, translation initiation and cancer. *Oncogene* **25**, 6416–6422 (2006).
60. Missiaglia, E. *et al.* Pancreatic Endocrine Tumors: Expression Profiling Evidences a Role for AKT-mTOR Pathway. *J. Clin. Oncol.* **28**, 245–255 (2010).
61. Yao, J. C. *et al.* Everolimus for Advanced Pancreatic Neuroendocrine Tumors. *N. Engl. J. Med.* **364**, 514–523 (2011).
62. Yao, J. C. *et al.* Genomic profiling of NETs: a comprehensive analysis of the RADIANT trials. *Endocr. Relat. Cancer* (2019) doi:10.1530/ERC-18-0332.
63. Scarpa, A. The landscape of molecular alterations in pancreatic and small intestinal neuroendocrine tumours. *Ann. Endocrinol.* **80**, 153–158 (2019).
64. Cao, Y. *et al.* Whole exome sequencing of insulinoma reveals recurrent T372R mutations in *YY1*. *Nat. Commun.* **4**, 2810 (2013).
65. Cromer, M. K. *et al.* Neomorphic effects of recurrent somatic mutations in Yin Yang 1 in insulin-producing adenomas. *Proc. Natl. Acad. Sci.* **112**, 4062–4067 (2015).
66. Hong, X. *et al.* Whole-genome sequencing reveals distinct genetic bases for insulinomas and non-functional pancreatic neuroendocrine tumours: leading to a new classification system. *Gut* (2019) doi:10.1136/gutjnl-2018-317233.
67. Wang, H. *et al.* Insights into beta cell regeneration for diabetes via integration of molecular landscapes in human insulinomas. *Nat. Commun.* **8**, 1–15 (2017).
68. Di Domenico, A. *et al.* Epigenetic landscape of pancreatic neuroendocrine tumours reveals distinct cells of origin and means of tumour progression. <http://biorxiv.org/lookup/doi/10.1101/2020.04.08.029785> (2020) doi:10.1101/2020.04.08.029785.
69. Pea, A. *et al.* Genetic Analysis of Small Well-differentiated Pancreatic Neuroendocrine Tumors Identifies Subgroups With Differing Risks of Liver Metastases: *Ann. Surg.* **271**, 566–573 (2020).
70. Venizelos, A. *et al.* The molecular characteristics of high-grade gastroenteropancreatic neuroendocrine neoplasms. *Endocr. Relat. Cancer* **29**, 1–14 (2022).
71. Bergsland, E. K. *et al.* Genomic profiling to distinguish poorly differentiated neuroendocrine carcinomas arising in different sites. *J. Clin. Oncol.* **34**, 4020–4020 (2016).
72. Tang, L. H., Basturk, O., Sue, J. J. & Klimstra, D. S. A Practical Approach to the Classification of WHO Grade 3 (G3) Well-differentiated Neuroendocrine Tumor (WD-NET) and Poorly Differentiated Neuroendocrine Carcinoma (PD-NEC) of the Pancreas. *Am. J. Surg. Pathol.* **40**, 1192–1202 (2016).
73. Lacombe, C. *et al.* Biomarkers of Response to Etoposide-Platinum Chemotherapy in Patients with Grade 3 Neuroendocrine Neoplasms. *Cancers* **13**, 643 (2021).
74. Yachida, S. *et al.* Small Cell and Large Cell Neuroendocrine Carcinomas of the Pancreas Are Genetically Similar and Distinct from Well-differentiated Pancreatic Neuroendocrine Tumors. *Am. J. Surg. Pathol.* **36**, 173–184 (2012).
75. Capdevila, J. *et al.* Epigenetic EGFR Gene Repression Confers Sensitivity to Therapeutic BRAFV600E Blockade in Colon Neuroendocrine Carcinomas. *Clin. Cancer Res.* **26**, 902–909 (2020).
76. Konukiewitz, B. *et al.* Pancreatic neuroendocrine carcinomas reveal a closer relationship to ductal adenocarcinomas than to neuroendocrine tumors G3. *Hum. Pathol.* **77**, 70–79 (2018).
77. Lee, S. M. & Sung, C. O. Comprehensive analysis of mutational and clinicopathologic characteristics of poorly differentiated colorectal neuroendocrine carcinomas. *Sci. Rep.* **11**, 6203 (2021).
78. Puccini, A. *et al.* Comprehensive Genomic Profiling of Gastroenteropancreatic Neuroendocrine Neoplasms (GEP-NENs). *Clin. Cancer Res.* **26**, 5943–5951 (2020).
79. Shamir, E. R. *et al.* Identification of high-risk human papillomavirus and Rb/E2F pathway genomic alterations in mutually exclusive subsets of colorectal neuroendocrine carcinoma. *Mod. Pathol. Off. J. U. S. Can. Acad. Pathol. Inc* **32**, 290–305 (2019).
80. Takizawa, N. *et al.* Molecular characteristics of colorectal neuroendocrine carcinoma; similarities with adenocarcinoma rather than neuroendocrine tumor. *Hum. Pathol.* **46**, 1890–1900 (2015).
81. Vijayvergia, N. *et al.* Molecular profiling of neuroendocrine malignancies to identify prognostic and therapeutic markers: a Fox Chase Cancer Center Pilot Study. *Br. J. Cancer* **115**, 564–570 (2016).
82. Kimiloğlu Şahan, E. *et al.* P53, KI-67, CD117 expression in gastrointestinal and pancreatic neuroendocrine tumours and evaluation of their correlation with clinicopathological and prognostic parameters. *Turk. J. Gastroenterol. Off. J. Turk. Soc. Gastroenterol.* **26**, 104–111 (2015).

83. Mafficini, A. & Scarpa, A. Genetics and Epigenetics of Gastroenteropancreatic Neuroendocrine Neoplasms. *Endocr. Rev.* **40**, 506–536 (2019).
84. Pizzi, S. *et al.* Genetic alterations in poorly differentiated endocrine carcinomas of the gastrointestinal tract. *Cancer* **98**, 1273–1282 (2003).
85. Chedgy, E. C. *et al.* Biallelic tumour suppressor loss and DNA repair defects in de novo small-cell prostate carcinoma. *J. Pathol.* **246**, 244–253 (2018).
86. Kawasaki, K. *et al.* An Organoid Biobank of Neuroendocrine Neoplasms Enables Genotype-Phenotype Mapping. *Cell* **183**, 1420–1435.e21 (2020).
87. van Riet, J. *et al.* The genomic landscape of 85 advanced neuroendocrine neoplasms reveals subtype-heterogeneity and potential therapeutic targets. *Nat. Commun.* **12**, 4612 (2021).
88. Yachida, S. *et al.* Comprehensive Genomic Profiling of Neuroendocrine Carcinomas of the Gastrointestinal System. *Cancer Discov.* [candisc;2159-8290.CD-21-0669v3](https://doi.org/10.1158/2159-8290.CD-21-0669) (2021) doi:10.1158/2159-8290.CD-21-0669.
89. Busico, A. *et al.* Gastroenteropancreatic High-Grade Neuroendocrine Neoplasms: Histology and Molecular Analysis, Two Sides of the Same Coin. *Neuroendocrinology* **110**, 616–629 (2020).
90. Chen, L. *et al.* Genetic Characteristics of Colorectal Neuroendocrine Carcinoma: More Similar to Colorectal Adenocarcinoma. *Clin. Colorectal Cancer* **20**, 177–185.e13 (2021).
91. Raj, N. & Reidy-Lagunes, D. Systemic Therapies for Advanced Pancreatic Neuroendocrine Tumors. *Hematol. Oncol. Clin. North Am.* **30**, 119–133 (2016).
92. de Mestier, L. *et al.* Digestive Neuroendocrine Neoplasms (NEN): French Intergroup clinical practice guidelines for diagnosis, treatment and follow-up (SNFGE, GTE, RENATEN, TENPATH, FPCD, GERCOR, UNICANCER, SFCD, SFED, SFRO, SFR). *Dig. Liver Dis.* **52**, 473–492 (2020).
93. Jilesen, A. P. J. *et al.* Postoperative Complications, In-Hospital Mortality and 5-Year Survival After Surgical Resection for Patients with a Pancreatic Neuroendocrine Tumor: A Systematic Review. *World J. Surg.* **40**, 729–748 (2016).
94. Mestier, L. de *et al.* Evaluating digestive neuroendocrine tumor progression and therapeutic responses in the era of targeted therapies: state of the art. *Endocr. Relat. Cancer* **21**, R105–R120 (2014).
95. Sarmiento, J. M., Farnell, M. B., Que, F. G. & Nagorney, D. M. Pancreaticoduodenectomy for islet cell tumors of the head of the pancreas: long-term survival analysis. *World J. Surg.* **26**, 1267–1271 (2002).
96. Frilling, A. *et al.* Recommendations for management of patients with neuroendocrine liver metastases. *Lancet Oncol.* **15**, e8–e21 (2014).
97. Modlin, I. M., Pavel, M., Kidd, M. & Gustafsson, B. I. Review article: somatostatin analogues in the treatment of gastroenteropancreatic neuroendocrine (carcinoid) tumours. *Aliment. Pharmacol. Ther.* **31**, 169–188 (2010).
98. Reichlin, S. Secretion of somatostatin and its physiologic function. *J. Lab. Clin. Med.* **109**, 320–326 (1987).
99. Nilsson, O. *et al.* Comparative studies on the expression of somatostatin receptor subtypes, outcome of octreotide scintigraphy and response to octreotide treatment in patients with carcinoid tumours. *Br. J. Cancer* **77**, 632–637 (1998).
100. Patel, Y. C. *et al.* The somatostatin receptor family. *Life Sci.* **57**, 1249–1265 (1995).
101. Corleto, V. D., Nasoni, S., Panzuto, F., Cassetta, S. & Fave, G. D. Somatostatin receptor subtypes: basic pharmacology and tissue distribution. *Dig. Liver Dis.* **36**, S8–S16 (2004).
102. Reubi, J. C., Kvolts, L., Krenning, E. & Lamberts, S. W. J. Distribution of somatostatin receptors in normal and tumor tissue. *Metabolism* **39**, 78–81 (1990).
103. Panzuto, F. *et al.* Long-term clinical outcome of somatostatin analogues for treatment of progressive, metastatic, well-differentiated entero-pancreatic endocrine carcinoma. *Ann. Oncol. Off. J. Eur. Soc. Med. Oncol.* **17**, 461–466 (2006).
104. Shojamaneh, H. *et al.* Prospective study of the antitumor efficacy of long-term octreotide treatment in patients with progressive metastatic gastrinoma. *Cancer* **94**, 331–343 (2002).
105. Caplin, M. E. *et al.* Lanreotide in Metastatic Enteropancreatic Neuroendocrine Tumors. *N. Engl. J. Med.* **371**, 224–233 (2014).
106. Rinke, A. *et al.* Placebo-Controlled, Double-Blind, Prospective, Randomized Study on the Effect of Octreotide LAR in the Control of Tumor Growth in Patients With Metastatic Neuroendocrine Midgut Tumors: A Report From the PROMID Study Group. *J. Clin. Oncol.* **27**, 4656–4663 (2009).
107. Faivre, S., Kroemer, G. & Raymond, E. Current development of mTOR inhibitors as anticancer agents. *Nat. Rev. Drug Discov.* **5**, 671–688 (2006).
108. Meric-Bernstam, F. & Gonzalez-Angulo, A. M. Targeting the mTOR Signaling Network for Cancer Therapy. *J. Clin. Oncol.* **27**, 2278–2287 (2009).
109. Corradetti, M. N. & Guan, K.-L. Upstream of the mammalian target of rapamycin: do all roads pass through mTOR? *Oncogene* **25**, 6347–6360 (2006).
110. Shida, T. *et al.* Expression of an activated mammalian target of rapamycin (mTOR) in gastroenteropancreatic neuroendocrine tumors. *Cancer Chemother. Pharmacol.* **65**, 889–893 (2010).
111. Yao, J. C. *et al.* Daily Oral Everolimus Activity in Patients With Metastatic Pancreatic Neuroendocrine Tumors After Failure of Cytotoxic Chemotherapy: A Phase II Trial. *J. Clin. Oncol.* **28**, 69–76 (2010).
112. Kulke, M. H. *et al.* A randomized, open-label, phase 2 study of everolimus in combination with pasireotide LAR or everolimus alone in advanced, well-differentiated, progressive pancreatic neuroendocrine tumors: COOPERATE-2 trial. *Ann. Oncol.* **28**, 1309–1315 (2017).
113. Faivre, S., Kroemer, G. & Raymond, E. Current development of mTOR inhibitors as anticancer agents. *Nat. Rev. Drug Discov.* **5**, 671–688 (2006).
114. Mendel, D. B. *et al.* In Vivo Antitumor Activity of SU11248, a Novel Tyrosine Kinase Inhibitor Targeting Vascular Endothelial Growth Factor and Platelet-derived Growth Factor Receptors: Determination of a Pharmacokinetic/Pharmacodynamic Relationship. *Clin. Cancer Res.* **9**, 327–337 (2003).
115. Pietras, K. & Hanahan, D. A Multitargeted, Metronomic, and Maximum-Tolerated Dose “Chemo-Switch” Regimen is Antiangiogenic, Producing Objective Responses and Survival Benefit in a Mouse Model of Cancer. *J. Clin. Oncol.* **23**, 939–952 (2005).
116. Casanovas, O., Hicklin, D. J., Bergers, G. & Hanahan, D. Drug resistance by evasion of antiangiogenic targeting of VEGF signaling in late-stage pancreatic islet tumors. *Cancer Cell* **8**, 299–309 (2005).
117. Inoue, S., Lemonnier, F. & Mak, T. W. Roles of IDH1/2 and TET2 mutations in myeloid disorders. *Int. J. Hematol.* **103**, 627–633 (2016).
118. Fjällskog, M.-L., Hessman, O., Eriksson, B. & Tiensuu Janson, E. Upregulated expression of PDGF receptor beta in endocrine pancreatic tumors and metastases compared to normal endocrine pancreas. *Acta Oncol.* **46**, 741–746 (2007).
119. Fjällskog, M.-L. H., Lejonklou, M. H., Eriksson, B. K. & Janson, E. T. Expression of Molecular Targets for Tyrosine Kinase Receptor Antagonists in Malignant Endocrine Pancreatic Tumors. **5** (2003).

120. Hansel, D. E. *et al.* Liver Metastases Arising from Well-Differentiated Pancreatic Endocrine Neoplasms Demonstrate Increased VEGF-C Expression. *Mod. Pathol.* **16**, 652–659 (2003).
121. Raymond, E. *et al.* Sunitinib malate for the treatment of pancreatic neuroendocrine tumors. *N. Engl. J. Med.* **364**, 501–513 (2011).
122. Faivre, S. *et al.* Safety, Pharmacokinetic, and Antitumor Activity of SU11248, a Novel Oral Multitarget Tyrosine Kinase Inhibitor, in Patients With Cancer. *J. Clin. Oncol.* (2016) doi:10.1200/JCO.2005.02.2194.
123. Kulke, M. H. *et al.* Activity of Sunitinib in Patients With Advanced Neuroendocrine Tumors. *J. Clin. Oncol.* **26**, 3403–3410 (2008).
124. Waldherr, C. *et al.* Tumor response and clinical benefit in neuroendocrine tumors after 7.4 GBq (90)Y-DOTATOC. *J. Nucl. Med. Off. Publ. Soc. Nucl. Med.* **43**, 610–616 (2002).
125. Brabander, T. *et al.* Long-Term Efficacy, Survival, and Safety of [177Lu-DOTA0,Tyr3]octreotate in Patients with Gastroenteropancreatic and Bronchial Neuroendocrine Tumors. *Clin. Cancer Res. Off. J. Am. Assoc. Cancer Res.* **23**, 4617–4624 (2017).
126. Bushnell Jr., D. L. *et al.* 90Y-edotreotide for metastatic carcinoid refractory to octreotide. *J. Clin. Oncol.* **28**, 1652–1659 (2010).
127. Kwekkeboom, D. J. *et al.* Treatment with the radiolabeled somatostatin analog [177Lu-DOTA0,Tyr3]octreotate: Toxicity, efficacy, and survival. *J. Clin. Oncol.* **26**, 2124–2130 (2008).
128. Severi, S. *et al.* Peptide receptor radionuclide therapy in the management of gastrointestinal neuroendocrine tumors: Efficacy profile, safety, and quality of life. *OncoTargets Ther.* **10**, 551–557 (2017).
129. Carlsen, E. A. *et al.* Peptide receptor radionuclide therapy in gastroenteropancreatic NEN G3: a multicenter cohort study. *Endocr. Relat. Cancer* **26**, 227–239 (2019).
130. Nicolini, S. *et al.* Investigation of receptor radionuclide therapy with 177Lu-DOTATATE in patients with GEP-NEN and a high Ki-67 proliferation index. *Eur. J. Nucl. Med. Mol. Imaging* **45**, 923–930 (2018).
131. Thang, S. P. *et al.* Peptide receptor radionuclide therapy (PRRT) in European Neuroendocrine Tumour Society (ENETS) grade 3 (G3) neuroendocrine neoplasia (NEN) - a single-institution retrospective analysis. *Eur. J. Nucl. Med. Mol. Imaging* **45**, 262–277 (2018).
132. Zhang, J. *et al.* Peptide Receptor Radionuclide Therapy in Grade 3 Neuroendocrine Neoplasms: Safety and Survival Analysis in 69 Patients. *J. Nucl. Med.* **60**, 377–385 (2019).
133. Botling, J. *et al.* High-grade progression confers poor survival in pancreatic neuroendocrine tumors. *Neuroendocrinology* (2019) doi:10.1159/000504392.
134. Vyas, M., Tang, L. H., Rekhman, N. & Klimstra, D. S. Alterations in Ki67 Labeling Following Treatment of Poorly Differentiated Neuroendocrine Carcinomas: A Potential Diagnostic Pitfall. *Am. J. Surg. Pathol.* **45**, 25–34 (2021).
135. Walter, T. *et al.* Poorly differentiated gastro-entero-pancreatic neuroendocrine carcinomas: Are they really heterogeneous? Insights from the FFCD-GTE national cohort. *Eur. J. Cancer* **79**, 158–165 (2017).
136. Garcia-Carbonero, R. *et al.* ENETS Consensus Guidelines for High-Grade Gastroenteropancreatic Neuroendocrine Tumors and Neuroendocrine Carcinomas. *Neuroendocrinology* **103**, 186–194 (2016).
137. Sorbye, H. *et al.* Predictive and prognostic factors for treatment and survival in 305 patients with advanced gastrointestinal neuroendocrine carcinoma (WHO G3): The NORDIC NEC study. *Ann. Oncol.* **24**, 152–160 (2013).
138. Fu, D., Calvo, J. A. & Samson, L. D. Balancing repair and tolerance of DNA damage caused by alkylating agents. *Nat. Rev. Cancer* **12**, 104–120 (2012).
139. Newlands, E. S., Stevens, M. F. G., Wedge, S. R., Wheelhouse, R. T. & Brock, C. Temozolomide: a review of its discovery, chemical properties, pre-clinical development and clinical trials. *Cancer Treat. Rev.* **23**, 35–61 (1997).
140. Koumariou, A. *et al.* Temozolomide in Advanced Neuroendocrine Neoplasms: Pharmacological and Clinical Aspects. *Neuroendocrinology* **101**, 274–288 (2015).
141. Gerson, S. L. MGMT: its role in cancer aetiology and cancer therapeutics. *Nat. Rev. Cancer* **4**, 296–307 (2004).
142. Cives, M. *et al.* Analysis of potential response predictors to capecitabine/temozolomide in metastatic pancreatic neuroendocrine tumors. *Endocr. Relat. Cancer* **23**, 759–767 (2016).
143. Kulke, M. H. *et al.* O6-methylguanine DNA methyltransferase deficiency and response to temozolomide-based therapy in patients with neuroendocrine tumors. *Clin. Cancer Res. Off. J. Am. Assoc. Cancer Res.* **15**, 338–345 (2009).
144. Schmitt, A. M. *et al.* Prognostic and Predictive Roles of MGMT Protein Expression and Promoter Methylation in Sporadic Pancreatic Neuroendocrine Neoplasms. *Neuroendocrinology* **100**, 35–44 (2014).
145. Walter, T. *et al.* O6-Methylguanine-DNA methyltransferase status in neuroendocrine tumours: prognostic relevance and association with response to alkylating agents. *Br. J. Cancer* **112**, 523–531 (2015).
146. Kelland, L. The resurgence of platinum-based cancer chemotherapy. *Nat. Rev. Cancer* **7**, 573–584 (2007).
147. Moertel, C. G., Kvols, L. K., O'Connell, M. J. & Rubin, J. Treatment of neuroendocrine carcinomas with combined etoposide and cisplatin. Evidence of major therapeutic activity in the anaplastic variants of these neoplasms. *Cancer* **68**, 227–232 (1991).
148. Turner, N. C. *et al.* Chemotherapy with 5-fluorouracil, cisplatin and streptozocin for neuroendocrine tumours. *Br. J. Cancer* **102**, 1106–1112 (2010).
149. Cejas, P. *et al.* Enhancer signatures stratify and predict outcomes of non-functional pancreatic neuroendocrine tumors. *Nat. Med.* **25**, 1260–1265 (2019).
150. Chan, C. S. *et al.* ATRX, DAXX or MEN1 mutant pancreatic neuroendocrine tumors are a distinct alpha-cell signature subgroup. *Nat. Commun.* **9**, 4158 (2018).
151. Simon, T. *et al.* DNA methylation reveals distinct cells of origin for pancreatic neuroendocrine carcinomas and pancreatic neuroendocrine tumors. *Genome Med.* **14**, 24 (2022).
152. Bates, S. E. Epigenetic Therapies for Cancer. *N. Engl. J. Med.* **383**, 650–663 (2020).
153. Flavahan, W. A., Gaskell, E. & Bernstein, B. E. Epigenetic plasticity and the hallmarks of cancer. *Science* **357**, (2017).
154. Jones, P. A. Functions of DNA methylation: islands, start sites, gene bodies and beyond. *Nat. Rev. Genet.* **13**, 484–492 (2012).
155. Schübeler, D. Function and information content of DNA methylation. *Nature* **517**, 321–326 (2015).
156. Park, J. W. & Han, J.-W. Targeting epigenetics for cancer therapy. *Arch. Pharm. Res.* **42**, 159–170 (2019).
157. Cedar, H. & Bergman, Y. Linking DNA methylation and histone modification: patterns and paradigms. *Nat. Rev. Genet.* **10**, 295–304 (2009).
158. Huynh, J. L. & Casaccia, P. Epigenetic mechanisms in multiple sclerosis: implications for pathogenesis and treatment. *Lancet Neurol.* **12**, 195–206 (2013).
159. Marinoni, I. *et al.* Hypo-methylation mediates chromosomal instability in pancreatic NET. *Endocr. Relat. Cancer* **24**, 137–146 (2017).
160. Daskalos, A. *et al.* Hypomethylation of retrotransposable elements correlates with genomic instability in non-small cell lung cancer. *Int. J. Cancer* **124**, 81–87 (2009).
161. Eden, A., Gaudet, F., Waghmare, A. & Jaenisch, R. Chromosomal instability and tumors promoted by DNA hypomethylation. *Science* **300**, 455 (2003).
162. Gonzalo, S. *et al.* DNA methyltransferases control telomere length and telomere recombination in mammalian cells. *Nat. Cell Biol.* **8**, 416–424 (2006).

163. Kemp, J. R. & Longworth, M. S. Crossing the LINE Toward Genomic Instability: LINE-1 Retrotransposition in Cancer. *Front. Chem.* **3**, (2015).
164. Choi, I.-S. *et al.* Hypomethylation of LINE-1 and Alu in well-differentiated neuroendocrine tumors (pancreatic endocrine tumors and carcinoid tumors). *Mod. Pathol.* **20**, 802–810 (2007).
165. Stefanoli, M. *et al.* Prognostic Relevance of Aberrant DNA Methylation in G1 and G2 Pancreatic Neuroendocrine Tumors. *Neuroendocrinology* **100**, 26–34 (2014).
166. Stricker, I. *et al.* Site- and Grade-specific Diversity of LINE1 Methylation Pattern in Gastroenteropancreatic Neuroendocrine Tumours. *Anticancer Res.* **32**, 3699–3706 (2012).
167. Arnold, C. N., Sosnowski, A., Schmitt-Gräff, A., Arnold, R. & Blum, H. E. Analysis of molecular pathways in sporadic neuroendocrine tumors of the gastro-entero-pancreatic system. *Int. J. Cancer* **120**, 2157–2164 (2007).
168. House, M. G. *et al.* Aberrant hypermethylation of tumor suppressor genes in pancreatic endocrine neoplasms. *Ann. Surg.* **238**, 423–431; discussion 431–432 (2003).
169. Liu, L. *et al.* Epigenetic alterations in neuroendocrine tumors: methylation of RAS-association domain family 1, isoform A and p16 genes are associated with metastasis. *Mod. Pathol.* **18**, 1632–1640 (2005).
170. Pizzi, S. *et al.* RASSF1A promoter methylation and 3p21.3 loss of heterozygosity are features of foregut, but not midgut and hindgut, malignant endocrine tumours. *J. Pathol.* **206**, 409–416 (2005).
171. Wild, A. *et al.* Frequent Methylation-Associated Silencing of the Tissue Inhibitor of Metalloproteinase-3 Gene in Pancreatic Endocrine Tumors. *J. Clin. Endocrinol. Metab.* **88**, 1367–1373 (2003).
172. Esteller, M. Cancer epigenomics: DNA methylomes and histone-modification maps. *Nat. Rev. Genet.* **8**, 286–298 (2007).
173. Hegi, M. E. *et al.* MGMT Gene Silencing and Benefit from Temozolomide in Glioblastoma. *N. Engl. J. Med.* **352**, 997–1003 (2005).
174. Qi, Z. & Tan, H. Association between MGMT status and response to alkylating agents in patients with neuroendocrine neoplasms: a systematic review and meta-analysis. *Biosci. Rep.* **40**, BSR20194127 (2020).
175. Lemelin, A. *et al.* O6-methylguanine-DNA methyltransferase (MGMT) status in neuroendocrine tumors: a randomized phase II study (MGMT-NET). *Dig. Liver Dis. Off. J. Ital. Soc. Gastroenterol. Ital. Assoc. Study Liver* **51**, 595–599 (2019).
176. Pipinikas, C. P. *et al.* Epigenetic dysregulation and poorer prognosis in DAXX-deficient pancreatic neuroendocrine tumours. *Endocr. Relat. Cancer* **22**, L13–L18 (2015).
177. April-Monn, S. L. *et al.* EZH2 Inhibition as New Epigenetic Treatment Option for Pancreatic Neuroendocrine Neoplasms (PanNENs). *Cancers* **13**, 5014 (2021).
178. Bremer, S. C. B. *et al.* Enhancer of Zeste Homolog 2 (EZH2) Is a Marker of High-Grade Neuroendocrine Neoplasia in Gastroenteropancreatic and Pulmonary Tract and Predicts Poor Prognosis. *Cancers* **14**, 2828 (2022).
179. Raj, N. *et al.* Real-Time Genomic Characterization of Metastatic Pancreatic Neuroendocrine Tumors Has Prognostic Implications and Identifies Potential Germline Actionability. *JCO Precis. Oncol.* 1–18 (2018) doi:10.1200/PO.17.00267.
180. Lin, W. *et al.* Loss of the retinoblastoma binding protein 2 (RBP2) histone demethylase suppresses tumorigenesis in mice lacking Rb1 or Men1. *Proc. Natl. Acad. Sci.* **108**, 13379–13386 (2011).
181. Lin, W. *et al.* Dynamic Epigenetic Regulation by Menin During Pancreatic Islet Tumor Formation. *Mol. Cancer Res.* **13**, 689–698 (2015).
182. Maggi, E. C. *et al.* Retinoblastoma-binding protein 2 (RBP2) is frequently expressed in neuroendocrine tumors and promotes the neoplastic phenotype. *Oncogenesis* **5**, e257 (2016).
183. Yang, G.-J. *et al.* The emerging role of KDM5A in human cancer. *J. Hematol. Oncol. J Hematol Oncol* **14**, 30 (2021).
184. Maggi, E. C. & Crabtree, J. S. Novel targets in the treatment of neuroendocrine tumors: RBP2. *Int. J. Endocr. Oncol.* **4**, 31–41 (2017).
185. Yang, G.-J. *et al.* Pharmacological inhibition of KDM5A for cancer treatment. *Eur. J. Med. Chem.* **226**, 113855 (2021).
186. Zeng, J. *et al.* The Histone Demethylase RBP2 Is Overexpressed in Gastric Cancer and Its Inhibition Triggers Senescence of Cancer Cells. *Gastroenterology* **138**, 981–992 (2010).
187. Teng, Y.-C. *et al.* Histone Demethylase RBP2 Promotes Lung Tumorigenesis and Cancer Metastasis. *Cancer Res.* **73**, 4711–4721 (2013).
188. Sharma, S. V. *et al.* A Chromatin-Mediated Reversible Drug-Tolerant State in Cancer Cell Subpopulations. *Cell* **141**, 69–80 (2010).
189. Mitsui, E. *et al.* Identification of ryuidine as a KDM5A inhibitor. *Sci. Rep.* **9**, 9952 (2019).
190. Yan, H. *et al.* Drug-Tolerant Cancer Cells Show Reduced Tumor-Initiating Capacity: Depletion of CD44+ Cells and Evidence for Epigenetic Mechanisms. *PLOS ONE* **6**, e24397 (2011).
191. Banelli, B. *et al.* The histone demethylase KDM5A is a key factor for the resistance to temozolomide in glioblastoma. *Cell Cycle* **14**, 3418–3429 (2015).
192. Oser, M. G. *et al.* The KDM5A/RBP2 histone demethylase represses NOTCH signaling to sustain neuroendocrine differentiation and promote small cell lung cancer tumorigenesis. *Genes Dev.* **33**, 1718–1738 (2019).
193. Liefke, R. *et al.* Histone demethylase KDM5A is an integral part of the core Notch-RBP-J repressor complex. *Genes Dev.* **24**, 590–601 (2010).
194. Gan, L. *et al.* Epigenetic regulation of cancer progression by EZH2: from biological insights to therapeutic potential. *Biomark. Res.* **6**, 10 (2018).
195. Kim, K. H. & Roberts, C. W. M. Targeting EZH2 in cancer. *Nat. Med.* **22**, 128–134 (2016).
196. Eich, M.-L., Athar, M., Ferguson, J. E., III & Varambally, S. EZH2-Targeted Therapies in Cancer: Hype or a Reality. *Cancer Res.* **80**, 5449–5458 (2020).
197. Margueron, R. & Reinberg, D. The Polycomb complex PRC2 and its mark in life. *Nature* **469**, 343–349 (2011).
198. Bracken, A. P. *et al.* EZH2 is downstream of the pRB-E2F pathway, essential for proliferation and amplified in cancer. *EMBO J.* **22**, 5323–5335 (2003).
199. Fujii, S. *et al.* MEK–ERK pathway regulates EZH2 overexpression in association with aggressive breast cancer subtypes. *Oncogene* **30**, 4118–4128 (2011).
200. Chang, C.-J. *et al.* EZH2 Promotes Expansion of Breast Tumor Initiating Cells through Activation of RAF1-β-Catenin Signaling. *Cancer Cell* **19**, 86–100 (2011).
201. Probst, A. V., Dunleavy, E. & Almouzni, G. Epigenetic inheritance during the cell cycle. *Nat. Rev. Mol. Cell Biol.* **10**, 192–206 (2009).
202. Jin, N. *et al.* A Phase II Trial of a Histone Deacetylase Inhibitor Panobinostat in Patients With Low-Grade Neuroendocrine Tumors. *The Oncologist* **21**, 785–786 (2016).
203. Italiano, A. *et al.* Tazemetostat, an EZH2 inhibitor, in relapsed or refractory B-cell non-Hodgkin lymphoma and advanced solid tumours: a first-in-human, open-label, phase I study. *Lancet Oncol.* **19**, 649–659 (2018).
204. Bruzzese, F. *et al.* Synergistic antitumor effect between vorinostat and topotecan in small cell lung cancer cells is mediated by generation of reactive oxygen species and DNA damage-induced apoptosis. *Mol. Cancer Ther.* **8**, 3075–3087 (2009).
205. Morel, D., Jeffery, D., Aspeslagh, S., Almouzni, G. & Postel-Vinay, S. Combining epigenetic drugs with other therapies for solid tumours — past lessons and future promise. *Nat. Rev. Clin. Oncol.* **17**, 91–107 (2020).

206. Detjen, K. *et al.* Models of Gastroenteropancreatic Neuroendocrine Neoplasms: Current Status and Future Directions. *Neuroendocrinology* **111**, 217–236 (2021).
207. Kawasaki, K., Fujii, M. & Sato, T. Gastroenteropancreatic neuroendocrine neoplasms: genes, therapies and models. *Dis. Model. Mech.* **11**, (2018).
208. Ney, A., Canciani, G., Hsuan, J. J. & Pereira, S. P. Modelling Pancreatic Neuroendocrine Cancer: From Bench Side to Clinic. *Cancers* **12**, 3170 (2020).
209. Allen, E. *et al.* Metabolic Symbiosis Enables Adaptive Resistance to Anti-angiogenic Therapy that Is Dependent on mTOR Signaling. *Cell Rep.* **15**, 1144–1160 (2016).
210. Inoue, M., Hager, J. H., Ferrara, N., Gerber, H.-P. & Hanahan, D. VEGF-A has a critical, nonredundant role in angiogenic switching and pancreatic β cell carcinogenesis. *Cancer Cell* **1**, 193–202 (2002).
211. Saghafinia, S. *et al.* Cancer cells retrace a stepwise differentiation program during malignant progression. *Cancer Discov.* (2021) doi:10.1158/2159-8290.CD-20-1637.
212. Piret, S. E. & Thakker, R. V. Mouse models for inherited endocrine and metabolic disorders. *J. Endocrinol.* **211**, 211–230 (2011).
213. Sadanandam, A. *et al.* A Cross-Species Analysis in Pancreatic Neuroendocrine Tumors Reveals Molecular Subtypes with Distinctive Clinical, Metastatic, Developmental, and Metabolic Characteristics. *Cancer Discov.* **5**, 1296–1313 (2015).
214. Evers, B. M. *et al.* Establishment and characterization of a human carcinoid in nude mice and effect of various agents on tumor growth. *Gastroenterology* **101**, 303–311 (1991).
215. Hofving, T. *et al.* The neuroendocrine phenotype, genomic profile and therapeutic sensitivity of GEPNET cell lines. *Endocr. Relat. Cancer* **25**, 367–380 (2018).
216. Beauchamp, R. D. *et al.* Human carcinoid cell production of paracrine growth factors that can stimulate fibroblast and endothelial cell growth. *Cancer Res.* **51**, 5253–5260 (1991).
217. Grozinsky-Glasberg, S., Shimon, I. & Rubinfeld, H. The Role of Cell Lines in the Study of Neuroendocrine Tumors. *Neuroendocrinology* **96**, 173–187 (2012).
218. Iguchi, H., Hayashi, I. & Kono, A. A Somatostatin-secreting Cell Line Established from a Human Pancreatic Islet Cell. **3** (1990).
219. Kaku, M., Nishiyama, T., Yagawa, K. & Abe, M. Establishment of a carcinoembryonic antigen-producing cell line from human pancreatic carcinoma. *Gan* **71**, 596–601 (1980).
220. Boora, G. K. *et al.* Exome-level comparison of primary well-differentiated neuroendocrine tumors and their cell lines. *Cancer Genet.* **208**, 374–381 (2015).
221. Vandamme, T. *et al.* Whole-exome characterization of pancreatic neuroendocrine tumor cell lines BON-1 and QGP-1. *J. Mol. Endocrinol.* **54**, 137–147 (2015).
222. Benten, D. *et al.* Establishment of the First Well-differentiated Human Pancreatic Neuroendocrine Tumor Model. *Mol. Cancer Res.* **16**, 496–507 (2018).
223. Chamberlain, C. E. *et al.* A Patient-derived Xenograft Model of Pancreatic Neuroendocrine Tumors Identifies Sapanisertib as a Possible New Treatment for Everolimus-resistant Tumors. *Mol. Cancer Ther.* **17**, 2702–2709 (2018).
224. Gueli, N., Toto, A., Palmieri, G., Delpino, A. & Ferrini, U. In vitro growth of a cell line originated from a human insulinoma. *J Exp Clin Cancer Res* (1987).
225. Tillotson, L. G. *et al.* Isolation, Maintenance, and Characterization of Human Pancreatic Islet Tumor Cells Expressing Vasoactive Intestinal Peptide. *Pancreas* **22**, 91–98 (2001).
226. Krampitz, G. W. *et al.* Identification of tumorigenic cells and therapeutic targets in pancreatic neuroendocrine tumors. *Proc. Natl. Acad. Sci.* **113**, 4464–4469 (2016).
227. Yang, Z. *et al.* Establishment and Characterization of a Human Neuroendocrine Tumor Xenograft. *Endocr. Pathol.* **27**, 97–103 (2016).
228. Kojima, N. In vitro reconstitution of pancreatic islets. *Organogenesis* **10**, 225–230 (2014).
229. Mohamed, A. *et al.* Pasireotide and octreotide antiproliferative effects and sst2 trafficking in human pancreatic neuroendocrine tumor cultures. *Endocr. Relat. Cancer* **21**, 691–704 (2014).
230. Mohamed, A. *et al.* Anti-proliferative and anti-secretory effects of everolimus on human pancreatic neuroendocrine tumors primary cultures: is there any benefit from combination with somatostatin analogs? *Oncotarget* **8**, 41044–41063 (2017).
231. Falletta, S. *et al.* mTOR inhibitors response and mTOR pathway in pancreatic neuroendocrine tumors. *Endocr. Relat. Cancer* **23**, 883–891 (2016).
232. Fujii, M. *et al.* A Colorectal Tumor Organoid Library Demonstrates Progressive Loss of Niche Factor Requirements during Tumorigenesis. *Cell Stem Cell* **18**, 827–838 (2016).
233. Dijkstra, K. K. *et al.* Patient-Derived Organoid Models of Human Neuroendocrine Carcinoma. *Front. Endocrinol.* **12**, (2021).
234. Herring, B. *et al.* Ex Vivo Modeling of Human Neuroendocrine Tumors in Tissue Surrogates. *Front. Endocrinol.* **12**, (2021).
235. Doornebal, E. J. *et al.* Human Immunocompetent Model of Neuroendocrine Liver Metastases Recapitulates Patient-Specific Tumour Microenvironment. *Front. Endocrinol.* **13**, (2022).
236. Corrò, C., Novellademunt, L. & Li, V. S. W. A brief history of organoids. *Am. J. Physiol.-Cell Physiol.* **319**, C151–C165 (2020).
237. Hirschhaeuser, F. *et al.* Multicellular tumor spheroids: an underestimated tool is catching up again. *J. Biotechnol.* **148**, 3–15 (2010).
238. Marsee, A. *et al.* Building consensus on definition and nomenclature of hepatic, pancreatic, and biliary organoids. *Cell Stem Cell* **28**, 816–832 (2021).
239. Weiswald, L.-B., Bellet, D. & Dangles-Marie, V. Spherical Cancer Models in Tumor Biology. *Neoplasia* **17**, 1–15 (2015).
240. Lancaster, M. A. & Knoblich, J. A. Organogenesis in a dish: Modeling development and disease using organoid technologies. *Science* **345**, 1247125 (2014).
241. Sato, T. *et al.* Single Lgr5 stem cells build crypt-villus structures in vitro without a mesenchymal niche. *Nature* **459**, 262–265 (2009).
242. Tuveson, D. & Clevers, H. Cancer modeling meets human organoid technology. *Science* **364**, 952–955 (2019).
243. Lê, H. *et al.* Patient-Derived Lung Tumoroids—An Emerging Technology in Drug Development and Precision Medicine. *Biomedicines* **10**, 1677 (2022).
244. Nath, S. & Devi, G. R. Three-dimensional culture systems in cancer research: Focus on tumor spheroid model. *Pharmacol. Ther.* **163**, 94–108 (2016).
245. Cukierman, E., Pankov, R., Stevens, D. R. & Yamada, K. M. Taking cell-matrix adhesions to the third dimension. *Science* **294**, 1708–1712 (2001).
246. Delarue, M. *et al.* Compressive Stress Inhibits Proliferation in Tumor Spheroids through a Volume Limitation. *Biophys. J.* **107**, 1821–1828 (2014).
247. Kelm, J. M., Timmins, N. E., Brown, C. J., Fussenegger, M. & Nielsen, L. K. Method for generation of homogeneous multicellular tumor spheroids applicable to a wide variety of cell types. *Biotechnol. Bioeng.* **83**, 173–180 (2003).
248. Al Tameemi, W., Dale, T. P., Al-Jumaily, R. M. K. & Forsyth, N. R. Hypoxia-Modified Cancer Cell Metabolism. *Front. Cell Dev. Biol.* **7**, (2019).

249. Vaupel, P., Flood, A. B. & Swartz, H. M. Oxygenation Status of Malignant Tumors vs. Normal Tissues: Critical Evaluation and Updated Data Source Based on Direct Measurements with pO₂ Microsensors. *Appl. Magn. Reson.* **52**, 1451–1479 (2021).
250. Friedrich, J., Ebner, R. & Kunz-Schughart, L. A. Experimental anti-tumor therapy in 3-D: Spheroids – old hat or new challenge? *Int. J. Radiat. Biol.* **83**, 849–871 (2007).
251. Kunz-Schughart, L. A., Freyer, J. P., Hofstaedter, F. & Ebner, R. The use of 3-D cultures for high-throughput screening: the multicellular spheroid model. *J. Biomol. Screen.* **9**, 273–285 (2004).
252. Sutherland, R. M. Cell and Environment Interactions in Tumor Microregions: The Multicell Spheroid Model. *Science* **240**, 177–184 (1988).
253. Hughes, C. S., Postovit, L. M. & Lajoie, G. A. Matrigel: a complex protein mixture required for optimal growth of cell culture. *Proteomics* **10**, 1886–1890 (2010).
254. Kleinman, H. K. & Martin, G. R. Matrigel: basement membrane matrix with biological activity. *Semin. Cancer Biol.* **15**, 378–386 (2005).
255. Orkin, R. W. *et al.* A murine tumor producing a matrix of basement membrane. *J. Exp. Med.* **145**, 204–220 (1977).
256. Thoma, C. R., Zimmermann, M., Agarkova, I., Kelm, J. M. & Krek, W. 3D cell culture systems modeling tumor growth determinants in cancer target discovery. *Adv. Drug Deliv. Rev.* **69–70**, 29–41 (2014).
257. Zhang, M., Boughton, P., Rose, B., Lee, C. S. & Hong, A. M. The Use of Porous Scaffold as a Tumor Model. *Int. J. Biomater.* **2013**, e396056 (2013).
258. Alessandri, K. *et al.* Cellular capsules as a tool for multicellular spheroid production and for investigating the mechanics of tumor progression in vitro. *Proc. Natl. Acad. Sci.* **110**, 14843–14848 (2013).
259. Kunz-Schughart, L. A., Kreutz, M. & Knuechel, R. Multicellular spheroids: a three-dimensional in vitro culture system to study tumour biology. *Int. J. Exp. Pathol.* **79**, 1–23 (1998).
260. Théry, M. Micropatterning as a tool to decipher cell morphogenesis and functions. *J. Cell Sci.* **123**, 4201–4213 (2010).
261. Vinci, M. *et al.* Advances in establishment and analysis of three-dimensional tumor spheroid-based functional assays for target validation and drug evaluation. *BMC Biol.* **10**, 29 (2012).
262. Torisawa, Y. *et al.* A multicellular spheroid array to realize spheroid formation, culture, and viability assay on a chip. *Biomaterials* **28**, 559–566 (2007).
263. Jaganathan, H. *et al.* Three-Dimensional In Vitro Co-Culture Model of Breast Tumor using Magnetic Levitation. *Sci. Rep.* **4**, 6468 (2014).
264. McMillan, E. A. *et al.* Chemistry-First Approach for Nomination of Personalized Treatment in Lung Cancer. *Cell* **173**, 864–878.e29 (2018).
265. Jaaks, P. *et al.* Effective drug combinations in breast, colon and pancreatic cancer cells. *Nature* 1–8 (2022) doi:10.1038/s41586-022-04437-2.
266. Lovitt, C. J., Shelper, T. B. & Avery, V. M. Evaluation of chemotherapeutics in a three-dimensional breast cancer model. *J. Cancer Res. Clin. Oncol.* **141**, 951–959 (2015).
267. Kim, T.-H., Mount, C. W., Gombotz, W. R. & Pun, S. H. The delivery of doxorubicin to 3-D multicellular spheroids and tumors in a murine xenograft model using tumor-penetrating triblock polymeric micelles. *Biomaterials* **31**, 7386–7397 (2010).
268. Wartenberg, M. *et al.* Regulation of the multidrug resistance transporter P-glycoprotein in multicellular tumor spheroids by hypoxia-inducible factor-1 and reactive oxygen species. *FASEB J.* **17**, 1–22 (2003).
269. Frankel, A., Buckman, R. & Kerbel, R. S. Abrogation of Taxol-induced G₂-M Arrest and Apoptosis in Human Ovarian Cancer Cells Grown as Multicellular Tumor Spheroids. *Cancer Res.* **57**, 2388–2393 (1997).
270. Barbone, D., Yang, T.-M., Morgan, J. R., Gaudio, G. & Broaddus, V. C. Mammalian target of rapamycin contributes to the acquired apoptotic resistance of human mesothelioma multicellular spheroids. *J. Biol. Chem.* **283**, 13021–13030 (2008).
271. Dardousis, K. *et al.* Identification of differentially expressed genes involved in the formation of multicellular tumor spheroids by HT-29 colon carcinoma cells. *Mol. Ther. J. Am. Soc. Gene Ther.* **15**, 94–102 (2007).
272. Frankel, A., Man, S., Elliott, P., Adams, J. & Kerbel, R. S. Lack of multicellular drug resistance observed in human ovarian and prostate carcinoma treated with the proteasome inhibitor PS-341. *Clin. Cancer Res. Off. J. Am. Assoc. Cancer Res.* **6**, 3719–3728 (2000).
273. Howes, A. L. *et al.* The phosphatidylinositol 3-kinase inhibitor, PX-866, is a potent inhibitor of cancer cell motility and growth in three-dimensional cultures. *Mol. Cancer Ther.* **6**, 2505–2514 (2007).
274. Friedrich, J., Seidel, C., Ebner, R. & Kunz-Schughart, L. A. Spheroid-based drug screen: considerations and practical approach. *Nat. Protoc.* **4**, 309–324 (2009).
275. Bhadriraju, K. & Chen, C. S. Engineering cellular microenvironments to improve cell-based drug testing. *Drug Discov. Today* **7**, 612–620 (2002).
276. Pampaloni, F., Reynaud, E. G. & Stelzer, E. H. K. The third dimension bridges the gap between cell culture and live tissue. *Nat. Rev. Mol. Cell Biol.* **8**, 839–845 (2007).
277. Dowden, H. & Munro, J. Trends in clinical success rates and therapeutic focus. *Nat. Rev. Drug Discov.* **18**, 495–496 (2019).
278. Weeber, F., Ooft, S. N., Dijkstra, K. K. & Voest, E. E. Tumor Organoids as a Pre-clinical Cancer Model for Drug Discovery. *Cell Chem. Biol.* **24**, 1092–1100 (2017).
279. Barretina, J. *et al.* The Cancer Cell Line Encyclopedia enables predictive modelling of anticancer drug sensitivity. *Nature* **483**, 603–607 (2012).
280. Ben-David, U. *et al.* Genetic and transcriptional evolution alters cancer cell line drug response. *Nature* **560**, 325–330 (2018).
281. Li, A. *et al.* Genomic Changes and Gene Expression Profiles Reveal That Established Glioma Cell Lines Are Poorly Representative of Primary Human Gliomas. *Mol. Cancer Res.* **6**, 21–30 (2008).
282. Stein, W. D., Litman, T., Fojo, T. & Bates, S. E. A Serial Analysis of Gene Expression (SAGE) Database Analysis of Chemosensitivity: Comparing Solid Tumors with Cell Lines and Comparing Solid Tumors from Different Tissue Origins. *Cancer Res.* **64**, 2805–2816 (2004).
283. Szakacs, G. Comparing Solid Tumors with Cell Lines: Implications for Identifying Drug Resistance Genes in Cancer. *Mol. Interv.* **4**, 323–325 (2004).
284. Sharifnia, T., Hong, A. L., Painter, C. A. & Boehm, J. S. Emerging Opportunities for Target Discovery in Rare Cancers. *Cell Chem. Biol.* **24**, 1075–1091 (2017).
285. Boj, S. F. *et al.* Organoid Models of Human and Mouse Ductal Pancreatic Cancer. *Cell* **160**, 324–338 (2015).
286. Gao, D. *et al.* Organoid Cultures Derived from Patients with Advanced Prostate Cancer. *Cell* **159**, 176–187 (2014).
287. Sachs, N. *et al.* A Living Biobank of Breast Cancer Organoids Captures Disease Heterogeneity. *Cell* **172**, 373–386.e10 (2018).
288. van de Wetering, M. *et al.* Prospective Derivation of a Living Organoid Biobank of Colorectal Cancer Patients. *Cell* **161**, 933–945 (2015).
289. Huang, L. *et al.* Ductal pancreatic cancer modeling and drug screening using human pluripotent stem cell- and patient-derived tumor organoids. *Nat. Med.* **21**, 1364–1371 (2015).

290. Pauli, C. *et al.* Personalized In Vitro and In Vivo Cancer Models to Guide Precision Medicine. *Cancer Discov.* **7**, 462–477 (2017).
291. Vlachogiannis, G. *et al.* Patient-derived organoids model treatment response of metastatic gastrointestinal cancers. *Science* **359**, 920–926 (2018).
292. Weeber, F. *et al.* Preserved genetic diversity in organoids cultured from biopsies of human colorectal cancer metastases. *Proc. Natl. Acad. Sci.* **112**, 13308–13311 (2015).
293. Drost, J. & Clevers, H. Organoids in cancer research. *Nat. Rev. Cancer* **18**, 407–418 (2018).
294. Sachs, N. & Clevers, H. Organoid cultures for the analysis of cancer phenotypes. *Curr. Opin. Genet. Dev.* **24**, 68–73 (2014).
295. Sato, T. *et al.* Long-term Expansion of Epithelial Organoids From Human Colon, Adenoma, Adenocarcinoma, and Barrett's Epithelium. *Gastroenterology* **141**, 1762–1772 (2011).
296. Drost, J. *et al.* Sequential cancer mutations in cultured human intestinal stem cells. *Nature* **521**, 43–47 (2015).
297. Duarte, A. A. *et al.* BRCA-deficient mouse mammary tumor organoids to study cancer-drug resistance. *Nat. Methods* **15**, 134 (2018).
298. Tiriác, H. *et al.* Organoid Profiling Identifies Common Responders to Chemotherapy in Pancreatic Cancer. *Cancer Discov.* **8**, 1112–1129 (2018).
299. Rinke, A. *et al.* Treatment of advanced gastroenteropancreatic neuroendocrine neoplasia, are we on the way to personalised medicine? *Gut* (2021) doi:10.1136/gutjnl-2020-321300.
300. Ooft, S. N. *et al.* Patient-derived organoids can predict response to chemotherapy in metastatic colorectal cancer patients. *Sci. Transl. Med.* **11**, (2019).
301. Wiedmer, T. *et al.* Autophagy Inhibition Improves Sunitinib Efficacy in Pancreatic Neuroendocrine Tumors via a Lysosome-dependent Mechanism. *Mol. Cancer Ther.* **16**, 2502–2515 (2017).
302. April-Monn, S. L. *et al.* Three-Dimensional Primary Cell Culture: A Novel Preclinical Model for Pancreatic Neuroendocrine Tumors. *Neuroendocrinology* **111**, 273–287 (2021).
303. Price, S. *et al.* A suspension technique for efficient large-scale cancer organoid culturing and perturbation screens. *Sci. Rep.* **12**, 5571 (2022).
304. Kopper, O. *et al.* An organoid platform for ovarian cancer captures intra- and interpatient heterogeneity. *Nat. Med.* **25**, 838–849 (2019).
305. Farkas, G. Simple and Reliable Conditions for Routine, Long-Term Culturing of Fetal Human Pancreatic Tissue Fragments. *Diabetes* **33**, 4 (1984).
306. Kuo, C. Y., Herrod, H. G. & Burghen, G. A. Formation of Pseudoislets from Human Pancreatic Cultures. *Pancreas* **7**, 320–325 (1992).
307. Scharp, D. W., Downing, R., Merrell, R. C. & Greider, M. Isolating the Elusive Islet. *Diabetes* **29**, 19–30 (1980).
308. Höpfner, M., Schuppan, D. & Scherübl, H. Treatment of gastrointestinal neuroendocrine tumors with inhibitors of growth factor receptors and their signaling pathways: Recent advances and future perspectives. *World J. Gastroenterol.* **14**, 2461–2473 (2008).
309. von Wichert, G. *et al.* Insulin-like Growth Factor-I Is an Autocrine Regulator of Chromogranin A Secretion and Growth in Human Neuroendocrine Tumor Cells1. *Cancer Res.* **60**, 4573–4581 (2000).
310. Wulbrand *et al.* Growth factor receptor expression in human gastroenteropancreatic neuroendocrine tumours. *Eur. J. Clin. Invest.* **28**, 1038–1049 (1998).
311. Karthaus, W. R. *et al.* Identification of Multipotent Luminal Progenitor Cells in Human Prostate Organoid Cultures. *Cell* **159**, 163–175 (2014).
312. Di Florio, A., Sancho, V., Moreno, P., Fave, G. D. & Jensen, R. T. Gastrointestinal hormones stimulate growth of Foregut Neuroendocrine Tumors by transactivating the EGF receptor. *Biochim. Biophys. Acta BBA - Mol. Cell Res.* **1833**, 573–582 (2013).
313. Siddique, Z.-L. *et al.* KRJ-I and BON cell lines: defining an appropriate enterochromaffin cell neuroendocrine tumor model. *Neuroendocrinology* **89**, 458–470 (2009).
314. Townsend, C. M., Ishizuka, J. & Thompson, J. C. Studies of Growth Regulation in a Neuroendocrine Cell Line. *Acta Oncol.* **32**, 125–130 (1993).
315. von Wichert, G. *et al.* Regulation of cyclin D1 expression by autocrine IGF-I in human BON neuroendocrine tumour cells. *Oncogene* **24**, 1284–1289 (2005).
316. Hilfenhaus, G. *et al.* Placental growth factor supports neuroendocrine tumor growth and predicts disease prognosis in patients. *Endocr. Relat. Cancer* **20**, 305–319 (2013).
317. Bagri, A., Tessier-Lavigne, M. & Watts, R. J. Neuropilins in Tumor Biology. *Clin. Cancer Res.* **15**, 1860–1864 (2009).
318. Fischer, C., Mazzone, M., Jonckx, B. & Carmeliet, P. FLT1 and its ligands VEGFB and PlGF: drug targets for anti-angiogenic therapy? *Nat. Rev. Cancer* **8**, 942–956 (2008).
319. Kim, K.-A. *et al.* R-Spondin Family Members Regulate the Wnt Pathway by a Common Mechanism. *Mol. Biol. Cell* **19**, 2588–2596 (2008).
320. Chaudhry, A., Funa, K. & Öberg, K. Expression of Growth Factor Peptides and Their Receptors in Neuroendocrine Tumors of the Digestive System. *Acta Oncol.* **32**, 107–114 (1993).
321. Hofmann, C. *et al.* Cell-cell contacts prevent anoikis in primary human colonic epithelial cells. *Gastroenterology* **132**, 587–600 (2007).
322. Beattie, G. M., Rubin, J. S., Mally, M. I., Otonkoski, T. & Hayek, A. Regulation of Proliferation and Differentiation of Human Fetal Pancreatic Islet Cells by Extracellular Matrix, Hepatocyte Growth Factor, and Cell-Cell Contact. *Diabetes* **45**, 1223–1228 (1996).
323. Ohgawara, H., Mochizuki, N., Karibe, S. & Omori, Y. Survival and B-Cell Function of Neonatal Pig Pancreatic Islet-Like Cell Clusters in an Extracellular Matrix. *Pancreas* **6**, 625–630 (1991).
324. Otonkoski, T., Beattie, G. M., Mally, M. I., Ricordi, C. & Hayek, A. Nicotinamide is a potent inducer of endocrine differentiation in cultured human fetal pancreatic cells. *J. Clin. Invest.* **92**, 1459–1466 (1993).
325. Briest, F. & Grabowski, P. PI3K-AKT-mTOR-Signaling and beyond: the Complex Network in Gastroenteropancreatic Neuroendocrine Neoplasms. *Theranostics* **4**, 336–365 (2014).
326. Tseng, Y.-Y. & Boehm, J. S. From cell lines to living biosensors: new opportunities to prioritize cancer dependencies using ex vivo tumor cultures. *Curr. Opin. Genet. Dev.* **54**, 33–40 (2019).
327. Cros, J. *et al.* Gly388Arg FGFR4 Polymorphism Is Not Predictive of Everolimus Efficacy in Well-Differentiated Digestive Neuroendocrine Tumors. *Neuroendocrinology* **103**, 495–499 (2016).
328. Vitale, G. *et al.* IFN-β Is a Highly Potent Inhibitor of Gastroenteropancreatic Neuroendocrine Tumor Cell Growth In vitro. *Cancer Res.* **66**, 554–562 (2006).
329. Zitzmann, K. *et al.* SOCS1 Silencing Enhances Antitumor Activity of Type I IFNs by Regulating Apoptosis in Neuroendocrine Tumor Cells. *Cancer Res.* **67**, 5025–5032 (2007).
330. Falconi, M. *et al.* ENETS Consensus Guidelines Update for the Management of Patients with Functional Pancreatic Neuroendocrine Tumors and Non-Functional Pancreatic Neuroendocrine Tumors. *Neuroendocrinology* **103**, 153–171 (2016).
331. Kaderli, R. M. *et al.* Therapeutic Options for Neuroendocrine Tumors: A Systematic Review and Network Meta-analysis. *JAMA Oncol.* **5**, 480–489 (2019).
332. Chou, W.-C. *et al.* Genes involved in angiogenesis and mTOR pathways are frequently mutated in Asian patients with pancreatic neuroendocrine tumors. *Int. J. Biol. Sci.* **12**, 1523–1532 (2016).

333. Cives, M. *et al.* DAXX mutations as potential genomic markers of malignant evolution in small nonfunctioning pancreatic neuroendocrine tumors. *Sci. Rep.* **9**, 18614 (2019).
334. Morschhauser, F. *et al.* Phase 2 multi-center study of tazemetostat (EPZ-6438), an inhibitor of enhancer of zeste-homolog 2 (EZH2), in patients with relapsed or refractory B-cell non-Hodgkin lymphoma (NHL). *J. Clin. Oncol.* **34**, TPS7582–TPS7582 (2016).
335. Faviana, P. *et al.* EZH2 Expression in Intestinal Neuroendocrine Tumors. *Appl. Immunohistochem. Mol. Morphol.* **27**, 689–693 (2019).
336. Boons, G. *et al.* PDX1 DNA Methylation Distinguishes Two Subtypes of Pancreatic Neuroendocrine Neoplasms with a Different Prognosis. *Cancers* **12**, 1461 (2020).
337. Barazeghi, E., Hellman, P., Norlén, O., Westin, G. & Ståhlberg, P. EZH2 presents a therapeutic target for neuroendocrine tumors of the small intestine. *Sci. Rep.* **11**, 22733 (2021).
338. Findeis-Hosey, J. J. *et al.* High-grade neuroendocrine carcinomas of the lung highly express enhancer of zeste homolog 2, but carcinoids do not. *Hum. Pathol.* **42**, 867–872 (2011).
339. Sperling, F., Misiak, D., Hüttelmaier, S., Michl, P. & Griesmann, H. IGF2BP1 Promotes Proliferation of Neuroendocrine Neoplasms by Post-Transcriptional Enhancement of EZH2. *Cancers* **14**, 2121 (2022).
340. Koyen, A. E. *et al.* EZH2 has a non-catalytic and PRC2-independent role in stabilizing DDB2 to promote nucleotide excision repair. *Oncogene* **39**, 4798–4813 (2020).
341. Gulati, N., Béguelin, W. & Giulino-Roth, L. Enhancer of zeste homolog 2 (EZH2) inhibitors. *Leuk. Lymphoma* **59**, 1574–1585 (2018).
342. McCabe, M. T. *et al.* EZH2 inhibition as a therapeutic strategy for lymphoma with EZH2-activating mutations. *Nature* **492**, 108–112 (2012).
343. Zakikhani, M., Blouin, M.-J., Piura, E. & Pollak, M. N. Metformin and rapamycin have distinct effects on the AKT pathway and proliferation in breast cancer cells. *Breast Cancer Res. Treat.* **123**, 271–279 (2010).
344. Han, X. *et al.* Aberration of ARID1A Is Associated With the Tumorigenesis and Prognosis of Sporadic Nonfunctional Pancreatic Neuroendocrine Tumors. *Pancreas* **49**, 514–523 (2020).
345. Driehuis, E. *et al.* Pancreatic cancer organoids recapitulate disease and allow personalized drug screening. *Proc. Natl. Acad. Sci.* **116**, 26580–26590 (2019).
346. Haverty, P. M. *et al.* Reproducible pharmacogenomic profiling of cancer cell line panels. *Nature* **533**, 333–337 (2016).
347. Driehuis, E., Kretschmar, K. & Clevers, H. Establishment of patient-derived cancer organoids for drug-screening applications. *Nat. Protoc.* 1–30 (2020) doi:10.1038/s41596-020-0379-4.
348. Ben-David, U., Beroukhim, R. & Golub, T. R. Genomic evolution of cancer models: perils and opportunities. *Nat. Rev. Cancer* **19**, 97–109 (2019).
349. Matano, M. *et al.* Modeling colorectal cancer using CRISPR-Cas9-mediated engineering of human intestinal organoids. *Nat. Med.* **21**, 256–262 (2015).
350. Kozłowski, M. T., Crook, C. J. & Ku, H. T. Towards organoid culture without Matrigel. *Commun. Biol.* **4**, 1–15 (2021).
351. Ye, S. *et al.* A Chemically Defined Hydrogel for Human Liver Organoid Culture. *Adv. Funct. Mater.* **30**, 2000893 (2020).
352. Peschke, K. *et al.* Identification of treatment-induced vulnerabilities in pancreatic cancer patients using functional model systems. *EMBO Mol. Med.* **14**, (2022).
353. Corsello, S. M. *et al.* The Drug Repurposing Hub: a next-generation drug library and information resource. *Nat. Med.* **23**, 405–408 (2017).
354. Roerink, S. F. *et al.* Intra-tumour diversification in colorectal cancer at the single-cell level. *Nature* **556**, 457–462 (2018).
355. Boonekamp, K. E., Dayton, T. L. & Clevers, H. Intestinal organoids as tools for enriching and studying specific and rare cell types: advances and future directions. *J. Mol. Cell Biol.* doi:10.1093/jmcb/mjaa034.
356. Hafner, M., Niepel, M., Chung, M. & Sorger, P. K. Growth rate inhibition metrics correct for confounders in measuring sensitivity to cancer drugs. *Nat. Methods* **13**, 521–527 (2016).
357. Hafner, M., Niepel, M. & Sorger, P. K. Alternative drug sensitivity metrics improve preclinical cancer pharmacogenomics. *Nat. Biotechnol.* **35**, 500–502 (2017).
358. Zindel, J. *et al.* Intraperitoneal microbial contamination drives post-surgical peritoneal adhesions by mesothelial EGFR-signaling. *Nat. Commun.* **12**, 7316 (2021).
359. Gulde, S. *et al.* Combined Targeting of Pathogenetic Mechanisms in Pancreatic Neuroendocrine Tumors Elicits Synergistic Antitumor Effects. *Cancers* **14**, 5481 (2022).
360. Jankovic, J. *et al.* Validation of Immunohistochemistry for Canine Proteins Involved in Thyroid Iodine Uptake and Their Expression in Canine Follicular Cell Thyroid Carcinomas (FTCs) and FTC-Derived Organoids. *Vet. Pathol.* **58**, 1172–1180 (2021).

6 Co-authorship publications

6.1 Manuscript 4: “*Intraperitoneal microbial contamination drives post-surgical peritoneal adhesions by mesothelial EGFR-signaling*”

Joel Zindel, Jonas Mittner, Julia Bayer, Simon L. April-Monn, Andreas Kohler, Ysbrand Nusse, Michel Dosch, Isabel Büchi, Daniel Sanchez-Taltavull, Heather Dawson, Mercedes Gomez de Agüero, Kinji Asahina, Paul Kubes, Andrew J. Macpherson, Deborah Stroka and Daniel Candinas

Nature Communications [10.1038/s41467-021-27612-x](https://doi.org/10.1038/s41467-021-27612-x)

Reprinted from ³⁵⁸ © 2021, The Authors.

Author contribution (CRediT):

I acquired and analyzed human data, including **methodology** (development and design of methodology, creation of models), **software** (programming and implementation of code and testing of existing computer code), **validation** (verification of the overall replication/reproducibility of experiments and results and other research outputs), **formal analysis** (application of statistical, mathematical, computational and other formal techniques to analyze and synthesize study data), **investigation** (conduction of research and investigation processes, performing experiments and data collection), **reviewing and editing** the final manuscript, and **visualization**.

Intraperitoneal microbial contamination drives post-surgical peritoneal adhesions by mesothelial EGFR-signaling

Joel Zindel ^{1,2}✉, Jonas Mittner ¹, Julia Bayer ¹, Simon L. April-Monn ³, Andreas Kohler ¹, Ysbrand Nusse ², Michel Dosch¹, Isabel Büchi¹, Daniel Sanchez-Taltavull¹, Heather Dawson³, Mercedes Gomez de Agüero¹, Kinji Asahina ^{4,5}, Paul Kubes ², Andrew J. Macpherson¹, Deborah Stroka ^{1,6} & Daniel Candinas ^{1,6}

Abdominal surgeries are lifesaving procedures but can be complicated by the formation of peritoneal adhesions, intra-abdominal scars that cause intestinal obstruction, pain, infertility, and significant health costs. Despite this burden, the mechanisms underlying adhesion formation remain unclear and no cure exists. Here, we show that contamination of gut microbes increases post-surgical adhesion formation. Using genetic lineage tracing we show that adhesion myofibroblasts arise from the mesothelium. This transformation is driven by epidermal growth factor receptor (EGFR) signaling. The EGFR ligands amphiregulin and heparin-binding epidermal growth factor, are sufficient to induce these changes. Correspondingly, EGFR inhibition leads to a significant reduction of adhesion formation in mice. Adhesions isolated from human patients are enriched in EGFR positive cells of mesothelial origin and human mesothelium shows an increase of mesothelial EGFR expression during bacterial peritonitis. In conclusion, bacterial contamination drives adhesion formation through mesothelial EGFR signaling. This mechanism may represent a therapeutic target for the prevention of adhesions after intra-abdominal surgery.

¹ Department of Visceral Surgery and Medicine, Inselspital, Bern University Hospital, University of Bern, Bern, Switzerland. ² Department of Pharmacology and Physiology and Snyder Institute for Chronic Diseases and Department of Microbiology, Immunology & Infectious Diseases, Cumming School of Medicine, University of Calgary, Calgary, AB, Canada. ³ Clinical Pathology Division and Translational Research Unit, Institute of Pathology, University of Bern, Bern, Switzerland. ⁴ Southern California Research Center for Alcoholic Liver and Pancreatic Diseases and Cirrhosis and Department of Pathology, Keck School of Medicine of the University of Southern California, Los Angeles, CA, USA. ⁵ Central Research Laboratory, Shiga University of Medical Science, Otsu, Shiga, Japan. ⁶ These authors contributed equally: Deborah Stroka, Daniel Candinas. ✉email: joel.zindel@dbmr.unibe.ch

The peritoneal body cavity is lined by the peritoneum—a monolayer of mesothelial cells and a sub-mesothelial layer of connective tissue—that allows free movement of intra-abdominal organs. Post-surgical adhesions form when two mesothelial surfaces are attached to each other by connective tissue by a fibrotic reaction, a process that can be initiated by coagulation, aggregation of macrophages, and intercellular adhesions between mesothelial cells^{1–3}. The resulting adhesions are defined as irreversible, vascularized fibrotic scars connecting abdominal organs and the abdominal wall at non-anatomic locations, restricting organ movement^{4,5}. Post-surgical peritoneal adhesions are a major health burden for patients and health care providers⁶. They are the leading cause of life-threatening intestinal occlusions^{7–9} and in the United States alone they are responsible for over 300,000 additional abdominal operations per year with annual costs of several billion dollars⁶. In addition, adhesions frequently lead to chronic post-operative abdominal pain. Currently, the only approved therapies for adhesions are barriers, such as implanted hydrogels, that physically separate internal tissues following surgery. However, the clinical use of hydrogels has not significantly reduced the incidence of adhesion-related disease, and scientific evidence does not support their routine use¹⁰. Therefore, adhesions are an unresolved clinical challenge which to date lack effective treatment.

A proposed driver of fibrotic conversion is the migration and proliferation of surface mesothelium¹¹ followed by a mesothelial-to-mesenchymal (MMT) transition¹². Targeting mesothelial cells reduced adhesion formation *in vitro*³ as well as *in vivo* in a sterile injury model¹¹. However, surgical procedures in the abdominal cavity often require extensive manipulation of the microbe-rich intestines. Therefore, these procedures are not 100% sterile but are often complicated by the contamination of the abdominal cavity with gut microbes. Indeed, some studies link microbial contamination and adhesion formation in humans and rodents^{8,13,14}. However, the mechanism how contaminating gut microbes drive adhesion formation remains to be uncovered.

In this work, we ask how microbe-induced inflammation in the peritoneal cavity contributes to adhesion formation. We demonstrate that mesothelial cells are the main source of fibroblast-like cells within adhesions by genetic inducible fate mapping. Using RNA-Sequencing, we show that the activation and trans-differentiation of the mesothelial cell niche are driven by EGFR-signaling, which is significantly upregulated in the presence of gut microbes. These findings are recapitulated in biopsies from human patients. Furthermore, peritoneal adhesions are reduced in a mouse model by targeting EGFR-signaling with the FDA-approved small molecule inhibitor Gefitinib¹⁵.

Results

Surgical injury and microbe contamination augment post-surgical peritoneal adhesions. To investigate the respective effects of sterile injury and microbe contamination on post-surgical adhesion formation, we developed a suitable animal model. First, a standardized surgical injury of the peritoneum was induced by creating a peritoneal button (PB) as previously described¹¹. Next, we used a limited cecal ligation and puncture (CLP) to release luminal contents, including microbes into the peritoneal cavity. Together, the PB and CLP components comprise a modular model system with a defined and localized sterile injury due to the PB (Fig. 1a, left panel) and a limited septic insult from the CLP (Fig. 1a, right panel). Both models could be applied individually or in combination (PB + CLP), allowing us to separate the effect of surgical trauma from the effect due to bacterial contamination. The PB + CLP model showed highly reproducible adhesion formation with zero mortality. Adhesions

were evaluated 7 days after surgery using a standardized indexing system (Fig. 1b, c and Table 1). This adhesion index is based on and correlates well with (Fig. S1a) previously published adhesion scores^{16–18}. In addition to published scores, that score adhesions for their overall tenacity and vascularization (Table 1), the adhesion index sums up this score from 6 distinct anatomic locations in the mouse peritoneal cavity (Fig. 1b) and therefore reflects the adhesion quantification used in human studies¹⁹.

Taking advantage of our modular adhesion model, we investigated the respective and combined effects of sterile injury and microbial contamination on adhesion formation. Mice underwent either sterile injury alone (PB), microbial contamination alone (CLP), or the combination of sterile injury and microbial contamination (PB + CLP). The combination of microbial contamination and sterile injury led to a significantly higher adhesion index (Fig. 1d) when compared with each insult alone. Next, to distinguish the effect of microbes vs fecal content in adhesion formation, we performed the PB + CLP model in germ-free (GF) mice and in gnotobiotic mice colonized with the stably defined moderately diverse mouse microbiota (sDMDMm2²⁰). Both were compared with specific-pathogen-free (SPF) microbiota. Mice were subjected to the PB + CLP model and kept under sterile conditions for one week. We confirmed the hygienic status of the experimental GF and gnotobiotic mice using culture-dependent (aerobic and anaerobic expansion cultures) and culture-independent (Sytox stain) analysis of fecal samples at the end of the experiment (Fig. S1b). GF animals had a significantly reduced adhesion index compared to colonized mice which were like colonized mice receiving injury (PB) only (Fig. 1e). There was no significant difference between the two colonized groups, sDMDMm2 and SPF (Fig. 1e). In addition, adhesions sampled from GF animals showed a decreased collagen content when compared with adhesions sampled from colonized mice (Fig. 1f). Corresponding to a decrease in adhesion formation, GF animals showed a significantly less pronounced increase of pro-inflammatory cytokines after surgery when compared with sDMDMm2 mice (Fig. S1c). Nonetheless, GF animals were able to mount an inflammatory response post-surgery, indicated by a profound influx of inflammatory leukocytes (neutrophils and monocytes) into the peritoneal cavity (Fig. S1d). However, when compared with colonized animals, the infiltration of leukocytes in GF animals consisted of more monocytes and less neutrophils (Fig. S1d). Next, we replaced the CLP with cecal slurry (CS) that was generated from feces of SPF mice. The effect of both, native and heat-inactivated CS on adhesion formation was comparable to CLP (Fig. S1e). Correspondingly, when mice were treated with broad-spectrum antibiotics prior to surgery, no reduction of the adhesion index was observed (Fig. S1f). This does not contradict the GF data where mice had no bacteria prior to surgery. Moreover, none of these regimens completely eradicate bacteria. Interestingly, the microbial contamination (CLP, CS) takes place throughout the entire peritoneum, yet adhesions only occurred locally at the site of injury. The administration of lipopolysaccharide (LPS) also resulted in an increase of adhesions over injury only, but the effect was smaller than that of CLP or CS (Fig. S1e). Taken together, these data suggest that contamination with gut microbes rather than intestinal content, drives the formation of post-surgical adhesions.

Increase in post-surgical collagen deposition correlates with the activation and proliferative expansion of mesothelial cells.

We next explored what drove collagen deposition after exposure to live gut microbiota. Masson's trichrome stained tissue sections showed consistent collagen deposition in adhesions within 7 days

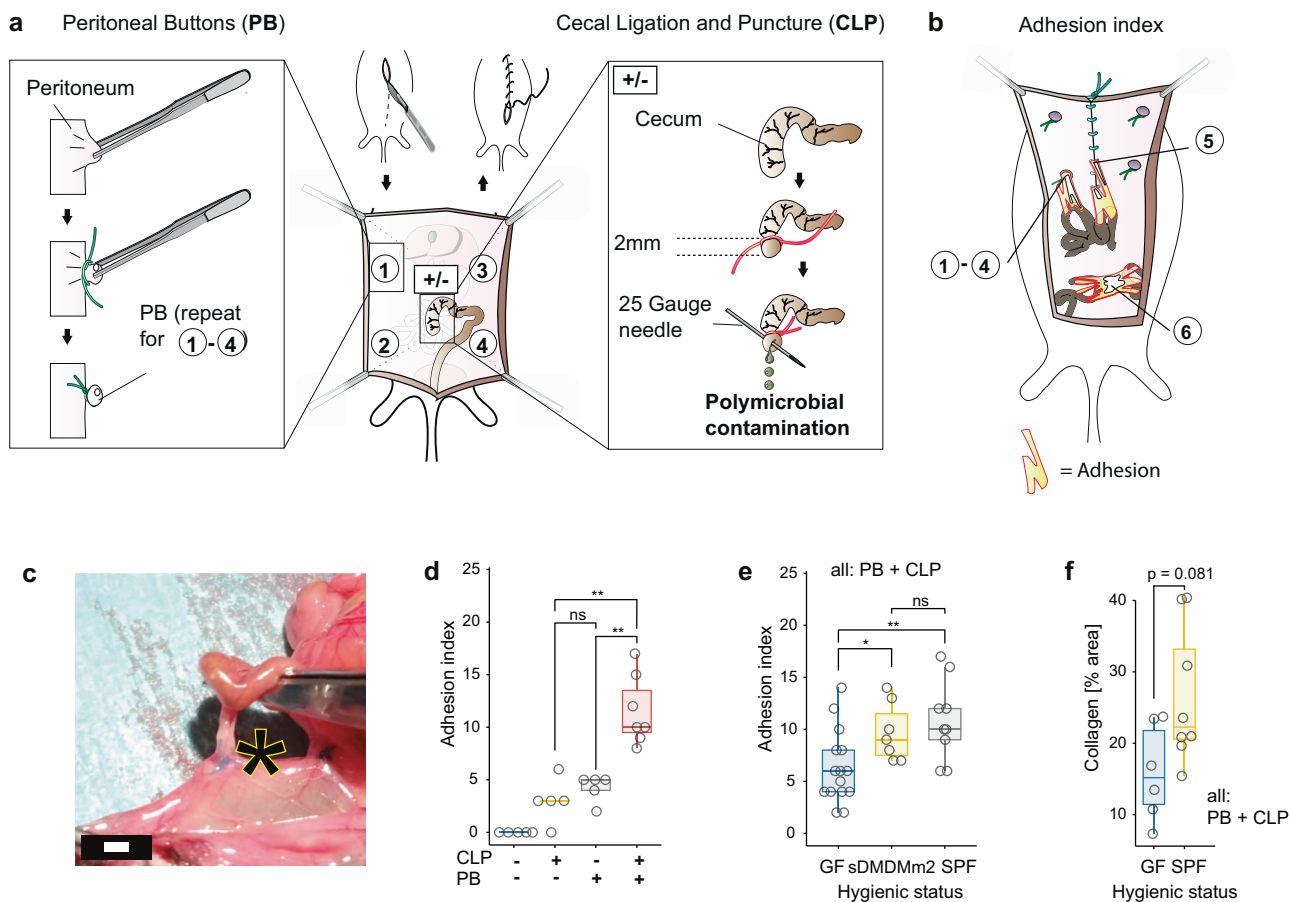


Fig. 1 Surgical injury and microbe contamination augment post-surgical peritoneal adhesions. **a** C57BL/6(J) mice were surgically injured by applying two peritoneal buttons (PB) per side (left panel) in combination with or without microbial contamination through cecal ligation and puncture (CLP) (right panel). **b** Surgical model resulted in the formation of peritoneal adhesions within 7 days post-surgery. Adhesions were scored for tenacity and vascularization at six locations and the sum of these scores is the adhesion index. **c** Representative macroscopic image of an adhesion (asterisk) between small intestine and PB. Scale bar: 1 mm. **d** Adhesion index 7 days post-surgery after CLP, PB, and PB + CLP in SPF mice. Data representative of $n = 5$ for Ctrl, 5 for CLP, 5 for PB and 7 for CLP + CLP independent animals, representing 2 independent experiments. Data are presented as individual values and boxplots (median, first and third quartile). CLP vs PB: $p = 0.39$, CLP vs. CLP + PB: $p = 0.0053$, PB vs CLP + PB: $p = 0.0053$ **e** Adhesion index resulting 7 days post-surgery in germ-free (GF), gnotobiotic (stable defined moderately diverse mouse microbiota, sDMDMm2) and specific-pathogen-free (SPF) mice. All mice underwent PB + CLP surgery. Data pooled from 2 independent experiments representative of $n = 15$ for GF, 7 for sDMDMm2, and 9 for SPF independent animals. Data are presented as individual values and boxplots (median, first and third quartile). GF vs. sDMDMm2: $p = 0.028$, GF vs. SPF: $p = 0.0097$, sDMDMm2 vs. SPF: $p = 0.63$. **f** Collagen quantification (% adhesion area) in GF and SPF mice 7 days after surgery (PB + CLP). Data representative of 6 for GF and 8 for SPF independent animals. Data are presented as individual values and boxplots (median, 25th, and 75th percentile). Wilcoxon test (two-sided) with Holm-Bonferroni correction for multiple testing. * $P < 0.05$, ** $P < 0.01$. Source data are provided as a Source Data file.

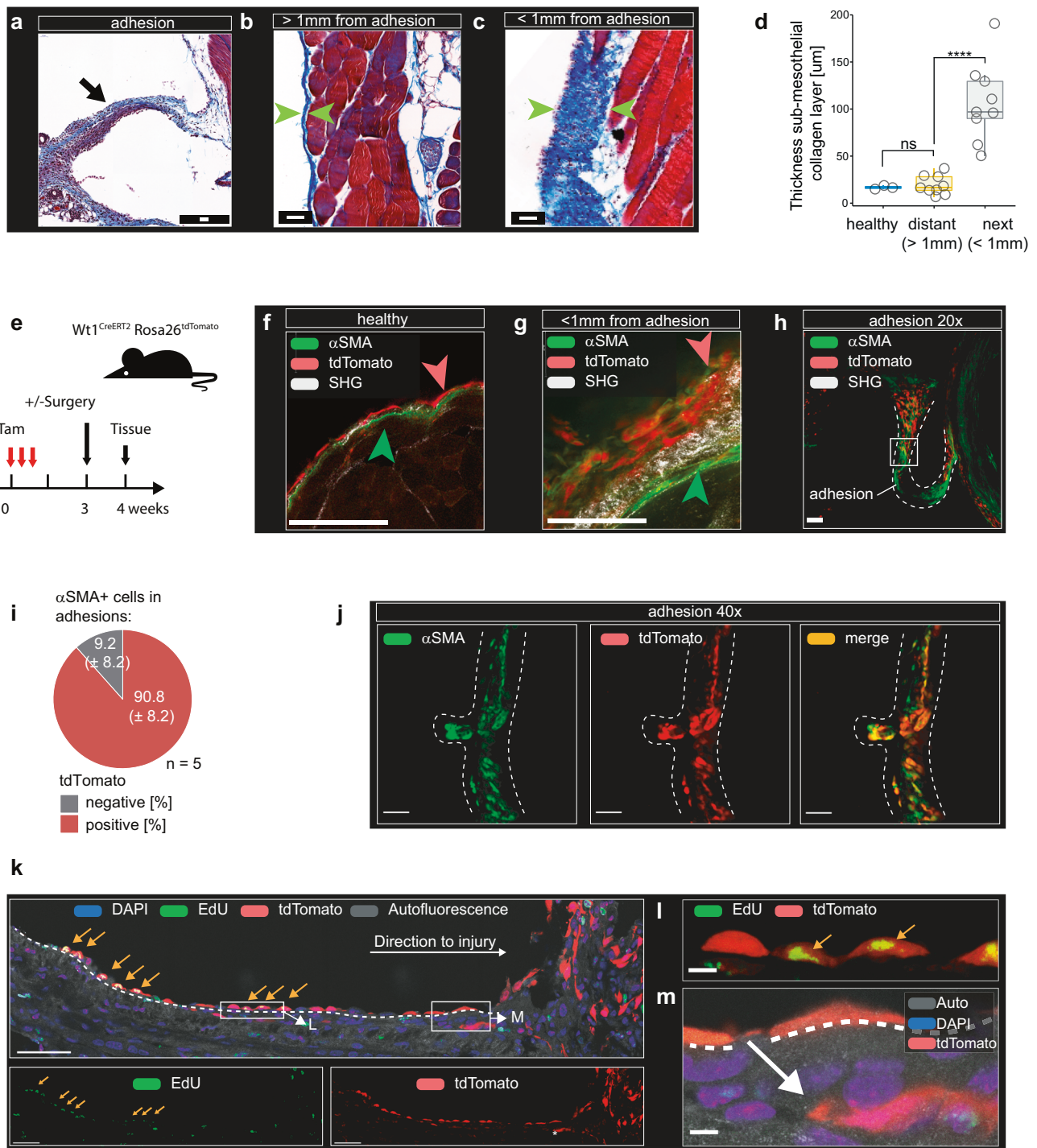
Table 1 Peritoneal adhesion index.

Grade	Description	Explanation
0	None	PB is free and covered with mesothelium
1	Flimsy	Separates spontaneously when opening the peritoneal cavity
2	Dense	Separates bluntly, without bleeding
3	Fibrotic/Vascularized	Needs sharp dissection, visible vascularization, bleeding occurs upon dissection
4	Complete	PB is completely covered by adhesion, dissection results in organ damage

PB peritoneal button.

post-surgery (Fig. 2a). Interestingly, the areas in proximity (within 1 mm) of surgical injury/adhesions showed an increased thickness of the sub-mesothelial collagen layer (Fig. 2c, d) when compared with distant (>1 mm) regions (Fig. 2b). The persistence of collagen secreting alpha smooth muscle actin (α -SMA) positive myofibroblasts has been considered a hallmark of fibrotic changes

in wound healing as well as in many fibrotic diseases^{21–23}. Therefore, we next probed the question of the origin of α -SMA positive myofibroblasts in adhesions in our model system. We hypothesized that myofibroblasts were either derived from the mesothelium or alternatively derived from sub-mesothelial fibroblasts²⁴. To discern these two possibilities, we used conditional



cell lineage tracing. Administration of Tamoxifen to *Wt1^{CreERT2} Rosa26^{tdTomato}* reporter mice permanently labeled mesothelial cells and their daughter cells with tdTomato (Fig. 2e, f)²⁵. In this system, cells derived from sub-mesothelial fibroblasts remain tdTomato negative (Fig. 2f). To appreciate the localization of these cells, we used whole mount microscopy on resected adhesions as previously described²⁶. This allowed optical sectioning of adhesions under a confocal microscope with subsequent three-dimensional reconstruction (Fig. S2a). In addition, we used multiphoton excitation to image collagen based on its second harmonic generation (SHG). Under homeostatic conditions, tdTomato positive mesothelial cells did not express α-SMA (Fig. 2f) and were clearly distinct from tdTomato negative, α-SMA positive, sub-mesothelial fibroblasts (Fig. 2f).

However, 7 days after PB + CLP, tdTomato positive mesothelial cells gave rise to α-SMA positive cells (Fig. 2g and Fig. S2b). These tdTomato/α-SMA double-positive cells were rounder when compared with homeostatic mesothelial cells and showed a multi-layered cell growth, compared to baseline mesothelium’s monolayer growth (Fig. 2g). Interestingly, mesothelial cells also become α-SMA positive when cultured in vitro (Fig. S2c) and α-SMA positive cells derived from mesothelial cells secreted collagen in vitro (Fig. S2d). In vivo, this phenotypic switch of mesothelial cells was concentrated at the sites of surgical injury (PB) and was associated with an increased thickness of the sub-mesothelial collagen layer, suggesting an increase in collagen production (Fig. 2d). Importantly, when examining α-SMA positive cells within adhesions, we found that many were

Fig. 2 Increase in post-surgical collagen deposition is correlated with activation and proliferative expansion of mesothelial cells. **a–c** Biopsies 7 days after surgery (PB + CLP) stained with Masson's trichrome staining. Biopsies were obtained from adhesions (**a**, arrow), distant regions (**b**) and regions within 1 mm of adhesions in animals that underwent surgery (**c**). Scale bar (**a–c**): 50 μ m. Images (**a–c**) are representative of $n = 9$ animals examined over 3 independent experiments. **d** Sub-mesothelial collagen layer thickness was quantified in biopsies from distant regions and regions within 1 mm of adhesion. Data represent $n = 3$ for healthy, 9 for distant and next independent animals examined over one independent experiment. Data are presented as individual values and boxplots (median, first and third quartile). Healthy vs. distant: $p = 0.86$, distant vs. next: $p = 0.000041$. **e** Administration of Tamoxifen (Tam) to *Wt1^{CreERT2} Rosa26^{tdTomato}* reporter mice permanently labeled mesothelial cells and their daughter cells with tdTomato. **f–h** Whole mount immunohistochemistry of biopsies obtained 7 days after surgery (PB + CLP). Green arrows indicate sub-mesothelial fibroblasts, red arrows indicate mesothelial cells. Collagen is visualized by its second harmonic generation (SHG). Scale bar: 50 μ m. **i** Quantification of *Wt1^{CreERT2} Rosa26^{tdTomato}* positive and negative fraction in alpha smooth muscle actin (α -SMA) positive cells within adhesions. **j** Magnification of adhesion shown in (**h**). Scale bar: 50 μ m. **k** 5-ethynyl-2'-deoxyuridine (EdU) was administered twice in the combined injury + CLP model as well as in unoperated control animals during the first twenty-four hours post-surgery. Frozen section immunohistochemistry of biopsies obtained 7 days after surgery (PB + CLP). Yellow arrows indicate proliferating mesothelial cells. Dashed white line indicates basement membrane. Arrow indicates a mesothelial cell crossing the basement membrane. Scale bar: 50 μ m. **l, m** magnification ($\times 60$) of areas indicated in (**k**). Wilcoxon test (two-sided) with Holm-Bonferroni correction for multiple-testing. **** $P < 0.0001$, n.s. $P \geq 0.05$ $n = 5$ (**f–j**) and $n = 3$ (**k**), representative of two independent experiments. Source data are provided as a Source Data file.

tdTomato positive, demonstrating that they were derived from mesothelial cells (Fig. 2h, j). Automated image analysis showed that about 90% of α -SMA positive cells were derived from the mesothelium (Fig. 2i). The capacity of mesothelial cells for mesenchymal transition has been described before and referred to as MMT^{12,25,27,28}.

In addition to a phenotypic change, the mesothelial cell niche showed a significant proliferative expansion. To show proliferation 5-ethynyl-2'-deoxyuridine (EdU) was administered during the first 24 h post-surgery (PB + CLP model) (Fig. 2k and Fig. S2e). Under baseline conditions, very few podoplanin positive mesothelial cells were EdU positive (Fig. S2f). However, post-surgery, the proportion of EdU positive nuclei increased within the mesothelium (Fig. 2k and Fig. S2g). EdU positive cells were often grouped together, distinguishing them as proliferative islands (Fig. 2l and Fig. S2g). These proliferative islands became larger and more confluent near the site of surgical injury (PB), which is also where adhesion formation occurred most frequently (Fig. S2h). At sites of injury, tdTomato positive cells also appeared to lose contact with the basement membrane (Fig. 2k) and to infiltrate the connective tissue (Fig. 2k, m). In summary, our data indicate that α -SMA positive myofibroblasts within adhesions arise from the mesothelial niche which undergoes a proliferative expansion and mesenchymal transition.

Mesothelial cells undergo a profound transcriptional change post-surgery. Next, we asked what cell signaling pathways were significantly altered in mesothelial cells after challenging the peritoneal compartment with sterile injury and microbial contamination. We performed RNA-sequencing analysis of mesothelial cells isolated at different time points post-surgery in the combined PB + CLP model. Mesothelial cells were immunopurified using an anti-glycoprotein M6A (GPM6A) antibody and magnetic beads (Fig. 3a). This isolation process resulted in 98% purity when validated by flow cytometry (Fig. 3b and Fig. S3a) and cytospin (Fig. S3b). The RNA from isolated mesothelial cells was processed for next-generation RNA-sequencing. A multi-dimensional scaling plot of all genes and all samples displayed a clear separation of timepoints (Fig. 3c). We identified a total of 9007 differentially expressed genes (DEG) throughout the time course (Fig. S3c). A gene set enrichment analysis was performed to provide an overview of altered pathways (Fig. 3d). We noted an activation of an inflammatory response, including increased cytokine production and the upregulation of canonical leukocyte migration factors (Fig. 3e). In addition, the inflamed mesothelium underwent profound changes in genes involved in the coagulation cascade (Fig. S3d). Taken together, these transcriptomic changes indicate a mesothelial reaction that might facilitate the infiltration

of leukocytes and the formation of a fibrin clot. The latter has been proposed as a preliminary scaffold necessary for a subsequent fibrotic conversion to an adhesion⁸.

More than half of the enriched gene ontology terms were not linked to inflammation. The sequential upregulation of genes needed for ribosome biogenesis (Fig. 3d, Nr. 1) was followed by an increase of mitotic cell cycle genes (Fig. 3d, Nr. 2). Several gene ontology terms that were upregulated involved pro-proliferative and anti-apoptotic signaling (Fig. 3d, Nr. 3) supporting the observed expansion of the mesothelial compartment. Further, several intracellular pathways were activated, such as mitogen-activated protein kinase (MAPK), signal transducer and activator of transcription 5 (STAT5) and phosphoinositide 3-kinase (PI3K) signaling, corresponding to cell activation and changes in adhesion, migration, and protein synthesis. In addition, we noted changes in expression of genes associated with cell-cell and cell-basement membrane adhesion/interaction molecules and other markers canonically associated with MMT (Fig. S4a). Altogether, these transcriptional findings suggest that mesothelial cells switch from their epithelial phenotype to assume a more mobile and potentially mesenchymal program.

Mesothelial cell activation is driven by receptor tyrosine kinases of the ERBB family. Next, we questioned what was driving proliferation of the mesothelium. Examination of the gene ontology network node "Proliferation/Activation" pointed to receptor tyrosine kinases (RTK) signaling as potential core driver for the observed changes in mesothelial cells (Fig. 3d). Among all RTKs, *ErbB2* showed the highest differential expression (log₂ fold change = 2.1, $p < 0.001$) when comparing germ-free with SPF mice. Similarly, *Egfr* (*ErbB1*), was significantly increased after surgery in SPF mice when compared with germ-free mice (Fig. 4c). In addition, the respective downstream pathways of *Egfr* and *ErbB2* were highly differentially expressed (Fig. 4a, b), including genes of the MAPK pathway (Fig. 4b). We next sought to confirm the upregulation and activation of EGFR in mesothelial cells in response to injury and bacterial contamination at the protein level. Interestingly, 24 h after injury, very few mesothelial cells remained within the peritoneal button injury (Fig. 4d). Therefore, we hypothesized that the increased mesothelial *Egfr* expression (Fig. 4a) must come from mesothelial cells that were isolated from regions adjacent to the injury. Indeed, the mesothelium within a few millimeters of peritoneal injuries showed a large increase of EGFR signaling as indicated by the activated form of EGFR (pEGFR) (Fig. 4e) whereas no pEGFR expression was found in distant mesothelium. Importantly, pEGFR showed a high degree of co-localization with the mesothelial cell marker podoplanin, suggesting that the observed

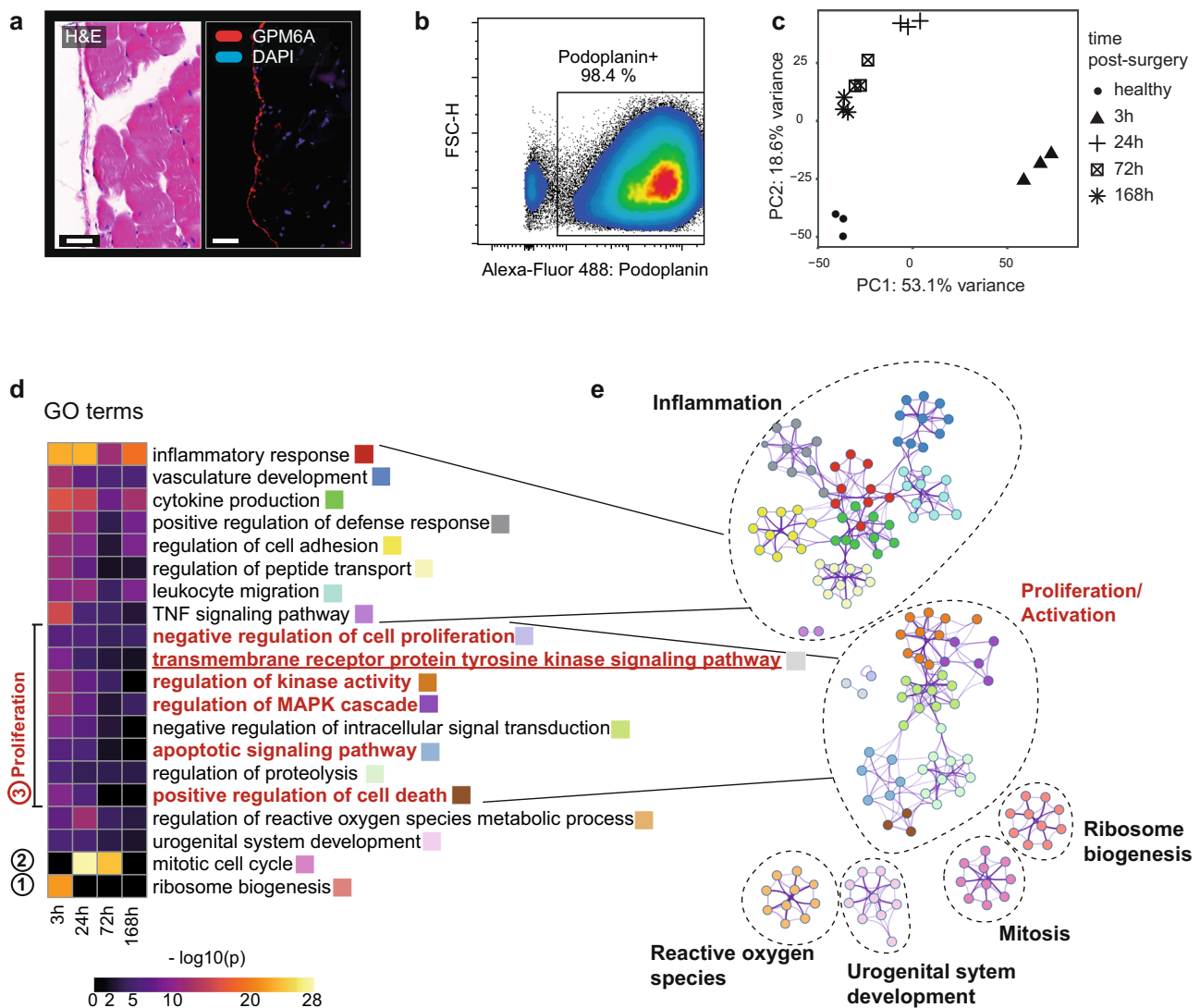


Fig. 3 Mesothelial cells undergo a profound transcriptional change post-surgery. **a** Cryosection of healthy abdominal wall. The mesothelium was stained by anti-glycoprotein M6A (GPM6A) antibody (right). Hematoxylin and eosin (H&E) staining (left). Scale bar: 50 μ m. Image is representative of $n = 3$ independent animals and two independent experiments (**b**) In vivo mesothelium digestion purified with anti-GPM6A magnetic beads purity control before undergoing RNA-Seq. **c** Principal components of log transformed read counts. **d** Differentially expressed genes (log₂fold change during time-course) with significance ($p < 0.01$) were loaded into Metascape to acquire gene ontology (GO) and KEGG pathway enrichment. Changes in ribosome biogenesis (Nr. 1), mitotic cell cycle (Nr. 2) and pro-proliferative/ anti-apoptotic signaling (Nr. 3) are highlighted. **e** GO network representation of enriched GO terms (color by cluster). $N = 3$ replicates (mice) sequenced per time point. Raw data were deposited at gene expression omnibus (GSE156127).

increase of pEGFR is specific for mesothelial cells. Furthermore, EGFR expression was still elevated 7 days after injury in SPF but not GF mice (Fig. S4b). Taken together, both RNA and protein data suggest that EGFR-signaling is specifically activated in mesothelial cells. This activation occurs in response to injury and is potentiated by microbial contamination.

EGFR ligands are produced by bone-marrow-derived macrophages and a B-cell subset that are recruited to the wound. We next asked the question what molecules ligate to EGFR and induce its activation post-surgery. EGFR expression seemed to be predominantly on the basolateral side of the healthy mesothelium (Fig. S5a). We initially hypothesized that surgical disruption of the mesothelial integrity may expose the basolateral receptor to the ligand available in the peritoneal cavity. This hypothesis was further supported by the observation that proliferative mesothelial cells were near the sites of surgical injury (Fig. 2k, Fig. S2f–h). Mesothelial cells produce a certain amount of EGFR ligands in an

autocrine fashion (Fig. S5b). However, EGFR mesothelial ligand transcripts were either unchanged or even decreased in SPF mice when comparing them with GF mice three hours post-surgery (Fig. S5b). We therefore hypothesized that EGFR ligands must be produced in a paracrine fashion by other cells such as peritoneal leukocytes. To investigate the difference in the inflammatory response between mice that underwent PB and PB + CLP we characterized the post-surgical chemotactic signature in the peritoneal cavity lavage fluid using a multiplexed mesoscale cytokine/chemokine screening. Hierarchical clustering of the cytokine/chemokine signature measured in the peritoneal lavage fluid uncovered a distinct proinflammatory neutrophil-recruiting cytokine signature in colonized mice that underwent CLP (Fig. S5c). This proinflammatory signature was well separated from GF mice undergoing CLP and colonized mice receiving only PB without CLP (Fig. S5c). Interestingly, hierarchical clustering revealed that the cytokine signature observed in GF mice with PB + CLP closely resembled that of colonized mice receiving only

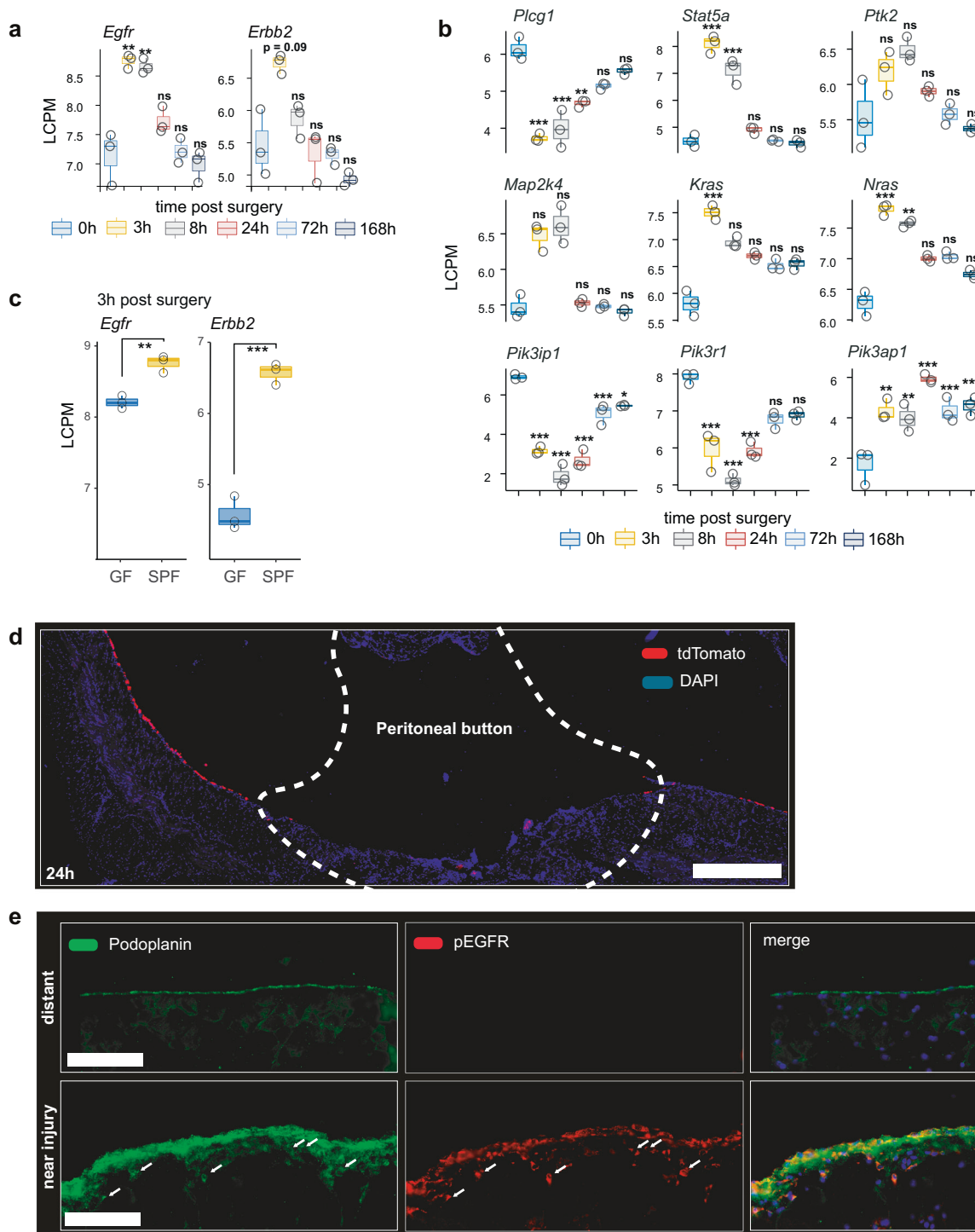


Fig. 4 Mesothelial cell activation is driven by receptor tyrosine kinases of the ERBB family. **a** Epidermal growth factor receptor (*Egfr*) and *Erbb2* were the main genes encoding for receptor kinases differentially expressed (log count per million, LCPM) over time. **b** Genes downstream of *Egfr* and *Erbb2* are differentially expressed as well (inhibitory genes are repressed). **c** Expression of *Egfr* and *Erbb2* genes in mesothelium isolated from germ-free (GF) and specific-pathogen-free (SPF) mice 3 h after sterile injury in combination with bacterial contamination (PB + CLP). Data (**a–c**) is representative of $n = 3$ independent animals examined in one experiment. Data are presented as individual values and boxplots (median, first and third quartile) **d** Peritoneal button, 24 h after injury of *Wt1^{CreERT2} Rosa26^{tdTomato}* reporter mice that were treated with Tamoxifen 2 weeks prior to experiment. Scale bar 500 μm . Data represents $n = 3$ animals of 2 independent experiments. **e** Peritoneal biopsies from healthy mice and from mice 3 days after surgery (PB + CLP). Scale bar 50 μm . Data represents $n = 8$ animals of 2 independent experiments. Differential expression testing according to the linear modeling as described in the methods section. * $P < 0.05$, ** $P < 0.01$, *** $P < 0.001$, n.s. $P \geq 0.05$. Exact p -values are provided in Supplementary Data 1. Raw data were deposited at gene expression omnibus (GSE156127).

the PB without CLP (Fig. S5c). Next, we performed flow cytometric characterization of the leukocyte influx into the peritoneal cavity. Corresponding to the chemokine profile, PB + CLP led to a significantly increased neutrophil recruitment when compared with PB alone (Fig. S5d, e). On the other hand, sterile damage (PB) alone led to an increased influx of monocytes (Fig. S5d, e) whereas the number of macrophages and B-cells was similar in both conditions. The difference between PB and PB + CLP was like the difference between GF and sDMDMm2 observed earlier (Fig. S1c, d). Next, we isolated peritoneal leukocytes 24 h post-surgery and found that peritoneal leukocytes isolated from colonized mice after CLP showed a significantly increased expression (quantitative PCR) of the EGFR ligand encoding genes amphiregulin (*Areg*), epiregulin (*Ereg*), and transforming-growth-factor alpha (*Tgfa*) when compared with peritoneal leukocytes isolated from mice without intraperitoneal microbe challenge (Fig. S5f). These findings suggested that contamination of the peritoneal compartment with live gut microbes leads to an increase in leukocyte recruitment, which produces EGFR ligands in the peritoneal cavity fluid. However, through different assays we were unable to detect EGFR ligands in the peritoneal fluid. We have recently shown, that macrophages can be recruited to peritoneal injuries by a direct route from the peritoneal cavity². Furthermore, a series of recent reports highlights the emerging role immune cell EGFR ligand production in the regulation of inflammation and tissue repair^{29–31}. To explore whether EGFR ligands were produced in a paracrine fashion by immune cells that infiltrate the peritoneal injury, we dissociated peritoneal injury biopsies into single-cell suspensions and performed single-cell RNA-Sequencing (Fig. 5a). Manually annotated (Seurat) and automatically annotated (SingleR) clustering confirmed the presence of mesothelial cells (*Krt19*⁺, *Gpm6A*⁺) and several distinct populations of CD45⁺ immune cells (Fig. 5b, Fig. S6a–c). As expected, the number of mesothelial cells within peritoneal buttons was very small in comparison to the number of infiltrating immune cells (Fig. 4d, Fig. 5c, d). This analysis showed that mesothelial cells were the only cells that expressed *Egfr* (Fig. 5c) but did not express significant amounts of EGFR ligands (Fig. S7a,b). Within injuries, the main ligands with known activity on EGFR homo- and hetero-dimers were heparin-binding epidermal growth factor (*Hbegf*) and *Areg* (Fig. 5d, Fig. S7a,b). The cells expressing the major amounts of *Hbegf* and *Areg* were bone marrow-derived macrophages (Fig. 5d). Interestingly, a small subset of B-cells also expressed *Areg*. This B-cell subset, characterized by the expression of *Ly6d*, *Cd79a*, *Ms4a1*, and *E330020D12Rik*, was only present in mice that underwent CLP in addition to injury (PB) (Fig. 5e). Next, we found that both AREG and HB-EGF led to a significant and dose-dependent increase of EGFR phosphorylation (pEGFR) in cultured primary mesothelial cells (Fig. 5f, g). We went on to interrogate what downstream pathways played a role in our model in comparison with the sterile model by Fischer et al., where ERK did not play a role³. In our system, the increase of pEGFR in turn activated MAPK/ERK pathway (Fig. 5g) and higher ligand concentrations led to an activation of the PI3K/AKT pathway (Fig. 5g). We observed no activation of the STAT3 pathway even with high ligand doses (Fig. 5g). Epidermal growth factor (EGF), which was not expressed in our scRNA-Seq experiment, resulted in an even stronger effect in vitro when compared with HB-EGF (Fig. S5g). Next, we tested whether EGFR agonists were sufficient to recapitulate the effect of bacterial contamination in our adhesion model. However, neither the injection of recombinant AREG nor recombinant EGF—which showed the strongest effect on mesothelial cells in vitro—were sufficient to increase the adhesion score in mice that underwent injury model (PB) (Fig. S5h).

Gefitinib, a small molecule inhibitor of EGFR reduces collagen deposition and MMT in vitro and post-surgical adhesion formation in vivo. Next, we asked whether pharmacological inhibition of EGFR can be exploited to prevent adhesion formation. Gefitinib was used to inhibit the phosphorylation of EGFR (Fig. 6a, b) and Selumetinib and Ly294002 were used to inhibit the downstream kinases mitogen-activated protein kinase kinase (MEK) and PI3K respectively (Fig. 6a, b). In vitro, Gefitinib led to a significant reduction of the collagen production (Fig. 6c) and migration (Fig. 6d–f) of mesothelial cells. Furthermore, Gefitinib was able to inhibit EGFR-induced MMT in cultured primary mesothelial cells (Fig. S8a). In vivo, the daily intraperitoneal administration of 100 mg/kg of Gefitinib³² resulted in a significant reduction of post-surgical adhesion formation (Fig. 6g). In addition, intraperitoneal treatment with Gefitinib resulted in a significant reduction of tdTomato positive mesothelium derived cells within adhesions (Fig. 6h, i). We also investigated the administration of Gefitinib by oral gavage with either 20 or 100 mg/kg daily or a once weekly dose of 400 mg/kg as previously described³². We found that oral application of Gefitinib or intraperitoneal doses of less than 50 mg/kg per day did not significantly reduce the adhesion index (Fig. S8b, c). This would suggest the need for a high local concentration (μ M range) to be effective. Using other kinase inhibitors such as the MEK inhibitor Selumetinib and PI3K inhibitor Ly294002 showed that inhibition of the MAPK/ERK but not the PI3K/AKT pathway results in a reduction of postoperative adhesions (Fig. 6g). Taken together, these findings suggest that EGFR signals through the MAPK/ERK pathway potentiate post-surgical adhesion formation.

Mesothelial EGFR expression of human patients with acute appendicitis is increased. To confirm the mesothelial upregulation of EGFR in response to bacterial contamination in humans, we retrospectively analyzed formalin-fixed paraffin-embedded tissues of human patients. Patients either underwent elective surgery due to malignancy without known bacterial peritonitis (control group, $n = 7$) or due to acute appendicitis ($n = 11$). The demographics of this patient cohort are displayed in Supplementary Table 1. We hypothesized that EGFR expression in mesothelial cells would be higher in acute appendicitis cases due to the bacterial contamination. Indeed, immunohistochemistry revealed a massive upregulation of EGFR in the whole mesothelium of patients with appendicitis (Fig. 7c–e, Fig. S9a) when compared with patients undergoing elective non-contaminated surgery (Fig. 7a, b, e, Fig. S9b). Interestingly, one outlier in the elective surgery group with relatively high mesothelial EGFR expression, proved to be a patient in which a malignant tumor perforated the intestine which arguably led to a bacterial contamination (Fig. 7e). The EGFR signal showed a very high colocalization with cytokeratin and calretinin, epithelial markers that are expressed by mesothelium (Fig. 7a–d). Furthermore, mesothelial cells from patients with acute appendicitis were significantly rounder when compared with mesothelial cells from patients undergoing elective surgery (Fig. 7c, d, f, g). These observations were consistent with our observations in the mouse model and reports in the literature that suggested that the roundness of mesothelial cells correlates with their ability to migrate³³. The clear correlation between mesothelial roundness and EGFR expression (Fig. 7g) possibly indicates a relationship between EGFR expression and migration in mesothelial cells. In some acute appendicitis patients, the deposition of granulation tissue enriched in EGFR positive cells (Fig. 7h) could be observed. Drawing from our mouse data, we speculate that these cells were of mesothelial origin and were activated allowing them to proliferate and migrate beyond their basement membrane (Fig. 7h).

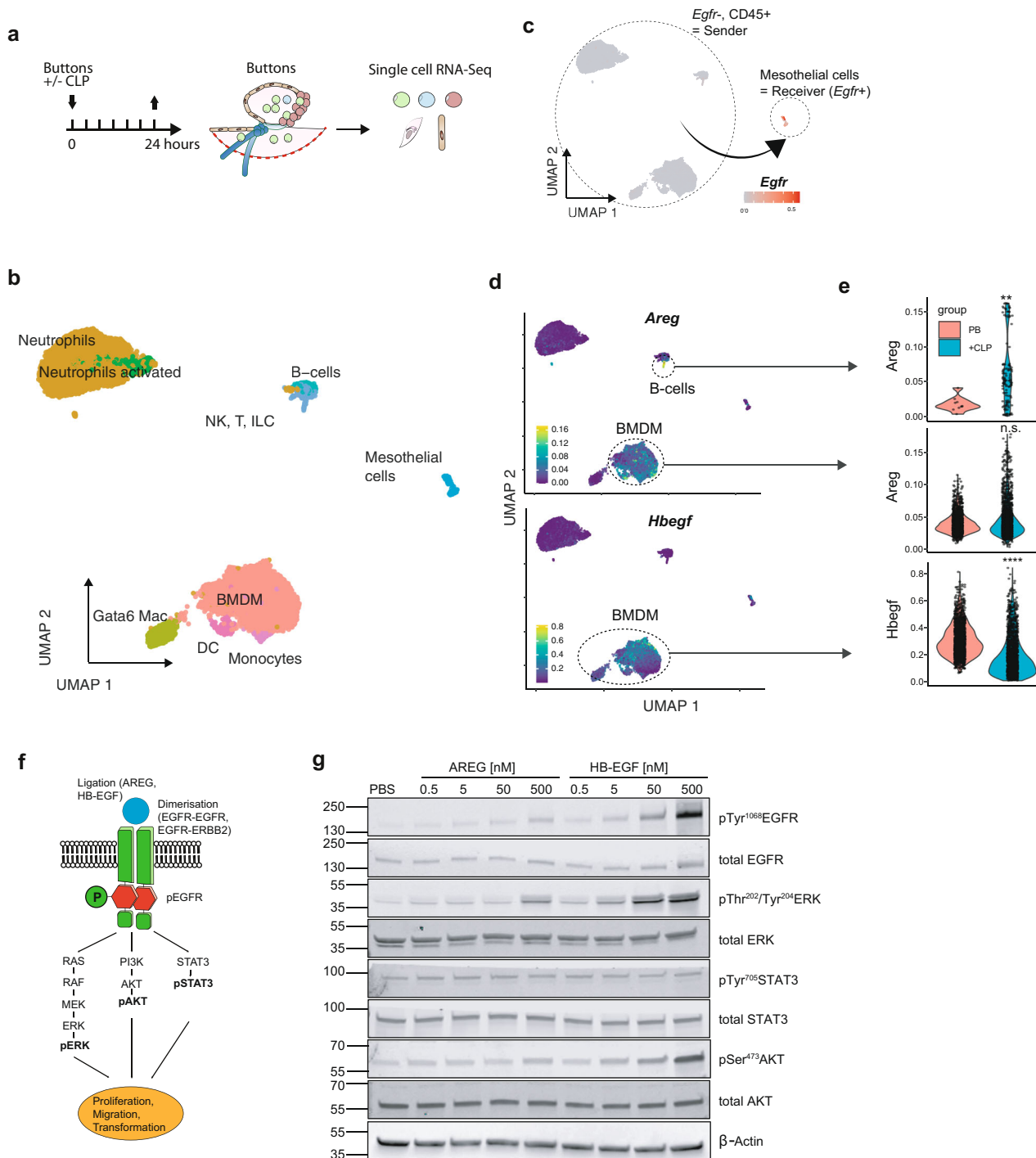
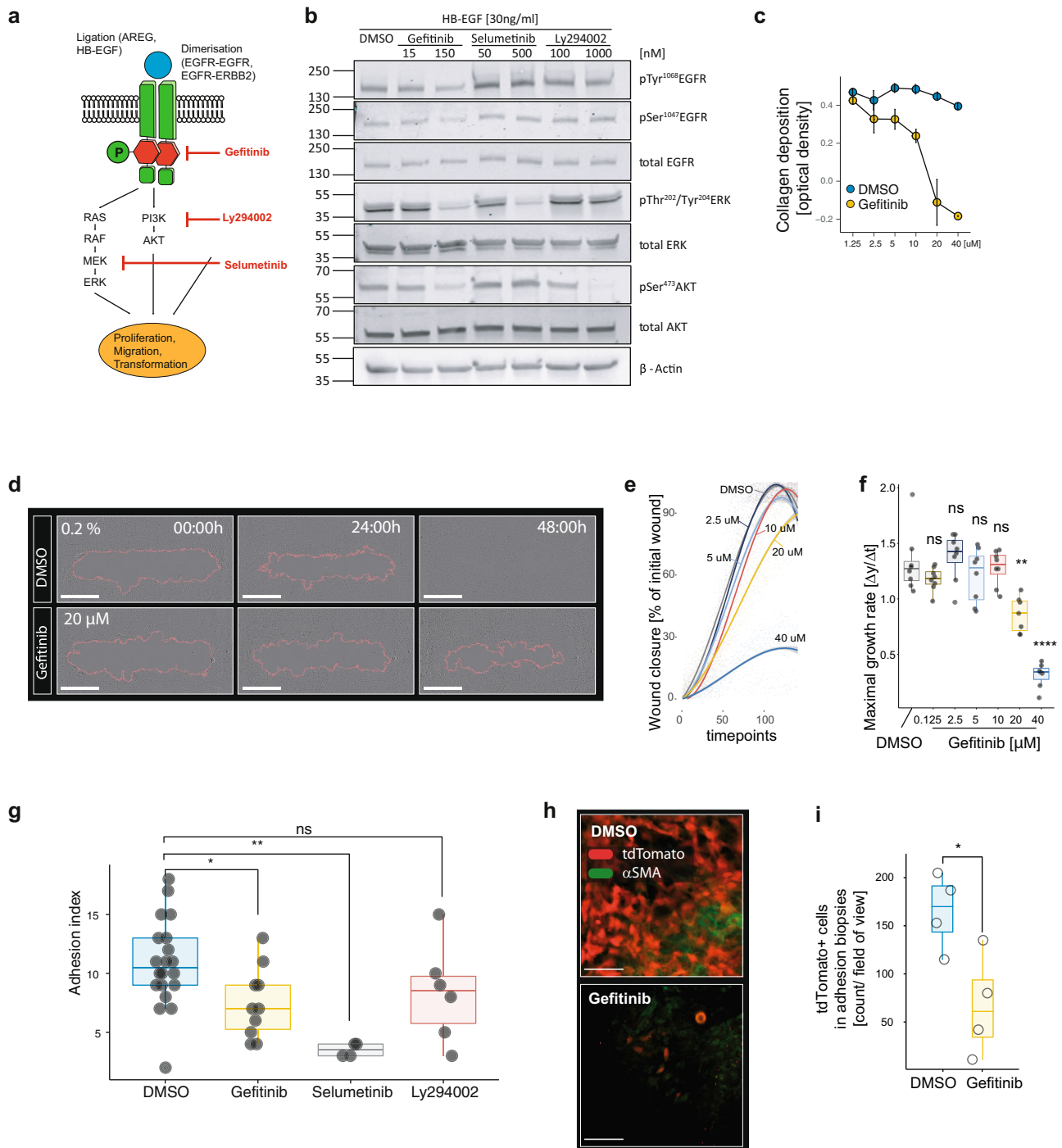


Fig. 5 EGFR-ligands are produced by bone-marrow derived macrophages and a B-cell subset that are recruited to the wound. **a** Illustration of single cell RNA-Sequencing experimental approach. Single cells were isolated from peritoneal buttons (PB) with or without cecal ligation and puncture (CLP). **b-d** UMAP plots colored by cell cluster (**b**), expression of epidermal growth factor receptor (*Egfr*) (**c**), expression of amphiregulin (*Areg*) and heparin-binding epidermal growth factor (*Hbegf*) respectively (**d**). **e** Expression of *Areg* and *Hbegf* by cell cluster and condition. Differential expression testing with FindMarkers function (Seurat). ** $P < 0.01$, **** $P < 0.0001$, n.s. $P \geq 0.05$. **f** Schematic illustration of signaling pathways downstream of EGFR. **g** Western blot stained for phospho-EGFR and the respective downstream molecules illustrated in (**f**). Primary mesothelial cells were incubated with amphiregulin (AREG) and heparin-binding epidermal growth factor (HB-EGF) with the indicated doses for 20 min. Single-cell data represents a pooled data set of $n = 4$ mice ($n = 2$ with CLP, $n = 2$ injury alone). The immunoblot shown in (**g**) represents two independent experiments. Raw data were deposited at gene expression omnibus (GSE186658) and Source Data are provided as Source Data File.



Indeed, when samples were co-stained with the mesothelial markers cytokerin and calretinin, we found that EGFR positivity was specific for mesothelial cells (Fig. 7h). Cumulatively, these data confirm that EGFR is expressed in activated mesothelial cells also in humans.

Human patients with fresh adhesions show elevated EGFR-agonist expression. Next, we wanted to confirm these retrospective observations on a prospective cohort of patients suffering from adhesions. We enrolled $n = 21$ consecutive patients undergoing either elective surgery, emergency surgery for sepsis, or second look emergency surgery. Second look emergency

surgery patients had to be re-operated due to any reason within 14 days after an initial intraabdominal procedure. The presence of adhesions was scored, and patients were grouped into three categories: no adhesions, old adhesions (patient had some adhesions, but they were visibly old and not due to recent surgery) and fresh adhesions either due to abdominal sepsis or recent abdominal surgery. The demographics of this second patient cohort are summarized in Supplementary Table 2. A population of EGFR positive cells was found in biopsies of patients with fresh adhesions (Fig. 8a). These cells also stained positive for mesothelin, suggesting a mesothelial origin of these cells (Fig. 8a). In addition, leukocytes from peritoneal washes of all patients were sampled. Gene expression of EGFR ligands by peritoneal

Fig. 6 Gefitinib, a small molecule inhibitor of EGFR inhibits adhesion formation in vivo. **a** Schematic illustration of signaling pathways downstream of the epidermal growth factor receptor (EGFR). Gefitinib inhibits the kinase domain of EGFR, Ly294002 inhibits phosphoinositide 3-kinase (PI3K), and Selumetinib inhibits mitogen-activated protein kinase kinase (MEK). **b** Western blot stained for phospho-EGFR and the respective downstream molecules illustrated in (a). Primary mesothelial cells were isolated and cultured for two passages before they were treated with heparin-binding epidermal growth factor (HB-EGF) and inhibitors for 20 min. **c** Collagen deposited by primary mesothelial within 3 days of culturing. Data represent $n = 3$ technical replicates examined over 2 independent experiments. Data are presented as mean \pm standard deviation. **d–f** Primary mesothelial cell cultures were treated with Gefitinib vs. dimethylsulfoxide (DMSO) control and scratch healing was assessed using real-time microscopy (**d**) and automated image analysis (**e**, **f**). Data represent $n = 8$ technical replicates examined over 2 independent experiments. Data are presented as individual values and boxplots (median, first and third quartile). P -values by t-test (two-tailed) with Holm Bonferroni correction for multiple testing. Scale bar of (**d**): 1 mm. **g** Adhesion index of mice 7 days after sterile injury (PB) in combination with bacterial contamination (CLP). Gefitinib 100 mg/kg once daily i.p., Selumetinib 50 mg/kg once daily p.o., Ly294002 25 mg/kg once daily i.p., or DMSO 20% once daily i.p. Data represent $n = 20$ for DMSO, 10 for Gefitinib, 4 for Selumetinib, and 6 for Ly294002 independent animals examined and pooled over 3 independent experiments. Data are presented as individual values and boxplots (median, first and third quartile). Wilcoxon test (two-sided) with Holm-Bonferroni correction for multiple-testing. DMSO vs. Gefitinib: $p = 0.017$, DMSO vs. Selumetinib: $p = 0.0058$, DMSO vs. Ly294002: $p = 0.16$. **h** Whole-mount immunohistochemistry of cleared adhesion biopsies 7 days after surgery in *Wt1^{CreERT2} Rosa26^{tdTomato}* mice. TdTomato and alpha smooth muscle actin (α -SMA) positive cells are indicated by red and green respectively. Scale bar 50 μ m. **i** Cell count of tdTomato+ cells in adhesion biopsies such as represented in (**h**). Data represent $n = 4$ independent animals per group (averaged over 2 biopsies per mouse, 2–4 fields of view each) examined over one independent experiment. Data are presented as individual values and boxplots (median, first and third quartile). t-test (two-tailed), $p = 0.028$. Statistical difference by. * $P < 0.05$, ** $P < 0.01$, **** $P < 0.0001$, n.s. $P \geq 0.05$. i.p. intraperitoneal p.o. per os. Source data are provided as a Source Data file.

leukocytes displayed significantly increased levels of amphiregulin (*AREG*) and epregrulin (*EREG*) in patients with fresh adhesions when compared with both control groups (Fig. 8b, c). Interestingly, epidermal growth factor (*EGF*) was significantly down-regulated when compared with controls (Fig. 8d). There was no significant difference in transforming-growth-factor alpha (*TGFA*) (Fig. S10a). In summary, these results replicate two key findings of our mouse model, fresh human adhesions contain EGFR positive cells that are derived from the mesothelium, and human peritoneal leukocytes produce EGFR ligands.

Discussion

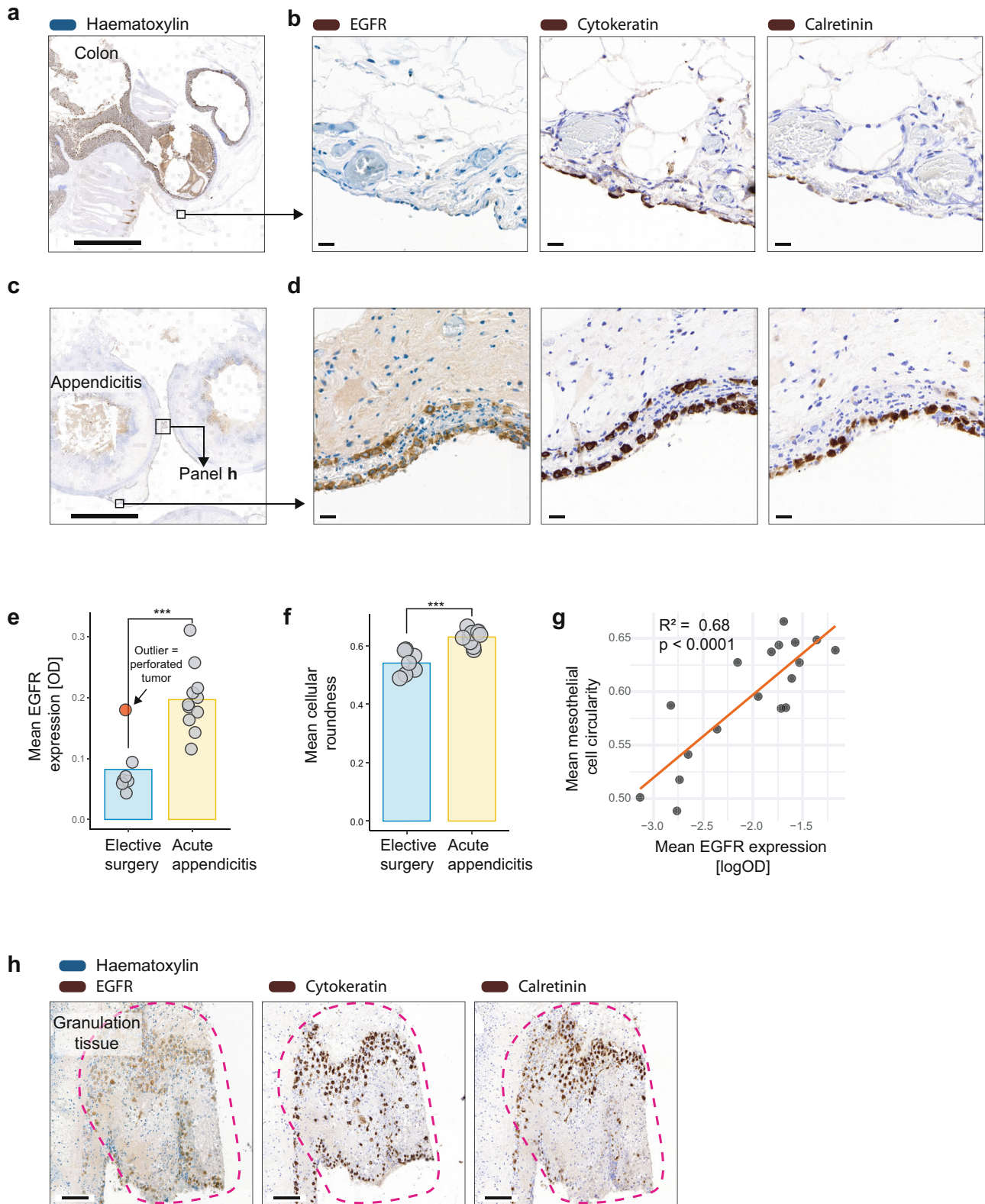
Adhesion formation is driven by a complex interaction of cytokines, coagulation, and growth factors relaying between immune and stromal cells at the site of surgical injury⁸. The duration and severity of the peritoneal inflammatory state is a crucial factor and epidemiologic studies in humans show a correlation between peritonitis, tumor necrosis factor alpha levels, and the severity of adhesions^{13,14}. Therefore, immunosuppression has been proposed as potential therapy to attenuate adhesion formation⁸. While this may be potentially rewarding in sterile situations, the use of immunosuppressive drugs seems problematic in cases of bacterial contamination. In fact, in a model of septic peritonitis, while anti-inflammatory and anti-coagulation treatment led to decreased adhesion formation, this treatment significantly increased mortality³⁴. This demonstrates that inflammation and coagulative compartmentalization of the peritoneal cavity are important mechanisms of innate immunity that prevent spread of contaminating microbes. However, the resulting adhesions result in considerable morbidity. Therefore, a better understanding of the origin of collagen-producing cells in this fibrotic disease, especially under circumstances of bacterial contamination, may help to find a way to prevent pathologic fibrosis while leaving innate immune function intact.

The capacity of mesothelial cells to undergo a mesothelial to mesenchymal transition has been reported in other diseases^{24,25,35,36}. Furthermore, it has been suggested that mesothelial cells are also an important cellular origin of adhesions, as shown with membrane dyes^{11,12,37}. More recently, Fischer et al. used an inducible genetic lineage tracing system based on the mesothelial cell marker *Procr* to show that adhesion myofibroblasts arose from mesothelial precursors³. Here, we used a *Wt1*-based genetic lineage tracing which aligns with these findings and demonstrates that the vast majority of myofibroblasts within adhesions are derived from the mesothelium,

and not from fibroblasts. Therefore, inhibiting the molecular mechanisms by which mesothelial cells become activated myofibroblasts may provide a means to ameliorate the major source of collagen found in adhesions.

Our data suggest that the proliferation of mesothelial cells is driven by receptor tyrosine kinases of the ERBB family such as EGFR and ERBB2, which is significantly more pronounced in the presence of contaminating gut microbes. We show that EGFR signaling is activated by AREG and HB-EGF, these are EGFR ligands that are derived by leukocytes which infiltrate the wound. EGFR signaling is potentiated by contaminating gut microbes. Firstly, this is due to an increase of EGFR ligand production by immune cells in the peritoneal lavage. Secondly, the mesothelium shows a profound upregulation of the receptor (EGFR) in response to contaminating microbes. The mechanism of this upregulation of EGFR in response to microbial challenge needs yet to be investigated. Furthermore, our data indicate that EGFR is expressed predominantly on the basolateral side of mesothelial cells. This could indicate that the EGFR-ligands produced by immune cells in the peritoneal cavity, only access their receptors at sites of disrupted mesothelial integrity. Indeed, similar mechanisms have been described for repair of injuries to the lung epithelium³⁸. Taken together, we provide mechanistic insight into EGFR signaling during post-surgical serosal wound healing and adhesion formation.

Our data suggest that EGFR inhibition may prevent post-surgical formation of adhesions. EGFR inhibition has been reported to prevent generalized peritoneal fibrosis³⁹, a different disease that shares some pathologic hallmarks with adhesion formation, such as mesothelial origin of collagen secreting myofibroblasts. Here, we show that many key observations in the mouse model were replicated in biopsies of adhesions from human patients. Patients undergoing surgery for acute appendicitis showed significantly elevated EGFR levels in the mesothelium when compared with patients undergoing elective surgery. Additionally, adhesions from patients show the presence of mesothelin/EGFR double-positive cells, suggesting that adhesions may be derived from mesothelial cells. Together, these data suggest that the EGFR-dependent mechanism we identify here is involved in human patients developing adhesions. In conclusion, inhibition of EGFR signaling may represent an avenue for preventing the development of adhesions in patients, by abrogating the expansion and differentiation of mesothelial cells into adhesions. This is particularly interesting because several small-



molecule EGFR-inhibitors, like Gefitinib used in this study, have already been approved for the treatment of non-small lung cancer. In our study, high Gefitinib concentrations were necessary to be effective on mesothelial cells in vitro and in vivo. This is a potential limitation to this approach. Further studies, such as retrospective analysis of patients that underwent abdominal surgery while being treated with EGFR-inhibitors as well as

prospective studies are warranted to investigate the benefit of EGFR-inhibition in preventing adhesions in human patients.

Methods

The research conducted complies with all relevant ethical regulations. Human studies and the use of human samples were approved by the Ethical commission of the Canton Bern (project ID: 2017-00573 and 2020-00077). Animal experiments

Fig. 7 Mesothelial EGFR expression of human patients with bacterial peritonitis is increased. **a–d** Biopsies from human patients. Patients either underwent surgery due to acute appendicitis (**c, d**) or for elective abdominal surgery such as tumor surgery (**a, b**). Formalin fixed and paraffin-embedded samples were stained with anti-human epidermal growth factor receptor (EGFR), anti-human cytokeratin and anti-human calretinin. (**a**) and (**c**) both show an overview. Scale bar: 5 mm. (**b**) and (**d**) show magnifications of (**a**) and (**c**) respectively, Scale bar: 20 μ m. **e** Mean EGFR expression was quantified in all patients. Outlier in red color represents an elective-surgery case that turned out to be a perforated tumor with potential bacterial contamination (not excluded for statistical testing). $P = 0.00075$. **f** Automated quantification of mesothelial cell roundness. $P = 0.00013$. **g** Linear regression shows a correlation between mean mesothelial EGFR expression and mean mesothelial roundness ($R^2 = 0.68$, $p < 0.0001$). **h** Area with suspected appendiceal adhesion covered up with granulation tissue. Magnification shows the abundance of EGFR positive cells in granulation tissue. Scale bar: 100 μ m. The images shown in (**a–d**) are representative of the quantification shown in (**e–f**). The images shown in (**h**) are representative of the appendicitis group of patients. Data are presented as mean and individual symbols. Data are representative of $n = 7$ for Elective and $n = 11$ for Appendicitis group. Patient demographics according to Supplementary Table 1. Indicated statistical differences in (**e**) and (**f**) by Wilcoxon test (two-sided). R-squared and p -value in (**g**) by linear regression. Source data are provided as a Source Data file. *** $P < 0.001$. OD: optical density.

were carried out in accordance with Swiss federal regulations and approved by the cantonal committee on animal experimentation in Bern Switzerland (BE 18/17 and BE 55/18). The experiments conducted in Canada were conducted in accordance with Canadian legislations and policies and approved by the institutional animal care committee of the University of Calgary in Calgary Canada (AC19-0148 JZ-PA).

Experimental animals. Female C57BL/6(J) mice with 8 to 12 weeks of age were purchased from Envigo, Netherlands. Animals were housed in specific-pathogen-free (SPF) conditions with free access to water and food, a 12 h day-night cycle in the central animal facility of the University of Bern, Switzerland. The ambient temperature was 20 ± 2 °C and humidity was kept at $50 \pm 10\%$. Female *Wt1^{CreERT2}Rosa26^{tdTomato}* reporter mice²⁵ were housed in SPF conditions with free access to water in the central animal facility of the University of Calgary, Canada. The ambient temperature was 21 °C, and humidity was kept at 32%. Female *Wt1^{CreERT2}Rosa26^{tdTomato}* reporter were used for experiments at age 10–12 weeks.

Germ-free and gnotobiotic mice. Female germ-free C57BL/6(J) mice were derived germ-free as previously described⁴⁰ and maintained germ-free in flexible film isolators in the Clean Animal Facility of the University of Bern, Switzerland. Germ-free mice were routinely monitored by culture-dependent (Luria-Bertani broth) and -independent (Gram and DNA-Sytox stains) methods to confirm sterility. Female gnotobiotic C57BL/6(J) mice colonized with stable defined moderately diverse mouse microbiota (sDMDMm2) containing 12 defined bacterial strains were generated²⁰ and maintained at the Clean Animal Facility of the University of Bern. Gnotobiotic mice were routinely monitored by 16 s rRNA gene sequencing by Ion Torrent PGM system.

Surgical procedure. General anesthesia was achieved using isoflurane anesthesia (2% v/v) and analgesia Buprenorphine 0.1 mg/kg body weight (Temgesic®, Indivior, #07680419310018) was administered subcutaneously. The abdomen was then shaved and prepared with alcohol solution. For all surgical models, a 2.5 cm median laparotomy was performed to access the abdominal cavity. Then, lesions were induced to trigger adhesion formation such as peritoneal buttons (PB) and cecal ligation and puncture (CLP). The abdomen was closed using a one-layer running suture (6-0 Prolene®, Ethicon). PB was performed as previously described⁴¹. In brief, a small portion of the peritoneum is grasped and ligated at its base using a polypropylene suture (4-0 Prolene®, Ethicon), creating a standardized peritoneal button. This is repeated for a total of four buttons, one in each quadrant. A modified sub-lethal CLP was performed. The model was performed as previously described³⁴. Different lengths of the cecum were ligated (4 and 2 mm) and punctured once through with a needle of different sizes (18, 21, and 25 Gauge). In the PB + CLP model the lesions of the PB and CLP models were combined. No standard antibiotics prophylaxis was administered. If perioperative antibiotics were given, they were administered 30–60 min prior to surgery by subcutaneous route. The antibiotic substance given were either Ceftriaxone (120 mg/kg, Fresenius Kabi, #61338002), Clindamycine (36 mg/kg, Pfizer, #61898002) or Amoxicillin + Clavulanic acid (200 + 20 mg/kg, Mepha, #56758004).

Evaluation parameters and tissue collection. For adhesion scoring and tissue collection, mice were anesthetized by subcutaneous injection of 6 μ l/g body weight of a cocktail of Fentanyl, Midazolam, and Medetomidine as previously described⁴². The abdominal wall was accessed using an inverted U-shaped incision and adhesions were scored by two different observers according to the scoring schemes proposed by Nair, Mazuji, and Zuhlke^{16–18}. In addition, an advanced scoring scheme called adhesion index was introduced as described in the results section. Blood was collected from the inferior vena cava using a 24 Gauge catheter (BD Insyte-W). Blood was incubated at room temperature for 60–90 min and centrifuged at $2000 \times g$ for 20 min, then the supernatant serum was collected. Collection of peritoneal fluid and peritoneal cells was done as previously described⁴³. In brief, the abdominal cavity was flushed with 5 ml of ice-cold phosphate-buffered saline (PBS) which was immediately re-aspirated and snap-frozen in liquid

nitrogen for analysis. Tissue biopsies of peritoneal buttons, peritoneal adhesions and healthy peritoneum control were taken and either snap-frozen or fixed in formalin for 4 h at RT.

Preparation and administration of small molecule inhibitors. Gefitinib (Sigma, #SML1657) and Ly294002 (Lucerna Chem, #HY-10108): Stock solutions were prepared by dissolving 100 mg/ml in DMSO. Stock solutions were diluted with saline to reach a final concentration of 20 mg/ml Gefitinib in 20% DMSO. Selumetinib (Lucerna Chem, #HY-50706) was dissolved in 10% DMSO in corn oil. Small molecule inhibitors were administered 2–3 h after the surgery and once daily thereafter. Gefitinib and Ly294002 were administered by intraperitoneal injection and Selumetinib by oral gavage, with the doses as specified in the manuscript and figure legends.

Cecal slurry (CS) stock preparation. CS was prepared as previously described⁴⁴. In brief, fecal content from ceca of C57BL/6(J) mice was collected and mixed with sterile water at a ratio of 0.5 ml water to 100 mg of cecal content. The suspension was then filtered consecutively through a 100 μ m and 70 μ m filter. The filtered solution was then mixed with an equal volume of 30% glycerol in PBS, resulting in a final CS stock solution in 15% glycerol in PBS. The CS stock was aliquoted and stored at -80 °C for later experiments. Heat inactivation of CS was performed by incubating CS stock solution for 20 min at 72 °C. Colony formation assays were performed before and after to confirm heat inactivation.

Immunohistochemistry. For immunohistochemistry formalin-fixed paraffin-embedded patient material was cut in 2.5 μ m thick serial sections followed by deparaffinization, rehydration, and antigen retrieval using an automated immunostainer (Bond RX, Leica Biosystems, GER). Antigen retrieval was performed for epidermal growth factor receptor (EGFR) with protease for 5 min at 37 °C. EGFR antibody was diluted 1:25 (Supplementary Table 3). Slides were counterstained with hematoxylin. Scans were acquired with an automated slide scanner Panoramic 250 (3DHitech version 3.0.2) at $\times 40$ magnification. Images were analyzed using the QuPath software⁴⁵.

Immunofluorescence. Formalin-fixed material, incubated overnight in 30% sucrose, was cut at 7 μ m in a cryostat (CM3050 S, Leica). After protein blocking (PBS, 5% goat serum), the slides were incubated with the primary antibody with concentrations according to Supplementary Table 3. This was followed by an incubation with a secondary antibody for 1 h at room temperature according to Supplementary Table 3.

Cytospin. Mesothelial cells were suspended in PBS containing 3% FCS with primary and secondary antibodies according to Supplementary Table 3. After staining, cells were centrifuged at $800 \times g$ onto a glass slide using Cytospin4® Cytocentrifuge (Thermo Fisher Scientific).

QuPath image analysis. Using QuPath software⁴⁶ digital-scanned tissue sections of EGFR IHC were first preprocessed in the built-in visual stain editor using default settings for estimation of stain vectors to improve staining quality. In each tissue section, the mesothelium was annotated by a pathologist (H.D.). Using a watershed segmentation method, cells were automatically detected and manually reconfirmed by a pathologist (H.D.) based on histomorphological features including cellular and nuclear shape. A minimum of 800 cells and a total of 77 parameters per cell (including cell perimeter, cell circularity, staining OD etc.) was quantified for each tissue sample. Results were exported as.csv files for statistical analysis in R.

For collagen quantification, sections were stained with Masson Trichrome (Sigma, #HT15-1KT) according to the manufacturer's instruction. Two independent and blinded investigators (JZ, JM) annotated the adhesion area and exported it to ImageJ⁴⁶. The RGB image was split into the respective red, green, and

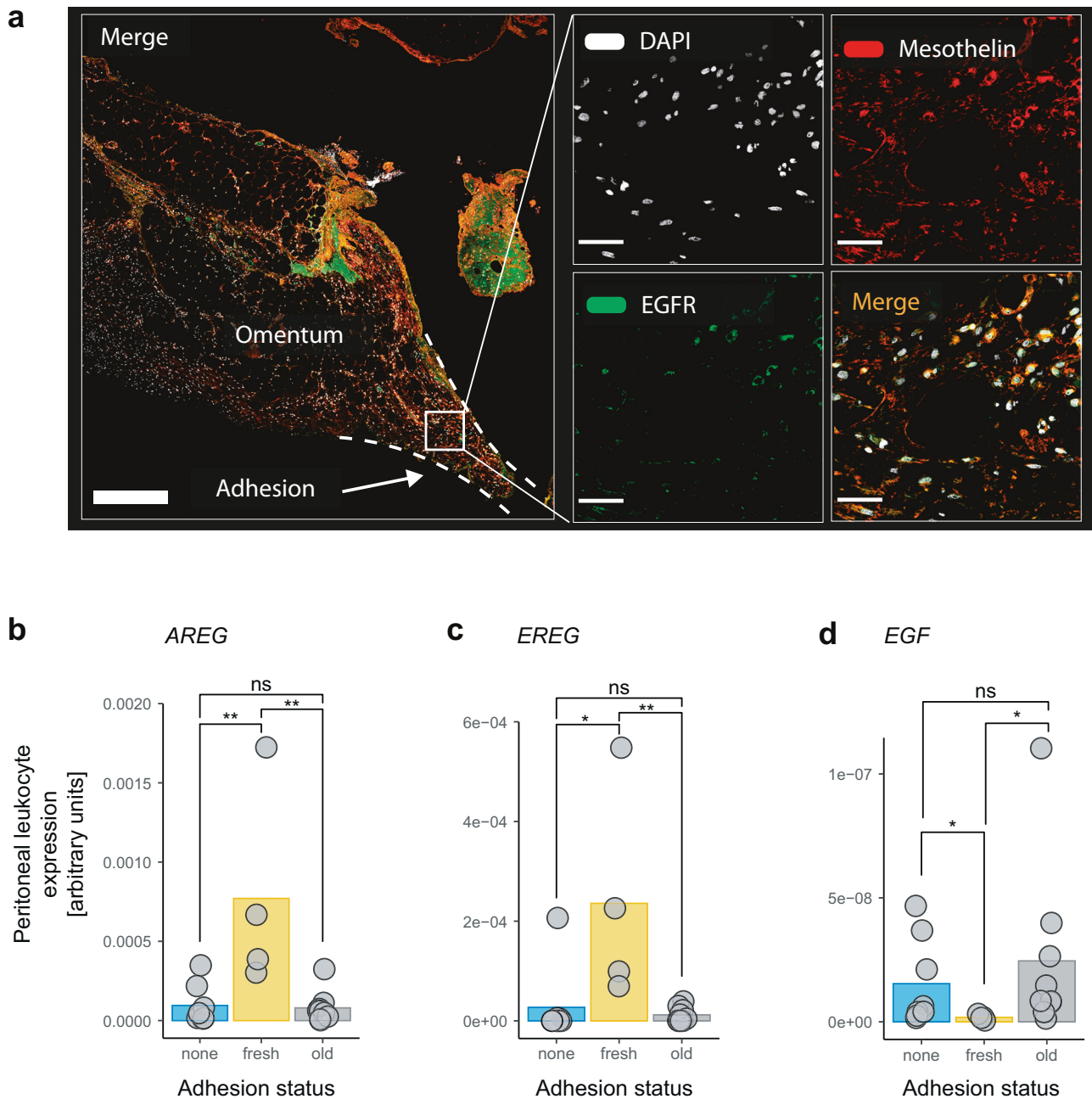


Fig. 8 Human patients with adhesions have EGFR positive cells of mesothelial origin in them and an elevated EGFR-agonist expression in their peritoneal leukocytes. **a** Biopsy from a patient with a fresh adhesion (13 days after initial surgery) stained for mesothelin and epidermal growth factor receptor (EGFR). Image depicts omental tissue that was adherent to a piece of intestine (the latter could not be included in the biopsy). Magnification shows cells that are double positive for mesothelin and EGFR. Scale bar overview: 500 μ m, Scale bar magnification: 50 μ m. Images are representative of $n = 4$ human patients. **b-d** Peritoneal leukocytes were isolated from patients with no, fresh or old adhesions. Expression of EGFR ligand genes was measured by quantitative polymerase chain reaction. **(b)** amphiregulin (AREG), none vs. fresh: $p = 0.0081$, none vs. old: $p = 0.96$, fresh vs. old: $p = 0.0056$. **(c)** epiregulin (EREG), none vs. fresh: $p = 0.016$, none vs. old: $p = 0.24$, fresh vs. old: $p = 0.0028$. **(d)** epidermal growth factor (EGF), none vs. fresh: $p = 0.028$, none vs. old: $p = 0.48$, fresh vs. old: $p = 0.02$, Data are represented as mean and individual symbols. Data represent $n = 8$ for none, 4 for fresh, and 9 for old individual patients of one independent cohort study. Patient demographics according to Supplementary Table 2. Indicated statistical differences by Wilcoxon test (two-sided) with Holm-Bonferroni correction for multiple-testing. * $P < 0.05$, ** $P < 0.01$, n.s. $P \geq 0.05$. Source data are provided as a Source Data file.

blue image components. Collagen formation was quantified by measuring the area percentage of blue channel above a threshold of 120 units (8-bit).

Isolation of primary mouse peritoneal mesothelial cells. Mice were anesthetized as described above. A 22 Gauge catheter was inserted into the peritoneal cavity and

the peritoneal cavity was flushed three times with 5 ml warm PBS containing 2 mM EDTA. The wash buffer was aspirated completely for each wash and discarded. Then, 5 ml of digestion buffer (0.5% Trypsin-EDTA, ThermoFisher, #15400-054) were injected and incubated for 10 min while the mouse was kept warm under an infrared light. The digestion buffer was aspirated, and the abdominal cavity was flushed three times with 5 ml ice cold PBS containing 2 mM EDTA and 3% FCS to

collect mesothelial cells. Cells were purified as previously described²⁵. In brief, cells were washed two times and then incubated with anti-mouse GPM6A (Clone Nr. 321, MBL, #D055-3) for 30 min at 4 °C. After centrifugation the cells were incubated with anti-rat IgG MicroBeads (Miltenyi, #130-048-502) and were purified by MACS Separation columns LS (Miltenyi, #130-042-401) according to their instructions. Cells were cultured in RPMI 1640 GlutaMAX™ medium (Gibco, #61870044) supplemented with 13% fetal bovine serum, Insulin-Transferrin-Selenium-Sodium Pyruvate (ThermoFisher, #51300044), 20 mM Hepes (Sigma, #H0887), and 100 U/ml Penicillin-Streptomycin (ThermoFisher, #15140122).

RNA-sequencing of mesothelial cells. Mesothelial cells at different time-points after surgical induction of peritoneal adhesions using the PB + CLP model were isolated and purified as described above. Cells were kept on ice for a maximum of 30 min. Total RNA was isolated from purified cells by ReliaPrep RNA Miniprep Systems (Promega, #Z6010) according to manufacturer's instructions. RNA quality was assessed using the Bioanalyzer (Agilent 2100 Bioanalyzer) and an RNA 6000 Nano Kit (Agilent Technologies, #5067-1512). Nucleic acid quantification was done using the Qubit RNA Assay (ThermoFisher Scientific, #Q32852). Total RNA was used as input for complementary DNA (cDNA) preparation. Fragments were sequenced using S1 cell flow on a NovaSeq 6000 operated by NovaSeq Control Software (v. 1.5). The reads obtained were trimmed for base call quality and the presence of adapter sequences. Raw fastq files were aligned to the mouse reference genome mm10 using HISAT2⁴⁷. The counts were counted with the featureCounts function of the R package Rsubread. The resulting read counts matrix was analyzed using a standardized Bioconductor workflow with limma, Glimma and edgeR packages in R (23). In brief, raw counts were transformed to counts per million (CPM) after the calculation of library size normalization factors using the edgeR package. Genes not expressing at least 1 CPM in 3 samples were filtered out. For gene differential expression analysis data were transformed and weighted using the voom package. Then a linear model was fitted in the limma package and contrasts were estimated for each gene. A log₂-fold change of 1 and $p < 0.01$ were considered as threshold of differentially expressed genes. Differentially expressed genes by limma pairwise comparison were subjected to gene set enrichment analysis using metascap <http://metascap.org/>(24).

Single-cell RNA-Sequencing of peritoneal buttons. Mice C57BL/6(J) underwent surgery to receive injury alone (PB) or in combination with bacterial contamination (PB + CLP). After 24 h mice were euthanized by injection anesthesia and subsequent intracardial perfusion with ice cold PBS with 2 mM EDTA. Peritoneal buttons were excised and digested for 30 min at 37 °C in IMDM (Gibco, #12440061) containing Ca, 25 mM Hepes, 2% FCS, 1 mg/ml Collagenase 1a (Sigma, #C9891-1g) and 0.1 mg/ml DNaseI (Roche, #10104159001). IMDM with 2 mM EDTA was used to stop the reaction and wash the cells. Then, samples were resuspended in 40% Percoll (VWR, #17-0891-01) and pipetted on top of 80% Percoll solution to create a gradient. After centrifugation (650 × g, 20 min), the interface was transferred again and washed in DPBS + 0.04% BSA. Finally, the sample was resuspended in DPBS + 0.04% BSA for library preparation. RNA-seq libraries were prepared from 10000 cells using the Chromium Single Cell 3' Library & Gel Bead Kit v3 (10xGenomics, #PN-1000075). Libraries were prepared according to the manufacturer's protocol. Sequencing was performed on a NovaSeq 6000 S2 flow cell operated by NovaSeq Control Software (v. 1.7). The function cellranger count from Cell Ranger was used to transform the fastq files. The reference genome was the mm10 available at Illumina Cell Ranger webpage. Next, we used the function cellranger mat2csv to generate the UMI matrix.

scRNA-Seq data analysis. Data analysis was done following the standard Seurat pipeline⁴⁸. The Seurat objects were created with the function Read10x. Cells expressing less than 200 genes were excluded. Dead cells, identified as cells with more than 10% reads coming from mitochondrial genes, were excluded. Doubles were removed using the doubletFinder function from the DoubletFinder package⁴⁹. The transformation was done using Seurat's SCT transform and the Seurat objects were merged using the merge function. We performed a Principal Component Analysis (PCA) of the Seurat object with the RunPCA function for all the cells. Clustering and dimensionality reduction were performed using FindNeighbors, FindClusters, and RunUMAP (dims = 1:30). Clusters merging and annotation were done manually within the Seurat workflow and unsupervised using the SingleR package⁵⁰ for validation. We used the MAGIC package for dropout correction for the gene expression visualization shown⁵¹.

Western blot. Protein extraction was performed with RIPA buffer completed with protease inhibitors. Concentration was measured with Bio-Rad microplate protein assay (Biorad, #500-0006). Identical amount of total protein was separated by SDS-PAGE and then transferred on a nitrocellulose membrane (Thermo Fisher, #IB23001) by semi-dry transfer. The membranes were incubated with primary antibodies (Supplementary Table 6) overnight at 4 °C and with secondary antibodies (Supplementary Table 6) for 1 h at room temperature. The proteins of interest were detected using Licor Odyssey infrared scanner operated by Li-cor Odyssey software (2.1.15). For normalization, membranes were incubated with HRP-conjugated β-actin antibody which was detected using enhanced chemiluminescence (WesternBright ECL Spray, Witec, #H K-12049-D50) and the Fusion-

FX7 system operated by the latest firmware (version 1.0.12). All uncropped and unprocessed scans can be found in the Source Data file. All loading controls are displayed in the Source Data file and representative loading controls were chosen for the main text figures.

Whole-mount tissue staining, clearing, and imaging. Whole-mount staining and tissue clearing were done as previously described²⁶. In brief, mice were perfused with PBS containing 5 mM EDTA. Adhesions/peritoneal buttons were dissected and fixed with 4% PFA/PBS for 2 h at 4 °C. Samples were washed 3 × 30 min in 1% Triton/PBS and then permeabilized and blocked in blocking buffer (1% Triton, 10% FCS, 0.02% sodium azide in PBS). Antibodies were diluted in blocking buffer and incubated for 24–48 h at 4 °C on a rotation device. After washing for 3 × 1 h in blocking buffer and 3 × 10 min in 1% Triton/PBS, the samples were dehydrated using an ethanol series (4 h 50%, 4 h 75%, 2 × 4 h 100%) with a pH of 9.0. Dehydrated samples were incubated in ethyl cinnamate (Sigma, #112372) for 2 h at room temperature and imaged within 2 days with an inverted Leica SP8 2-photon confocal microscope (Leica Microsystems) operated by Leica LAS X software.

Multiplex cytokine assay (Mesoscale). Cytokine measurements were done from mice following PB + CLP model using the Meso Scale Discovery system (MSD, Rockville, Maryland). Serum and peritoneal fluid were collected as described above and stored at –80 °C. The assay was performed according to the manufacturer's instructions. In brief, the MSD system employs a multiplexed immuno-sandwich assay. Each well was prepared with a cocktail of up to 10 specific capture antibodies. Diluted samples and serially diluted standards were pipetted into 2 plates of the customized 19-plex assay. After incubation, cytokine was detected using a cocktail of up to 10 specific, SULFO-TAG-conjugated, detection antibodies. The plate was read in a Meso Scale plate reader and cytokine concentration was calculated from a standard curve, which was fitted for each cytokine using a 4-parameter logistic regression model.

Flow cytometry. Suspended cells were isolated from the peritoneal cavity by repeatedly flushing the peritoneal cavity with ice cold PBS containing 3% FCS and 2 mM EDTA (FACS buffer). Cells were filtered through a 40 μm cell strainer (Falcon, #352340) and after centrifugation re-suspended in erythrocyte lysis buffer (Qiagen, #160018730) for 5 min at room temperature. Cells were washed in PBS and stained with fixable viability dye (eFluor 506, eBioscience, #65-0866-14) diluted in PBS for 20 min on ice. Single-cell suspensions were incubated with fluorescence-coupled antibodies diluted in FACS buffer according to titration (Supplementary Table 5). Finally, cell data were acquired on a LSR II SORP H271 (BD Biosciences). Flow cytometric analysis was done using FlowJo (Treestar). In all experiments, FSC-H versus FSC-A was used to gate on singlets with dead cells excluded using the fluorescence-coupled fixable viability dye.

Gene expression analysis. Tissue samples were snap-frozen in liquid nitrogen. Total RNA was isolated from the tissue by NucleoZOL reagent and following manufacturer's protocol (Macherey-Nagel, #740404.200). RNA concentration and quality were analyzed by spectrophotometer NanoDrop ND-1000 (Thermo Scientific). A total of 500 ng RNA was used for cDNA synthesis by reverse transcription (Omniscript RT Kit 200, Qiagen, #205113). Quantitative PCR was performed using TaqMan gene expression assays (ThermoFisher Scientific) and a real-time PCR cycler (ABI 7900, SDS 2.3 software). Primer and probe sequences were purchased from ThermoFisher Scientific (Supplementary Table 4). Relative changes in mRNA were calculated.

Human samples. Both patient cohorts presented in this study were approved by the Ethical commission of the Canton Bern (project ID: 2017-00573 and 2020-00077). All patients gave their informed consent. Participants did not receive any form of compensation. Histology was performed as described above. The isolation of peritoneal leukocytes was performed as previously described⁵². In brief, suction bags were removed after the surgical procedure was finished. The suction fluid was filtered through a 100 μm filter and a Ficoll gradient (GE Healthcare, #17-5442-02) was performed by pipetting 10 ml Ficoll under 35 ml peritoneal lavage fluid in a 50 ml falcon tube. Tubes were centrifuged at 800 × g, 4 °C, 20 min, no brake. The interface was collected and transferred to a new tube and after centrifugation resuspended in Erythrocyte lysis buffer (Qiagen, #160018730) for 1 min at room temperature. After one wash with PBS and centrifugation at 800 × g for 5 min, the pellet was lysed for RNA isolation.

Statistics. Statistical tests were performed using R⁵³. Grouped data were compared using non-parametric tests (Wilcoxon). Multiple testing was corrected using Holm's sequential Bonferroni post-hoc test and $p = 0.05$ was considered the threshold of significance. P -values are graphically represented according to the New England Journal of Medicine style: $p > 0.05$: ns, $p \leq 0.05$: *, $p \leq 0.01$: **, and $p \leq 0.001$: ***.

Reporting summary. Further information on research design is available in the Nature Research Reporting Summary linked to this article.

Data availability

The RNA-Seq data generated in this study have been deposited in the Genome Expression Omnibus (GEO) database under accession code [GSE156127](https://www.ncbi.nlm.nih.gov/assembly/GSE156127). The scRNA-Seq data generated in this study are deposited in the GEO database under accession code [GSE186658](https://www.ncbi.nlm.nih.gov/assembly/GSE186658). The publicly available data (Mus musculus genome assembly, mm10) used in this study are available in the National Center for Biotechnology Information (NCBI) database under accession code GRCm38 [https://www.ncbi.nlm.nih.gov/assembly/GCF_000001635.20/]. The remaining data are available within the Article, Supplementary Information or Source Data file. Source data are provided with this paper.

Received: 26 August 2020; Accepted: 1 December 2021;

Published online: 16 December 2021

References

- Sulaiman, H. et al. Growth of nerve fibres into murine peritoneal adhesions. *J. Pathol.* **192**, 396–403 (2000).
- Zindel, J. et al. Primordial GATA6 macrophages function as extravascular platelets in sterile injury. *Science* **371**, eabe0595 (2021).
- Fischer, A. et al. Post-surgical adhesions are triggered by calcium-dependent membrane bridges between mesothelial surfaces. *Nat. Commun.* **11**, 3068 (2020).
- Polymeneas, G., Theodosopoulos, T., Stamatidis, A. & Kourias, E. A comparative study of postoperative adhesion formation after laparoscopic vs open cholecystectomy. *Surg. Endosc.* **15**, 41–43 (2001).
- Ellis, H. et al. Adhesion-related hospital readmissions after abdominal and pelvic surgery: a retrospective cohort study. *Lancet* **353**, 1476–1480 (1999).
- Sikirica, V. et al. The inpatient burden of abdominal and gynecological adhesiolysis in the US. *BMC Surg.* **11**, 13 (2011).
- Nieuwenhuijzen, M., Reijnen, M. M., Kuijpers, J. H. & van Goor, H. Small bowel obstruction after total or subtotal colectomy: a 10-year retrospective review. *Br. J. Surg.* **85**, 1242–1245 (1998).
- Hellebrekers, B. W. & Kooistra, T. Pathogenesis of postoperative adhesion formation. *Br. J. Surg.* **98**, 1503–1516 (2011).
- Cates, W., Farley, T. M. & Rowe, P. J. Worldwide patterns of infertility: is Africa different? *Lancet* **2**, 596–598 (1985).
- ten Broek, R. P. et al. Benefits and harms of adhesion barriers for abdominal surgery: a systematic review and meta-analysis. *Lancet* **383**, 48–59 (2014).
- Tsai, J. M. et al. Surgical adhesions in mice are derived from mesothelial cells and can be targeted by antibodies against mesothelial markers. *Science Translational Medicine* **10**, <https://doi.org/10.1126/scitranslmed.aan6735> (2018).
- Sandoval, P. et al. Mesothelial-to-mesenchymal transition in the pathogenesis of post-surgical peritoneal adhesions. *J. Pathol.* **239**, 48–59 (2016).
- Parker, M. C. et al. The SCAR-3 study: 5-year adhesion-related readmission risk following lower abdominal surgical procedures. *Colorectal Dis.* **7**, 551–558 (2005).
- Kaidi, A. A. et al. Tumor necrosis factor- α : a marker for peritoneal adhesion formation. *J. Surg. Res.* **58**, 516–518 (1995).
- Kazandjian, D. et al. FDA approval of gefitinib for the treatment of patients with metastatic EGFR mutation-positive non-small cell lung cancer. *Clin. Cancer Res.* **22**, 1307–1312 (2016).
- Zuhlke, H. V., Lorenz, E. M., Straub, E. M. & Savvas, V. [Pathophysiology and classification of adhesions]. *Langenbecks Archiv fur Chirurgie. Supplement II, Verhandlungen der Deutschen Gesellschaft fur Chirurgie. Deutsche Gesellschaft fur Chirurgie. Kongress*, 1009–1016 (1990).
- Mazuji, M. K., Kalambaheti, K. & Pawar, B. Prevention of adhesions with polyvinylpyrrolidone. *Arch. Surg.* **89**, 1011–1015 (1964).
- Nair, S. K., Bhat, I. K. & Aurora, A. L. Role of proteolytic enzyme in the prevention of postoperative intraperitoneal adhesions. *Arch. Surg.* **108**, 849–853 (1974).
- Coccolini, F. et al. Peritoneal adhesion index (PAI): proposal of a score for the “ignored iceberg” of medicine and surgery. *World J. Emerg. Surg.* **8**, 6 (2013).
- Uchimura, Y. et al. Complete genome sequences of 12 species of stable defined moderately diverse mouse microbiota 2. *Genome Announcements* **4**, <https://doi.org/10.1128/genomeA.00951-16> (2016).
- Bochaton-Piallat, M.-L., Gabbiani, G. & Hinz, B. The myofibroblast in wound healing and fibrosis: answered and unanswered questions. *F1000Research* **5**, F1000 Faculty Rev–F1000 Faculty1752 (2016).
- Tomasek, J. J., Gabbiani, G., Hinz, B., Chaponnier, C. & Brown, R. A. Myofibroblasts and mechano-regulation of connective tissue remodelling. *Nat. Rev. Mol. Cell Biol.* **3**, 349–363 (2002).
- Hinz, B. et al. Recent developments in myofibroblast biology: paradigms for connective tissue remodeling. *Am. J. Pathol.* **180**, 1340–1355 (2012).
- Chen, Y. T. et al. Lineage tracing reveals distinctive fates for mesothelial cells and submesothelial fibroblasts during peritoneal injury. *J. Am. Soc. Nephrol.* **25**, 2847–2858 (2014).
- Li, Y., Wang, J. & Asahina, K. Mesothelial cells give rise to hepatic stellate cells and myofibroblasts via mesothelial–mesenchymal transition in liver injury. *Proc. Natl. Acad. Sci.* **110**, 2324–2329 (2013).
- Klingberg, A. et al. Fully automated evaluation of total glomerular number and capillary tuft size in nephritic kidneys using lightsheet microscopy. *J. Am. Soc. Nephrol.* **28**, 452–459 (2017).
- Devuyt, O., Margettes, P. J. & Topley, N. The pathophysiology of the peritoneal membrane. *J. Am. Soc. Nephrol.* **21**, 1077–1085 (2010).
- Rynne-Vidal, A. et al. Mesothelial-to-mesenchymal transition as a possible therapeutic target in peritoneal metastasis of ovarian cancer. *J. Pathol.* **242**, 140–151 (2017).
- Ko, J. H., Kim, H. J., Jeong, H. J., Lee, H. J. & Oh, J. Y. Mesenchymal stem and stromal cells harness macrophage-derived amphiregulin to maintain tissue homeostasis. *Cell Rep.* **30**, 3806–3820.e3806 (2020).
- Minutti, C. M. et al. A macrophage-pericyte axis directs tissue restoration via amphiregulin-induced transforming growth factor beta activation. *Immunity* **50**, 645–654.e646 (2019).
- Zaiss, D. M. W., Gause, W. C., Osborne, L. C. & Artis, D. Emerging functions of amphiregulin in orchestrating immunity, inflammation, and tissue repair. *Immunity* **42**, 216–226 (2015).
- Zhang, Q. et al. Effect of weekly or daily dosing regimen of Gefitinib in mouse models of lung cancer. *Oncotarget* **8**, 72447–72456 (2017).
- Dixit, R., Ai, X. & Fine, A. Derivation of lung mesenchymal lineages from the fetal mesothelium requires hedgehog signaling for mesothelial cell entry. *Development* **140**, 4398–4406 (2013).
- Echtenacher, B., Weigl, K., Lehn, N. & Mannel, D. N. Tumor necrosis factor-dependent adhesions as a major protective mechanism early in septic peritonitis in mice. *Infect. Immun.* **69**, 3550–3555 (2001).
- Mutsaers, S. E. et al. Mesothelial cells in tissue repair and fibrosis. *Front. Pharmacol.* **6**, 113 (2015).
- Mutsaers, S. E., Prele, C. M., Pengelly, S. & Herrick, S. E. Mesothelial cells and peritoneal homeostasis. *Fertil. Steril.* **106**, 1018–1024 (2016).
- Rinkevich, Y. et al. Identification and prospective isolation of a mesothelial precursor lineage giving rise to smooth muscle cells and fibroblasts for mammalian internal organs, and their vasculature. *Nat. Cell Biol.* **14**, 1251–1260 (2012).
- Vermeer, P. D. et al. Segregation of receptor and ligand regulates activation of epithelial growth factor receptor. *Nature* **422**, 322–326 (2003).
- Wang, L. et al. Inhibition of EGF Receptor Blocks the Development and Progression of Peritoneal Fibrosis. *J. Am. Soc. Nephrol.* **27**, 2631–2644 (2016).
- Smith, K., McCoy, K. D. & Macpherson, A. J. Use of axenic animals in studying the adaptation of mammals to their commensal intestinal microbiota. *Semin. Immunol.* **19**, 59–69 (2007).
- Bianchi, E. et al. Ghrelin ameliorates adhesions in a postsurgical mouse model. *J. Surg. Res.* **201**, 226–234 (2016).
- Fleischmann, T., Jirkof, P., Henke, J., Arras, M. & Cesarovic, N. Injection anaesthesia with fentanyl–midazolam–medetomidine in adult female mice: importance of antagonization and perioperative care. *Lab. Anim.* **50**, 264–274 (2016).
- Ray, A. & Dittel, B. N. Isolation of mouse peritoneal cavity cells. *J. Visualized Exp.* **1488**, <https://doi.org/10.3791/1488> (2010).
- Starr, M. E. et al. A new cecal slurry preparation protocol with improved long-term reproducibility for animal models of sepsis. *PLoS ONE* **9**, e115705 (2014).
- Bankhead, P. et al. QuPath: Open source software for digital pathology image analysis. *Sci. Rep.* **7**, 16878 (2017).
- Schneider, C. A., Rasband, W. S. & Eliceiri, K. W. NIH Image to ImageJ: 25 years of image analysis. *Nat. Methods* **9**, 671–675 (2012).
- Kim, D., Langmead, B. & Salzberg, S. L. HISAT: a fast spliced aligner with low memory requirements. *Nat. Methods* **12**, 357–360 (2015).
- Hao, Y. et al. Integrated analysis of multimodal single-cell data. *Cell* **184**, 3573–3587.e3529 (2021).
- McGinnis, C. S., Murrow, L. M. & Gartner, Z. J. DoubletFinder: doublet detection in single-cell RNA sequencing data using artificial nearest neighbors. *Cell Syst.* **8**, 329–337.e324 (2019).
- Aran, D. et al. Reference-based analysis of lung single-cell sequencing reveals a transitional profibrotic macrophage. *Nat. Immunol.* **20**, 163–172 (2019).
- van Dijk, D. et al. Recovering gene interactions from single-cell data using data diffusion. *Cell* **174**, 716–729.e727 (2018).
- Dosch, M. et al. Connexin-43-dependent ATP release mediates macrophage activation during sepsis. *eLife* **8**, <https://doi.org/10.7554/eLife.42670> (2019).
- (2019), R. C. T. R: A language and environment for statistical computing. R Foundation for Statistical Computing, Vienna, Austria. URL <https://www.R-project.org/>.

Acknowledgements

Flow Cytometry & Cell Sorting Core Facility and Live Cell Imaging Core Facility, Department of Biomedical Research, University of Bern. Microscopy was performed with devices supported by the Microscopy Imaging Center (MIC) of the University of Bern. We thank Pamela Nicholson and the Next Generation Sequencing Platform, University of Bern, for their support in planning our scRNA-Seq experiment. They performed RNA quality control assessments, generation of libraries, and sequencing. We thank José A. Galván and the translational research unit of the institute for pathology, they performed the immunohistochemistry on human samples. We thank Riccardo Tombolini for lab management, breeding of mice, and technical support with surgical models. Swiss national science foundation: P1BEP3_181641, J.Z., 310030_179479, A.J.M. European Research Council: ERC advanced grant HHMM-Neonates project no.742195, A.J.M. Natural Sciences and Engineering Research Council: NSERC RGPIN/07191-2019, P.K. Damon Runyon Cancer Research Foundation: Robert Black Fellowship, DRG-2401-20, Y.N.

Author contributions

J.Z., M.G.D.A., A.J.M., D.S., and D.C. designed the research studies. J.Z., J.M., J.B., Y.N., M.D., and I.B. conducted the experiments. J.Z. and J.M. performed all surgical models. A.K., S.L.A.M., and H.D. acquired and analyzed human data. D.S.T. performed RNA-Seq analysis. K.A. and P.K. provided *Wt1^{CreERT2} Rosa26^{tdTomato}* reporter mice and the necessary knowledge and infrastructure for their use. A.J.M. and M.G.D.A. provided germ-free animals as well as the knowledge how to use them. J.Z. wrote the manuscript. All authors provided input. D.S. and D.C. were responsible for the overall execution of the study.

Competing interests

The authors declare no competing interests.

Additional information

Supplementary information The online version contains supplementary material available at <https://doi.org/10.1038/s41467-021-27612-x>.

Correspondence and requests for materials should be addressed to Joel Zindel.

Peer review information *Nature Communications* thanks Thomas Griffith, Manuel López-Cabrera, Yuval Rinkevich, and Seiji Yano for their contribution to the peer review of this work. Peer reviewer reports are available.

Reprints and permission information is available at <http://www.nature.com/reprints>

Publisher's note Springer Nature remains neutral with regard to jurisdictional claims in published maps and institutional affiliations.



Open Access This article is licensed under a Creative Commons Attribution 4.0 International License, which permits use, sharing, adaptation, distribution and reproduction in any medium or format, as long as you give appropriate credit to the original author(s) and the source, provide a link to the Creative Commons license, and indicate if changes were made. The images or other third party material in this article are included in the article's Creative Commons license, unless indicated otherwise in a credit line to the material. If material is not included in the article's Creative Commons license and your intended use is not permitted by statutory regulation or exceeds the permitted use, you will need to obtain permission directly from the copyright holder. To view a copy of this license, visit <http://creativecommons.org/licenses/by/4.0/>.

© The Author(s) 2021

6.2 Manuscript 5: “Combined Targeting of Pathogenetic Mechanisms in Pancreatic Neuroendocrine Tumors Elicits Synergistic Antitumor Effects”

Sebastian Gulde, Alessia Foscarini, Simon L. April-Monn, Edoardo Genio, Alessandro Mrangelo, Swapna Satam, Daniel Helbling, Massimo Falconi, Rodrigo A. Toledo, Jörg Schrader, Aurel Perren, Ilaria Marinoni and Natalia S. Pellegata

Cancers [10.3390/cancers14225481](https://doi.org/10.3390/cancers14225481)

Reprinted from ³⁵⁹ © 2022, The Authors.

Author contribution (CRediT):

I acquired and analyzed human data and was involved in **methodology** (development and design of methodology, creation of models), **software** (programming and implementation of code and testing of existing computer code), **validation** (verification of the overall replication/reproducibility of experiments and results and other research outputs), **formal analysis** (application of statistical, mathematical, computational and other formal techniques to analyze and synthesize study data), **investigation** (conduction of research and investigation processes, performing experiments and data collection), **writing and preparation** of the original draft and **reviewing and editing** the final manuscript, and **visualization**.

Article

Combined Targeting of Pathogenetic Mechanisms in Pancreatic Neuroendocrine Tumors Elicits Synergistic Antitumor Effects

Sebastian Gulde ^{1,2}, Alessia Foscari ^{1,2,3}, Simon L. April-Monn ⁴, Edoardo Genio ^{1,2,3},
Alessandro Marangelo ^{1,2,3}, Swapna Satam ^{1,2}, Daniel Helbling ⁵, Massimo Falconi ⁶, Rodrigo A. Toledo ⁷,
Jörg Schrader ^{8,9}, Aurel Perren ⁴, Ilaria Marinoni ⁴ and Natalia S. Pellegata ^{1,2,3,*}

¹ Institute for Diabetes and Cancer, Helmholtz Zentrum München, Ingolstaedter Landstrasse 1, 85764 Neuherberg, Germany

² Joint Heidelberg-IDC Translational Diabetes Program, Heidelberg University Hospital, 69120 Heidelberg, Germany

³ Department of Biology and Biotechnology “L. Spallanzani”, University of Pavia, 27100 Pavia, Italy

⁴ Institute of Pathology, University of Bern, 3012 Bern, Switzerland

⁵ OnkoZentrum Zurich, 8038 Zurich, Switzerland

⁶ Pancreatic Surgery Unit, Pancreas Translational and Clinical Research Centre, IRCCS San Raffaele Scientific Institute, 20132 Milan, Italy

⁷ CIBERONC, Gastrointestinal and Endocrine Tumors, VHIO, 08035 Barcelona, Spain

⁸ Department of Medicine, University Medical Center Hamburg-Eppendorf, 20251 Hamburg, Germany

⁹ Department of Medicine, Klinikum Nordfriesland, 25813 Husum, Germany

* Correspondence: natalia.pellegata@helmholtz-muenchen.de; Tel.: +49-089-31872633; Fax: +49-089-31873360



Citation: Gulde, S.; Foscari, A.; April-Monn, S.L.; Genio, E.; Marangelo, A.; Satam, S.; Helbling, D.; Falconi, M.; Toledo, R.A.; Schrader, J.; et al. Combined Targeting of Pathogenetic Mechanisms in Pancreatic Neuroendocrine Tumors Elicits Synergistic Antitumor Effects. *Cancers* **2022**, *14*, 5481. <https://doi.org/10.3390/cancers14225481>

Academic Editor: Daruka Mahadevan

Received: 12 October 2022

Accepted: 3 November 2022

Published: 8 November 2022

Publisher's Note: MDPI stays neutral with regard to jurisdictional claims in published maps and institutional affiliations.



Copyright: © 2022 by the authors. Licensee MDPI, Basel, Switzerland. This article is an open access article distributed under the terms and conditions of the Creative Commons Attribution (CC BY) license (<https://creativecommons.org/licenses/by/4.0/>).

Simple Summary: Pancreatic neuroendocrine tumors (PanNETs) are often diagnosed when advanced or metastatic, and at this stage curative surgery is no longer an option. Given that available treatments for advanced disease have shown limited efficacy, novel therapies are urgently needed. In this scenario, we selected two drugs, inhibiting pathways known to be activated in PanNETs, and evaluated their efficacy in various preclinical tumor models. We chose a PI3K inhibitor (buparlisib) and a CDK4/6 inhibitor (ribociclib). We first tested these drugs, alone or in combination, on established cell lines representing distinct PanNET differentiation states. The combination buparlisib plus ribociclib reduced the proliferation of the cell lines more effectively than the single drugs. Inhibition of downstream target genes and/or proteins explained the drugs' anti-proliferative activity. Buparlisib, but not ribociclib, promoted cell death. We then demonstrated that the combination treatment with buparlisib and ribociclib inhibits the viability of primary islets from a genetic animal model of PanNETs (*Men1*-deficient mice), without significantly affecting viability and function of primary islets from wild-type mice. Noteworthy, treatment of primary patient-derived PanNET cultures supported the efficacy of the combination treatment. Our findings indicate that the combined inhibition of PI3K and CDK4/6 pathways is a potentially effective therapeutic option for PanNETs.

Abstract: Pancreatic neuroendocrine neoplasms (PanNENs) are the second most common malignancy of the pancreas. Surgery remains the only curative treatment for localized disease. For patients with inoperable advanced or metastatic disease, few targeted therapies are available, but their efficacy is unpredictable and variable. Exploiting prior knowledge on pathogenetic processes involved in PanNEN tumorigenesis, we tested buparlisib (PI3K inhibitor) and ribociclib (CDK4/6 inhibitor), as single agents or in combination, in different preclinical models. First, we used cell lines representative of well-differentiated (INS-1E, NT-3) and poorly differentiated (BON-1) PanNENs. The combination of buparlisib with ribociclib reduced the proliferation of 2D and 3D spheroid cultures more potently than the individual drugs. Buparlisib, but not ribociclib, induced apoptosis. The anti-proliferative activity of the drugs correlated with downstream target inhibition at mRNA and protein levels. We then tested the drugs on primary islet microtissues from a genetic PanNET animal model (*Men1*-defective mice) and from wild-type mice: the drug combination was effective against the former without altering islet cell physiology. Finally, we treated PanNET patient-derived islet-like 3D tumoroids: the combination of buparlisib with ribociclib was effective in three out of four samples.

Combined targeting of PI3K and CDK4/6 is a promising strategy for PanNENs spanning various molecular and histo-pathological features.

Keywords: pancreatic NETs; buparlisib; ribociclib; combination therapy; primary human tumoroids

1. Introduction

Pancreatic neuroendocrine neoplasms (PanNENs) account for <3% of all pancreatic tumors, but their incidence has been increasing in recent decades [1], in part due to more accurate diagnosis. PanNENs are classified as functioning or non-functioning depending on whether they cause symptoms of hormonal hypersecretion, with the latter group accounting for 60–90% of cases [2]. Among functioning PanNET, insulinoma are most frequent. PanNENs are characterized by a heterogeneous and unpredictable clinical behavior, which depends on their stage of progression, pathological grade and hormone secretion. PanNETs are usually indolent tumors, but they all have malignant potential. To better stratify patients for prognostic purposes, the World Health Organization (WHO) introduced a new classification of PanNENs in 2017, which divides these neoplasms into grade 1 (G1) to G3 pancreatic neuroendocrine tumors (PanNETs), and G3 neuroendocrine carcinomas (PanNECs). The classification in the various grades is based on proliferation rate (i.e., mitotic count and Ki67 index), histomorphology and molecular biomarkers [2]. The grading of the tumors has a significant impact on the overall survival of the patients, which ranges from >10 years for G1 PanNETs, to approximately 6 years for G2 tumors, to less than 10 months for aggressive PanNECs [3,4].

Surgical resection is the first-line and the only potentially curative treatment for patients with localized disease. Medical treatment for patients with unresectable or metastatic PanNETs includes somatostatin analogues (SSAs) as first-line therapy, and either everolimus (mTOR inhibitor), sunitinib (multikinase inhibitor), temozolomide, streptozocin, or peptide receptor radionuclide therapy (PRRT) with radiolabeled SSAs as second-line treatments [5]. However, none of these treatment options are curative, and only a fraction of patients treated profit. Therefore, the identification of more effective, targeted therapies for aggressive PanNENs is highly clinically relevant.

Although mostly sporadic, PanNET can develop as a component of hereditary multi-tumor syndromes, including multiple endocrine neoplasia type 1 (MEN1), von Hippel-Lindau (VHL) disease, and, more rarely, neurofibromatosis type 1 (NF-1), and tuberous sclerosis (TSC) [6]. MEN1 syndrome is caused by inactivating germline mutations of the MEN1 tumor suppressor gene [7]. MEN1 is also mutated in 40% of sporadic, well-differentiated PanNETs [6]. The importance of the *Men1* gene as the driver of PanNET tumorigenesis has been demonstrated by studies of mice with defective *Men1* function (heterozygous knockout *Men1*^{+/-} mice), where PanNET development was observed at high incidence during their life-span, thereby recapitulating the situation seen in MEN1 patients [8]. Recent NGS studies have shed light into the somatic mutations playing a role in PanNET development and progression [9,10]. Inactivation of *ATRX/DAXX* and hyperactivation of the PI3K/AKT/mTOR pathway are recurring features in PanNET tumorigenesis. The latter is driven by mutations in mTOR-related genes (e.g., *PI3CA*, *TSC2*, *PTEN*, *DEPDC5*), by the loss of chromosomal regions containing *TSC2* (16p) and *PTEN* (10q23), by overexpression of various tyrosine kinase receptors, and by the activation of Akt [11,12]. PI3K/AKT/mTOR pathway activation correlates with worse patient outcome [10].

Inactivation of the retinoblastoma pathway was originally implicated in PanNET tumorigenesis based on studies of double knockout mice having inactivation of Rb1 and Tp53: Tp53^{+/-}; Rb^{+/-} and Tp53^{-/-}; Rb^{+/-} mice developed non-invasive islet carcinoma, together with other neuroendocrine and non-neuroendocrine tumors [13]. The cyclin-dependent kinases CDK4 and CDK6 phosphorylate Rb1 and inhibit its function. Gene amplification and overexpression of CDK4 and CDK6 was demonstrated in the majority

of PanNET patients [14]. Interestingly, the deletion of *Cdk4* in *Men1*^{+/-} mice (*Men1*^{+/-}; *Cdk4*^{-/-} mice) abrogated PanNET formation, thereby suggesting that CDK4 is a critical downstream target of Men1-dependent tumorigenesis [15]. Repression by promoter methylation of p16INK4a, a cyclin-dependent kinase (CDK) inhibitor that enforces RB1 tumor-suppressive activity by inhibiting its phosphorylation by CDK4 and CDK6, is common in PanNETs [12]. These data support a role for CDKs and cell cycle regulation in PanNETs.

Given the relevance of an overactivation of the PI3K pathway in several cancers, agents that can block this signaling cascade at various levels have been generated and several are already in clinics. Buparlisib, a PI3K inhibitor, has been evaluated for its anti-tumor efficacy in human and rodent PanNET cell lines in vitro, and was found to inhibit cell proliferation and induce apoptosis as a single agent [16–18]. Buparlisib in combination with streptozotocin also showed antitumor effects in vivo in a xenograft model of liver dissemination obtained upon intrasplenic INS-1E cells injection [16].

Among the available CDK4/6 inhibitors, palbociclib as a monotherapy was evaluated in a small number of unselected and heavily pretreated patients with G1/2 PanNETs [19]. This trial failed to show the therapeutic effects of this drug. However, it brought to light the need for a molecular-based patient stratification: given the heterogeneity of PanNETs, a stratification based on the genetic mutations (e.g., in *MEN1*) is needed to select the patients that might benefit from this treatment. Therefore, further evaluation of CDK4/6 inhibitors against PanNETs in the clinics is warranted [20].

The aim of our study was to identify a novel and effective treatment strategy for PanNETs by exploiting the knowledge of relevant pathogenetic mechanisms involved in these tumors. By using different preclinical in vitro models, including patient-derived primary 3D tumoroids, we report that the combination treatment of a small-molecule, orally available, pan-class I PI3K inhibitor (buparlisib) with a CDK4/6 inhibitor (ribociclib) suppresses PanNET cell growth and holds promise for future clinical implementation.

2. Materials and Methods

2.1. Cell Lines

INS-1E cells were obtained from Pierre Maechler and maintained in RPMI 1640 Medium GlutaMAX™ (61870044, Life Technologies—Carlsbad, CA, USA) supplemented with 5% FBS (10500064, Life Technologies), 1% Penicillin/Streptomycin (15070063, Life Technologies), 1 mM Pyruvate (11360-039, Life Technologies), 10 mM HEPES (15630-056, Life Technologies), and 50 μM 2-Mercaptoethanol (31350-010, Life Technologies). NT-3 cells were cultivated in RPMI 1640 Medium GlutaMAX™ with 10% FBS, 1% Penicillin/Streptomycin, 20 ng/mL EGF (AF-100-15, Peprotech – Cranbury, NJ, USA), 10 ng/mL FGF (100-18B, Peprotech) on plates coated with 50 μg/mL H₂O Collagen from human placenta (C7521, Sigma-Aldrich—St. Louis, MI, USA), as previously reported [21]. NT-3 cells carry a homozygous missense mutation of *MEN1* (chromosome 11, position 64572018; c.1621A>G; p.T541A) [21]. The BON1 cells were provided by E.J. Speel, Maastricht, Netherlands and cultured in DMEM/Ham's F12 (11320033, Life Technologies) with 10% FBS and 1% Penicillin/Streptomycin.

2.2. Primary Human Cultures

All subjects involved in the study gave consent and primary cell cultures have been approved by the cantonal ethic commission Bern, projects ID 105-2015 and ID 2019-01154. Patient samples were isolated and cultured following the described protocol [22]. Cryopreserved tumor tissues of four PanNET patients were used for in vitro drug screening. In short, washed pieces of 1 mm³ were dissociated in digestion medium (10 mg/mL collagenase IV (Worthington, Columbus, OH, USA), 0.25% Trypsin-EDTA (Sigma-Aldrich), 0.2 mg/mL DNase (Roche—Basel, Switzerland) in advanced DMEM-F12, HEPES 10 mM, 1% L-glutamine, 1% penicillin-streptomycin-amphotericin B) in a gentle MACS™ dissociator (Miltenyi Biotec, Solothurn, Switzerland). Debris of collagen were removed using a

70- μm strainer, followed by a red blood cell lysis with ACK lysis buffer (Thermo Fisher Scientific, Waltham, MS, USA). Fibroblasts were partially removed, exploiting their differential adhesion capacity to plastic surfaces. Cells were then dissociated into single cells and resuspended and maintained in Advanced DMEM-F12 + GF medium (DMEM-F12, 5% FBS, Hepes 10 mM, 1% L-glutamine (200 mM), 1% penicillin (100 IU/mL), 1% streptomycin (0.1 mg/mL), 1% amphotericin B (0.25 mg/mL) (Merck, Darmstadt, Germany), 20 ng/mL EGF, 10 ng/mL bFGF (Thermo Fisher Scientific), 100 ng/mL PIGF, and 769 ng/mL IGF-1 (Selleckchem, Boston, MS, USA)), and in 24-well Corning® Costar® ultra-low attachment (ULA) plates (Corning—New York, USA) (500 μL /well, $3\text{--}5 \times 10^5$ cells/well) in a humidified cell incubator (21% O₂, 5% CO₂, 37 °C). After 2 days of recovery phase, cells were counted and resuspended in fresh AdvDMEM + GF medium supplemented with growth-factor-reduced Matrigel and plated in 96-well ULA plates ($3\text{--}4 \times 10^3$ cells/well). For drug screening, isolated cells were resuspended in fresh Advanced DMEM-F12 + GF medium supplemented with 123 μg /mL growth-factor-reduced Matrigel® (Corning) and plated in 96-well ULA plates (50 μL /well, $3\text{--}4 \times 10^3$ cells/well). RealTime-Glo™ MT Cell Viability (RTG) assay (Promega, Madison, WI, USA) was used to continually monitor cell viability of 3-D human primary PanNET cultures. The RTG assay was performed according to the manufacturer's instructions, and luminescence was measured in an Infinite® 200 PRO plate reader (Tecan, Männedorf, Switzerland).

2.3. Animal Husbandry and Primary Islet-Cell Isolation

Heterozygous knockout mice of the *Men1*^{tm12qw} strain [23] (synonym *Men1*^{T/+}) were bred and maintained in agreement with general husbandry rules approved by the Helmholtz Zentrum München and as approved by the government of Upper Bavaria, Germany (Az 55.2-1-54-2532-117-2016). Mice were killed by cervical dislocation. Islets were isolated by injection of 3 mL CollagenaseP (#11213857001, Roche) solution into the bile duct. Pancreas tissue was digested at 37 °C for 15 min. The reaction was stopped by adding 10 mL ice-cold Hanks' buffer containing 0.2% bovine serum albumin (#11926.04, Serva-Heidelberg, Germany), followed by filtration using a 500 μm strainer. Islets were hand-picked and single cells were obtained by trypsin incubation. A total of 5000 single cells were then seeded into each well of a hanging drop system (#IPS-06-010, Gravity Plates from Insphero-Schlieren, Switzerland) to obtain 3D microtissues (spheroids) of equal size.

2.4. Immunofluorescence of Islets Microtissues (Pseudoislets)

Pseudoislets were transferred to 1.5 mL tubes, centrifuged at $500 \times g$ for 5 min, and the supernatant was then removed. Islets were fixed for 1 h at RT using 4% Formaldehyde (P087.1, Carl Roth—Karlsruhe, Germany). After washing with PBS, 40 μL of 60 °C HistoGel™ (HG-4000-012, Thermo Fisher) were added to the tubes. The HistoGel-pseudoislet mixture was immediately transferred onto parafilm, allowing it to form a droplet. After it solidified at 4 °C, the droplet was placed in a tissue processing cassette. Dehydration with a standard dehydration program was performed on a tissue processor and the droplet was embedded in paraffin. Immunofluorescence was performed on formalin-fixed paraffin-embedded (FFPE) 4- μm sections as previously described [24]. In brief, sections were deparaffinized, boiled in citric acid, permeabilized and blocked. Then, the sections were incubated with primary antibodies (Supplementary Table S2) overnight at 4 °C and secondary antibodies (Supplementary Table S2) for 1 h at RT. Finally, nuclei were counterstained with DAPI (dilution 1:2000) and the sections were mounted. Images were taken using a confocal microscope (Olympus FluoView 1200; Olympus Corporation).

2.5. Drug Treatments and In Vitro Assays

Buparlisib (HY-70063, MedChemExpress—Monmouth Junction, NJ, USA) and ribociclib (HY-15777, MedChemExpress) were dissolved in DMSO and used at the concentrations indicated in the figures. The 2D proliferation was measured after 72 h of treatment with

drugs or DMSO controls using the CyQUANT[®] NF kit (#C35006, Thermo Fisher Scientific) and following the manufacturer's instructions.

Apoptosis was measured by assessing the Caspase 9 activity in treated cells after 72 h using the Caspase-Glo[®] 9 Assay System (#G8211, Promega) following the manufacturer's instructions and using reagents including MG-132 inhibitor.

Three-dimensional spheroids were generated by seeding 1000 INS-1E and BON-1, or 2000 NT-3, cells into each well of a 96-well ULA plate (Corning). For primary cells, 5000 islet cells were seeded into each well of a hanging drop system (#IPS-06-010, Insphero). Three-dimensional cell viability was measured at time 0 (pre-treatment) and at 24 h, 48 h and 72 h post-treatment using the RealTime-Glo[™] MT Cell Viability Assay (#G9712, Promega) and following the manufacturer's instructions. Three-dimensional spheroid size was measured by taking images of the spheroids on the indicated days and analyzing the spheroid size using ImageJ. The combination index CI after the Chou–Talalay method was calculated by using the CompuSyn software [25].

2.6. Glucose-Stimulated Insulin Secretion (GSIS)

To assess the capacity of primary mouse islet cells to secrete insulin, a glucose-stimulated insulin secretion (GSIS) assay was performed. The assay was performed in 96-well plates with one 3D microtissue per well. In brief, spheroids were washed three times with medium and then starved for 1 h in 1 mM Glucose. After washing, spheroids were incubated for 60 min with 2.8 mM Glucose (Baseline). Baseline supernatant was collected, spheroids washed and incubated for 60 min with 16.5 mM Glucose (Insulin), and Insulin supernatant was collected. To analyze the amount of secreted insulin, the Baseline and Insulin supernatants were measured using an Ultra Sensitive Insulin ELISA Kit (#90080, CrystalChem-Elk Grove Village, IL, USA) following the manufacturer's instructions.

2.7. RNA Isolation and qPCR

RNA was isolated using the RNeasy Mini Kit (#74104, Qiagen—Hilden, Germany) and RNA concentration was determined by a Spectrophotometer NanoDrop ND-1000 (Thermo Fisher Scientific). cDNA was generated using the High-Capacity RNA-to-cDNA[™] Kit (#4387406, Thermo Fisher Scientific). Gene expression was measured using Taqman assays (Thermo Fischer Scientific) according to Supplementary Table S1 and Fast Advanced Master Mix (#4444557, Thermo Fisher Scientific).

2.8. Protein Extraction and Western Blotting

Cells were collected and lysed using RIPA buffer (#R0278, Sigma-Aldrich) supplemented with protease (#04693124001, Roche) and phosphatase inhibitors (#04906845001, Roche Diagnostics). Pierce BCA Protein Assay Kit (#23225, Thermo Fisher Scientific) was used to measure protein concentrations. Primary antibodies (Supplementary Table S2) were applied at 4 °C overnight and secondary antibodies (Supplementary Table S2) at room temperature for 1 h. Proteins were visualized using the SuperSignal West Pico Chemiluminescent Substrate Kit (#34080, Thermo Fisher Scientific).

2.9. Embedding of Human Tumoroids

For micro-cell-block (MCB) preparation, patient-derived tumoroids corresponding to $3\text{--}5 \times 10^4$ cells were collected on the day of isolation (D0) and from the 96-well ULA plate at the end of drug screening (D12). Cells were captured in plasma-thrombin clots and fixed, counterstained with Hematoxylin, and embedded in paraffin for sectioning and staining. Embedded material was cut into 2.5- μm -thick serial sections followed by deparaffinization, rehydration and antigen retrieval with the help of an automated immunostainer (Bond RX, Leica Biosystems, Germany). Antigen retrieval was performed in Tris for 30 min at 100 °C for synaptophysin (1:100, 27G12, Novocastra, Leica Biosystem—Deer Park, USA). Primary antibody incubation was 30 min at the specified dilutions. For visualization, a Bond Polymer Refine Detection kit, using DAB (3,3'-Diaminobenzidine), was used as the

chromogen. Slides were counterstained with hematoxylin. Scans were acquired with an automated slide scanner Panoramic 250 (3DHitech, Hungary) at 20× magnification. Images were acquired using QuPath software.

3. Results

3.1. Effect of Buparlisib and Ribociclib on Proliferation and Apoptosis of 2D Cultures of PanNET Cells

With the aim of identifying a novel therapeutic approach for PanNENs, we investigated the effect that the inhibition of two key processes involved in pancreatic tumorigenesis (i.e., the PI3K pathway and cell cycle) would have on the oncogenic features of the tumor cells. Specifically, we tested the PI3K inhibitor buparlisib (BKM120) and the CDK4/6 inhibitor ribociclib (LEE011) alone or in combination in vitro against experimental models representative of well-differentiated and poorly differentiated PanNENs. Specifically, we used the INS-1E cell line (from a rat insulinoma), and the recently established human NT-3 cell line (from a human G2 PanNET) as models of well-differentiated tumors. Indeed, they express markers of NET cells, secrete insulin upon glucose stimulation, and show intermediate (INS-1E) or low (NT-3) proliferation rates [16,21,26]. In our studies, we also included human BON-1 cells, characterized by high proliferation rates, genetic alterations compatible with an aggressive behavior, and partial loss of typical markers of neuroendocrine differentiation [27,28]. Cells were treated with the two drugs alone or in combination, or with DMSO (vehicle control) for 72 h, and then cell proliferation was assessed.

INS-1E cells responded well to the treatments, and the individual drugs were able to reduce cell proliferation in a dose-dependent manner (Figure 1A). The combination of buparlisib + ribociclib showed the strongest effect, as demonstrated by the lower IC₅₀. The single treatment with ribociclib had the weakest effect, and higher doses of this drug were needed to decrease proliferation. The drug combination allowed the reduction of the drug concentration of buparlisib by >70% and of ribociclib by 23% to reach effects that were equally good, or even superior, to the single drugs (Figure 1A). NT-3 cells were in general less sensitive to buparlisib and ribociclib when compared with INS-1E cells (Figure 1B), and the maximum reduction in cell proliferation in all treatment groups was −30%. Comparing the single treatments, buparlisib and ribociclib had a similar effect in NT-3 cells, resulting in comparable IC₅₀ values (Figure 1B). Similar to INS-1E cells, the drug combination showed a better effect than the single drug regimens, with an IC₅₀ value that was reduced for buparlisib, not for ribociclib.

Both drugs were more effective in BON-1 cells versus the other cell lines, as attested by the lowest IC₅₀ values for each agent (Figure 1C). Remarkably, the drug combination led to a strong reduction in proliferation, supporting a synergistic effect of buparlisib and ribociclib in these cells.

To verify whether the tested drugs not only reduce proliferation but also induce apoptosis of PanNET cells, we measured Caspase9 activity in the three cell lines 72 h after treatment. In INS-1E cells, both buparlisib alone and the drug combination induced apoptosis in a dose-dependent manner, whereas ribociclib alone did not (Figure 2A,B). Direct comparison showed no difference in apoptotic rates between buparlisib as a single agent and the drug combination, indicating that buparlisib is responsible for inducing apoptosis, consistent with its mechanism of action. In NT-3 cells, low concentrations of both buparlisib alone and the drug combination had no pro-apoptotic effects, whereas a clear synergistic effect of both drugs was observed for mid-range concentrations (Figure 2C,D). Ribociclib did not induce apoptosis at any concentration. In contrast, ribociclib at high doses promoted apoptosis in BON-1 cells, while buparlisib alone and the drug combination induced it in a dose-dependent manner (Figure 2E,F).

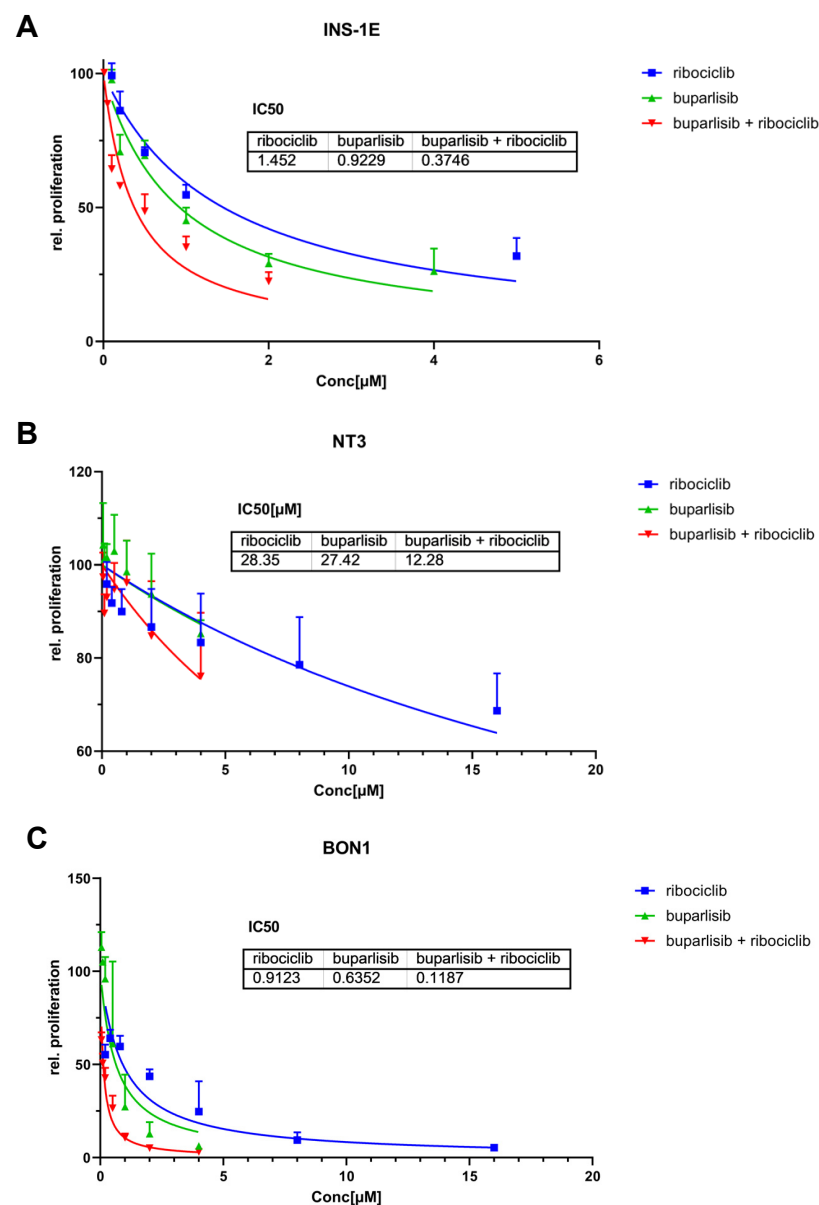


Figure 1. Effect of buparlisib and ribociclib on cell proliferation of INS-1E, NT-3 and BON-1 PanNET cells in 2D culture. INS-1E (A), NT-3 (B) and BON-1 (C) cells were treated with buparlisib, ribociclib, a combination of both drugs or DMSO vehicle control. Cell proliferation was measured after 72 h of treatment. The DMSO control was set to 100% and nonlinear regression was used to determine the IC₅₀. Data shows the mean \pm SD from three independent experiments with three technical replicates each.

3.2. Effect of Buparlisib and Ribociclib on Downstream Pathway Inhibition in 2D Cultures of PanNET Cells

We have shown that, in a 2D system, our treatment approach was able to reduce the proliferation and induce apoptosis of both PanNET cell lines. To verify that the observed phenotypes were indeed explained by pathway inhibition and not by unspecific effects, we set out to assess different downstream effectors of the PI3K/AKT or the CDK4/6 pathway. For the former, we analyzed the effect of the drug treatments on the phosphorylation of AKT, a well-known downstream target of the PI3K pathway. Treatment with buparlisib alone and with the drug combination significantly reduced the P-AKT/AKT signal ratio in INS-1E, NT-3 and BON-1 cells (Figure 3A–C). Treatment with DMSO (vehicle control) and ribociclib had no effect on AKT phosphorylation, as expected (Figure 3A–C). This

confirmed the downregulation of the PI3K/AKT pathway in PanNEN cells after treatment with the PI3K inhibitor buparlisib. We also performed Western blotting for P-Rb, the target of CDK4/6, which however only gave reliable results for the two human cell lines (NT-3, BON-1). Here, we could see that ribociclib alone or in combination with buparlisib, but not buparlisib alone, decreased the phosphorylation of Rb, as previously reported in other human tumor cell types [29] (Figure 3D,E).

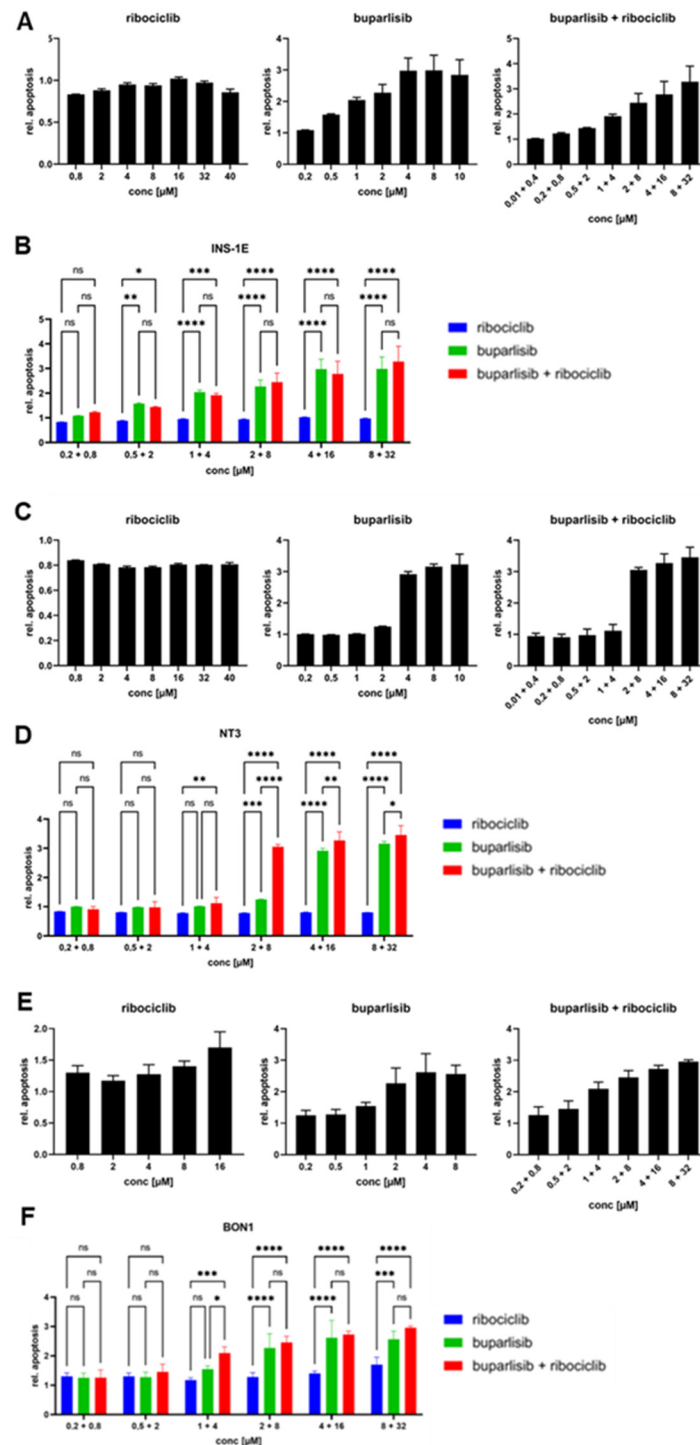


Figure 2. Apoptosis induction upon treatment of INS-1E, NT-3 and BON-1 cells as 2D cultures. INS-1E (A,B), NT-3 (C,D) and BON-1 (E,F) cells were treated with buparlisib, ribociclib, a combination of both drugs or DMSO vehicle control, and caspase 9 activity was measured after 72 h. (A,C,E) A

range of concentrations was used to evaluate the effect of the drug treatments. (B,D,F) Comparison of the different treatment regimens. Data was normalized to the DMSO control; the mean \pm SD from three independent experiments with three technical replicates each is shown. Two-way ANOVA. ns, not significant; *, $p < 0.05$; **, $p < 0.01$; ***, $p < 0.001$; ****, $p < 0.0001$.

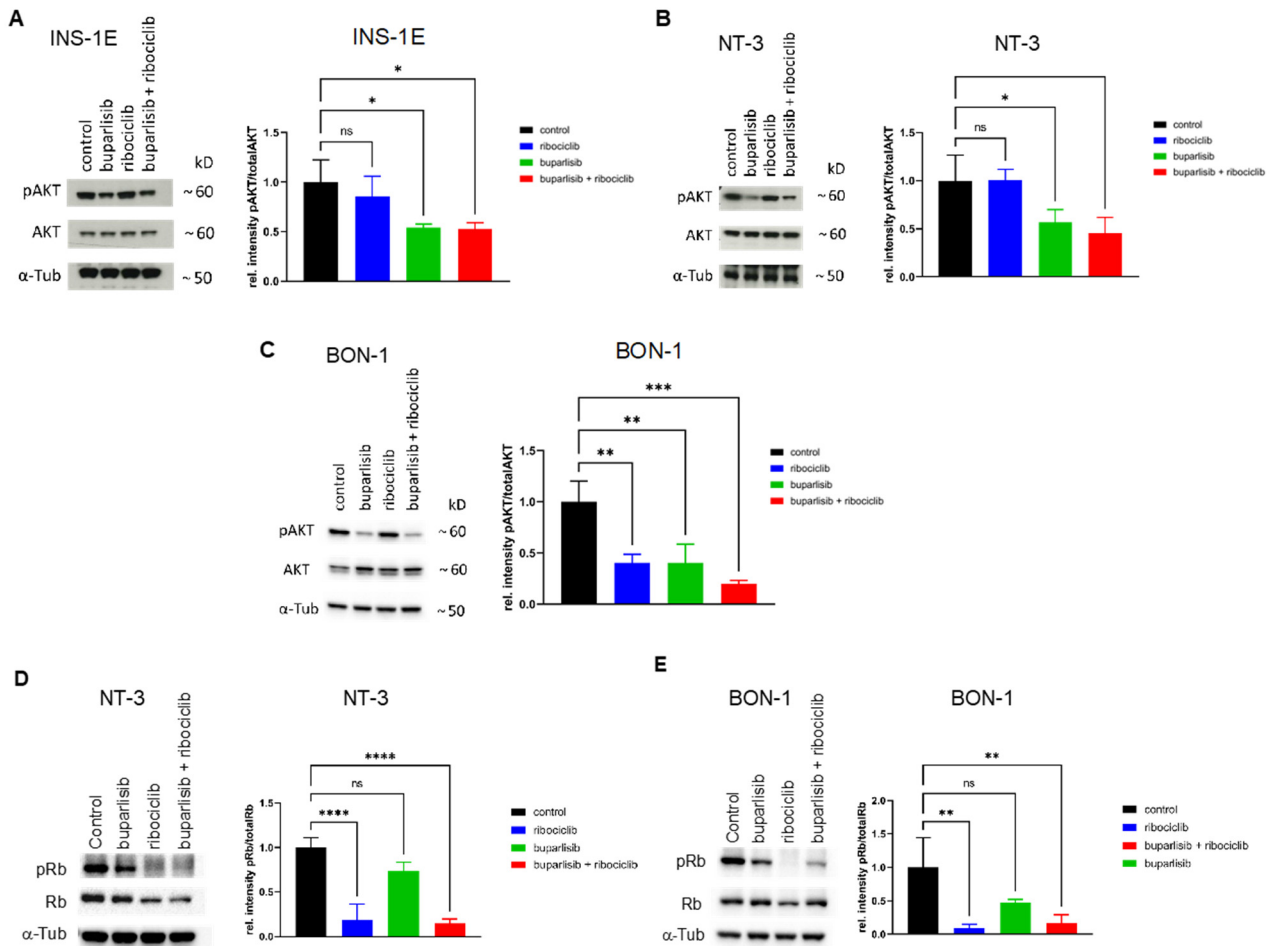


Figure 3. Inhibition of targets of the PI3K pathway and of CDK4/6 confirmed by WB. (A–C) Expression of phospho-Akt (P-AKT) and total Akt in INS-1E (A), NT-3 (B) and BON-1 (C) cells treated with buparlisib, ribociclib or their combination. α -Tubulin was used as loading control. Shown is one representative immunoblot (out of three). Additionally, the ratio of the band intensities for P-AKT/AKT is given for each cell line. The mean \pm SD from three independent experiments is shown. (D,E) Expression of phospho-Rb (P-Rb) and total Rb in NT-3 (D) and BON-1 (E) cells treated with buparlisib, ribociclib or their combination. α -Tubulin was used as loading control. One representative immunoblot (out of three) is shown. Additionally, the ratio of the band intensities for P-Rb/Rb is given for each cell line. The mean \pm SD from three independent experiments is shown; ns, not significant; *, $p < 0.05$; **, $p < 0.01$; ***, $p < 0.001$; ****, $p < 0.0001$.

To confirm CDK4/6 inhibition, we analyzed the expression of two genes that are involved in the CDK-P-RB-E2F signaling cascade, namely *Ccna1* (cyclin A1) and *Pcna* (PCNA). The results showed a strong reduction in the expression of these target genes in all lines when treated with ribociclib alone or with the drug combination (Figure 4A–C). In contrast, buparlisib alone only slightly reduced *PCNA* expression in BON-1 cells, while it did not reduce gene expression in the other two cell lines (Figure 4A–C). This data confirmed that the treatment with ribociclib downregulates CDK4/6 signaling in PanNET cells.

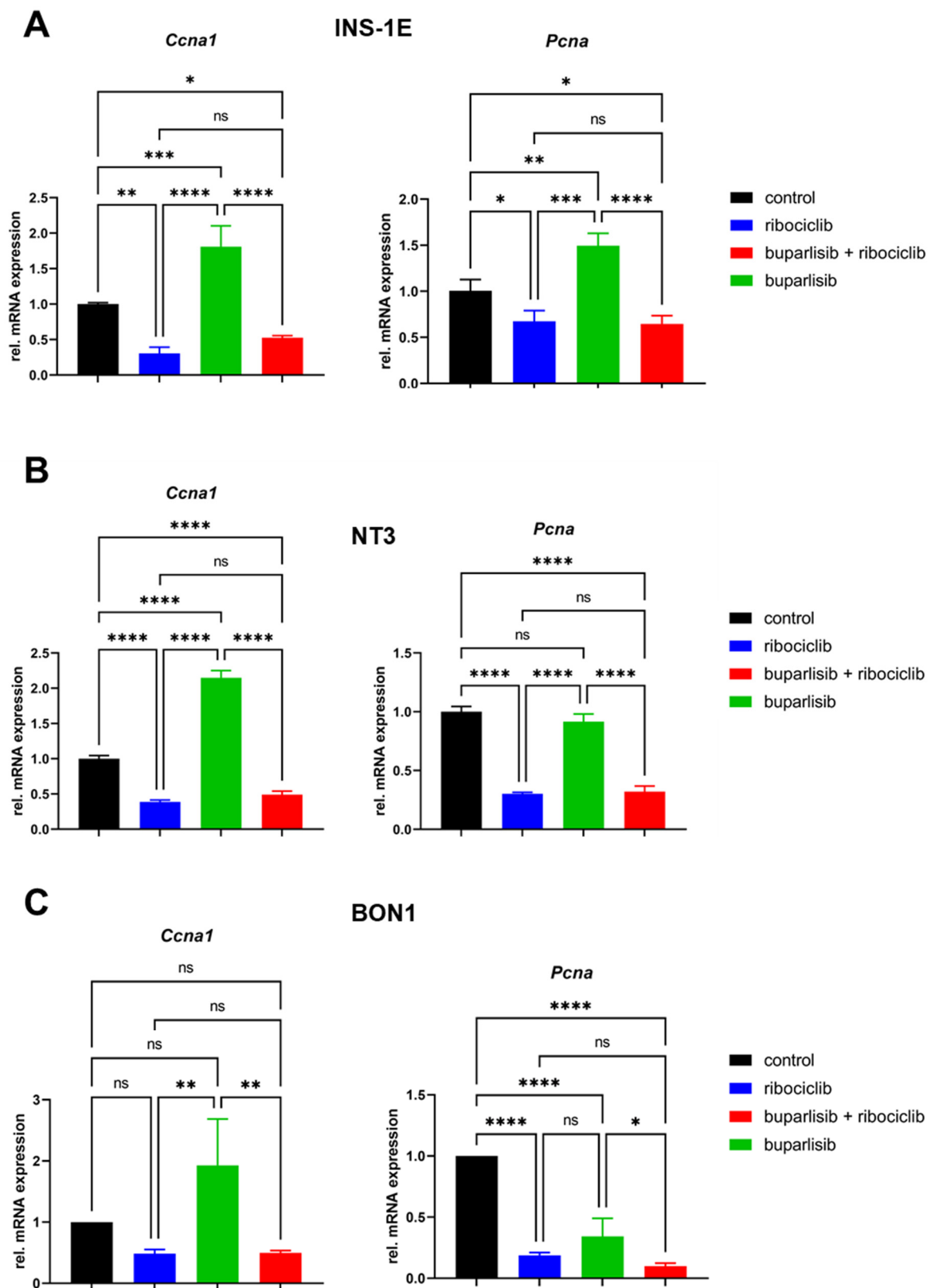


Figure 4. Inhibition of targets of CDK4/6 confirmed by qRT-PCR. Expression of *Ccna1* (cyclin A) and *Pcna* in INS-1E (A), NT-3 (B) and BON-1 (C) cells 72 h after treatment with the indicated drugs. qRT-PCR was carried out using specific TaqMan probes and data were normalized against vehicle control. The mean \pm SD of three independent biological replicates is shown. ns, not significant; *, $p < 0.05$; **, $p < 0.01$; ***, $p < 0.001$; ****, $p < 0.0001$ (by 1way ANOVA).

PanNET cells by following the changes in spheroid size during treatment. Moreover, to assess the long-term effects of the drugs, we longitudinally followed spheroid growth for 14 days after treatment. Spheroid size was measured at day 0 (start of the treatment), and then at days 3, 7, 11 and 14 post-treatment.

INS-1E spheroids showed a progressive darkening of the center of the sphere following the combination treatment (Supplementary Figure S1). At the 72 h timepoint, both buparlisib and the drug combination suppressed growth, while ribociclib did not (Figure 6A,B). An effect on the size and on the opacity of the INS-1E spheroids (versus control) could be appreciated already 72 h after treatment with the drug combination (Figure 6A,B and Supplementary Figure S1). After 14 days, the anti-proliferative effect of both buparlisib and the drug combination was more noticeable: these two regimens completely stopped the growth of INS-1E spheroids (Figure 6A,B). At the 14 days time point, ribociclib had significantly inhibited spheroid growth versus vehicle control (Figure 6B).

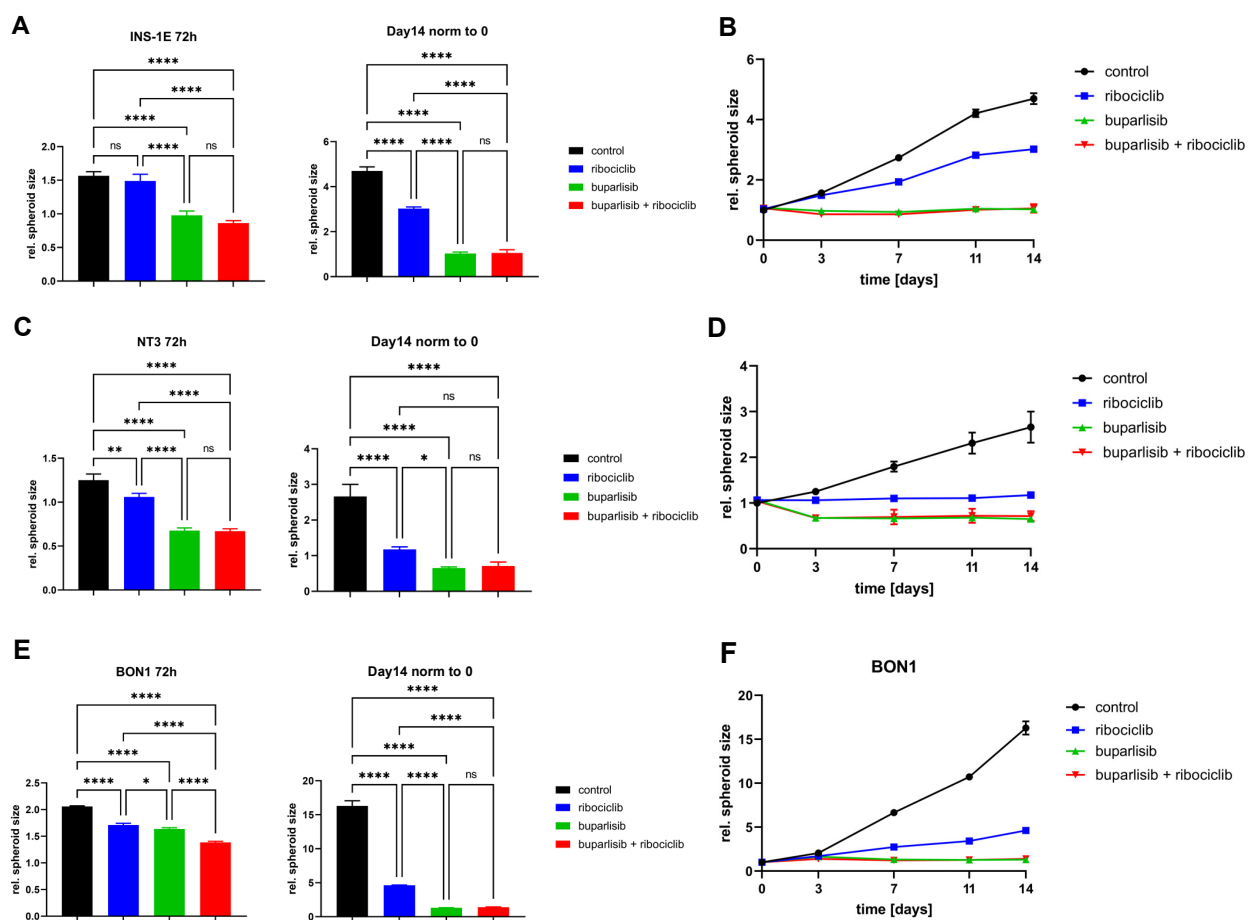


Figure 6. Effect of buparlisib and ribociclib on growth of INS-1E, NT-3 and BON-1 PanNET cells in 3D culture. (A,C,E) Changes in spheroid size at 72 h (3d) and 14d after treatment with buparlisib, ribociclib or their combination in INS-1E (A), NT-3 (C) and BON-1 (E) cells. (B,D,F) Effect of the treatments on the relative spheroid size (versus day 0) over the course of 14 days in INS-1E (B), NT-3 (D) and BON-1 (F) cells. Data shows the mean \pm SD from three independent experiments with eight technical replicates each. ns, not significant; *, $p < 0.05$; **, $p < 0.01$; ***, $p < 0.0001$ (by 1way ANOVA).

Similar to INS-1E cells NT-3 cell spheroids also showed a clear reduction in size and a progressive darkening of the center during treatment (Figure 6C,D and Supplementary Figure S1). After 72 h, buparlisib, ribociclib and their combination suppressed NT-3 spheroid growth, with buparlisib and the combination showing the strongest inhibition (Figure 6C,D). While ribociclib stopped cell growth versus day 0, buparlisib and the combination treatment even led to a slight reduction of spheroid size (Figure 6C). Ribociclib

as a single agent was more effective against NT-3 cell spheroids than INS-1E spheroids already after 72 h and its anti-tumor effect was even more pronounced after 14 days (Figure 6C,D). At this time point, no increase in size was measured upon buparlisib and combination treatment (Figure 6C,D).

Similarly, a strong effect of buparlisib and the drug combination was observed in BON-1 cells, and was especially prominent at the 14-day time point (Figure 6E,F). Ribociclib as a single agent was able to suppress the growth of BON-1 spheroids, especially considering the high proliferation rate of these cells when vehicle-treated (Figure 6E). Thus, in the long term, buparlisib and the combination buparlisib + ribociclib completely suppressed spheroid growth in all PanNET cell lines, whereas ribociclib alone reduced cell growth, with NT-3 and BON-1 being especially affected.

3.4. Effect of Buparlisib and Ribociclib on Viability, Growth and Function of Islet Microtissues Derived from Mice with *Men1* Gene Deletion

Buparlisib and ribociclib were found to significantly suppress the proliferation/viability of both 2D and 3D cultures of established PanNET cell lines. We then wondered whether these drugs could also be effective against primary PanNET cells. Mice heterozygous for the deletion of exon 3 of the *Men1* gene (*Men1*^{T/+}), develop insulinomas (β cell tumors) from the age of 12 months, which closely resemble their cognate human tumors [23]. Thus, we employed these mice to test the efficacy of our drugs. We isolated islets from *Men1*^{T/+} mice ($n = 9$) at the age of 18 months. To verify whether the drugs also have an effect on healthy islets, we also isolated and treated islets from control *Men1*^{+/+} ($n = 5$) mice. To overcome the issue that freshly isolated islets differ in size and could affect therapy response, islets were digested and then reconstituted as 3D microtissues (pseudo-islets) containing the same number of cells (Supplementary Figure S2). Pseudo-islets of both groups were treated with 5 μ M buparlisib, 20 μ M ribociclib or their combination (buparlisib 5 μ M + ribociclib 20 μ M). Interestingly, neither the single drugs nor their combination significantly affected the viability of healthy islet cells of *Men1*^{+/+} littermates (Figure 7A). In contrast, treatment with buparlisib or ribociclib was effective at reducing the viability of PanNET cells from *Men1*^{T/+} mice (Figure 7A), with the former drug working significantly better than the latter. The drug combination was the most effective treatment (Figure 7A). The difference in sample size between the two mouse groups might affect the statistics.

Glucose-stimulated insulin secretion is one of the most important physiological features of the pancreatic islets, which is carried out by the pancreatic β cells, the cells of origin of the tumors developing in *Men1*^{T/+} mice. In view of a possible translation of these drugs in clinical practice, it is important to know whether they perturb insulin secretion. Thus, we generated pseudo-islets from islets isolated from *Men1*^{T/+} and *Men1*^{+/+} mice, and treated them with buparlisib and ribociclib, alone or in combination, as done for the cell viability assays. After 72 h of treatment, spheroids were starved before measuring baseline insulin secretion (incubation with 2.8 mM glucose), or secretion upon stimulation with high glucose (incubation with 16.5 mM glucose). As expected, the low baseline insulin secretion of pseudo-islets from *Men1*^{+/+} significantly increased upon glucose stimulation (Figure 7B). The treatment with both drugs, alone or in combination, did not affect insulin secretion in control *Men1*^{+/+}-derived pseudo-islets (Figure 7B). *Men1*^{T/+} pseudo-islets showed a higher baseline insulin secretion compared to the pseudo-islets of *Men1*^{+/+} mice (Figure 7B). With the exception of an increase in basal insulin levels in pseudo-islets from *Men1*^{T/+} mice, we could not see an effect of the glucose stimulation in any other condition (Figure 7B). These results suggest that insulin secretion is perturbed in pseudo-islets of tumor-bearing heterozygous *Men1*^{T/+} mice. As the drugs showed no effect on the ability of pseudo-islets of *Men1*^{+/+} mice to secrete insulin upon glucose stimulation, it can be concluded that these treatments do not interfere with this physiological function of pancreatic islets.

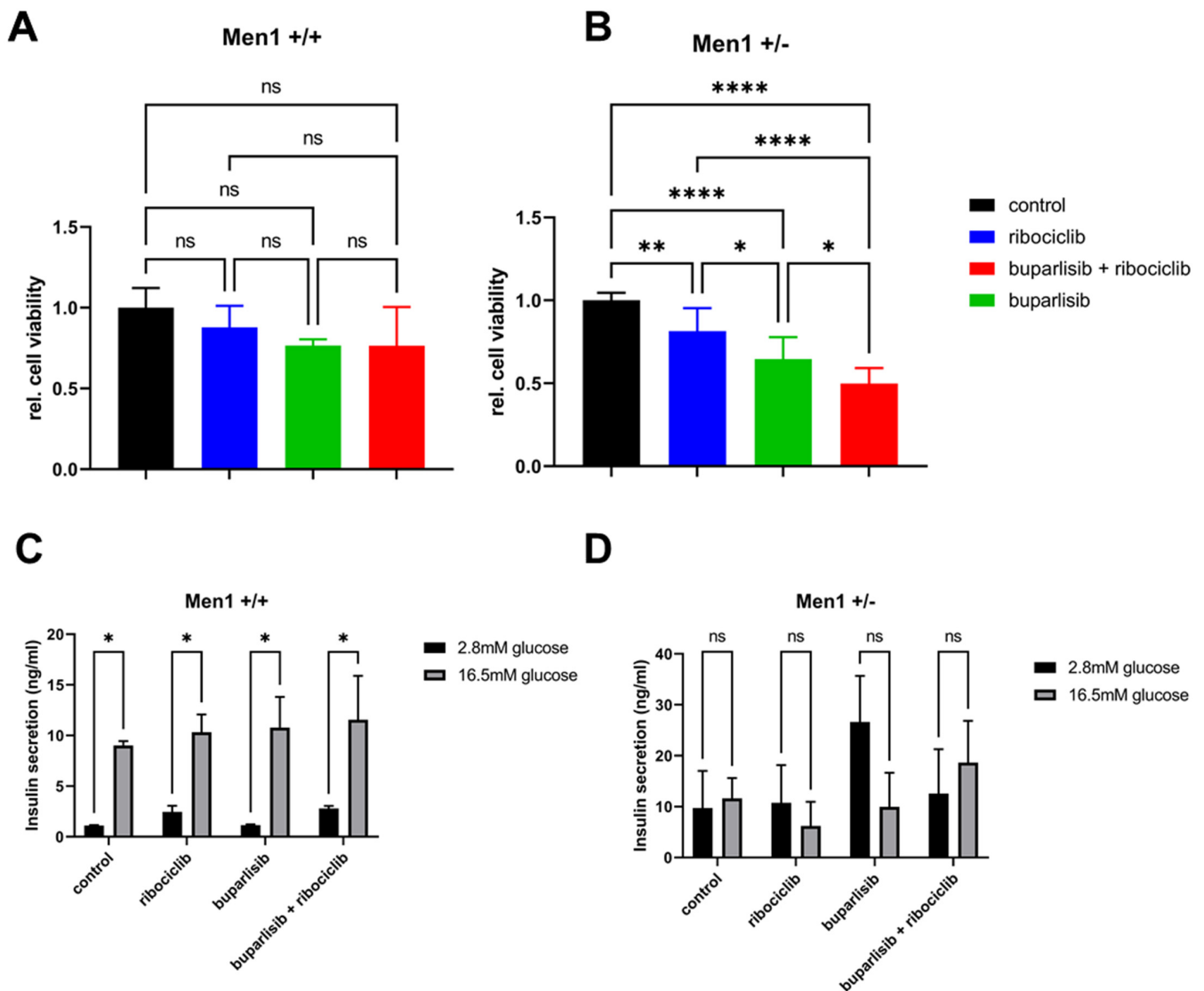


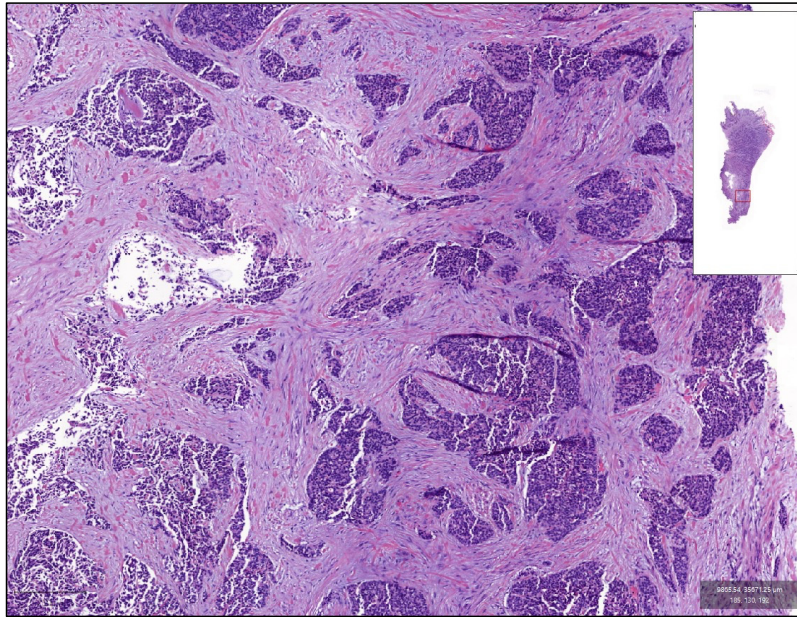
Figure 7. Effect of buparlisib and ribociclib on growth and glucose-stimulated insulin secretion of primary 3D islet microtissues from *Men1* knockout and control mice. (A,B) Primary islets were isolated from age-matched (18 months) heterozygous *Men1*^{T/+} (A) and *Men1*^{+/+} control (B) mice. Single cells were obtained from the islets and 3D microtissues generated using a hanging-drop system. Spheroids were treated with DMSO, or buparlisib and ribociclib alone or in combination, for 72 h after spheroid formation and cell viability was measured. The relative cell viability normalized to the initial measurement and the DMSO control is shown. Data shows the mean ± SD from primary cells of nine *Men1*^{T/+} mice (with tumors) and five *Men1*^{+/+} mice with 4–14 technical replicates each (depending on total amount of cells). One-way ANOVA. Ns, not significant; *, *p* < 0.05; **, *p* < 0.01; ****, *p* < 0.0001. (C,D) Glucose-stimulated insulin secretion of primary 3D microtissues. Primary islets were isolated, processed and treated for 72 h as above. They were serum-deprived, incubated with low glucose (2.8 mM, baseline level) or with high glucose (16.5 mM) for 1 h. Then, insulin secretion was assessed using a specific ELISA assay using the supernatants. Data shows the mean ± SD from primary cells of three *Men1*^{T/+} and 3 *Men1*^{+/+} mice with three technical replicates each. One-way ANOVA. ns, not significant; *, *p* < 0.05.

3.5. Effect of Buparlisib and Ribociclib on the Viability of Human-Derived PanNET 3D Tumoroids

To determine whether the antitumor effect of buparlisib and ribociclib harbors translational relevance, we treated patient-derived 3D tumoroids obtained from four tumors of four patients (two primary tumors and two liver metastases) with the two drugs alone or

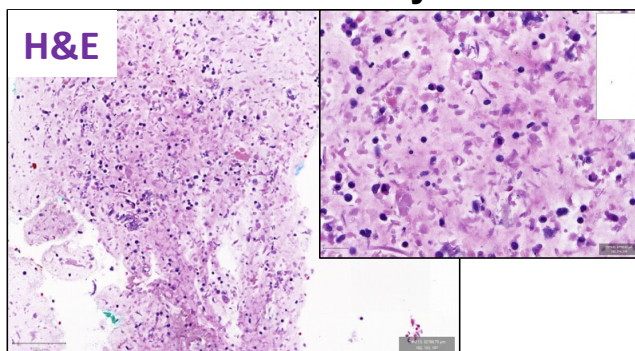
in combination. Patient information is available in Supplementary Table S3. Tumor tissues were digested and reconstituted as 3D microtissues (tumoroids), which were then treated with various drug concentrations over a 7-day period (drug doses are reported in Figure 8C). Part of these microtissues were embedded on the day of isolation (D0) and 12 days later (D12) to verify morphology and marker expression. As previously described [22], patient-derived tumoroids in vitro retained both the histomorphology in the original tumors from which they were derived, as well as the expression of neuroendocrine cell markers (e.g., synaptophysin) (Figure 8A,B).

A PNET4 original tumor tissue



B

MCB Day 0



MCB Day D12

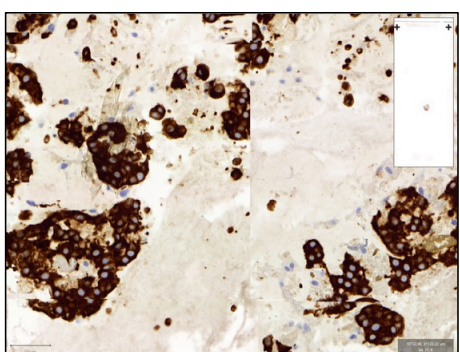
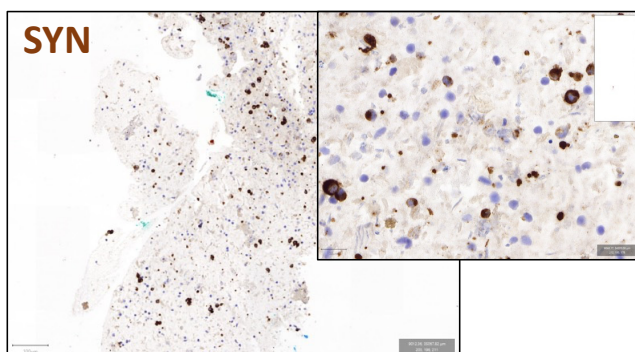
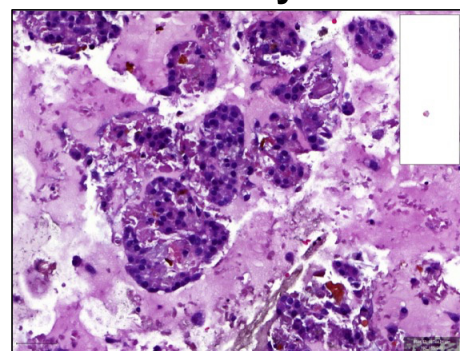


Figure 8. Cont.

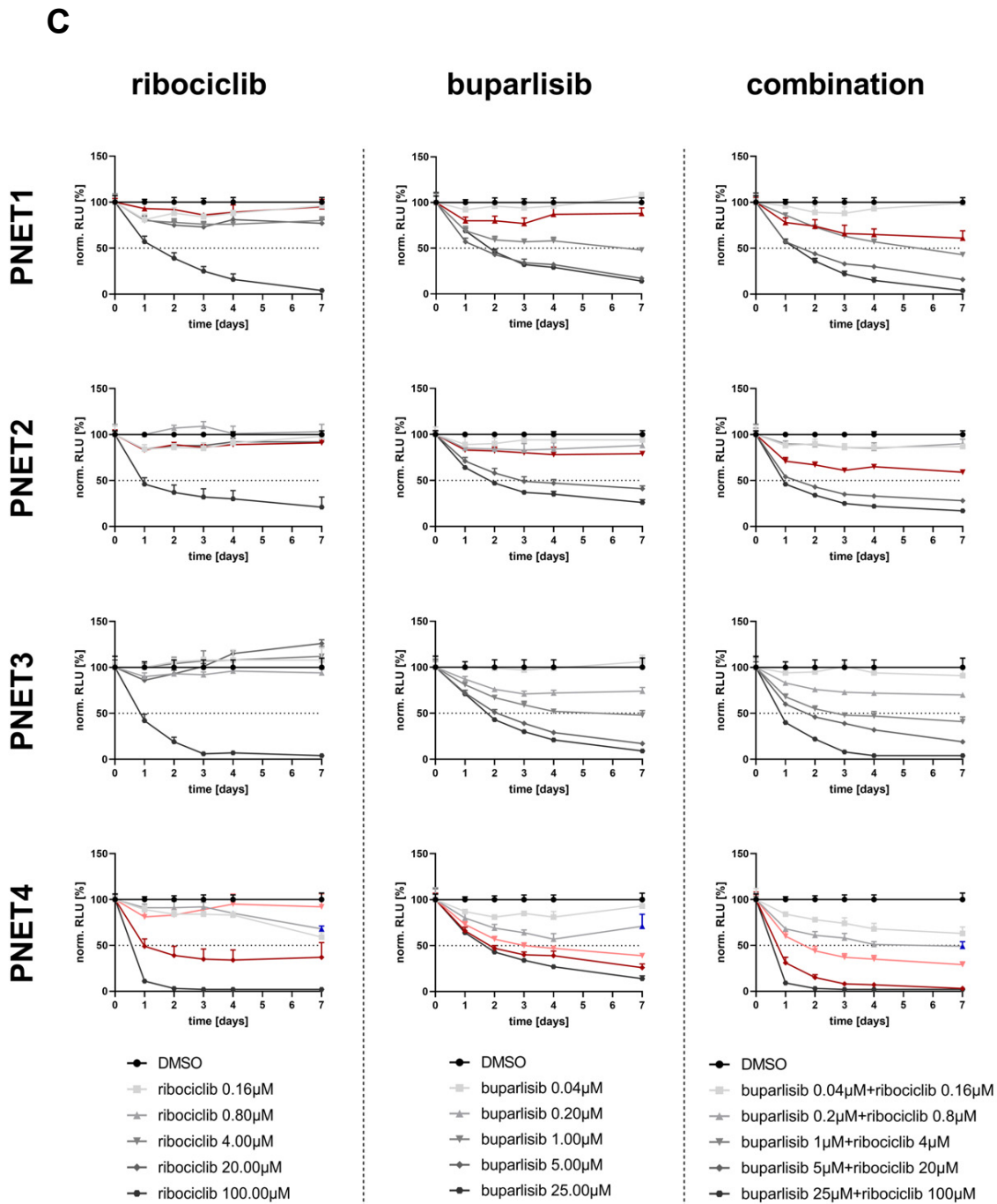


Figure 8. Effect of buparlisib and ribociclib on cell viability of primary human 3D tumoroids. (A,B) Representative images of sample PNET4. (A) H&E staining (H&E) of the original tumor tissue. Scale bar (250 µm). (B) H&E staining and staining for synaptophysin of micro-cell-block samples from the day of isolation (Day 0) and DMSO-treated samples 12 days post-isolation (Day 12). MCB = Micro-cell-block; SYN = Synaptophysin. Scale bar MCB Day 0 (100 µm), scale bar inset (20 µm), scale bar MCB Day 12 (50 µm). (C) Cell viability curves of human tumoroids PNET1, PNET2, PNET3 and PNET4 treated with different concentrations of buparlisib, ribociclib and their combination for 7 days. For clarity, each single treatment and the combination are shown separately. Drug concentrations are

reported below the graphs. Drug concentrations for which the combination was more effective than the individual drugs are illustrated in red. Data were first normalized per-well using a RTG baseline measurement for each individual well and then normalized to the average of the corresponding DMSO control of the respective day. Data represent means \pm SEM ($n = 1$ per patient, three technical replicates). RLU, relative luminescence unit.

Comparable to our findings using established PanNET cell lines and primary islet microtissues from *Men1*^{T/+} mice, we observed a dose-dependent decrease in viability when treating the human 3D tumoroids with the two drugs (Figure 8C, Supplementary Figure S3). Buparlisib as a single agent was more effective than ribociclib in all samples except PNET4. Seven days after treatment, the combination of buparlisib with ribociclib was more effective than the individual treatments in samples PNET1 and PNET2, and showed a synergistic effect in PNET4, as calculated using the Chou–Talalay method [30,31] (Figure 8B, Supplementary Figure S3). The combination showed a superior antitumor effect in three out of four samples for certain drug concentrations, which are indicated in red in the viability curves (Figure 8C), and marked with an asterisk in Supplementary Figure S3. Sample PNET4 displayed the strongest sensitivity to the drug combination, mostly due to a stronger response to ribociclib versus the other primary cultures. Interestingly, in PNET4 the lower doses of buparlisib lost their efficacy with time, thereby showing an increased cell viability at the 7-day time point compared with earlier time points (Figure 8C). In contrast, the same doses of buparlisib, when combined with ribociclib, did not lead to an increase in cell viability, but actually to a further decrease when compared to earlier time points (Figure 8C).

4. Discussion

In our study, we targeted PI3K and CDK4/6 signaling and found that this approach holds promise for the treatment of PanNETs. Indeed, the combination of buparlisib and ribociclib leads to additive/synergistic antitumor effects in established PanNET cells (in both 2D and 3D culture systems), as well as in primary islet tumor microtissues from *Men1*^{T/+} knockout mice. Importantly, this drug combination also exhibited antiproliferative effects in patient-derived primary PanNET 3D tumoroid cultures.

For our studies, we selected cell lines representative of well-differentiated (INS-1E, NT-3 cells) and poorly differentiated (BON-1) PanNENs, and employed clinically relevant doses of both drugs in view of a potential translation of our findings [32,33]. Overall, the combination of buparlisib with ribociclib was more effective than each agent alone at suppressing the proliferation of all cell lines in 2D, with the effect being synergistic for BON-1 cells (proliferation) and for NT-3 cells (apoptosis) and additive in the remaining settings. Buparlisib as a single agent was more effective than ribociclib at inhibiting cell proliferation, with the exception of NT-3 cells, which were equally sensitive to both drugs. The data on the efficacy of buparlisib against BON-1 cells in vitro are in agreement with a previous study [18]. The higher responsiveness of NT-3 cells to CDK4/6 inhibition fits with the data obtained in *Men1*^{+/-}; *Cdk4*^{-/-} double knockout mice, where PanNETs formation dependent on *Men1* gene inactivation was abrogated [15]. Indeed, NT-3 cells have a non-functional menin (the product of the *MEN1* gene) [21], hence are “addicted” to enhanced cell division. Thus, blocking CDK4 activity (i.e., inhibiting cell cycle progression) in these cells is predicted to have a strong negative effect on cell proliferation.

The ability to promote tumor cell death is a highly desirable feature of anti-cancer therapies and has clinical relevance. Thus, we assessed the ability of both drugs to induce apoptosis. In both INS-1E and BON-1 cells, apoptosis was exclusively mediated by buparlisib. In contrast, a synergistic effect of buparlisib and ribociclib to promote apoptosis in NT-3 cells was observed, in line with the higher sensitivity of these cells to CDK4/6 inhibition.

The response of PanNET cells to the selected drugs correlated with the inhibition of the corresponding downstream targets: P-AKT for buparlisib, and P-Rb for ribociclib. Ribo-

ciclib also elicited the downregulation of *Ccna1* and *Pcna*, direct targets of E2F transcription factors, which become active following Rb phosphorylation. Therefore, the effects of the drugs on proliferation and apoptosis are mediated by downstream pathway inhibition and not by off-target effects.

Three-dimensional spheroids, which better mimic the physiological microenvironment of solid tumors, were shown to have a higher predictive value of therapy efficacy than standard 2D cultures [34–36], and are currently the preferred in vitro cancer model for drug testing. For this reason, we extended our therapy studies to 3D spheroid cultures of PanNET cells. Using a 14-day treatment regimen, we observed a synergistic effect of the combination buparlisib and ribociclib on the suppression of the viability of all three cell lines, and on the reduction of spheroid size of INS-1E and NT-3 cells, but not BON-1 cells. The drug concentrations that elicited the strongest effect were higher than in the 2D cell culture setting, a fact that has been previously reported and results from the structure of the spheroids [34,37]. Similar to the 2D culture system, NT-3 were also more responsive to ribociclib when grown as 3D organotypic cultures. Currently, we have no explanation as to why ribociclib is less effective against 3D versus 2D cultures of BON-1 cells.

To further validate the efficacy of our treatment approach, we extended our analyses to primary PanNET cells from *Men1*^{T/+} mice grown as 3D islet microtissues. The drugs reduced the viability of primary PanNET microtissues both as single agents and in combination, with the latter being the most effective condition. Interestingly, no significant effect of the drugs (neither alone nor in combination) was observed on the viability of primary 3D microtissues established from islets of wild-type littermates (*Men1*^{+/+}), thereby pointing to a selective efficacy of the treatment regimen for the tumor cells versus wild-type islets. Additionally, treatment of wild-type islet microtissues with the drugs did not significantly affect insulin secretion, the most important physiological role of pancreatic β cells, which are the major cellular components of the islets and the cells of origin of tumors in this mouse model. Three-dimensional PanNET microtissues from *Men1*^{T/+} mice failed to respond to glucose, suggesting β cell dysfunction.

In addition to primary islet cells from mice, we set out to test out treatment approach in patient-derived primary 3D tumoroid cultures. Specifically, we established 3D tumoroids from four human PanNET tissues (two primary tumors and two metastases), and treated them with buparlisib and ribociclib as single agents or in combination. Importantly, we confirmed that the patient-derived tumoroids preserved the histomorphology and the expression of neuroendocrine cell markers of the tumors from which they were derived. Similar to the results obtained using PanNET cell lines and murine primary islet cells, our drugs could also reduce the viability of human primary PanNET cells, with the combination of buparlisib and ribociclib giving the strongest results in three out of four patients' samples. This effect was most remarkable in PNET4, where we saw a strong synergistic effect of our combination treatment 7 days after treatment. Overall, the different patient-derived primary PanNET cultures showed a variable sensitivity to our drugs, which is not entirely unexpected given the documented heterogeneity of these tumors.

The PNET4 sample was obtained from the liver metastasis of an aggressive and recurrent PanNET developing in a female patient (37 years) which did not respond to standard sunitinib treatment. Remarkably, PNET4 showed the highest sensitivity to ribociclib when compared to the other human primary PanNETs. No information about the genetic makeup of the tumors from which the primary cultures were derived is available. This, combined with the low number of samples analyzed, limits the possibility of correlating the drug response to specific genetic mutations/molecular subtypes in the primary PanNETs. Nevertheless, our analysis demonstrates that this therapeutic approach was effective in three out of four samples, eliciting the same effect as higher doses of buparlisib alone. The possibility to decrease buparlisib concentrations is interesting for future clinical applications as it would reduce the drug's side effects. Moreover, the combination buparlisib and ribociclib might be an option for tumors that showed resistance to standard therapies. The analysis of additional primary human PanNETs is required to confirm our findings.

The activation of the PI3K/Akt/mTOR pathway in PanNET tumorigenesis led to the clinical use of drugs targeting this pathway. The drug for which more information is currently available is everolimus, an inhibitor of the mTORC1 complex [38], which has been FDA-approved for the treatment of patients with unresectable, locally advanced or metastatic PanNETs [39]. Indeed, everolimus significantly prolonged progression-free survival (PFS) in a large Phase III trial of advanced PanNETs [40]. However, inhibition of mTORC1 removes negative feedback in Akt, thereby causing undesired Akt activation and leading to therapy resistance [41]. Therefore, agents blocking the pathway upstream at the level of PI3K are expected to bypass therapy resistance.

5. Conclusions

By demonstrating that the combination treatment of buparlisib with ribociclib is effective against PanNET cell lines representative of tumors with different differentiation states, and having different molecular signatures, as well as against primary mouse and human PanNET cells, our studies provide the rationale for the clinical implementation of drugs co-targeting PI3K and CDK4/6 signaling pathways in PanNETs.

Supplementary Materials: The following supporting information can be downloaded at: <https://www.mdpi.com/article/10.3390/cancers14225481/s1>, Figure S1: Effect of the combination buparlisib and ribociclib on 3D spheroid cultures of the PanNET cell lines; Figure S2: Primary 3D microtissues from mouse pancreatic islets (pseudo-islets). Figure S3: Representative primary human 3D tumoroids; Figure S4: Effect of buparlisib, ribociclib and their combination on human-derived PanNET 3D tumoroids; Table S1: List of TaqMan gene expression assays used for qPCR; Table S2: List of antibodies used for Western blotting; Table S3: Clinico-pathological features of the patients from whom PanNET tissues were obtained at surgery to establish primary cultures.

Author Contributions: Conceptualization, S.G., R.A.T. and N.S.P.; methodology, A.F., E.G. and S.S.; validation, S.G., S.L.A.-M. and A.F.; formal analysis, I.M. and N.S.P.; investigation, S.G., A.M., E.G. and S.L.A.-M.; resources, D.H., M.F. and J.S.; data curation, S.G. and S.L.A.-M.; writing—original draft preparation, S.G., A.F. and S.L.A.-M.; writing—review and editing, A.P., I.M. and N.S.P.; visualization, S.G., E.G. and S.L.A.-M.; supervision, N.S.P.; funding acquisition, N.S.P. All authors have read and agreed to the published version of the manuscript.

Funding: This work was supported by the German Research Foundation (Deutsche Forschungsgemeinschaft-DFG) within the CRC/Transregio 205/2, project number 314061271-TRR 205 (to NSP); and by the Deutsche Krebshilfe (# 70113629 to NSP). Ilaria Marinoni was supported by Wilhelm Sander Stiftung (# 2017.073.2). Aurel Perren was supported by the Swiss Cancer Research Foundation (KFS-4227-08-2017).

Institutional Review Board Statement: The study was conducted according to the guidelines of the Declaration of Helsinki, and it was approved by the Swiss cantonal authorities (Kantonale Ethikkommission Bern, Ref.-Nr. KEK-BE 105/2015 and KE-BE 2019-01154) and the Italian ethics commission (Comitato Etico, CE 252/2019). All patient materials were used according to the Human Research Act and had signed an institutional form of broad consent.

Informed Consent Statement: Informed consent was obtained from all subjects involved in the study.

Data Availability Statement: All data that support the findings of this study are available from the corresponding authors upon reasonable request.

Acknowledgments: The authors thank Elke Pulz for excellent technical assistance.

Conflicts of Interest: The authors declare that they have no conflicts of interest to disclose.

References

1. Hallet, J.; Law, C.H.; Cukier, M.; Saskin, R.; Liu, N.; Singh, S. Exploring the rising incidence of neuroendocrine tumors: A population-based analysis of epidemiology, metastatic presentation, and outcomes. *Cancer* **2015**, *121*, 589–597. [[CrossRef](#)]
2. Coelho, S.; Costa, C.; Santos, A.P.; Souto, P.; Oliveira, J.; Oliveira, J.; Azevedo, I.; Torres, I.; Bento, M.J. Pancreatic neuroendocrine neoplasms: Survival trend analysis of a comprehensive center. *Endocr. Oncol.* **2022**, *2*, 32–41. [[CrossRef](#)]

3. Botling, J.; Lamarca, A.; Bajic, D.; Norlén, O.; Lönngren, V.; Kjaer, J.; Eriksson, B.; Welin, S.; Hellman, P.; Rindi, G.; et al. High-Grade Progression Confers Poor Survival in Pancreatic Neuroendocrine Tumors. *Neuroendocrinology* **2020**, *110*, 891–898.
4. Dasari, A.; Shen, C.; Halperin, D.; Zhao, B.; Zhou, S.; Xu, Y.; Shih, T.; Yao, J.C. Trends in the Incidence, Prevalence, and Survival Outcomes in Patients With Neuroendocrine Tumors in the United States. *JAMA Oncol.* **2017**, *3*, 1335–1342.
5. Rinke, A.; Auernhammer, C.J.; Bodei, L.; Kidd, M.; Krug, S.; Lawlor, R.; Marinoni, I.; Perren, A.; Scarpa, A.; Sorbye, H.; et al. Treatment of advanced gastroenteropancreatic neuroendocrine neoplasia, are we on the way to personalised medicine? *Gut* **2021**, *70*, 1768–1781.
6. Scarpa, A. The landscape of molecular alterations in pancreatic and small intestinal neuroendocrine tumours. *Ann. Endocrinol.* **2019**, *80*, 153–158. [[CrossRef](#)]
7. Chandrasekharappa, S.C.; Guru, S.C.; Manickam, P.; Olufemi, S.E.; Collins, F.S.; Emmert-Buck, M.R.; Debelenko, L.V.; Zhuang, Z.; Lubensky, I.A.; Liotta, L.A.; et al. Positional cloning of the gene for multiple endocrine neoplasia-type 1. *Science* **1997**, *276*, 404–407.
8. Mohr, H.; Pellegata, N.S. Animal models of MEN1. *Endocr. Relat. Cancer* **2017**, *24*, T161–T177. [[CrossRef](#)]
9. Chan, C.S.; Laddha, S.V.; Lewis, P.W.; Koletsky, M.S.; Robzyk, K.; Da Silva, E.; Torres, P.J.; Untch, B.R.; Li, J.; Bose, P.; et al. ATRX, DAXX or MEN1 mutant pancreatic neuroendocrine tumors are a distinct alpha-cell signature subgroup. *Nat. Commun.* **2018**, *9*, 4158.
10. Scarpa, A.; Chang, D.K.; Nones, K.; Corbo, V.; Patch, A.M.; Bailey, P.; Lawlor, R.T.; Johns, A.L.; Miller, D.K.; Mafficini, A.; et al. Whole-genome landscape of pancreatic neuroendocrine tumours. *Nature* **2017**, *543*, 65–71.
11. Briest, F.; Grabowski, P. PI3K-AKT-mTOR-signaling and beyond: The complex network in gastroenteropancreatic neuroendocrine neoplasms. *Theranostics* **2014**, *4*, 336–365. [[CrossRef](#)]
12. Maharjan, C.K.; Ear, P.H.; Tran, C.G.; Howe, J.R.; Chandrasekharan, C.; Quelle, D.E. Pancreatic Neuroendocrine Tumors: Molecular Mechanisms and Therapeutic Targets. *Cancers* **2021**, *13*, 5117. [[CrossRef](#)]
13. Harvey, M.; Vogel, H.; Lee, E.Y.; Bradley, A.; Donehower, L.A. Mice deficient in both p53 and Rb develop tumors primarily of endocrine origin. *Cancer Res.* **1995**, *55*, 1146–1151.
14. Tang, L.H.; Contractor, T.; Clausen, R.; Klimstra, D.S.; Du, Y.C.; Allen, P.J.; Brennan, M.F.; Levine, A.J.; Harris, C.R. Attenuation of the retinoblastoma pathway in pancreatic neuroendocrine tumors due to increased cdk4/cdk6. *Clin. Cancer Res.* **2012**, *18*, 4612–4620.
15. Gillam, M.P.; Nimbalkar, D.; Sun, L.; Christov, K.; Ray, D.; Kaldis, P.; Liu, X.; Kiyokawa, H. MEN1 tumorigenesis in the pituitary and pancreatic islet requires Cdk4 but not Cdk2. *Oncogene* **2015**, *34*, 932–938.
16. Bollard, J.; Patte, C.; Massoma, P.; Goddard, I.; Gadot, N.; Benslama, N.; Hervieu, V.; Ferraro-Peyret, C.; Cordier-Bussat, M.; Scoazec, J.Y.; et al. Combinatorial Treatment with mTOR Inhibitors and Streptozotocin Leads to Synergistic In Vitro and In Vivo Antitumor Effects in Insulinoma Cells. *Mol. Cancer Ther.* **2018**, *17*, 60–72. [[CrossRef](#)]
17. Passacantilli, I.; Capurso, G.; Archibugi, L.; Calabretta, S.; Caldarella, S.; Loreni, F.; Delle Fave, G.; Sette, C. Combined therapy with RAD001 e BEZ235 overcomes resistance of PET immortalized cell lines to mTOR inhibition. *Oncotarget* **2014**, *5*, 5381–5391. [[CrossRef](#)]
18. Valentino, J.D.; Li, J.; Zaytseva, Y.Y.; Mustain, W.C.; Elliott, V.A.; Kim, J.T.; Harris, J.W.; Campbell, K.; Weiss, H.; Wang, C.; et al. Cotargeting the PI3K and RAS pathways for the treatment of neuroendocrine tumors. *Clin. Cancer Res.* **2014**, *20*, 1212–1222. [[CrossRef](#)]
19. Grande, E.; Teulé, A.; Alonso-Gordoa, T.; Jiménez-Fonseca, P.; Benavent, M.; Capdevila, J.; Custodio, A.; Vera, R.; Munarriz, J.; La Casta, A.; et al. The PALBONET Trial: A Phase II Study of Palbociclib in Metastatic Grade 1 and 2 Pancreatic Neuroendocrine Tumors (GETNE-1407). *Oncologist* **2020**, *25*, 745–e1265. [[CrossRef](#)]
20. Pusceddu, S.; Corti, F.; Milione, M.; Centonze, G.; Prinzi, N.; Torchio, M.; de Braud, F. Are Cyclin-Dependent Kinase 4/6 Inhibitors Without Future in Neuroendocrine Tumors? *Oncologist* **2020**, *25*, e1257–e1258. [[CrossRef](#)]
21. Benten, D.; Behrang, Y.; Unrau, L.; Weissmann, V.; Wolters-Eisfeld, G.; Burdak-Rothkamm, S.; Stahl, F.R.; Anlauf, M.; Grabowski, P.; Möbs, M.; et al. Establishment of the First Well-differentiated Human Pancreatic Neuroendocrine Tumor Model. *Mol. Cancer Res.* **2018**, *16*, 496–507. [[CrossRef](#)] [[PubMed](#)]
22. April-Monn, S.L.; Wiedmer, T.; Skowronska, M.; Maire, R.; Schiavo Lena, M.; Trippel, M.; Di Domenico, A.; Muffatti, F.; Andreasi, V.; Capurso, G.; et al. Three-Dimensional Primary Cell Culture: A Novel Preclinical Model for Pancreatic Neuroendocrine Tumors. *Neuroendocrinology* **2021**, *111*, 273–287.
23. Bertolino, P.; Tong, W.M.; Galendo, D.; Wang, Z.Q.; Zhang, C.X. Heterozygous Men1 mutant mice develop a range of endocrine tumors mimicking multiple endocrine neoplasia type 1. *Mol. Endocrinol.* **2003**, *17*, 1880–1892. [[PubMed](#)]
24. Gulde, S.; Wiedemann, T.; Schillmaier, M.; Valença, I.; Lupp, A.; Steiger, K.; Yen, H.Y.; Bäuerle, S.; Notni, J.; Luque, R.; et al. Gender-Specific Efficacy Revealed by Head-to-Head Comparison of Pasireotide and Octreotide in a Representative In Vivo Model of Nonfunctioning Pituitary Tumors. *Cancers (Basel)* **2021**, *21*, 3097. [[CrossRef](#)]
25. Chou, T.C.; Martin, N. *CompuSyn for Drug Combinations: PC Software and User's Guide: A Computer Program for Quantitation of Synergism and Antagonism in Drug Combinations, and the Determination of IC50 and ED50 and LD50 Values*; ComboSyn Inc.: Paramus, NJ, USA, 2005. Available online: <https://www.combosyn.com/> (accessed on 2 August 2022).
26. Merglen, A.; Theander, S.; Rubi, B.; Chaffard, G.; Wollheim, C.B.; Maechler, P. Glucose sensitivity and metabolism-secretion coupling studied during two-year continuous culture in INS-1E insulinoma cells. *Endocrinology* **2004**, *145*, 667–678. [[CrossRef](#)]

27. Luley, K.B.; Biedermann, S.B.; Künstner, A.; Busch, H.; Franzenburg, S.; Schrader, J.; Grabowski, P.; Wellner, U.F.; Keck, T.; Brabant, G.; et al. A Comprehensive Molecular Characterization of the Pancreatic Neuroendocrine Tumor Cell Lines BON-1 and QGP-1. *Cancers* **2020**, *12*, 691.
28. Vandamme, T.; Peeters, M.; Dogan, F.; Pauwels, P.; Van Assche, E.; Beyens, M.; Mortier, G.; Vandeweyer, G.; de Herder, W.; Van Camp, G.; et al. Whole-exome characterization of pancreatic neuroendocrine tumor cell lines BON-1 and QGP-1. *J. Mol. Endocrinol.* **2015**, *54*, 137–147. [[PubMed](#)]
29. Wong, C.H.; Ma, B.B.Y.; Hui, C.W.C.; Lo, K.W.; Hui, E.P.; Chan, A.T.C. Preclinical evaluation of ribociclib and its synergistic effect in combination with alpelisib in non-keratinizing nasopharyngeal carcinoma. *Sci. Rep.* **2018**, *8*, 8010.
30. Chou, T.C. Drug combination studies and their synergy quantification using the Chou-Talalay method. *Cancer Res.* **2010**, *70*, 440–446. [[CrossRef](#)]
31. Chou, T.-C. The combination index (CI < 1) as the definition of synergism and of synergy claims. *Synergie* **2018**, *7*, 49–50.
32. Rodon, J.; Braña, I.; Siu, L.L.; De Jonge, M.J.; Homji, N.; Mills, D.; Di Tomaso, E.; Sarr, C.; Trandafir, L.; Massacesi, C.; et al. Phase I dose-escalation and -expansion study of buparlisib (BKM120), an oral pan-Class I PI3K inhibitor, in patients with advanced solid tumors. *Investig. New Drugs* **2014**, *32*, 670–681.
33. EMA. *European Medicines Agency: EMEA/H/C/004213/0000—Assessment Report Kisqali—International Non-Proprietary Name: Ribociclib*; European Medicines Agency: London, UK, 2017.
34. Jensen, C.; Teng, Y. Is It Time to Start Transitioning From 2D to 3D Cell Culture? *Front. Mol. Biosci.* **2020**, *7*, 33. [[CrossRef](#)] [[PubMed](#)]
35. Kapałczyńska, M.; Kolenda, T.; Przybyła, W.; Zajączkowska, M.; Teresiak, A.; Filas, V.; Ibbs, M.; Bliźniak, R.; Łuczewski, Ł.; Lamperska, K. 2D and 3D cell cultures—A comparison of different types of cancer cell cultures. *Arch. Med. Sci.* **2018**, *14*, 910–919. [[PubMed](#)]
36. Poornima, K.; Francis, A.P.; Hoda, M.; Eladl, M.A.; Subramanian, S.; Veeraraghavan, V.P.; El-Sherbiny, M.; Asseri, S.M.; Hussamuldin, A.B.A.; Surapaneni, K.M.; et al. Implications of Three-Dimensional Cell Culture in Cancer Therapeutic Research. *Front. Oncol.* **2022**, *12*, 891673. [[CrossRef](#)] [[PubMed](#)]
37. Melissaridou, S.; Wiechec, E.; Magan, M.; Jain, M.V.; Chung, M.K.; Farnebo, L.; Roberg, K. The effect of 2D and 3D cell cultures on treatment response, EMT profile and stem cell features in head and neck cancer. *Cancer Cell Int.* **2019**, *19*, 16.
38. Tanaka, C.; O'Reilly, T.; Kovarik, J.M.; Shand, N.; Hazell, K.; Judson, I.; Raymond, E.; Zumstein-Mecker, S.; Stephan, C.; Boulay, A.; et al. Identifying optimal biologic doses of everolimus (RAD001) in patients with cancer based on the modeling of preclinical and clinical pharmacokinetic and pharmacodynamic data. *J. Clin. Oncol.* **2008**, *26*, 1596–1602. [[CrossRef](#)]
39. Oberstein, P.E.; Saif, M.W. Novel agents in the treatment of unresectable neuroendocrine tumors. Highlights from the "2011 ASCO Annual Meeting". Chicago, IL, USA.; June 3-7, 2011. *J. Pancreas* **2011**, *12*, 358–361.
40. Yao, J.C.; Shah, M.H.; Ito, T.; Bohas, C.L.; Wolin, E.M.; Van Cutsem, E.; Hobday, T.J.; Okusaka, T.; Capdevila, J.; de Vries, E.G.; et al. Everolimus for advanced pancreatic neuroendocrine tumors. *N. Engl. J. Med.* **2011**, *364*, 514–523. [[CrossRef](#)]
41. Rozengurt, E.; Soares, H.P.; Sinnet-Smith, J. Suppression of feedback loops mediated by PI3K/mTOR induces multiple overactivation of compensatory pathways: An unintended consequence leading to drug resistance. *Mol. Cancer Ther.* **2014**, *13*, 2477–2488. [[CrossRef](#)]

6.3 Manuscript 6: “*Validation of Immunohistochemistry for Canine Proteins Involved in Thyroid Iodine Uptake and Their Expression in Canine Follicular Cell Thyroid Carcinomas (FTCs) and FTC-Derived Organoids*”

Jana Jankovic, Martina Dettwiler, Martin González Fernández, Eve Tièche, Kerstin Hahn, Simon April-Monn, Matthias S. Dettmer, Martin Kessler, Sven Rottenberg, and Miguel Campos

Veterinary pathology [10.1177/03009858211018813](https://doi.org/10.1177/03009858211018813)

Reprinted from ³⁶⁰ © 2021, The Authors

Author contribution (CRediT):

I was involved in the **methodology** (development and design of methodology, creation of models), **validation** (verification of the overall replication/reproducibility of experiments and results and other research outputs), and **investigation** (conduction of research and investigation processes, performing experiments and data collection) for this manuscript.

Validation of Immunohistochemistry for Canine Proteins Involved in Thyroid Iodine Uptake and Their Expression in Canine Follicular Cell Thyroid Carcinomas (FTCs) and FTC-Derived Organoids

Veterinary Pathology

1-9

© The Author(s) 2021

Article reuse guidelines:

sagepub.com/journals-permissions

DOI: 10.1177/03009858211018813

journals.sagepub.com/home/vet



Jana Jankovic¹ , Martina Dettwiler¹ , Martin González Fernández¹, Eve Tièche¹, Kerstin Hahn¹, Simon April-Monn¹ , Matthias S. Dettmer¹, Martin Kessler², Sven Rottenberg¹, and Miguel Campos¹

Abstract

Thyrotropin receptor (TSHR), sodium iodide symporter (NIS), pendrin, and thyroid peroxidase (TPO) are essential for the uptake of iodine by follicular thyroid cells. The aim of this study was to establish immunohistochemistry (IHC) protocols for TSHR, NIS, pendrin, and TPO in canine tissues and characterize their expression in organoids derived from canine follicular cell thyroid carcinoma (FTC) and in the respective primary tumors. This constitutes a fundamental step to establish organoids as a model to study the uptake of iodine in canine FTC. Commercially available antibodies directed against human proteins were selected. Antibody specificity was confirmed by western blot using lysates of the HTori-3 human thyroid cell line and healthy canine thyroid gland. IHC was validated using HTori-3 cells and a set of canine normal tissues including healthy thyroid gland. The expression of TSHR, NIS, pendrin, and TPO was evaluated in 3 organoid lines derived from FTC and respective primary tumors. All 4 antibodies produced specific bands by western blot and cytoplasmic labeling in follicular cells by IHC in both human HTori-3 cells and canine thyroid gland. NIS also showed basolateral membrane immunolabeling in follicular cells. All 4 proteins were highly expressed in organoids derived from FTC. The expression was similar or higher compared to the primary tumors. The results of this study characterize organoids derived from canine FTC as a suitable in vitro model to investigate iodine uptake, opening new research possibilities in the field of canine thyroid cancer therapy.

Keywords

dogs, endocrine gland neoplasms, immunohistochemistry, iodine metabolism, organoids, thyroid carcinoma, thyroid-stimulating hormone receptor, western blot

Thyroid tumors represent 1% to 2% of all neoplasms in dogs. Median age at presentation is 9 to 10 years, and Boxers, Beagles, Golden Retrievers, and Siberian Huskies are overrepresented.^{6,37} Ninety percent of canine thyroid tumors detected clinically are malignant and can be classified as either follicular cell thyroid carcinoma (FTC), which arises from thyroid follicular cells, or medullary thyroid carcinoma (MTC), which arises from the parafollicular cells (C-cells).¹⁸ FTC accounts for 70% of canine thyroid carcinomas while MTC has a prevalence of 30%.⁸ Radioiodine-131 (¹³¹I) is an effective treatment modality for invasive canine FTC and is associated with a median survival time of 27 to 30 months, while untreated dogs have a median survival time of 3 months.^{30,36} Furthermore, ¹³¹I could constitute the only effective therapy against thyroid cancer metastases. However, treatment efficacy critically depends on the uptake of ¹³¹I by the primary tumor and its metastases.

To improve treatment efficacy in dogs, research on modulation of ¹³¹I uptake by thyroid cancer cells is needed. One particularly important aspect therein is the development of an adequate in vitro model of canine FTC and the evaluation of the expression of proteins involved in iodine uptake.

Thyrotropin receptor (TSHR), sodium iodide symporter (NIS), pendrin, and thyroid peroxidase (TPO) are essential for

¹University of Bern, Bern, Switzerland

²Tierklinik Hofheim, Hofheim, Germany

Supplemental material for this article is available online.

Corresponding Author:

Jana Jankovic, Department of Clinical Veterinary Science, Vetsuisse Faculty, University of Bern, Länggassstrasse 128, 3012 Bern, Switzerland.

Email: Jana.jankovic@vetsuisse.unibe.ch

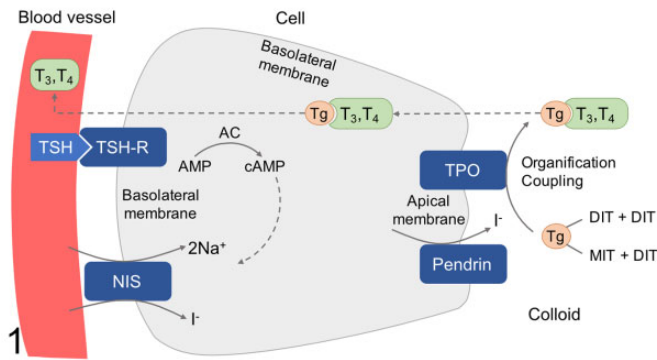


Figure 1. Schematic representation of proteins involved in iodine uptake and thyroid hormone production in thyroid follicular cells. Thyrotropin (TSH) stimulation of TSH receptor (TSHR) activates adenylate cyclase (AC) generating cyclic AMP (cAMP). This stimulates transcription of sodium-iodide symporter (NIS), thyroglobulin (Tg), and thyroid peroxidase (TPO), as well as NIS-mediated iodide uptake. Iodide is transferred across the apical membrane by pendrin. TPO mediates the oxidation of iodide (I^-) to iodine (I^0) and the iodination of tyrosine residues within the thyroglobulin backbone, a process known as organification. The coupling of monoiodotyrosine (MIT) and diiodotyrosine (DIT) leads to the production of triiodothyronine (T3) and tetraiodothyronine (T4). These ultimately undergo endocytosis and are released to the blood stream.

the uptake and organification of iodine by thyroid follicular cells and play a crucial role in the production of thyroid hormones (Fig. 1).^{16,25} TSHR is a G-protein-coupled receptor composed of 2 subunits (an extracellular thyrotropin-binding region and a transmembrane and cytosolic part responsible for intracellular signaling) and is located in the basolateral membrane of thyroid follicular cells.³⁹ Thyrotropin binds to the TSHR activating intracellular signaling via G-proteins and cyclic adenosine monophosphate (cAMP), which stimulates transcription of NIS, thyroglobulin, and TPO, as well as NIS-mediated iodide uptake (Fig. 1).^{24,29} Functional TSHR is also present in extrathyroidal cells such as in cardiomyocytes, hematopoietic cells, human abdominal preadipocytes, orbital fibroblasts, and hair follicles.^{4,5,11,19} NIS is a membrane glycoprotein mainly expressed in thyroid tissue, but also in salivary glands, gastric mucosa, and lactating mammary glands.² In thyroid follicular cells, NIS mediates the active transport of iodide ions across the basolateral membrane.³⁹ Pendrin is an anion transporter with 11 or 12 transmembrane domains and transports iodide across the apical membrane of thyroid follicular cells.³⁹ TPO is a crucial enzyme responsible for organification of iodine and biosynthesis of thyroid hormones. It catalyzes the iodination and coupling of tyrosine residues in thyroglobulin, leading to the synthesis of triiodothyronine and thyroxine.²⁰ Research on the expression of TSHR, NIS, pendrin, and TPO in thyroid follicular cells with the aim of modulating iodine uptake could lead to improvement of radioiodine treatment of thyroid diseases.

Tissue-derived adult stem cells and cancer cells can be grown in 3D matrix with high efficiency into self-organizing

organotypic structures termed organoids.¹⁰ Cancer organoids recapitulate features of the original tumor and can model clinically relevant drug responses, providing a unique opportunity for personalized cancer therapy and could constitute an ideal in vitro model to investigate modulation of iodine uptake by thyroid cancer cells.¹⁰ In humans, long-term organoid cultures have been developed from colon, esophagus, pancreas, stomach, liver, retina, and endometrium, as well as from metastatic colon, prostate, and breast cancer.^{7,10} Our group has recently developed stable organoid cultures derived from canine FTC, to our knowledge the first organoid culture from spontaneous thyroid cancer in any species. In order to establish patient-derived thyroid organoids as a model for iodine uptake and therapeutic studies in canine FTC, we aimed to validate the expression and subcellular localization of TSHR, NIS, pendrin, and TPO, matching it to the primary tumors. To date, immunohistochemistry (IHC) for canine proteins involved in iodine uptake has only been validated for TSHR.²² The aim of this study was to establish IHC protocols for TSHR, NIS, pendrin, and TPO in canine tissue and to evaluate their expression in matched canine primary FTC and FTC-derived organoids.

Materials and Methods

Tissue Samples

Samples of healthy canine thyroid gland ($n = 3$) and FTC ($n = 3$) were available through the biobank of the Vetsuisse Faculty, University of Bern. This tissue collection comprises samples of thyroid tumors collected during surgery for diagnostic and curative purposes, and of healthy thyroid glands collected after euthanasia from dogs that had to be euthanized for other reasons. Parts of the thyroid samples were either stored in DMSO-containing freezing medium (45% FCS, LubioScience; 10% DMSO Sigma-Aldrich; 45% DMEM ThermoFisher) at -150°C (for culture), were snap frozen in liquid nitrogen and stored at -80°C (for western blot), or were fixed in 10% neutral buffered formalin for 24 to 48 hours. The latter underwent paraffin embedding and subsequent histopathological evaluation by a board-certified pathologist (MD). Thyroid tumors were classified according to World Health Organization guidelines as follicular cell tumors (follicular, compact, follicular-compact, papillary, poorly differentiated, undifferentiated, carcinosarcoma) or medullary tumors.¹⁸ IHC for thyroglobulin (rabbit polyclonal, Agilent Technologies) and calcitonin (rabbit polyclonal, Agilent Technologies) was performed in all tumors to aid classification. The distinction between adenoma and carcinoma was based on histologic evidence of capsular invasion, vascular invasion, or metastases.

Two-Dimensional Cell Culture (HTori-3)

The human thyroid epithelial cell line HTori-3 cell line was cultured as described and maintained in complete medium (RPMI-1640, 10% FBS, 1% L-glutamine, 1% penicillin-streptomycin-amphotericin B; ThermoFisher,) in standard

T-75 flasks in a humidified cell incubator (21% O₂, 5% CO₂, 37 °C).³⁵ Cells were split and plated into 6-well plates 3 days before embedding, allowing an initial 72-hour baseline of uninterrupted growth acquiring 70% to 80% confluency before cell collection. For immunohistochemical analyses, HTori-3 cells at 3 passages post-thawing were processed into micro-cell-blocks (MCB), as previously described.³ In brief, 1.0×10^6 trypsinized cells were collected in a 1.5 mL Eppendorf tube. Cells were washed with warm DPBS and pelleted by centrifugation at 450g. After aspiration of the supernatant, cells were resuspended in human plasma derived from whole blood (Inter-regional Blood Transfusion SRC) and Thrombin (Diagnostec) (ratio 5:1) followed by 3-minute incubation at room temperature (RT). The clot was fixed with 4% PFA for 45 minutes protected from light. After a DPBS wash, supernatant was aspirated and cells were incubated in hematoxylin and DPBS solution (ratio 1:8) on a rocker shaker for 15 minutes at RT. The counterstained clot was transferred to a plastic micro-cassette for paraffin embedding for IHC.

For western blot analysis, HTori-3 cells at 3 passages post-thawing were harvested, 1.0×10^6 cells for each replicate ($n = 8$ technical replicates). Cells were washed with warm PBS before plates were put on ice at 4 °C. Using a cell scraper cells were detached and instantly collected in a 1.5 mL Eppendorf tube followed by a short spin 450g at 4 °C. Subsequently, the cells were snap frozen in liquid nitrogen and stored at -80 °C until processing.

Organoid Cultures

The protocol for establishing organoid cultures derived from canine FTC is described extensively elsewhere (Tièche et al, unpublished data). Briefly, tumor samples from 3 euthyroid dogs with naturally occurring FTC of compact type (case 1), follicular-compact type (case 2), follicular type (case 3) were frozen in DMSO-containing freezing medium (45% FCS, LubioScience; 10% DMSO, Sigma-Aldrich; 45% DMEM, ThermoFisher) within 24 hours after thyroidectomy and stored at -150 °C until processing. After thawing, the tissue was digested with collagenase IV and dissociated mechanically. Cells were subsequently seeded in Cultrex Basement Membrane Extract (Amsbio) in 30 µl droplets on 24-well culture plates (Huberlab). Five hundred microliters of prewarmed culture medium was added after 30 to 45 minutes. The basic culture medium composed of Advanced DMEM/F12 (ThermoFisher), supplemented with L-glutamine (ThermoFisher), HEPES buffer (Sigma-Aldrich), penicillin-streptomycin (ThermoFisher), N-acetylcysteine (Sigma-Aldrich), B-27 supplement (ThermoFisher), epithelial growth factor (Preprotech), Noggin, Rspodin-1 (both self-produced using stably transduced 293 HEK cells, provided by Dr Calvin Kuo, Stanford University), and ROCK-inhibitor Y-27632 (AbMole Bioscience). Organoids were cultured in a 5% CO₂ atmosphere and medium was changed twice a week. Organoids were passaged after 9 to 14 days using TrypLE Express (ThermoFisher) for 10 minutes and mechanical dissociation. After 15 to 24 days

(passage 1), organoids were formalin-fixed, pelleted in 2.5% agarose, paraffin-embedded, and processed for hematoxylin-eosin staining and IHC. Thyroid follicular cell origin of the organoids was confirmed with IHC for thyroid transcription factor-1 (TTF-1) and thyroglobulin.

Antibodies

Commercially available antibodies directed against human proteins were selected according to the homology of the epitopes (accessed in NCBI) to the canine protein. Rabbit polyclonal anti-TPO antibody (ab203057, Abcam), rabbit polyclonal anti-SLC26A4 (pendrin) antibody (ab98091, Abcam), rabbit polyclonal anti-TSHR (C-terminal) antibody (ab188902, Abcam), and mouse monoclonal anti-SLC5A5/NIS antibody (LS-C16858, LifeSpan BioSciences, LabForce) were used.

Western Blot

To prepare the protein lysate, HTori-3 cells and samples from snap frozen healthy canine thyroid gland were homogenized in RIPA buffer with phosphatase (Thermo Scientific) and protease inhibitor (Thermo Scientific), sonicated (amplitude 30 for 1 minute), and centrifuged at 12 000 rpm for 20 minutes. The supernatants were then recovered and protein concentration was determined by BCA protein assay kit (Thermo Scientific). Samples were mixed in Protein Loading Buffer with 2-mercaptoethanol (made in Institute of Animal Pathology, Vetsuisse Faculty, Bern, Switzerland). After electrophoresis (SDS-PAGE) on a 7.5% polyacrylamide gel, samples were transferred to PVDF membranes for 1 hour at 100 V in transfer buffer (25 mM TRIS, 192 mM glycine, 20% methanol, pH 8.3). Membranes were blocked in 5% nonfat dry milk in TBS-T (TRIS 100 mM, pH 7.5, NaCl 0.9%, Tween 0.05%) for 1 hour at RT. Antibodies for NIS, pendrin, and TPO were diluted according to the manufacturer's instructions. TSHR was diluted 1 in 750 after a trial with 1 in 1000 dilution produced a blot of insufficient quality. Incubation with primary antibodies for TSHR (1 in 750 dilution), NIS (1 in 1000 dilution), pendrin (1 in 500 dilution), and TPO (1 in 1000 dilution) was performed in TBS-T overnight at 4 °C. Membranes were washed 3 times for 10 minutes in TBS-T and incubated with anti-rabbit (TSHR, pendrin, TPO 1 in 2500 dilution, Cell Signaling Technology) and anti-mouse (NIS, 1 in 2500 dilution, Cell Signaling Technology) secondary antibodies for 1 hour at RT. After washing 6 times for 5 minutes in TBS-T, blots were revealed using a commercial ECL mixture (GE Healthcare Life Sciences). Images were taken using a Vilber Fusion FX (Colégien, France) machine.

Immunohistochemistry

For antibody validation, the following formalin-fixed and paraffin-embedded (FFPE) canine tissues were used as a positive control: healthy thyroid gland (all antibodies), salivary gland (NIS), stomach (NIS), and skin (TSHR). In addition,

FFPE pellets of human HTori-3 cells were also used as positive control for all antibodies. As a negative control, the following FFPE canine tissue were used: small intestine (TSHR), liver (NIS, pendrin, TPO), lymph node (NIS, pendrin, TPO), skin (NIS, pendrin, TPO), and brain (NIS, TPO). This tissue selection was based on the expression of the respective antigens in human tissues that were reported to highly express or to specifically lack expression of respective proteins.^{2,5,9,15,25}

These tissues were obtained from dogs euthanized for different reasons, few hours after euthanasia, and were processed as described above. After successful antibody validation, protein expression was evaluated on FFPE sections of the 3 FTCs and the organoid lines derived from these tumors.

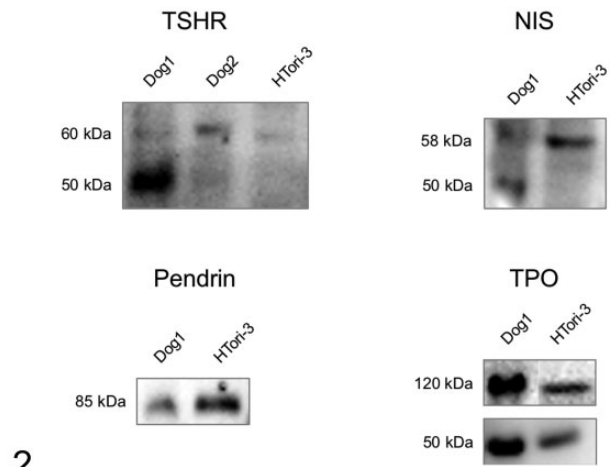
From all tissues, pelleted cells, and organoids, 5- μ m sections were mounted on positively charged glass slides. After dewaxing and rehydration, endogenous peroxidase was blocked with 3% H₂O₂ for 20 minutes. Antigen retrieval was performed in citrate buffer (10 mM sodium citrate, 0.05% Tween 20, pH 6.0) by microwaving at 90 °C for 5 minutes for TSHR, and by pressure cooking for NIS (115 °C, 0.7 bar for 20 minutes), pendrin (107 °C, 0.3 bar for 20 minutes), and TPO (107 °C, 0.3 bar for 10 minutes). Ten percent goat serum was used as blocking agent. Sections were incubated with primary antibodies horizontally in a humid chamber for 1 hour at RT for pendrin (1 in 100 dilution) and overnight at 4 °C for TSHR (1 in 50 dilution), NIS (1 in 100 dilution), and TPO (1 in 100 dilution). Evaluation of the optimal concentration of each primary antibody was performed with serial antibody dilutions using healthy canine thyroid gland as positive control. As a negative control for all antibodies, the primary antibody was replaced with PBS. After washing with PBS, incubation with biotinylated link secondary antibodies (Dako LSAB2 System Streptavidin-HRP, Dako North America) was performed. 3-Amino-9-ethylcarbazole (AEC) in substrate buffer solution (Dako AEC Substrate Chromogen, Dako North America) served as chromogen and was allowed to react for 9 minutes. After washing, sections were counterstained with hematoxylin, rinsed in tap water, and mounted with cover slips.

All sections were examined by 2 investigators (JJ, MD), who were blinded to the clinical information of the patients. The distribution of immunohistochemical labeling in neoplastic cells was subjectively scored as follows: 0 (no positive cells), 1 (1% to 33% positive cells), 2 (33% to 66% positive cells), and 3 (67% to 100% positive cells). Labelling intensity was subjectively scored as follows: 0 (negative), 1 (weak), 2 (moderate), and 3 (strong).¹³ Photomicrographs from immunolabeled healthy thyroid gland and tumors were taken from scanned slides using a Panoramic p250 scanner (3D HISTECH), and from organoids with an Olympus BX51 microscope (Olympus) using the CellSens Standard software (Olympus).

Results

Western Blot

TSHR, NIS, pendrin, and TPO produced specific protein bands in the western blot of canine thyroid tissue and human thyroid



2

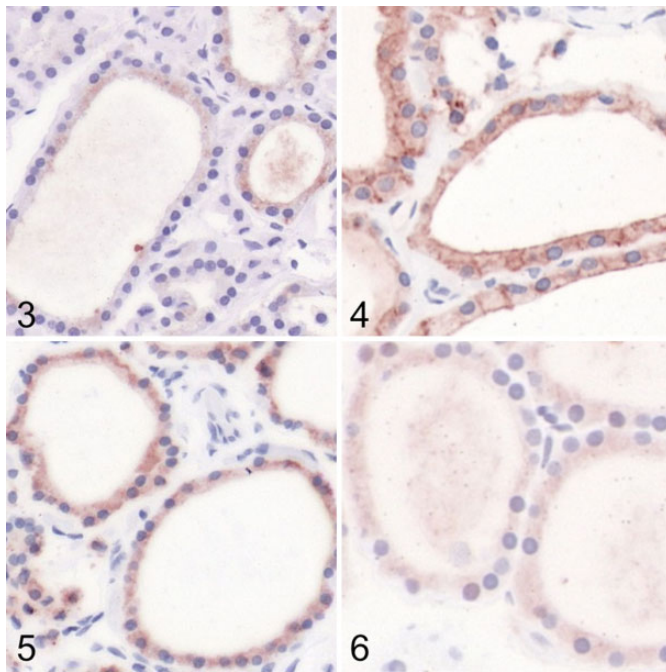
Figure 2. Western blot results for thyrotropin receptor (TSHR), sodium iodide symporter (NIS), pendrin, and thyroid peroxidase (TPO) protein lysate from healthy canine thyroid gland (dog 1 and dog 2 samples) and HTori-3 healthy human thyroid cell line. TSHR showed bands at 50 and 60 kDa for healthy canine thyroid gland and at 60 kDa for HTori-3 cells. NIS revealed bands at 50 kDa for canine thyroid gland and at 58 kDa for HTori-3 cells. Pendrin showed a band at 85 kDa for both healthy canine thyroid gland and HTori-3 cells. TPO showed bands at 50 kDa and 120 kDa for both canine thyroid gland and HTori-3 cells.

cell line HTori-3. TSHR showed bands at 50 and 60 kDa for healthy canine thyroid gland and at 60 kDa for HTori-3 cells. NIS revealed bands at 50 kDa for canine thyroid gland and at 58 kDa for HTori-3 cells. Pendrin showed a band at 85 kDa for both healthy canine thyroid gland and HTori-3 cells. TPO showed bands at 50 kDa and 120 kDa for both canine thyroid gland and HTori-3 cells (Fig. 2).

The predicted molecular weight of NIS in dogs is 68 kDa (Uniprot E2RMU7) and in humans 68.6 kDa (Uniprot Q92911) to 87 kDa have been reported.^{17,31,39} The predicted molecular weight of TSHR in dogs is 86.4 kDa (Uniprot P14763) and in humans 84 to 86.8 kDa (Uniprot P16473).^{32,39} The predicted molecular weight of pendrin in humans and dogs is 85.8 kDa (Uniprot O43511, E2RRQ1) and the predicted molecular weight of TPO in dogs is 101.4 kDa (Uniprot Q8HYB7) and in humans 100 to 110 kDa (Uniprot P07202).^{15,26,33,34}

Validation of Immunohistochemistry

Immunohistochemistry for all antibodies showed specific positive labeling in human HTori-3 cells as well as in healthy canine thyroid gland. Specific positive labeling was also observed in the additional canine positive controls: salivary gland (NIS), stomach (NIS), and skin (TSHR). Describing the IHC labeling in detail, HTori-3 cells showed moderate membranous and weak cytoplasmic labeling for TSHR, weak membranous and cytoplasmic labeling for NIS, strong membranous and moderate cytoplasmic labeling for pendrin, and very weak



Figures 3–6. Healthy thyroid gland, dog. Immunoperoxidase; AEC chromogen with hematoxylin counterstain. **Figure 3.** Thyroid follicular cells show weak to moderate cytoplasmic immunolabeling for thyrotropin receptor. **Figure 4.** Strong immunolabeling for sodium iodide symporter is concentrated on the membrane of thyroid follicular cells, in addition to moderate cytoplasmic labeling. **Figure 5.** Thyroid follicular cells show strong cytoplasmic immunolabeling for pendrin. **Figure 6.** Thyroid follicular cells show weak cytoplasmic immunolabeling for thyroid peroxidase.

cytoplasmic labeling for TPO (Suppl Figs. S1–S4). In healthy canine thyroid gland, thyroid follicular cells showed weak to moderate cytoplasmic labeling for TSHR, weak cytoplasmic labeling for TPO, moderate cytoplasmic labeling for NIS, and strong cytoplasmic labeling for pendrin (Figs. 3–6). For NIS, additional immunolabeling of the basolateral membrane was observed in thyroid follicular cells, stronger than the cytoplasmic labeling (Fig. 4). Parathyroid gland and C-cells were negative for all 4 antibodies. In healthy canine salivary gland and stomach (additional positive controls for NIS), NIS showed labeling of salivary gland ductal epithelial cells and of gastric mucous neck cells (Suppl Figs. S5, S6). In healthy canine skin (additional positive controls for TSHR), TSHR showed labeling in epidermal and hair follicle keratinocytes and hair follicle mesenchyme (Suppl Fig. S7). No immunolabeling was observed in any of the respective negative controls: healthy canine small intestine (TSHR), skin, brain, liver, and lymph nodes (NIS and TPO), and skin, liver, and lymph nodes (pendrin). Furthermore, the sections incubated with PBS without primary antibody remained unlabeled for all antibodies (Suppl Figs. S8–S10).

IHC of Organoids and Primary Tumors

The results of the IHC of the 3 primary follicular cell carcinomas (follicular, compact, and follicular-compact) and 3

Table 1. Immunohistochemistry Results for Thyrotropin receptor (TSHR), Sodium Iodide Symporter (NIS), Pendrin, and Thyroid Peroxidase (TPO) in 3 Primary Canine Follicular Cell Thyroid Carcinomas (FTC) and in 3 Organoid Lines Derived From These Tumors. Case 1, Compact FTC; Case 2, Follicular-Compact FTC; Case 3, Follicular FTC.

Antibody	Section (primary tumor/organoid) ^a	Percentage of positive cells ^b	Labeling intensity ^c
TSHR	Follicular FTC	2	2
	Organoid	3	3
	Compact FTC	3	2
	Organoid	3	2
	Follicular-compact FTC	2	2
	Organoid	3	3
NIS	Follicular FTC	1	2
	Organoid	3	3
	Compact FTC	3	1
	Organoid	3	2
	Follicular-compact FTC	3	3
	Organoid	3	1
Pendrin	Follicular FTC	1	2
	Organoid	3	3
	Compact FTC	3	1
	Organoid	3	3
	Follicular-compact FTC	2	1
	Organoid	3	3
TPO	Follicular FTC	1	1
	Organoid	3	2
	Compact FTC	1	1
	Organoid	3	2
	Follicular-compact FTC	1	1
	Organoid	3	3

^aCase 1 = compact FTC; Case 2 = follicular-compact FTC; Case 3 = follicular FTC.

^b0 = no positive cells; 1 = 1% to 33% positive cells; 2 = 33% to 66% positive cells; 3 = 67% to 100% positive cells.

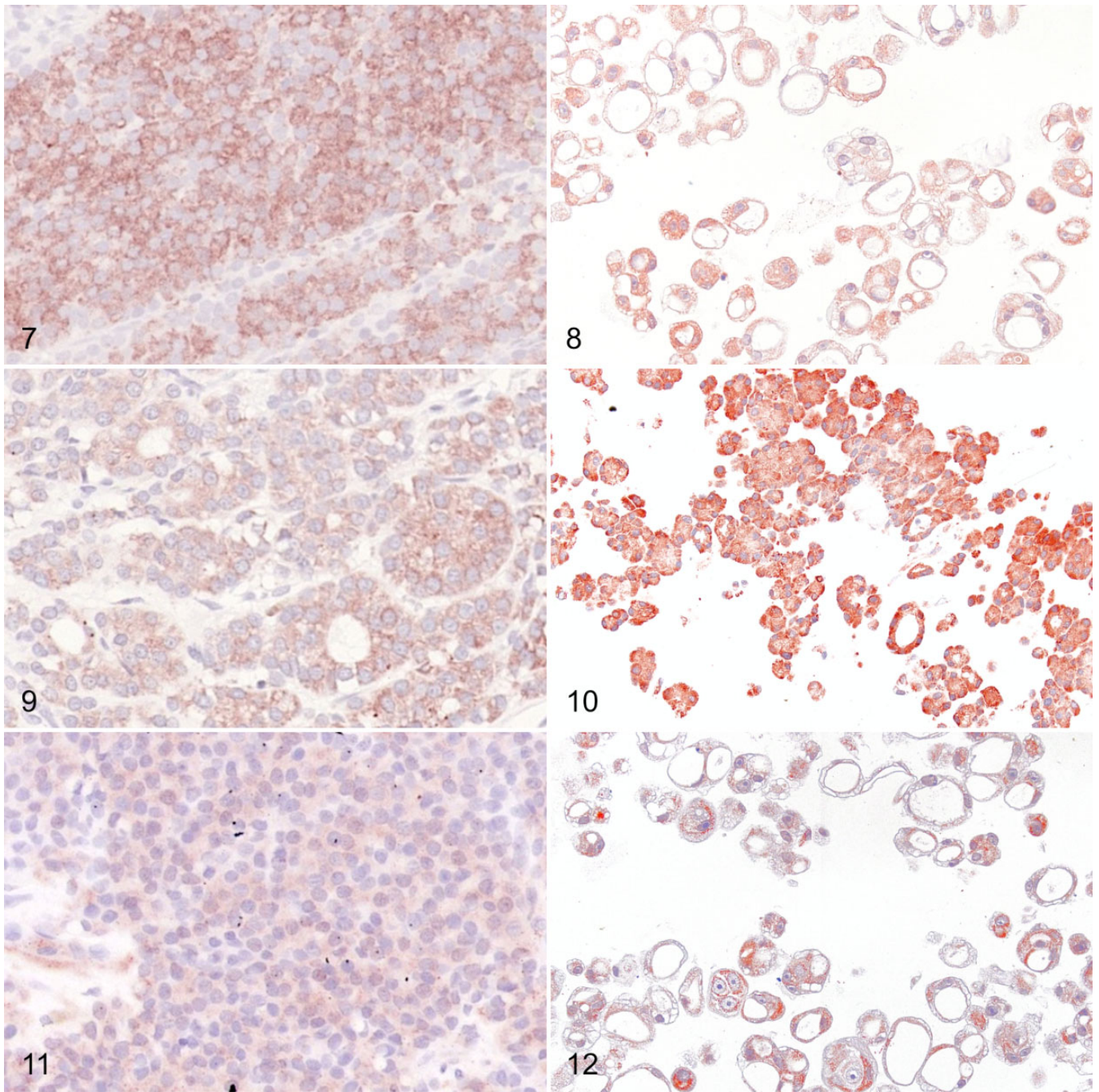
^c0 = negative; 1 = weak; 2 = moderate; 3 = strong.

organoid lines derived from these tumors are summarized in Table 1 and illustrated in Figures 7 to 16. All tumors and organoid lines showed at least weak expression of all markers tested. Distinct labelling patterns were mostly consistent between primary tumors and the corresponding organoids.

Discussion

In this study, IHC protocols were established for TSHR, NIS, pendrin, and TPO in canine tissue. To the best of our knowledge, this is the first study to validate IHC for such a complete group of proteins involved in the uptake of iodine and thyroid hormone production in dogs. Furthermore, this study showed that organoids derived from canine FTC conserve the expression of these proteins and provide a new in vitro model to investigate modulation of iodine uptake. Such a model may help to improve and optimize radioiodine therapy for canine thyroid follicular carcinoma.

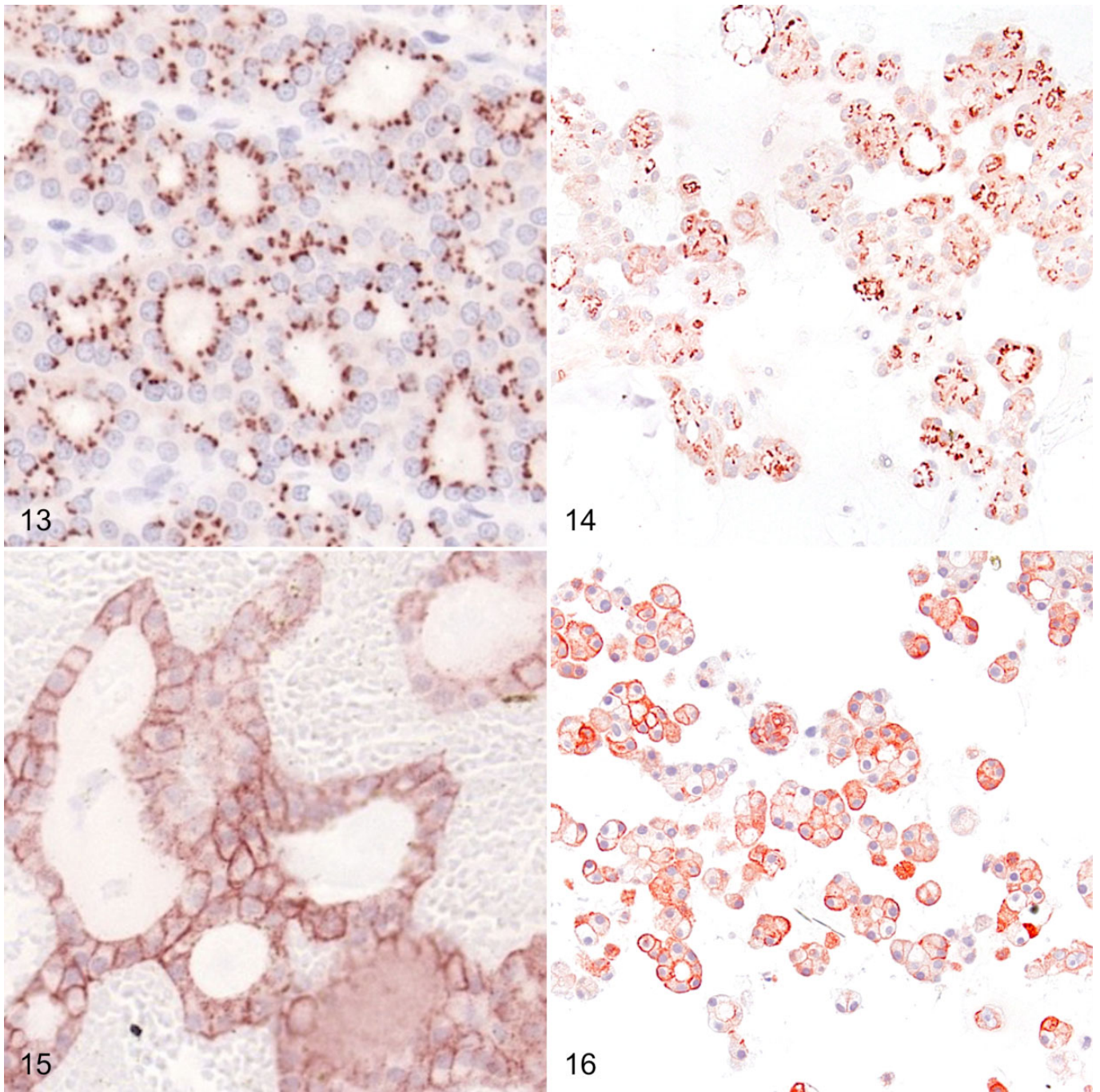
In order to confirm that our antibodies raised against human proteins could detect the target proteins, we performed western



Figures 7–8. Compact follicular cell thyroid carcinoma (FTC), dog, case 1, and organoids derived from this tumor. Both primary tumor cells (Fig. 7) and organoid cells (Fig. 8) show moderate to strong cytoplasmic labeling for thyrotropin receptor. Immunoperoxidase; AEC chromogen with hematoxylin counterstain. **Figures 9–10.** Follicular-compact FTC, dog, case 2, and organoids derived from this tumor. Primary tumor cells (Fig. 9) display moderate cytoplasmic immunolabeling for pendrin, while organoid cells (Fig. 10) show strong cytoplasmic labeling. Immunoperoxidase; AEC chromogen with hematoxylin counterstain. **Figures 11–12.** Compact follicular cell thyroid carcinoma (FTC), dog, case 1, and organoids derived from this tumor. Weak cytoplasmic immunolabeling for thyroid peroxidase in the primary tumor (Fig. 11), and moderate to strong cytoplasmic immunolabeling in the organoids (Fig. 12). Immunoperoxidase; AEC chromogen with hematoxylin counterstain.

blot and IHC on the HTori-3 human thyroid cell line, which expresses features of thyroid epithelial function, including iodide trapping and thyroglobulin production.¹ Our results show that the antibodies used could detect not only human but

also canine TSHR, NIS, pendrin, and TPO. Western blot for NIS showed bands at 50 kDa in canine healthy thyroid gland and around 58 kDa in the human cell line. Although NIS has a molecular mass of approximately 87 kDa in its fully



Figures 13–14. Follicular-compact follicular cell thyroid carcinoma (FTC), dog, case 2, and organoids derived from this tumor. Both primary tumor cells (Fig. 13) and organoid cells (Fig. 14) display focal granular immunolabeling for sodium iodide symporter (NIS) in the apical cytoplasm. Immunoperoxidase; AEC chromogen with hematoxylin counterstain. **Figures 15–16.** Follicular FTC, dog, case 3. Both primary tumor cells (Fig. 15) and organoid cells (Fig. 16) show a strong membranous and a weak cytoplasmic labelling for NIS. Immunoperoxidase; AEC chromogen with hematoxylin counterstain.

glycosylated form, several studies have shown that it is possible to detect a partially glycosylated form with western blot at 50 to 56 kDa.^{14,17,39} Western blot for TSHR showed bands at 50 and 60 kDa in the canine healthy thyroid gland and 60 kDa in the HTori-3 cells. Although the molecular mass of TSHR is 84 kDa, a glycosylated form at 63 kDa and a non-glycosylated

form at 50 kDa have been detected by western blot in human thyroid gland tissue.^{21,39} We believe our western blot detected the glycosylated form of TSHR in HTori-3 cells and both glycosylated and non-glycosylated forms in canine healthy thyroid gland, as already described in previous studies.^{21,39} The predicted molecular weight for pendrin of 85 kDa corresponded to

the observed bands in both healthy canine thyroid gland and HTori-3 thyroid cell line. Western blot of TPO revealed bands at 50 and 120 kDa in both canine healthy thyroid gland and the HTori-3 human cell line. The predicted molecular weight of TPO is approximately 100 to 110 kDa.^{15,26} The detection of TPO bands at slightly higher molecular weight than 116 kDa has been attributed to varying reducing conditions of the technique.²³ Simultaneously, the detection of bands of TPO at lower molecular weights (around 54 kDa) has also been described to correspond to TPO cleavage during sample solubilization and trypsination.^{23,38} Further developments in the project could include the use of synthetic proteins, both full-sized and isoforms in various states of glycosylation, as a positive control for western blot. In addition, mass spectrometry could help in the identification of the different bands.

Our results correlated with the reported human expression patterns for all markers. For example, we observed specific NIS immunolabeling in mucous neck cells of canine stomach and in ductal epithelial cells of canine salivary gland, identical to human tissues. This finding is in agreement with the fact that these organs typically show iodine uptake in canine scintigraphy studies.^{2,28} Furthermore, TSHR immunolabeling was present in keratinocytes of the epidermis and hair follicles, and in the mesenchyme of hair follicles of canine skin. Previous human studies have shown that intracutaneous TSHR is fully functional in situ, and that hair follicle of female individuals are direct targets for nonclassical, extrathyroidal TSH bioregulation.^{5,9} These findings additionally corroborate our western blot results; thus, the specificity of these antibodies for the canine protein orthologues can be presumed.

The second aim of this study was to investigate the expression of TSHR, NIS, pendrin, and TPO in canine follicular thyroid carcinomas and organoids derived from these tumors. Although TSHR is a membranous protein, we mainly observed cytoplasmic labeling in follicular cells in canine FTCs, but also in healthy thyroid gland. This is in agreement with several studies in both humans and dogs.^{12,22}

NIS also performs its function in the basolateral membrane of the thyrocyte. In our study, we observed basolateral membranous immunolabeling as well as cytoplasmic immunolabeling in both healthy canine thyroid gland and in FTC cells, although basolateral labeling was stronger. In humans, immunolabeling for NIS is also described at the basolateral membrane in healthy thyroid gland and in follicular carcinoma.^{2,12}

Although pendrin and TPO are functional at the apical membrane of thyroid follicular cells, we observed diffuse cytoplasmic labeling of these cells with both markers in healthy canine thyroid gland and in FTC cells as reported in humans.^{12,25,27}

Organoids derived from canine FTC showed immunolabeling for TSHR, NIS, pendrin, and TPO comparable to the primary tumors. This proves that these proteins are expressed in the cultured organoids and could constitute an interesting in vitro model for research on modulation of iodine uptake and improvement of radioiodine therapy. Interestingly, the labeling intensity for all markers was commonly stronger in the organoids than in the primary tumors. This could be explained by

the fact that iodine was not included in the culture medium, and these proteins were overexpressed. Other explanations could be that organoids originated from a part of the tumor with higher protein expression than the part taken for the paraffin block, or that the disparities in expression are caused by different micro-environmental conditions during fixation in formaldehyde due to volume differences.

In conclusion, antibodies directed against human TSHR, NIS, pendrin, and TPO are suitable to detect the canine orthologues. IHC protocols using the validated antibodies were established for canine healthy thyroid gland tissue, FTCs, and organoids derived from FTCs. FTC organoids conserve expression of these proteins and hence potentially constitute an in vitro model to perform research on modulation of iodine uptake and improvement of radioiodine therapy for thyroid cancer.

Acknowledgements

We thank Sohvi Blatter and Olivia Richard, who trimmed the tumor samples, and Erika Bürgi, Manuela Bozzo, and Bettina de Breuyn for preparing the slides for IHC. We thank Paola Francica and Nadja Gerber for their support in western blot and IHC, and Renaud Sylvain Maire for assisting with 2D cell cultures (HTori-3). We thank Marine Inglebert and Ismar Klebic for their support in the culture of organoids.

Declaration of Conflicting Interests

The author(s) declared no potential conflicts of interest with respect to the research, authorship, and/or publication of this article.

Funding

The author(s) disclosed receipt of the following financial support for the research, authorship, and/or publication of this article: This work was supported by Albert Heim Stiftung, the Tierärztliche Verrechnungsstelle (TVS), ECVIM-CA Clinical Studies Fund, the European Society of Veterinary Endocrinology, and the Small Animal Clinic of the Vetsuisse Faculty, University of Bern.

ORCID iD

Jana Jankovic  <https://orcid.org/0000-0002-5469-9975>

Martina Dettwiler  <https://orcid.org/0000-0001-9404-7122>

Simon April-Monn  <https://orcid.org/0000-0002-8941-7990>

References

1. Ajjan RA, Watson PF, Weetman AP. Detection of IL-12, IL-13, and IL-15 messenger ribonucleic acid in the thyroid of patients with autoimmune thyroid disease. *J Clin Endocrinol Metab.* 1997;**82**(2):666–669.
2. Altorjay Á, Dohán O, Szilágyi A, et al. Expression of the Na⁺/I⁻ symporter (NIS) is markedly decreased or absent in gastric cancer and intestinal metaplastic mucosa of Barrett esophagus. *BMC Cancer.* 2007;**7**:5.
3. April-Monn SL, Wiedmer T, Skowronska M, et al. Three-dimensional primary cell culture: a novel preclinical model for pancreatic neuroendocrine tumors. *Neuroendocrinology.* 2021;**111**(3):273–287. doi:10.1159/000507669
4. Bell A, Gagnon A, Grunder L, et al. Functional TSH receptor in human abdominal preadipocytes and orbital fibroblasts. *Am J Physiol Cell Physiol.* 2000;**279**(2):C335–C340.
5. Bodo E, Kromminga A, Biro T, et al. Human female hair follicles are a direct, nonclassical target for thyroid-stimulating hormone. *J Invest Dermatol.* 2009;**129**(5):1126–1139.

6. Brodey RS, Kelly DF. Thyroid neoplasms in the dog. A clinicopathologic study of fifty-seven cases. *Cancer*. 1968;**22**(2):406–416.
7. Broutier L, Masrogiovanni G, Verstegen MM, et al. Human primary liver cancer derived organoid cultures for disease modeling and drug screening. *Nat Med*. 2017;**23**(12):1424–1435.
8. Campos M, Ducatelle R, Rutteman G, et al. Clinical, pathologic, and immunohistochemical prognostic factors in dogs with thyroid carcinoma. *J Vet Inter Med*. 2014;**28**(6):1805–1813.
9. Cianfarani F, Baldini E, Cavalli A, et al. TSH receptor and thyroid-specific gene expression in human skin. *J Invest Dermatol*. 2010;**130**(1):93–101.
10. Drost J, Clevers H. Organoids in cancer research. *Nat Rev Cancer*. 2018;**18**(7):407–418.
11. Drvota V, Janson A, Norman C, et al. Evidence for the presence of functional thyrotropin receptor in cardiac muscle. *Biochem Biophys Res Commun*. 1995;**211**(2):426–431.
12. Faggiano A, Caillou B, Lacroix L, et al. Functional characterization of human thyroid tissue with immunohistochemistry. *Thyroid*. 2007;**17**(3):203–211.
13. Finotello R, Schiavo L, Ressel L, et al. Lipoygenase-5 expression in canine urinary bladder: normal urothelium, cystitis and transitional cell carcinoma. *J Comp Pathol*. 2019;**170**:1–9.
14. Galrao AL, Camargo RY, Friguglietti CU, et al. Hypermethylation of a new distal sodium/iodide symporter (NIS) enhancer (NDE) is associated with reduced NIS expression in thyroid tumors. *J Clin Endocrinol Metab*. 2014;**99**(6):E944–E952.
15. Godlewska M, Krasuska W, Czarnocka B. Biochemical properties of thyroid peroxidase (TPO) expressed in human breast and mammary-derived cell lines. *PLoS One*. 2018;**13**(3):e0193624.
16. Henderson BE, Ross RK, Casagrande JT. Endogenous hormones as a major factor in human cancer. *Cancer Res*. 1982;**42**(8):3232–3239.
17. Hingorani M, Spitzweg C, Vassaux G, et al. The biology of the sodium iodide symporter and its potential for targeted gene delivery. *Curr Cancer Drug Targets*. 2010;**10**(2):242–267.
18. Kiupel M, Capen C, Miller M, et al. Histological classification of the endocrine system of domestic animals. In: Schulman FY, ed. *WHO International Histological Classification of Tumors of Domestic Animals*. 2nd ed. Armed Forces Institute of Pathology; 2008:25–39.
19. Klein JR. Physiological relevance of thyroid stimulating hormone and thyroid stimulating hormone receptor in tissues other than the thyroid. *Autoimmunity*. 2003;**36**(6-7):417–421.
20. Mondal S, Raja K, Schweizer U, et al. Chemistry and biology in the biosynthesis and action of thyroid hormones. *Angew Chem Int Ed Engl*. 2016;**55**(27):7606–7630.
21. Patindbadla SA, Seetharamaiah GS, Dallas JS, et al. Differential reactivities of recombinant glycosylated ectodomains of mouse and human thyrotropin receptors with patient autoantibodies. *Endocrinology* 1997;**138**(4):1559–1566.
22. Pessina P, Castillo V, Sartore I, et al. Semiquantitative immunohistochemical marker staining and localization in canine thyroid carcinoma and normal thyroid gland. *Vet Comp Oncol*. 2016;**14**(3):e102–e112.
23. Portmann L, Fitch FW, Havran W, et al. Characterization of the thyroid microsomal antigen, and its relationship to thyroid peroxidase, using monoclonal antibodies. *J Clin Invest*. 1988;**81**(4):1217–1224.
24. Riedel C, Levy O, Carrasco N. Post-transcriptional regulation of the sodium/iodide symporter by thyrotropin. *J Biol Chem*. 2001;**276**(24):21458–21463.
25. Senou M, Khalifa C, Thimmesch M, et al. A coherent organization of differentiation proteins is required to maintain an appropriate thyroid function in the pendred thyroid. *J Clin Endocrinol Metab*. 2010;**95**(8):4021–4030.
26. Skopek E, Patzl M, Nachreiner RF. Detection of autoantibodies against thyroid peroxidase in serum samples of hypothyroid dogs. *Am J Vet Res*. 2006;**67**(5):809–814.
27. Skubis-Zegadlo J, Nikodemska A, Przytul E, et al. Expression of pendrin in benign and malignant human thyroid tissues. *Br J Cancer*. 2005;**93**(1):144–151.
28. Spitzweg C, Joba W, Schriever K. Analysis of human sodium iodide symporter immunoreactivity in human exocrine glands. *J Clin Endocrinol Metab*. 1999;**84**(11):4178–4184.
29. Tuncel M. Thyroid stimulating hormone receptor. *Mol Imaging Radionucl Ther*. 2017;**26**(1):87–91.
30. Turrel JM, McEntee MC, Burke BP, et al. Sodium iodide I 131 treatment of dogs with nonresectable thyroid tumors: 39 cases (1990–2003). *J Am Vet Med Assoc*. 2006;**229**(4):542–548.
31. UniProtKB Protein knowledgebase. Solute carrier family 5 member 5. Accessed April 2018. <https://www.uniprot.org/uniprot/E2RMU7>
32. UniProtKB Protein knowledgebase. Thyrotropin receptor. Accessed April 2018. <https://www.uniprot.org/uniprot/P14763>
33. UniProtKB Protein knowledgebase. Pendrin. Accessed April 2018. <https://www.uniprot.org/uniprot/E2RRQ1>
34. UniProtKB Protein knowledgebase. Thyroid peroxidase. Accessed April 2018. <https://www.uniprot.org/uniprot/Q8HYB7>
35. Williams DW, Wynford-Thomas D, Williams ED. Control of human thyroid follicular cell proliferation in suspension and monolayer culture. *Mol Cell Endocrinol*. 1987;**51**(1–2):33–40.
36. Worth AT, Zuber RM, Hocking M. Radioiodide (131I) therapy for the treatment of canine thyroid carcinoma. *Aust Vet J*. 2005;**83**(4):208–214.
37. Wucherer LK, Wilke V. Thyroid cancer in dogs: an update based on 638 cases (1995–2005). *J Am Anim Hosp Assoc*. 2010;**46**(4):249–254.
38. Yokoyama N, Taurug A. Porcine thyroid peroxidase: relationship between the native enzyme and an active, highly purified tryptic fragment. *Mol Endocrinol*. 1988;**2**(9):838–844.
39. Zabczynska M, Kozłowska K, Pocheć E. Glycosylation in the thyroid gland: vital aspects of glycoprotein function in thyrocyte physiology and thyroid disorders. *Int J Mol Sci*. 2018;**19**(9):2792.

7 Curriculum vitae

8 List of publications

April-Monn, S.L., Detjen ,K., Kirchner, P., Trippel, M.A., Grob, T., Maire, R.S., Kollár, A., Kunze, K., Horst, D., Sadowski, M.C., Schrader, J., Marinoni, I., Wiedenmann, B., and Perren A. (2022). Tumoroids of advanced high-grade neuroendocrine neoplasms mimic patient chemotherapy responses and guide the design of personalized combination therapies. *Under review*

A revised and expanded version of this manuscript is deposited on BioRxiv at <https://www.biorxiv.org/content/10.1101/2022.12.10.519855v2.full.pdf+html>

April-Monn, S.L., Kirchner, P., Wiedenmann, B., Perren, A. (2022). Matching therapy response in patients and patient-derived tumoroids of advanced high-grade neuroendocrine neoplasms. *Gene Expression Omnibus GSE213504*

Gulde S., Foscarini A., **April-Monn S.L.**, Genio E., Marangelo A., Satam S., Helbling D., Falconi M., Toledo R.A., Schrader J., Perren A., Marinoni I., & Pellegata N.S. (2022). Combined Targeting of Pathogenetic Mechanisms in Pancreatic Neuroendocrine Tumors Elicits Synergistic Antitumor Effects. *Cancers*, 14(22), 5481. <https://doi.org/10.3390/cancers14225481>

Zindel, J., Mittner, J., Bayer, J., **April-Monn, S. L.**, Kohler, A., Nusse, Y., Dosch, M., Büchi, I., Sanchez-Taltavull, D., Dawson, H., Gomez de Agüero, M., Asahina, K., Kubes, P., Macpherson, A. J., Stroka, D., & Candinas, D. (2021). Intraperitoneal microbial contamination drives post-surgical peritoneal adhesions by mesothelial EGFR-signaling. *Nature Communications*, 12(1), 7316. <https://doi.org/10.1038/s41467-021-27612-x>

April-Monn, S. L., Andreasi, V., Schiavo Lena, M., Sadowski, M. C., Kim-Fuchs, C., Buri, M. C., Ketkar, A., Maire, R., Di Domenico, A., Schrader, J., Muffatti, F., Doglioni, C., Partelli, S., Falconi, M., Perren, A., & Marinoni, I. (2021). EZH2 Inhibition as New Epigenetic Treatment Option for Pancreatic Neuroendocrine Neoplasms (PanNENs). *Cancers*, 13(19), 5014. <https://doi.org/10.3390/cancers13195014>

Jankovic, J., Dettwiler, M., Fernández, M. G., Tièche, E., Hahn, K., **April-Monn, S.**, Dettmer, M. S., Kessler, M., Rottenberg, S., & Campos, M. (2021). Validation of Immunohistochemistry for Canine Proteins Involved in Thyroid Iodine Uptake and Their Expression in Canine Follicular Cell Thyroid Carcinomas (FTCs) and FTC-Derived Organoids. *Veterinary Pathology*, 58(6), 1172–1180. <https://doi.org/10.1177/03009858211018813>

April-Monn, S. L., Wiedmer, T., Skowronska, M., Maire, R., Schiavo Lena, M., Trippel, M., Di Domenico, A., Muffatti, F., Andreasi, V., Capurso, G., Doglioni, C., Kim-Fuchs, C., Gloor, B., Zatelli, M. C., Partelli, S., Falconi, M., Perren, A., & Marinoni, I. (2020). Three-Dimensional Primary Cell Culture: A Novel Preclinical Model for Pancreatic Neuroendocrine Tumors. *Neuroendocrinology*, 111(3), 273–287. <https://doi.org/10.1159/000507669>

Liu, H., He, Z., **April, S. L.**, Trefny, M. P., Rougier, J.-S., Salemi, S., Olariu, R., Widmer, H. R., & Simon, H.-U. (2019). Biochemical re-programming of human dermal stem cells to neurons by increasing mitochondrial membrane potential. *Cell Death & Differentiation*, 26(6), 1048–1061. <https://doi.org/10.1038/s41418-018-0182-8>

9 Declaration of originality

Declaration of Originality

Last name, first name: April-Monn, Simon

Matriculation number: 07-592-462

I hereby declare that this thesis represents my original work and that I have used no other sources except as noted by citations.

All data, tables, figures and text citations which have been reproduced from any other source, including the internet, have been explicitly acknowledged as such.

I am aware that in case of non-compliance, the Senate is entitled to withdraw the doctorate degree awarded to me on the basis of the present thesis, in accordance with the “Statut der Universität Bern (Universitätsstatut; UniSt)”, Art. 69, of 7 June 2011.

Bern, 22.11.2022

Place, date

Signature